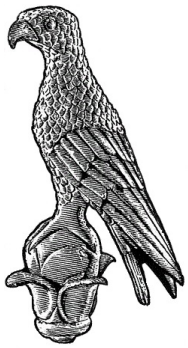

UNIVERSITY OF IOANNINA
SCHOOL OF SCIENCES
DEPARTMENT OF PHYSICS

Study of ^{241}Am(n,f) reaction at the CERN n_TOF facility

Zinovia Eleme

PH.D. THESIS

IOANNINA 2022

This research is co-financed by Greece and the European Union (European Social Fund- ESF) through the Operational Programme «Human Resources Development, Education and Lifelong Learning» in the context of the project "Strengthening Human Resources Research Potential via Doctorate Research – 2nd Cycle" (MIS-5000432), implemented by the State Scholarships Foundation (ΙΚΥ).

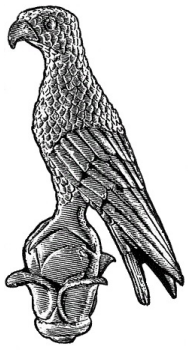

ΠΑΝΕΠΙΣΤΗΜΙΟ ΙΩΑΝΝΙΝΩΝ
ΣΧΟΛΗ ΘΕΤΙΚΩΝ ΕΠΙΣΤΗΜΩΝ
ΤΜΗΜΑ ΦΥΣΙΚΗΣ

Μελέτη της αντίδρασης $^{241}\mathbf{Am(n,f)}$ στις εγκαταστάσεις n_TOF του CERN

Ζηνοβία Ελεμέ

ΔΙΔΑΚΤΟΡΙΚΗ ΔΙΑΤΡΙΒΗ

ΙΩΑΝΝΙΝΑ 2022

Το έργο συγχρηματοδοτείται από την Ελλάδα και την Ευρωπαϊκή Ένωση (Ευρωπαϊκό Κοινωνικό Ταμείο) μέσω του Επιχειρησιακού Προγράμματος «Ανάπτυξη Ανθρώπινου Δυναμικού Εκπαίδευση και Διά Βίου Μάθηση», στο πλαίσιο της Πράξης «Ενίσχυση του ανθρώπινου ερευνητικού δυναμικού μέσω της υλοποίησης διδακτορικής έρευνας- 2ος κύκλος» (MIS-5000432), που υλοποιεί το Ίδρυμα Κρατικών Υποτροφιών (ΙΚΥ).

Επιχειρησιακό Πρόγραμμα
Ανάπτυξη Ανθρώπινου Δυναμικού,
Εκπαίδευση και Διά Βίου Μάθηση
Με τη συγχρηματοδότηση της Ελλάδας και της Ευρωπαϊκής Ένωσης

Three-member advisory committee:

- Nikolaos Patronis, Associate Professor, Physics Department, University of Ioannina, Greece **(Supervisor)**.
- Roza Vlastou, Emeritus Professor, Physics Department, National Technical University of Athens, Greece.
- Michael Kokkoris, Professor, Physics Department, National Technical University of Athens, Greece.

Seven-member PhD thesis examination committee:

- Nikolaos Patronis, Associate Professor, Physics Department, University of Ioannina, Greece **(Supervisor)**.
- Roza Vlastou, Emeritus Professor, Physics Department, National Technical University of Athens, Greece.
- Michael Kokkoris, Professor, Physics Department, National Technical University of Athens, Greece.
- Nicola Colonna, Director of research, Instituto Nazionale di Fisica Nucleare (INFN), Sezione di Bari, Bari, Italy.
- Nikolaos Nicolis, Associate Professor, Physics Department, University of Ioannina, Greece.
- Panagiotis Kokkas, Professor, Physics Department, University of Ioannina, Greece.
- Ioannis Papadopoulos, Associate Professor, Physics Department, University of Ioannina, Greece.

"I have passed through fire and deep water, since we parted. I have forgotten much that I thought I knew, and learned again much that I had forgotten."

— J.R.R. Tolkien, *The Lord of the Rings*

Acknowledgements

I believe there is no secret recipe or magic ingredient so that someone can complete the cycle of research years that we call PhD studies. But on the other hand, it is very important for the researcher in the early stages of his/her career to be surrounded by people that can be companions through this long journey. In the next paragraphs, I would like to thank those who generously shared with me some of their time, wisdom, expertise, smiles and encouragement and contributed to this work.

First of all, I would like to thank my supervisor Nikolas Patronis, who guided all these years patiently my steps in the research field. He is such a brilliant physicist that transmits me enthusiasm for this science, shares his knowledge with every conversation we have and he is always there to help me deal with the challenges of this work. Our collaboration over the years, which began with my Diploma and continued through the M.Sc. and PhD, will always be cherished in my memory.

Moreover, I owe special thanks to Roza Vlastou and Michael Kokkoris for their advice and insightful instructions all these years of our collaboration. Their encouragement as well as their uplifting spirit over critical moments was extremely valuable for me.

I would also like to thank Xenofon Aslanoglou who all these years is a teacher for me and he is always willing to give me valuable advice and knowledge. His presence in the laboratory gives an aura of optimism that is priceless.

From the depths of my heart, I would like to express my gratitude to my "little boss" at CERN, who is none other than Athanasios Stamatopoulos. Thanos undertook the task of training me before and during the experiment, imparting knowledge and hands-on skills that were necessary both for conduction the experiment as well as for the data analysis process.

A special thank you is reserved for Andreas Tsinganis, who as the initiator of this experiment, was always available and willing to offer his help in navigating through the difficulties of this project. I admire and appreciate Andrea's character because his comments and suggestions were always to the point.

Furthermore, I would like to thank Nicola Colonna, Enrico Chiaveri, Laurent Tassan-Got and Daniela Macina for their support and scientific advice during my stay at CERN. It was a pleasure for me to meet them all. The realization of the experiment and the days I spent at CERN would not be the same without the support of friends and colleagues within the n_TOF Collaboration with whom I had the pleasure to work with. I thank Veatriki Michalopoulou, Sebastian Urlass, Samuel Bennet, Adhitya Sekhar, Alice Manna, Michael Bacak, Marta Sabatè-Gillarte, Massimo Barbagallo, Federica Mingrone, Mario Mastromarco and the rest of the n_TOF local team of 2018.

Moreover, I would like to say a special thank you to Peter Schillebeeckx, Jan Heyse, Goedele Sibbens, Andre Moens, David Vanleeuw and Carlos Paradela-Dobarro from the EC-JRC Geel. Their hospitality during my visit at Geel and their warm welcome in the Target Preparation Laboratory for the characterization of the samples of my experiment, will be forever memorable.

I am grateful to Paraskevi Dimitriou for her valuable guidance in the theoretical calculations of this work. With her aid, advice, optimism and kindness during my visit in IAEA in Vienna, in the middle of a Covid-19 pandemic period, she has earned my appreciation and admiration.

Likewise, I would like to thank the members of my group in Nuclear Physics Laboratory in Ioannina, with whom I had the pleasure to work all these years in similar or parallel projects. My special thanks go to Efstathia Georgali, Elisso Stamati, Maria Peoviti and Stella Goula. Together I believe we spent beautiful moments inside and outside the office. Like an original "Πυρηνικίνα", I would also like to thank Paris Gianneios and George Alestas for the discussions we had about relevant and unrelated aspects of the life of a PhD student.

I would like to thank Lavrentios Kazantzidis, for supporting me and encouraging me all these years and for making this period of my life more brighter. Finally, I would like to thank my family and close friends, for making everything better with their love, trust and support.

All these little ingredients, were exactly what it took for my to close this cycle of my life by working in a pleasant atmosphere, overcoming difficulties and turn the teamwork into dreamwork.

To my parents, Yiannis and Katerina

Contents

List of Publications

In Scientific Proposals:

- N. Patronis, **Z. Eleme**, M. Diakaki, A. Tsinganis, R. Vlastou, M. Kokkoris, M.E. Stamati, V. Michalopoulou, A. Stamatopoulos, M. Barbagallo, N. Colonna, J. Heyse, M. Mastromarco, A. Mengoni, A. Moens, G. Noguere, A.J. Praena, P. Schillebeeckx, G. Sibbens, L. Tassan-Got and D. Vanleeuw, "Measurement of the fission cross-section of ^{243}Am at EAR-1 and EAR-2 of the CERN n_TOF facility", CERN-INTC-2020-048, INTC-P-566, (2020), https://cds.cern.ch/record/2730930

In Peer-Reviewed Journals:

- E. Georgali, **Z. Eleme**, N. Patronis, X. Aslanoglou, M. Axiotis, M. Diakaki, V. Foteinou, S. Harissopulos, A. Kalamara, M. Kokkoris, A. Lagoyannis, N. G Nicolis, G. Provatas, A. Stamatopoulos, S. Stoulos, A. Tsinganis, E. Vagena, R. Vlastou and S. M. Vogiatzi, "The (n,2n) reaction for the lightest stable erbium isotope 162Er from reaction threshold up to 19 MeV", Physical Review C 98, 014622 (2018), DOI:10.1103/PhysRevC.98.014622

- E. Georgali, N. Patronis, A. Anastasiadis, X. Aslanoglou, M. Axiotis, **Z. Eleme**, S. Harissopulos, A. Kalamara, K. Karfopoulos, M. Kokkoris, A. Lagoyannis, M. Peoviti, C. Potiriadis, M. I. Savva, I. E. Stamatelatos, M. E. Stamati, A. Stamatopoulos, E. Vagena, T. Vasilopoulou and R. Vlastou, "Experimental study of the 165Ho(n, 2n) reaction: Cross section measurements for the population of the 164Ho ground state and isomeric state from the threshold up to 20 MeV", Physical. Review C 102, 034610 (2020), DOI:10.1103/PhysRevC.102.034610

- **Z. Eleme**, N. Patronis, A. Stamatopoulos, A. Tsinganis, M. Kokkoris, V. Michalopoulou, M. Diakaki, R. Vlastou, L Tassan-Got, N. Colonna, J. Heyse et al., "First results of the ^{241}Am(n,f) cross section measurement at the Experimental Area 2 of the n_TOF facility at CERN", EPJ Web Conf. 239 05014 (2020), DOI:10.1051/epjconf/202023905014

- V. Michalopoulou, M. Axiotis, S. Chasapoglou, **Z. Eleme**, G. Gkatis, A. Kalamara, M. Kokkoris, A. Lagoyannis, N. Patronis, A. Stamatopoulos, A. Tsantiri and R. Vlastou, "Measurement of the ^{232}Th(n,f) cross section with quasi-monoenergetic neutron beams in the energy range 2–18 MeV", Eur. Phys. J. A, 57, 306 (2021), DOI:10.1140/epja/s10050-021-00613-6

In Conference Proceedings:

- N. Patronis, X. Aslanoglou, M. Axiotis, **Z. Eleme**, V. Foteinou, S. Harissopulos, A. Kalamara, M. Kokkoris, G. Provatas and R. Vlastou "Neutron reaction studies in the rare earth region: First results for the ^{162}Er(n,2n)^{161}Er physics case", HNPS Advances in Nuclear Physics 22, 45-50 (2014), DOI: 10.12681/hnps.1929

- **Z. Eleme**, M. Alexandropoulou, A. Georgiadou, K. Ioannides, M. Kokkoris, N. Patronis, A. Stamatopoulos, K. Stamoulis, A. Tsinganis, R. Vlastou and the nTOF Collaboration, "Determination of the Neutron Beam Spatial Profile at nTOF EAR-2 using the CR-39 Track Detectors", HNPS Advances in Nuclear Physics 23, 28-33 (2015), DOI:10.12681/hnps.1903

- **Z. Eleme**, S. Gerovasili, N. Patronis, E. Georgali, K.G. Ioannides, A. Kalamara, M. Kokkoris, C. Papachristodoulou, T. Stamatopoulos, A. Tsinganis, R. Zanni-Vlastou and the nTOF Collaboration, "Neutron beam spatial profile at nTOF using CR-39 nuclear track detectors", HNPS Advances in Nuclear Physics 25, 109-114 (2017), DOI:10.12681/hnps.1960

- E. Georgali, **Z. Eleme**, N. Patronis, X. Aslanoglou, M. Axiotis, M. Diakaki, V. Foteinou, A. Georgiadou, S. Harissopulos, A. Kalamara, M. Kokkoris, A. Lagoyannis, N. Nikolis, G. Provatas, S. Stoulos, A. Tsinganis, E. Vagena, R. Vlastou and S.M. Vogiatzi, "Study of the ^{162}Er(n,2n)^{161}Er reaction from the reaction threshold up to 19 MeV neutron energy", HNPS Advances in Nuclear Physics 25, 102-108 (2017), DOI:10.12681/hnps.1959

- S. Chasapoglou, V. Michalopoulou, A. Stamatopoulos, A. Kalamara, M. Kokkoris, R. Vlastou, A. Lagoyannis, **Z. Eleme** and N. Patronis, "Study of the ^{234,236}U(n,f) and ^{232}Th(n,f) cross sections in the energy range between 14.8 and 19.2 MeV with Micromegas detectors", HNPS Advances in Nuclear Physics 26, 230-234 (2018), DOI:10.12681/hnps.1826

- A. Kalamara, S. Chasapogloou, V. Michalopoulou, A. Stamatopoulos, **Z. Eleme**, M. Kokkoris, A. Lagoyannis, N. Patronis and R. Vlastou, "Measurement of the ^{234}U(n,f) cross section in the energy range between 14.8 and 17.8 MeV using Micromegas detectors", HNPS Advances in Nuclear Physics 27, 25-32 (2019), DOI:10.12681/hnps.2675

- S. Chasapogloou, A. Tsantiri, A. Kalamara, M. Kokkoris, V. Michalopoulou, A. Stamatopoulos, R. Vlastou, A. Lagoyannis, **Z. Eleme** and N. Patronis, "Study of the ^{232}Th(n,f) cross section at NCSR 'Demokritos' using Micromegas Detectors", HNPS Advances in Nuclear Physics 27, 106-111 (2019), DOI:10.12681/hnps.2994

- E. Georgali, N. Patronis, A. Anastasiadis, M. Axiotis, **Z. Eleme**, S. Harissopulos, A. Kalamara, K. Karfopoulos, M. Kokkoris, A. Lagoyannis, M. Peoviti, C. Potiriadis, M. Savva, I. Stamatelatos, M.E. Stamati, A. Stamatopoulos, T. Vasilopoulou and R. Vlastou, "Study of the ^{165}Ho(n,2n)^{164}Ho reaction at near threshold energies", HNPS Advances in Nuclear Physics 27, 160-167 (2019), DOI:10.12681/hnps.3001

- E. Mitsi, S. Chasapoglou, A. Kalamara, M. Kokkoris, V. Michalopoulou, A. Stamatopoulos, R. Vlastou, A. Lagoyannis, M. Axiotis, N. Patronis and **Z. Eleme**, "A detailed

study of the high energy neutron flux (15-20 MeV) at NCSR "Demokritos" using a BC501A liquid scintillator", HNPS Advances in Nuclear Physics 27, 143-147 (2019), DOI:10.12681/hnps.2996

- **Z. Eleme**, N. Patronis, A. Stamatopoulos, A. Tsinganis, M. Kokkoris, V. Michalopoulou, M. Diakaki, R. Vlastou, L. Tassan-Got, N. Colonna, J. Heyse, M. Barbagallo, M. Mastromarco, D. Macina, E. Chiaveri and the nTOF Collaboration, "Cross section measurement of ^{241}Am(n,f) reaction at the Experimental Area 2 of the nTOF facility at CERN: First Results", HNPS Advances in Nuclear Physics 27, 189-194 (2019), DOI:10.12681/hnps.3008

Abstract

High accuracy cross section data of neutron-induced reactions of minor actinides, are needed over a wide energy range for the feasibility, design and sensitivity studies on innovative nuclear reactors (Accelerator Driven Systems -ADS and Generation IV Fast Neutron Reactors). The concept of these systems is to incinerate/transmutate the existing actinides found in high-level nuclear waste. With the incineration/transmutation, both the half-life of the radioactive isotopes can be reduced as well as the volume of these pollutants or their wastes, so that the final nuclear waste from the reactor material that should be stored is less hazardous. Representing almost 1.8% of the actinide mass in spent PWR UO_X fuel, the ^{241}Am isotope ($T_{1/2} = 433y$) is considered one of the possible candidates for incineration/transmutation. On top of that, its production rate increases within the spent fuel through the β-decay of ^{241}Pu ($T_{1/2} = 14.3y$). Consequently, the accurate determination of the fission reaction rate of ^{241}Am over an extended energy range is of prime importance. In the present thesis, the ^{241}Am(n,f) reaction cross section was measured with Micromegas detectors at the vertical experimental area (EAR-2) of the n_TOF facility at CERN, taking advantage of the high instantaneous neutron flux and using the time-of-flight technique. For the measurement, six targets of ^{241}Am were used with a total activity of $0.1\,GBq$, whereas two targets of ^{235}U and two targets of ^{238}U were employed as reference and served as neutron flux monitors. In this work, a detailed description of the experimental set-up is given along with the data analysis procedure that was followed. The resulting nuclear cross section data, covering a broad spectrum from the meV up to the MeV neutron energy region, are presented and compared with previous data and nuclear data evaluations. Finally, the experimental results are framed with theoretical calculations that were performed using the TALYS-1.95 code.

Περίληψη

Για τις μελέτες σκοπιμότητας, σχεδιασμού και ευαισθησίας σε καινοτόμους πυρηνικούς αντιδραστήρες (Επιταχυντικά Συστήματα Ενισχυτών Ενέργειας -ADS και 4ης Γενιάς Αντιδραστήρες Ταχέων Νετρονίων), απαιτούνται υψηλής ακρίβειας πυρηνικά δεδομένα ενεργών διατομών, κυρίως για αντιδράσεις νετρονίων με ελάσσονες ακτινίδες. Οι νέοι αυτοί αντιδραστήρες ταχέων νετρονίων επιτρέπουν την αποτέφρωση/μεταστοιχείωση των υπαρχόντων ακτινίδων σε πυρηνικά απόβλητα υψηλής ραδιολογικής και χημικής τοξικότητας. Με την αποτέφρωση/μεταστοιχείωση, μπορεί να μειωθεί τόσο ο χρόνος ημιζωής των ραδιενεργών ισοτόπων όσο και ο όγκος αυτών των ρύπων ή των αποβλήτων τους, έτσι ώστε τα τελικά πυρηνικά απόβλητα από το υλικό των αντιδραστήρων που πρέπει να αποθηκευτούν να είναι λιγότερο επιβλαβή για το περιβάλλον. Αντιπροσωπεύοντας περίπου το 1.8% σε αναλωμένο καύσιμο πυρηνικών αντιδραστήρων PWR UO_X, το ισότοπο ^{241}Am ($T_{1/2} = 433y$) θεωρείται ένα από τα υποψήφια ισότοπα για αποτέφρωση/μεταστοιχείωση. Επιπλέον, ο ρυθμός παραγωγής του αυξάνεται εντός του αναλωμένου καυσίμου μέσω της β-αποδιέγερσης του ^{241}Pu ($T_{1/2} = 14.3y$). Κατά συνέπεια, ο ακριβής προσδιορισμός του ρυθμού αντίδρασης σχάσης του ισοτόπου ^{241}Am σε ένα εκτεταμένο εύρος ενέργειας είναι πρωταρχικής σημασίας. Στην παρούσα διατριβή, η ενεργός διατομή της αντίδρασης ^{241}Am(n,f) μετρήθηκε με ανιχνευτές Micromegas στην κατακόρυφη πειραματική περιοχή (EAR-2) της εγκατάστασης n_TOF στο CERN, λαμβάνοντας ωφέλεια από την υψηλή στιγμιαία ροή νετρονίων και χρησιμοποιώντας την τεχνική του χρόνου πτήσης. Για τη μέτρηση χρησιμοποιήθηκαν έξι στόχοι ^{241}Am με συνολική ενεργότητα $0.1\,GBq$, ενώ δύο στόχοι ^{235}U και δύο στόχοι ^{238}U χρησιμοποιήθηκαν ως στόχοι αναφοράς και χρησίμευσαν στην καταγραφή της ροής των νετρονίων. Σε αυτή την εργασία δίνεται μια λεπτομερής περιγραφή της πειραματικής διάταξης καθώς και της διαδικασίας ανάλυσης δεδομένων που ακολουθήθηκε. Τα πυρηνικά δεδομένα ενεργών διατομών που προέκυψαν, καλύπτοντας ένα ευρύ φάσμα από την meV έως την MeV ενεργειακή περιοχή νετρονίων, παρουσιάζονται και συγκρίνονται με προηγούμενα δεδομένα και αξιολογήσεις πυρηνικών δεδομένων. Τέλος, τα πειραματικά αποτελέσματα πλαισιώνονται με θεωρητικούς υπολογισμούς που πραγματοποιήθηκαν χρησιμοποιώντας τον κώδικα TALYS-1.95.

Chapter 1

Introduction

1.1 Historical facts

Americium does not exist naturally on Earth. It is a man-made element that was discovered together with Curium at the end of World War II, in 1944 by the American scientists Glenn T. Seaborg, Ralph A. James, Leon O. Morgan and Albert Ghiorso in the Metallurgical Laboratory at the University of Chicago, latter known as the Argonne National Laboratory, in the frame of the Manhattan Project. The discovery of $_{95}$Am and $_{96}$Cu was announced live on the radio during an American children's program called "Quiz Kids", on November 11, 1945 by Seaborg [1–3]. Seaborg shared the news about the already declassified discovery, that was initially intended to be formally announced at the forthcoming American Chemical Society (ACS) national meeting on November 16, of two new elements with atomic numbers 95 and 96, in an attempt to satisfy a listener's curiosity about the synthesis of new elements in addition to the already known Plutonium and Neptunium.

Due to their difficulty in the isolation process and the frustration in the attempt to prove their chemical existence, it was initially proposed for Americium to be named as "delirium", which means derangement/madness in Latin and for Curium to be named as "pandemonium", which includes the ancient Greek verb "δαίω" meaning "I spread to everyone their destiny". Latter on, the element with atomic number 95 got its current name from the continent of America, only due to its position in the Periodic Table as the sixth element of the actinide series, where the analogous lanthanide element was the Europium, named after the European continent. Additionally, the element with atomic number 96 was proposed to be named Curium, in honor of Pierre and Marie Curie, as a tribute to their pioneering work in the study of the radioactivity at the end of the 19^{th} century.

The nucleosynthesis of ^{241}Am, according to the following nuclear process, consists of two consecutive neutron capture reactions and one β-decay starting from the ^{239}Pu found mainly in spent nuclear fuel, but also in areas where nuclear weapons and nuclear explosives are tested:

$$^{239}_{94}Pu \xrightarrow{(n,\gamma)} {}^{240}_{94}Pu \xrightarrow{(n,\gamma)} {}^{241}_{94}Pu \xrightarrow[14.35\ y]{\beta^-} {}^{241}_{95}Am \tag{1.1}$$

Thereinafter, ^{241}Am ($T_{1/2} = 433y$) decays to daughter ^{237}Np ($T_{1/2} = 2.144E{+}6y$) with simultaneous emission of α and γ radiation according to the following formula:

$$^{241}_{95}Am \xrightarrow[432.6\ \mathrm{y}]{\alpha} {}^{237}_{93}Np + \alpha + \gamma \tag{1.2}$$

As illustrated in the decay scheme of ^{241}Am in Figure 1.1, the energy of the released alpha particles is $5.485\,MeV$ 85% of the times, and $5.443\,MeV$ 13% of the times. In addition, the most intense γ -line is detected at $59.5\,keV$ with 35.9% intensity.

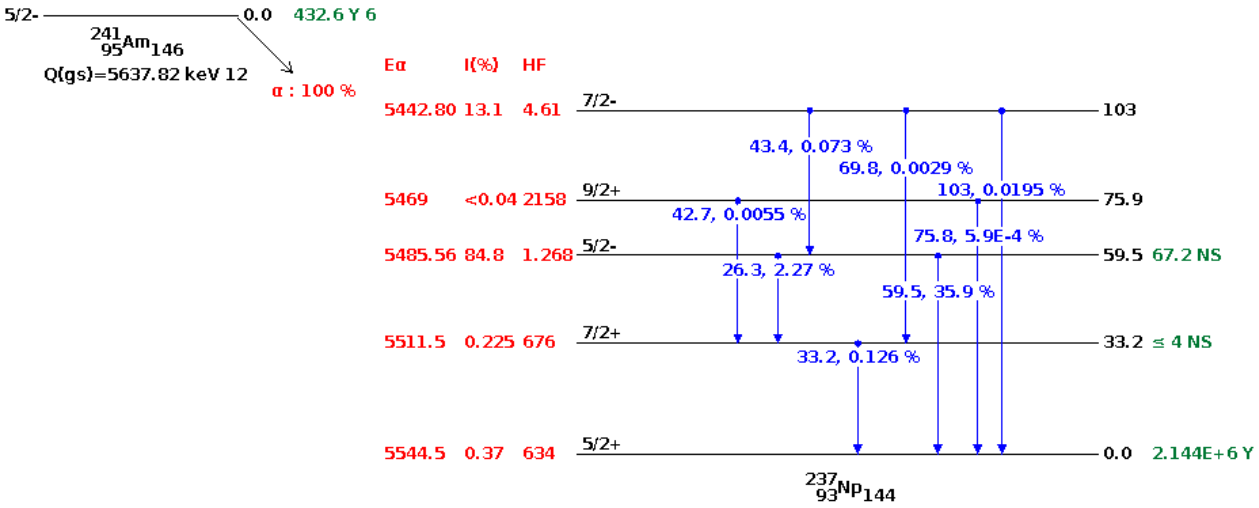

Figure 1.1: Part of the decay scheme of ^{241}Am to ^{237}Np [4].

1.2 Practical applications of Americium-241

The transuranic element $_{95}$Am (element which is higher that Uranium) and especially the isotope ^{241}Am, is not an exotic nuclide but is found in various occasions, ranging from space and nuclear laboratories to every day life. Some examples of its practical uses and applications are listed below:

- **Laboratory source**: In nuclear physics laboratories, the ^{241}Am isotope is widely used in detector set-ups for calibration purposes since it emits both α and γ radiation according to equation 1.2. Moreover, it is used as a neutron source in combination with Beryllium, known as ^{241}AmBe source. The alpha particles emitted from the ^{241}Am source interact with ^{9}Be to produce neutrons via the following nuclear reaction:

$$^{9}_{4}Be + {}^{4}_{2}He \rightarrow {}^{12}_{6}C + {}^{1}_{0}n + \gamma \tag{1.3}$$

- **Radioisotope Thermoelectric Generator (RTG) power**: RTGs are employed to power satellites and space exploration equipment. They constitute a type of nuclear batteries that provide power through the natural radioactive decay of a suitable material. The natural decay heat of the radioisotope is converted into electricity by solid-state thermoelectric converters [5]. ESA (European Space Agency) in synergy with NASA (National Aeronautics and Space Administration) are exploring the viability of using ^{241}Am as a power source for space use as an alternative to ^{238}Pu. Stockpiles of Plutonium

around the world are rapidly reduced and also the trading costs among countries of possession are more deterrent. Modelling of ^{241}Am as an alternative fuel source [6, 7] has shown that among various radionuclides, ^{241}Am is favoured in replacing the current ^{238}Pu fuel with additional design considerations, despite its lower heat production. Among the advantages of ^{241}Am that favor its use is the longer half-life ($T_{1/2} = 433y$) in comparison to ^{238}Pu ($T_{1/2} = 88y$), therefore having the ability to power future space missions for hundreds of years. It is therefore of significant importance, given that ^{241}Am is properly separated and extracted from nuclear waste and especially from Plutonium, to be used as fuel for the future and benefit both nuclear and space sectors.

- **Smoke detectors**: Back to Earth, ^{241}Am saves million of lives every year since it exists inside household and industrial ion chamber smoke detectors that are installed in the ceilings to prevent fires. A small quantity of radioactive ^{241}Am ($< 40\,kBq$) is utilized inside a sealed source, which does not pose a health hazard itself, since the alpha radiation is absorbed in a few centimeters of air and cannot penetrate the outer layer of human skin. According to the detector's configuration, the emitted alpha particles from the ^{241}Am source pass through a space between two electrodes which is filled with air, therefore demarcating an ionization chamber. The alpha particles ionize the air and as a result a constant electric current passes through the capacitor plates. In the presence of smoke, smoke particles enter the ionization chamber and absorb some of the alpha particles causing a drop in the electric current which triggers an alarm.

- **Industrial uses**: ^{241}Am sources are used for a variety of industrial gauging purposes as for example in glass, metal and plastic industry during control process analysis to measure the thickness of materials as they are manufactured, as well as in petroleum industry for well logging [8].

- **Nuclear fuel in future advanced nuclear systems**: The ^{241}Am isotope is one of the main actinide candidates to be used in Generation IV nuclear reactors [9] and Accelerator Driven Systems (ADS) as burn-up fuel. The reprocessing of ^{241}Am will lead to significant reduction in the decay heat load in geological disposal facilities, as well as to the mitigation of the overall volume of the stored radioactive spent fuel.

1.3 Nuclear power production

Every year the electricity demands are increasing worldwide. Nowadays around 10% of the world's electricity is generated by approximately 440 nuclear power reactors spread between more than 30 countries globally. According to the Power Reactor Information System (PRIS) of the International Atomic Energy Agency (IAEA) [10], more than 50 new reactors are under construction. Figure 1.2 shows the distribution of the produced electrical power in addition to the number of currently operational nuclear reactors among the countries that produce nuclear energy. Even more impressive is the nuclear share graph in Figure 1.3, that refers to the ratio of the nuclear electricity production over the total electricity production from the available sources of each country. The number of countries that rely on nuclear energy for more than 30% of their electricity needs, is remarkable.

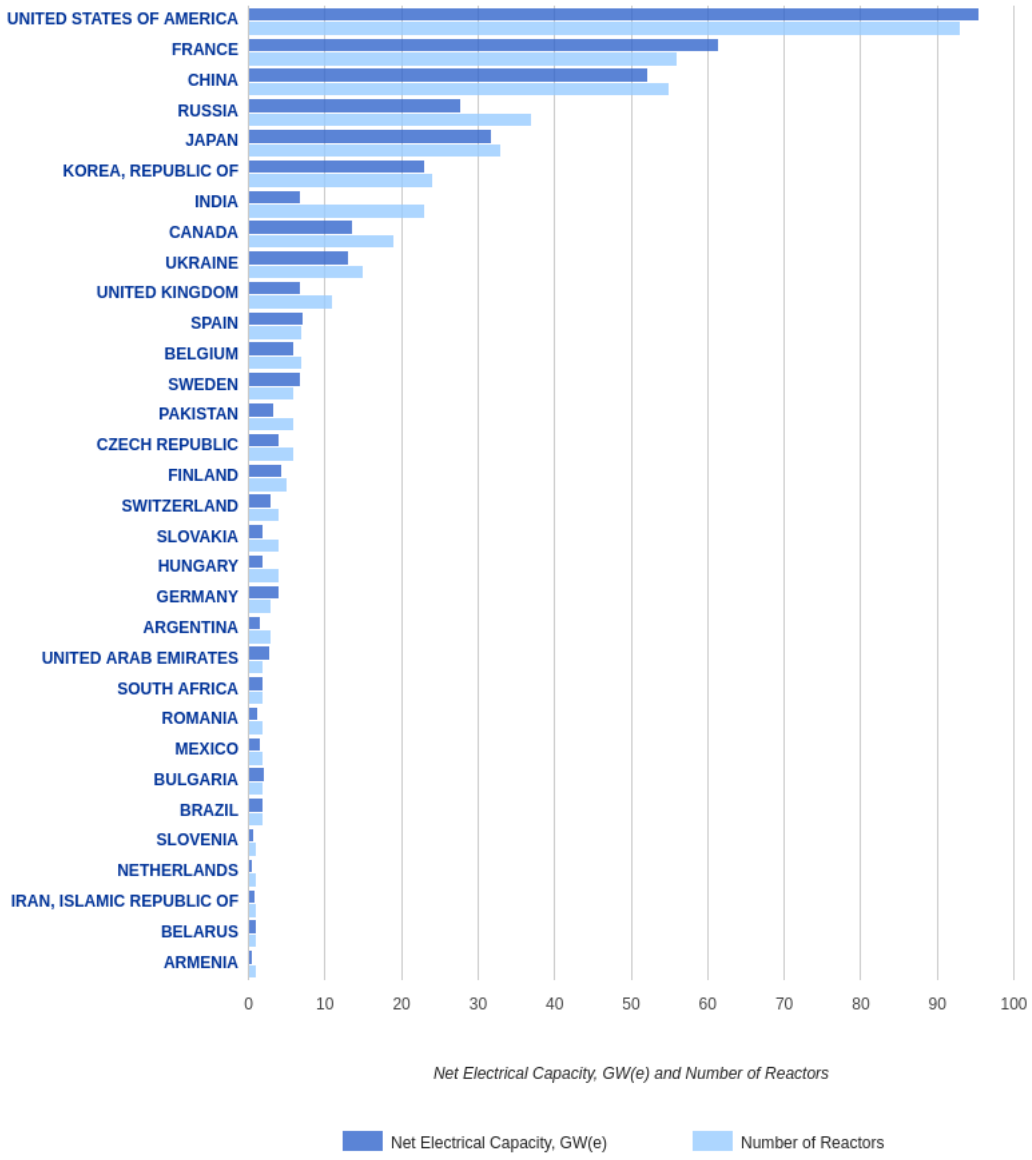

Figure 1.2: Nuclear electricity production and number of operational nuclear reactors per country [10].

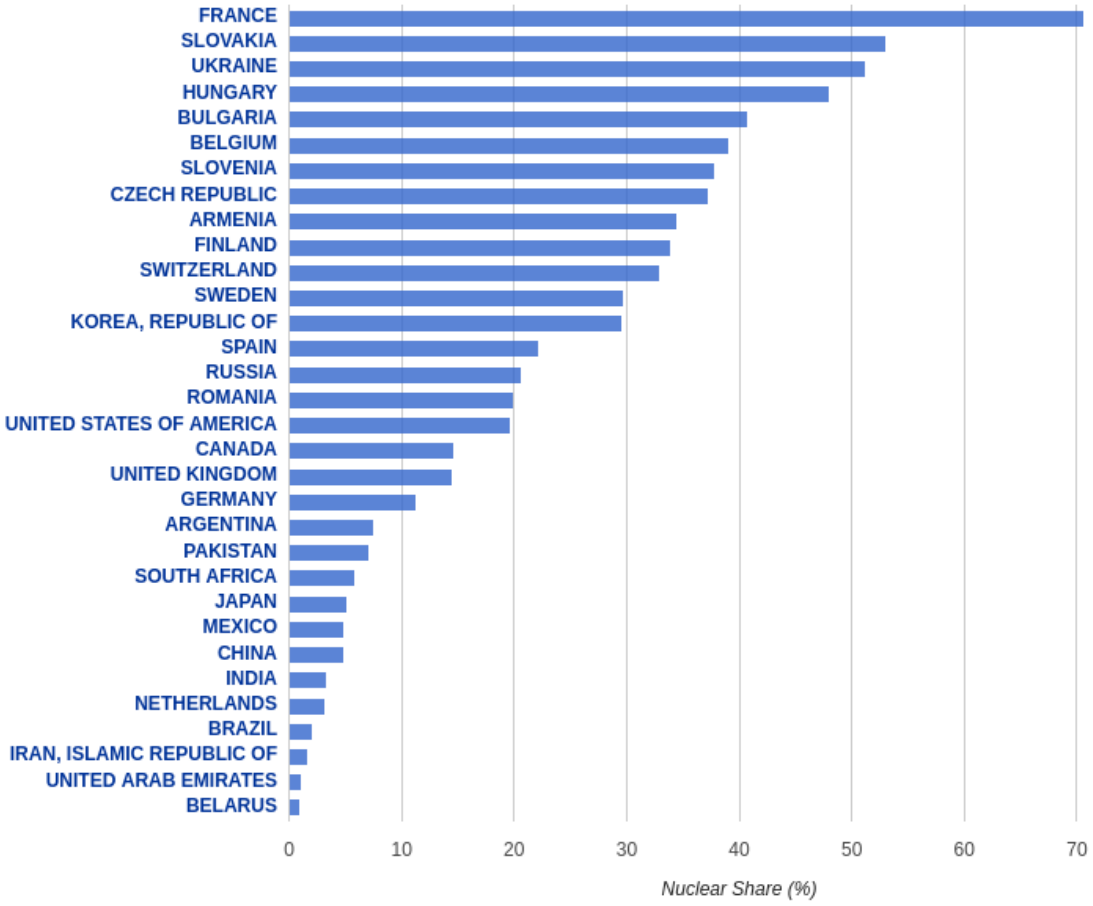

Figure 1.3: Nuclear share of electricity production per country [11].

1.4 Transmutation of minor actinides through advanced nuclear systems

Nuclear energy is produced as a result of the fission reactions that take place inside the core of the reactor. This energy heats the water that surrounds the nuclear core to produce steam. Next, the steam spins large turbine generators resulting in the generation of electricity. A single fission event occurs when a thermal neutron is captured by a fissile element, creating an unstable compound nucleus which splits into two lighter fission products (or fission fragments) emitting on average $2-3$ neutrons and releasing heat and radiation (Figure 1.4). Approximately $200\,MeV$ are released for each fission reaction and most of this amount is carried by the fission products as kinetic energy. Additionally, the emitted neutrons hold $2\,MeV$ each on average. These neutrons are thermalized and captured again by other fissile atoms therefore creating "fission chain reactions".

The most common fuel used in nuclear reactors is Uranium. The natural abundance of mined Uranium consists of ^{238}U ($\sim 99.2742\%$), ^{235}U ($\sim 0.7204\%$) and traces of ^{234}U ($\sim 0.0054\%$). Nevertheless the Uranium oxide (UOx) nuclear fuel has to be enriched to $\sim 3-5\%$ in ^{235}U , since this is the isotope that mainly sustains the fission chain reactions in a typical conventional reactor. Although ^{238}U constitutes the highest percentage of nuclear fuel (over $\sim 93\%$), it is not actually consumed via fission in the majority of commercial reactors that are based on

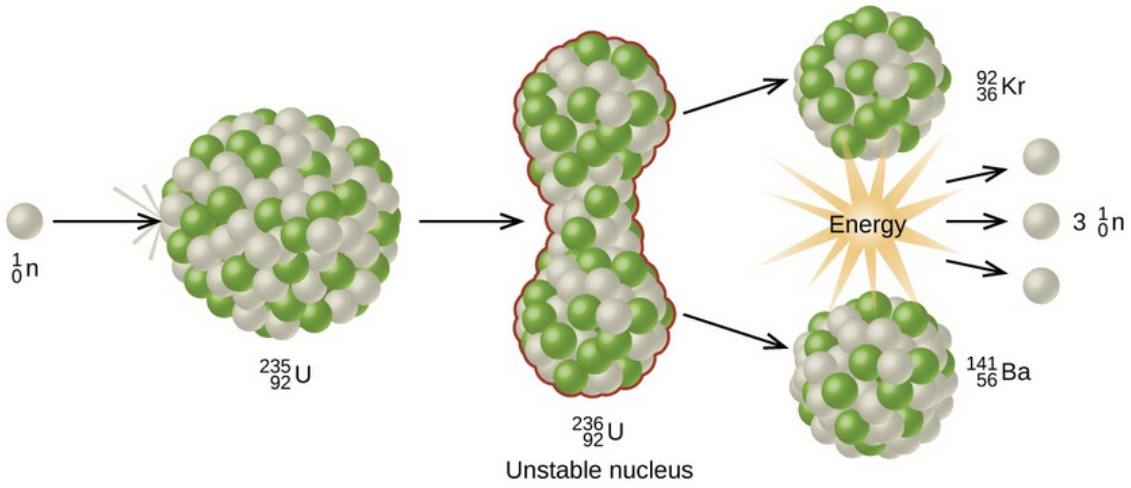

Figure 1.4: An example of the fission process [12].

a thermal neutron spectrum because its (n, f) cross section is almost zero. Nonetheless, the (n, γ) cross section of ^{238}U is high enough to result in the formation of transuranic elements inside the nuclear core, the so-called actinides. The two main elements that are encountered in the higher percentage in nuclear fuel namely Uranium (U) and Plutonium (Pu) are classified as major actinides, whereas Neptunium (Np), Americium (Am) and Curium (Cm) are known as minor actinides (MAs). Figure 1.5, illustrates the sequence of transmutation of chain reactions for the formation of the above mentioned actinides within nuclear fuel.

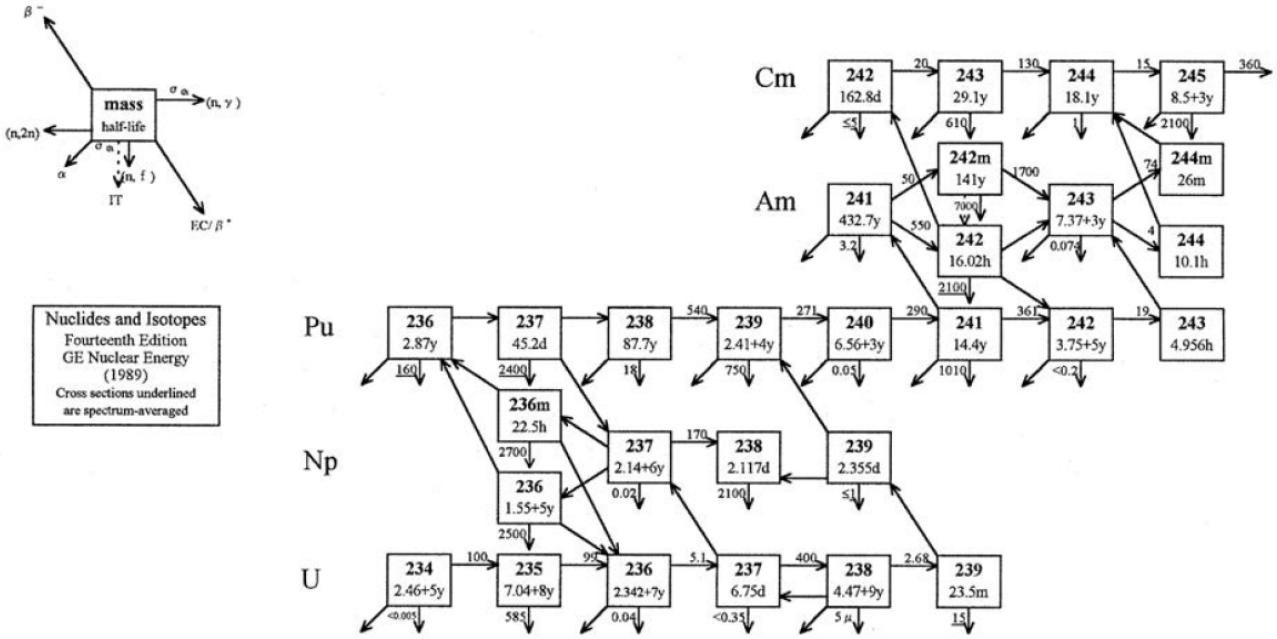

Figure 1.5: Transmutation chain reactions of actinides starting from Uranium isotopes [13].

In once-through open fuel cycle reactors, fuel is removed when the presence of fission products is high enough that chain reactions can no longer be sustained. New milled and/or repro-

cessed Uranium nuclear fuel is reloaded in the reactor core typically every 3 years. The large (n, γ) reaction cross section of some fission products that build up (e.g ^{135}Xe), decreases the population of thermal neutrons that are available for fission, reducing in this way the reactivity of the nuclear reactor. This effect is known as "fission product poisoning". The irradiated (or else spent fuel) that is removed, contains, in addition to unburned Uranium, fission products and actinides. The spent fuel is cooled on-site in the nuclear power plant in specially designed spent fuel pools before being transferred and gathered in long term geological repositories.

Despite their relatively small mass in spent fuel, actinides are the primary contributors to long term radiotoxicity and long term heat generation in spent fuel. As shown in Figure 1.6, for the first approximately 300 years, fission products dominate the heat load in a Pressurized Water Reactor (PWR) spent fuel which accounts for 70% of current operational reactors on a global scale. Gradually their role as main heat producers is taken over by more long-lived actinides. After fission products have decayed, the actinides dominate the radiological hazard completely.

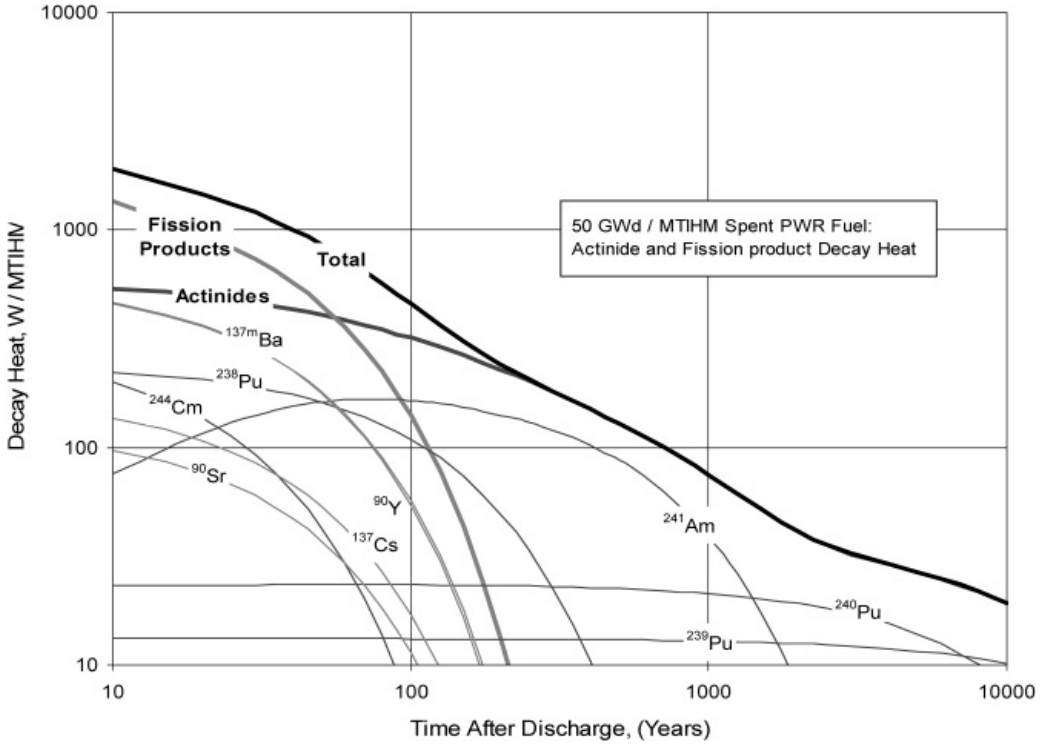

Figure 1.6: Dominant decay heat contributors in spent PWR fuel irradiated to 50 GWd/MTIHM [14].

In order to reduce a potential environmental hazard and at the same time increase the available volume in geological repositories, the idea is to reprocess these actinides by transmutating long half-life waste to less troublesome isotopes with less radiotoxicity. In practice, the concept is to collect the existing actinides from the spent nuclear fuel of conventional reactors and use them as fuel in advanced nuclear systems. These systems are either Generation IV Fast Neutron Reactors (FNRs) which are based on a fast neutron spectrum or a combination of Accelerator Driven Systems (ADS) and PWRs in a subcritical mode where the neutrons are produced from a high current proton accelerator (linear or cyclotron) via spallation process. In both scenarios, a fast neutron spectrum is fundamental, since actinides are more favored to

fission with high energy neutrons. As depicted in Figure 1.7, the low neutron energy part of a thermal reactor will boost the capture of neutrons from the actinides for the creation of higher Z radionuclides, since in this energy part the ratio capture/fission is usually larger than unity. On the contrary, after a few hundreds of keV the (n, γ) reaction cross section drops completely and fission is the dominant reaction mechanism.

Consequently, for the development of advanced nuclear systems, high accuracy fission cross section data are needed for several actinides in a wide energy range with emphasis in the fast region. Among these actinides, the ^{241}Am isotope is of particular interest since is one of the main contributors in the decay heat of spent PWR UOx fuel.

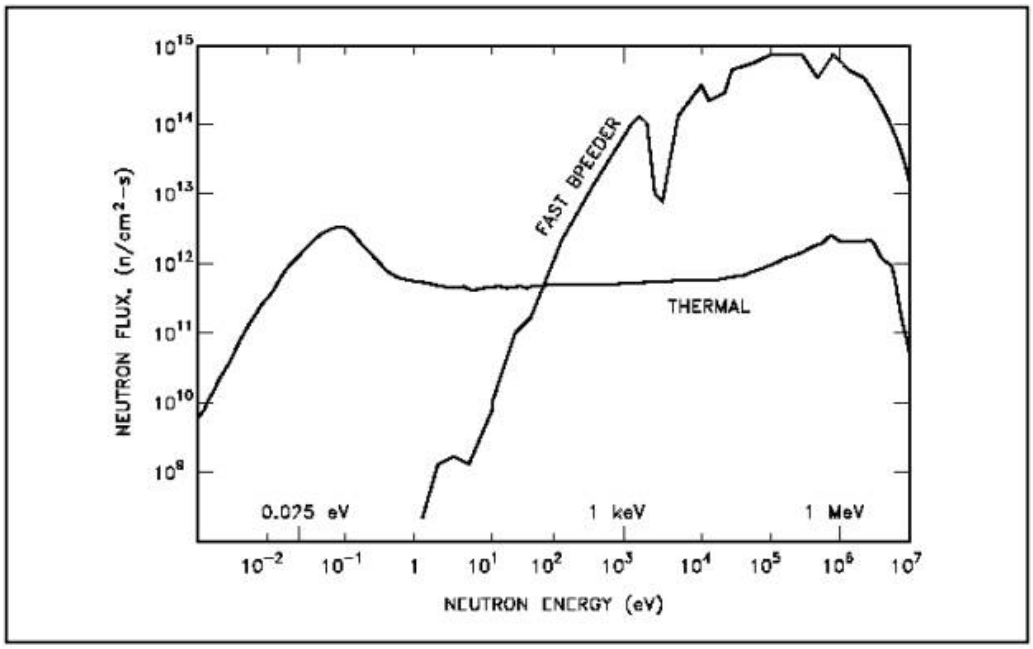

Figure 1.7: Comparison of the neutron spectrum from a conventional reactor and a fast breeder [15].

1.5 Motivation of the ^{241}Am(n,f) study

Facing already the consequences of climate change and the greenhouse effect, the use of Nuclear Energy has already been recognized (United Nations Conference on Climate Change, Paris 2015, [16]) as one of the main sources of energy with zero greenhouse emissions. The production of energy with zero CO_2 emissions, is considered absolutely necessary, in order to limit the increase of the average temperature below $2\,^{\circ}C$ in comparison to the pre-industrial levels. On the other hand, one of the major issues that arises from the current use of Nuclear Reactor facilities, is the presence of isotopes of transuranic elements in large quantities in the nuclear waste. These isotopes are produced in the reactor core through a sequence of neutron capture reactions and alpha decays, originating primarily from the ^{238}U isotope, which exists as a component of the burning elements. The main produced transuranic chemical elements are Plutonium (Pu), Neptunium (Np), Americium (Am) and the Curium (Cm). The above mentioned elements belong to the family of actinides, which are responsible for the long-term radiotoxicity of nuclear wastes, as it remains critical for over one hundred thousand years.

Nowadays, technology has advanced considerably for the safe operation of new generation reactors that can use the incineration of existing nuclear waste as a way of generating energy, free of greenhouse gas emissions. Studies on the capabilities, design and sensitivity of these reactors (Accelerator Driven Systems-ADS [17], Generation IV Fast Neutron Reactors) that could address the issue of nuclear waste transmutation have already been produced. These studies have shown that fuels enriched in actinides can be used but require high precision cross section data for various neutron-induced reactions, with neutron energies ranging from thermal up to several tens of MeV. The "Nuclear Data High Priority Request List" [18], from the Nuclear Energy Agency (NEA), lists the needs for data from various fields, including reactor design. In addition, the OECD (Organisation for Economic Co-operation and Development)/NEA WPEC (Working Party on International Nuclear Data Evaluation Co-operation) Final Report (Subgroup 26) [19], summarizes the accuracy of the nuclear data associated with the design of these advanced nuclear systems. Table 1.1 highlights the present uncertainties and target requirements for the neutron-induced fission cross section of ^{241}Am relevant to future nuclear reactors. In this scope, recent attention has lead to the investigation of Americium isotopes, classified as high-level nuclear waste from conventional reactors, that could be used as a burnable minor actinide in future nuclear reactors [20].

	Uncertainty (%)	
Energy Range (MeV)	**Existing**	**Target**
2.23 - 6.07	11.7	5.7
1.35 - 2.23	9.8	1.4
0.498 - 1.35	8.3	1.2
0.183 - 0.498	8.3	4

Table 1.1: Existing and target uncertainties of the ^{241}Am(n,f) cross section [19].

The isotope ^{241}Am ($T_{1/2} = 433y$) is present in high percentage in nuclear waste, representing about 1.8% of the mass of actinides in nuclear waste of Pressurised Water Reactors' (PWR) UO_X fuel [21]. Its concentration is further increased due to its production by the β-decay of

^{241}Pu with a half-life of 14.3 years. It is clear that both the production of ^{241}Am in conventional reactors (including its further accumulation through the decomposition of ^{241}Pu) and its destruction by transmutation, are crucial to the design of the recycling of existing nuclear waste. Sensitivity studies of these new nuclear power systems, have shown that high precision nuclear cross section measurements are required for the ^{241}Am(n,f) reaction [22]. However, despite the efforts of the scientific community, the accuracy of the nuclear data for the neutron-induced fission cross section of the ^{241}Am for these applications is still insufficient.

The unique advantages of the n_TOF facility at CERN and more specifically the high instantaneous neutron flux and the suppressed background conditions of Experimental Area 2 (EAR-2), facilitate the possibility of producing accurate experimental data in a wide range of neutron energy from thermal up to the MeV scale. The study of the neutron-induced fission cross section of ^{241}Am in EAR-2 is ideal for addressing two main challenges of the measurement. Firstly, the high specific activity of the isotope which is 127 MBq/mg and actually poses a limit in the mass of the samples that can be used in the experiment. This limit is attributed to the increased alpha particle background that originates from the natural decay of ^{241}Am and decreases the signal-to-background ratio. Secondly, the shape of the cross section itself, that displays a steep fission threshold with its value decreasing rapidly below 1 MeV incident neutron energy.

1.6 Status of previous fission data

Among the available experimental data for the ^{241}Am(n,f) reaction cross section, serious discrepancies are observed especially in the plateau of the fission reaction. As illustrated in Figure 1.8, for the neutron energy region between 300 keV to 30 MeV, the most systematic data set is the one from Dabbs et al. [23]. The most recent measurement is the one from Belloni et al. [24], that was performed at n_TOF in Experimental Area 1 (EAR-1) in 2003. Despite the good agreement of the results with the previous data, due to limiting counting statistics of the measurement, the results were given in a rather coarse energy bin.

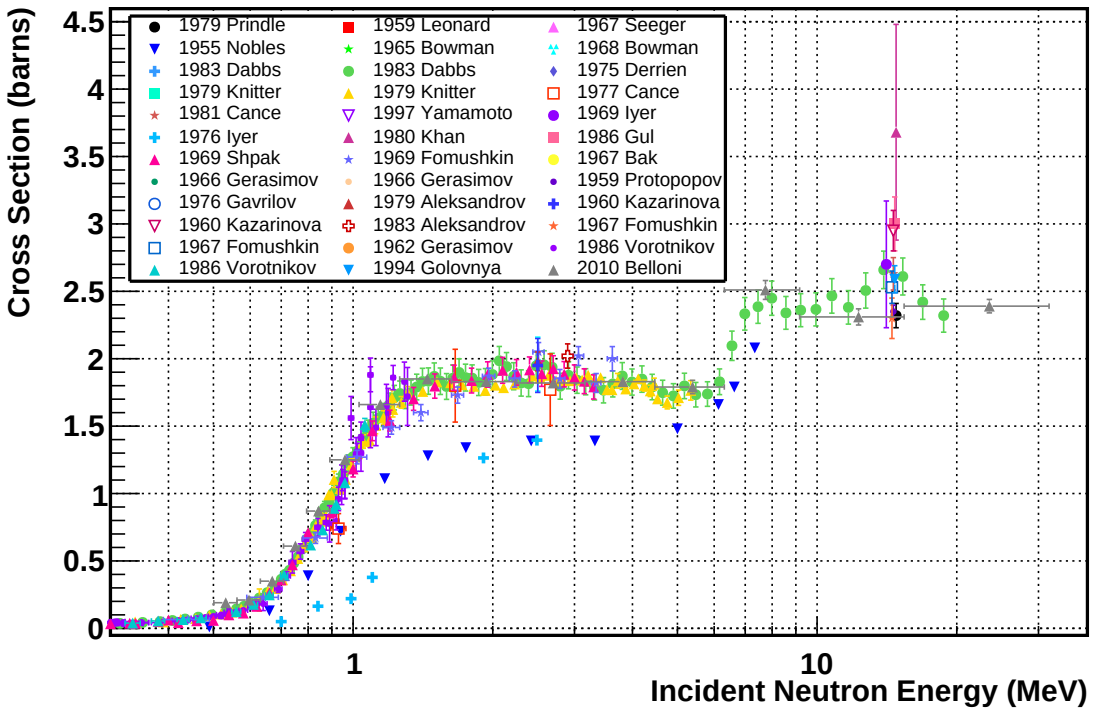

Figure 1.8: Previous measurements of the ^{241}Am(n,f) reaction above 300 keV retrieved from the EXFOR database.

Chapter 2

Experimental Details

The ^{241}Am(n,f) measurement, carried out in the summer of 2018 at the vertical experimental area of the n_TOF facility at CERN (**C**onseil **E**uropéen pour la **R**echerche **N**ucléaire), was part of the last experiments (Phase III) that were performed before the long shut down of CERN that started at the end of 2018 and lasted two years. During this period, several changes and upgrades occurred both in the accelerator complex of CERN and inside the n_TOF facility. These upgrades include, but are not limited to, the replacement of the ten years old lead spallation target of the neutron facility with a new one, along with the construction of a new experimental station (NEAR) located $\sim 3\,m$ from the neutron source, designed and oriented mainly to serve nuclear astrophysics studies and activation measurements. At the moment, the commissioning of the facility is in progress and some of the features of the new beam concerning the neutron flux, are expected to deviate from the ones that will be discussed in what follows. In this chapter, an overview of the experimental set-up will be presented including the description of the neutron facility and the actinide samples used, the principle of operation of the detectors, the electronics and the data acquisition chain.

2.1 The n_TOF facility at CERN

n_TOF is a neutron Time-Of-Flight facility located at CERN in Geneva, Switzerland. The facility was initiated in 1998 from the idea of Carlo Rubbia [25] and is based on a spallation neutron source aiming to produce high precision cross section data. The neutron-induced reaction cross sections measured at n_TOFplay an important role in a wide variety of research fields, ranging from stellar nucleosynthesis, the investigation of nuclear level densities, to applications of nuclear technology, medical applications, the transmutation of nuclear waste, accelerator driven systems and nuclear fuel cycle investigations.

The neutron beams are produced using the pulsed beam of $20\,GeV/c$ protons which are delivered from the Proton Synchrotron accelerator (PS) of CERN. The proton beam impinges on the n_TOF cylindrical lead primary target with dimensions 40 x 60 cm^2 (length x diameter) and approximately 300 neutrons per proton are produced covering a wide energy spectrum from thermal up to the GeV energy region. The proton beam has a time width of $7\,ns$ RMS with a maximum repetition rate of $0.8\,Hz$ (1.2 sec between consecutive bunches). The proton accelerator delivers two kind of pulses: the dedicated pulses with a nominal intensity of ~ 7 x 10^{12} protons per bunch and the parasitic ones with half of the intensity.

The n_TOF facility consists of two experimental halls where measurements can run in parallel. At 185 m distance horizontally with respect to the lead target in an underground tunnel, lies the first experimental area (EAR-1) which became operational in 2001, while the second experimental area (EAR-2) which received its first beam in July 2014, is located approximately 19.5 m above the spallation target and vertical to the direction of the proton beam at the ground level. A graphical representation of the facility is shown in Figure 2.1.

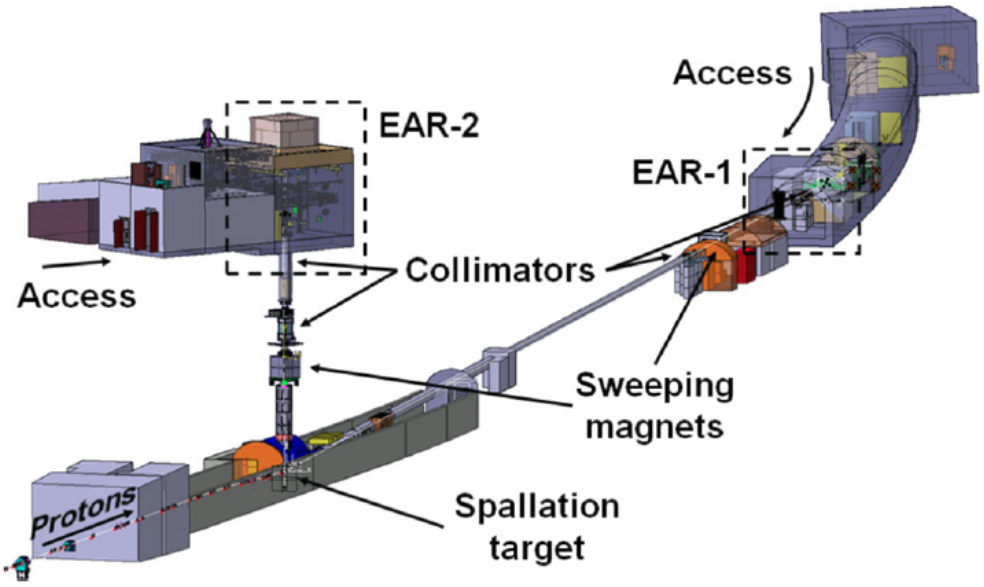

Figure 2.1: A layout of CERN's n_TOF facility, showing the lead spallation target, the two neutron flight-paths and the two corresponding experimental areas along with some key beam-line elements [26].

Together with the high instantaneous neutron flux and the wide energy range, due to the different flight-paths and the morphology of the lead target, the two experimental areas exhibit unique characteristics. In particular, EAR-1 offers high energy resolution as well as a wider time-of-flight spread of high energy neutrons allowing the accurate determination of excitation functions up to the GeV energy region. On the other hand, EAR-2 despite the fact that the energy resolution is inferior with respect to EAR-1 (due to the shorter flight path), offers almost 40 times higher neutron flux and is more suitable for measurements with high activity and low mass samples.

2.1.1 The spallation target

The lead target is surrounded by a 1 cm thick layer of water in constant circulation that serves as coolant. For EAR-2, this water layer acts as a moderator as well. In the horizontal neutron beam-line (EAR-1) the water layer is accompanied by an extra 4 cm thick layer of either demineralized or borated water for the suppression of the thermal part of the neutron spectrum. The borated water is obtained with a 1.28% mass fraction of boric acid (H_3BO_3) enriched with ^{10}B . In Figure 2.2, a cross section view of the lead target along with the corresponding cooling and moderating material layers, is shown. The choice of the borated water has an impact on the neutron flux in EAR-1, because of the high cross section of the ^{10}B(n,a) reaction. As previously

mentioned, the enhanced cross section of the ^{10}B(n,a) reaction at low neutron energies results in a significant suppression of the thermal part of the neutron energy distribution. The comparison of the evaluated neutron fluxes between the two experimental areas is shown in Figure 2.3.

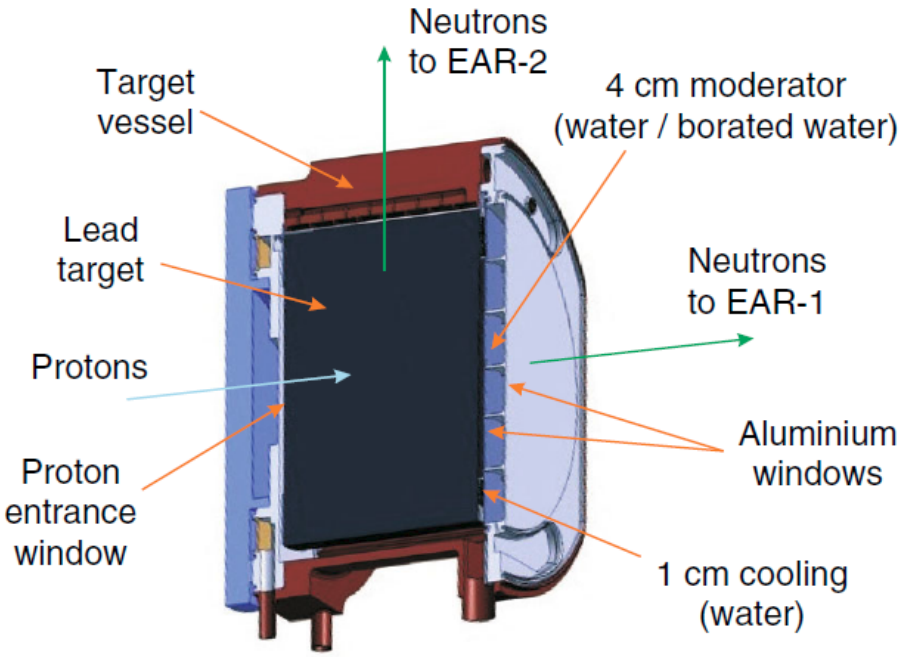

Figure 2.2: Cross section of the lead spallation target used during the period 2008-2018 (Phase II and III of n_TOF) [26].

2.1.2 The vertical experimental area EAR-2

The ^{241}Am(n,f) measurement was carried out at the second experimental area of the infrastructure which is located approximately 19.5 m above the lead spallation target, at ground level. In Figure 2.4, the beam optics components and other beam related elements which are responsible for the final shape and dimension of the neutron beam reaching the experimental hall, are visualized.

The beam line is kept under low vacuum at $\sim 10^{-2}\,mbar$ as to keep neutron scattering/attenuation and neutron-induced background as low as possible. Following the flight path of the neutrons, the first collimator lies 7.4 m above the spallation target, is made of Fe and has 1 m length and 20 cm inner diameter. A few meters above, at 10.4 m, there is a strong permanent magnet with a field of 253 mT that ensures the divergence of the charged particles originating from the spallation process, steering them away from the neutron beam line. Next, at 11.4 m from the neutron source, there is a filter station which is equipped with eight neutron filters. These filters are inserted along the neutron flight path when special needs arise with respect to the neutron beam energy distribution. Last but not least, the final shaping of the neutron beam is attributed to the second collimator which is located 15.04 m above the lead target and has an outer diameter of 68 cm. The first part of the collimator consists of 2 m of Fe followed by 1 m of borated polyethylene (B-PE) where the last 0.4 m have a core

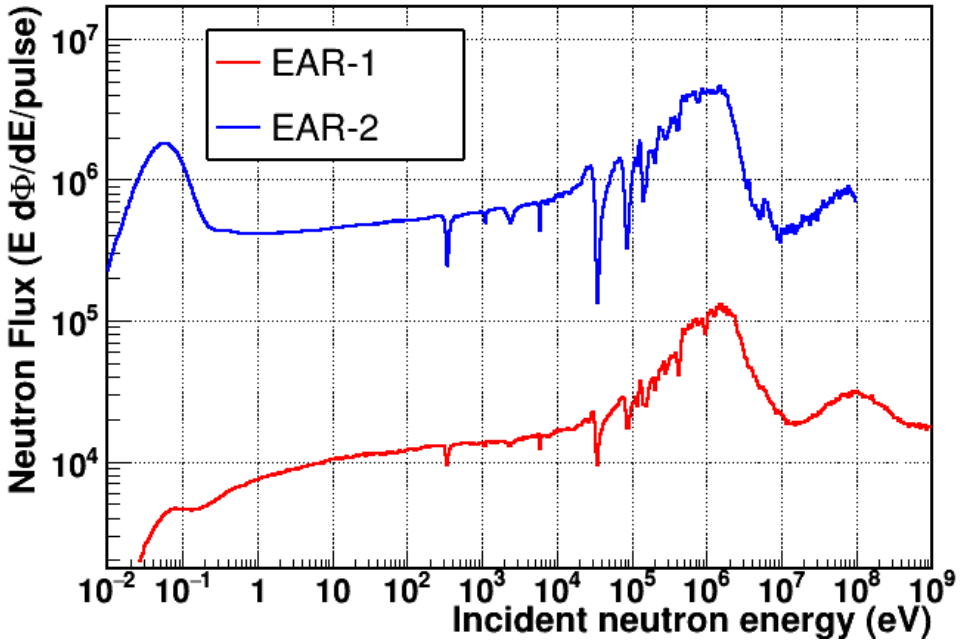

Figure 2.3: The evaluated neutron flux as a function of the incident neutron energy in isolethargic units (100 bpd) in experimental EAR-1 and EAR-2 using the capture collimator set-up. The observed dips in the flux are attributed to structural materials of the target (^{17}Al , ^{54}Mn) and the ^{16}O which is present in the water surrounding the lead spallation target. Moreover, the suppressed low energy neutron spectrum in EAR-1 due to the borated water is visible.

of boron-carbide (B_4C) cylinders. The inner diameter of the second collimator can be altered between two set-up configurations: the "capture" with a diameter of 2.2 cm and the "fission" with a diameter of 6.7 cm. This is actually a choice that depends on the type of measurement carried-out in the experimental hall. Right after the end of the second collimator, Pb disks with a total thickness of 0.12 cm are installed. The floor of the bunker at EAR-2 is located at 18.16 m above the spallation target. According to simulations, the focal point of the neutron beam is positioned at 1.08 m from the floor of the experimental area, although it is up to the experimentalists to arrange the measurement set-up by positioning the detectors at a convenient distance. The ceiling of the bunker is located at a distance of 23.66 m with respect to the center of the target. On the roof of the building the beam dump is installed in order to absorb the neutron beam. It consists mainly of a B-PE core surrounded by Fe blocks and finally shielded by concrete.

For the ^{241}Am(n,f) experimental campaign it was decided to use the fission collimator with a 6.7 cm diameter in order to couple the spatial profile of the neutron beam with the diameter of the actinide samples which was 6 cm. Due to its relatively short half-life of 433 y, ^{241}Am has a specific activity of 127 MBq/mg. As a consequence, it is crucial to keep the emitted alpha activity per surface at tolerable/manageable levels in order to prevent the detectors' mechanical damage due to radiation.

In general, the construction of the vertical flight path of the n_TOF facility in 2014 extended the capabilities of the facility and allowed the execution of challenging cross section measurements of radioactive samples of high activity and small mass. For instance, the ^{241}Am(n,f) cross

section was measured in 2003 in EAR-1 [24] but the data had a very coarse energy resolution providing essentially an average cross section value. The reason was the adopted high pulse height threshold that had to be set in order to reject the sample-induced alpha background, therefore strongly reducing statistics. Therefore in EAR-2, due to the 10 times shorter flight path, the conditions for the conduction of such a challenging measurement are more favorable. In particular, due to the higher instantaneous flux, the smaller mass of the radioactive samples used and the better signal-to-background ratio, the obtained data are expected to have a better energy resolution and improved statistics.

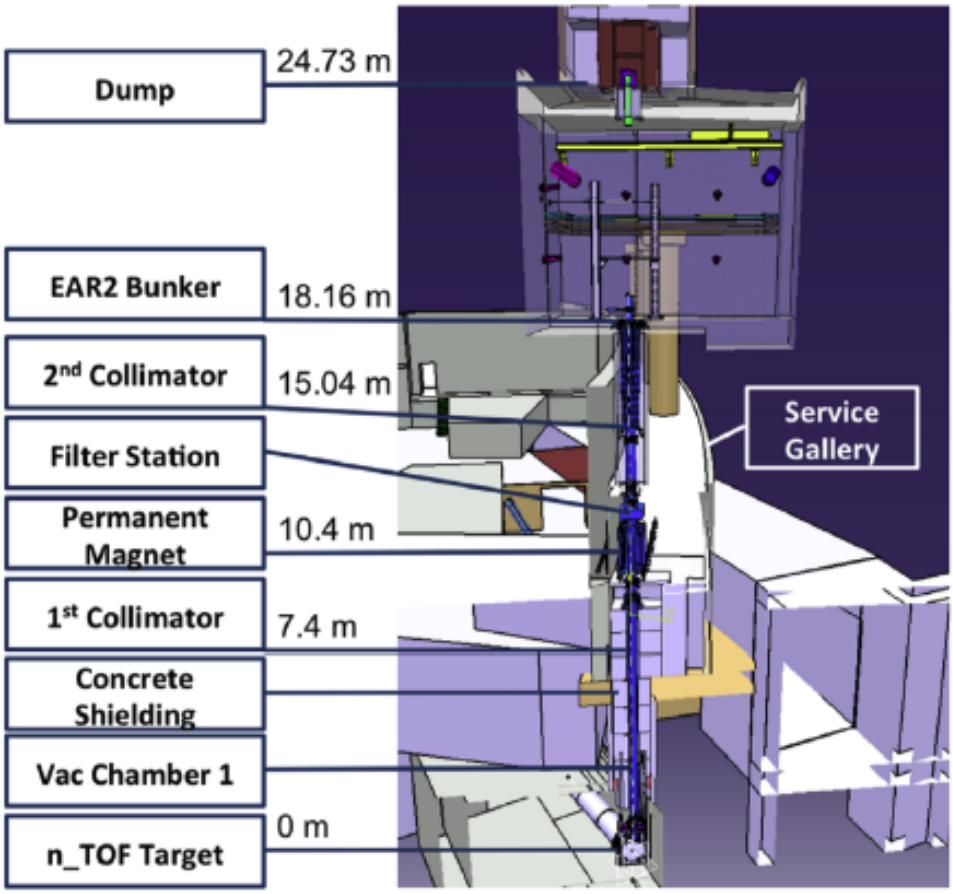

Figure 2.4: General layout of the vertical flight-path of EAR-2 starting from the lead spallation target at the bottom until the beam dump on top. Also, the various beam line components along with their distances with respect to the target are visible [27].

2.2 The time-of-flight technique

Neutrons are uncharged particles and therefore cannot be accelerated to a desired energy. In order to determine the neutron energy at time-of-flight facilities such as n_TOF, where the neutron spectrum covers almost 10 orders of magnitude in energy, from thermal up to hundreds of MeV, the time-of-flight technique is employed. In reality, the quantity that can be directly measured is the time (usually referred to as "tof") that a neutron travels across a fixed geometrical flight path, from the moment of its creation inside the lead spallation target until it reaches the experimental area and interacts with the sample inducing a signal in the detector. In classical terms, the neutron energy can be derived from the equation:

$$E_n = \frac{1}{2} M_n u^2 = \frac{1}{2} M_n \Big(\frac{L}{t}\Big)^2 \tag{2.1}$$

where $M_n = 939.55\, MeV/c^2$ is the neutron mass, u is the neutron speed, L is the fixed geometrical flight path that the neutron travels and t is the measured time-of-flight of the neutron. Above a few tens of MeV, for the conversion of the neutron time-of-flight to energy, the relativistic expression should be considered as follows:

$$E_n = M_n c^2(\gamma - 1) = M_n c^2 \left(\frac{1}{\sqrt{1 - (\frac{L}{tc})^2}} - 1 \right) \tag{2.2}$$

where $c = 299.792458\, m/\mu s$ is the speed of light and γ is the Lorentz factor. The relative resolution of the n_TOF facility can be calculated as:

$$\frac{\Delta E_n}{E_n} = 2\sqrt{\Big(\frac{\Delta t}{t}\Big)^2 + \Big(\frac{\Delta L}{L}\Big)^2} \tag{2.3}$$

At n_TOF, prior to the arrival of neutrons, the emission of a prompt γ component takes place, which is related to the spallation process and its induced pulse scales with the intensity of the proton bunch. During the spallation process, a shower consisting of $\gamma - rays$, very high energetic neutrons related to this process and other relativistic particles, is created and gives rise to a pulse of high amplitude and width which causes the first signal in the detectors of the experimental area. This signal which is referred to as the "$\gamma - flash$", constitutes the start signal of the time-of-flight measurement and points out the time of creation of the neutrons as follows:

$$t_0 = tflash - \frac{L}{c} \tag{2.4}$$

where $tflash$ stands for the time-of-flight of the the recorded $\gamma - flash$ signal and $\frac{L}{c}$ is the time needed for a photon to travel along a flight path L which is actually the time that the $\gamma - flash$ needs to travel, starting from the moment that the proton beam impinges on the lead spallation target until it reaches the experimental area. Therefore, the estimation of the time-of-flight of a neutron inducing a signal to the detector is calculated as follows:

$$t = tof - t_0 = tof - \Big(tflash - \frac{L}{c}\Big) = tof - tflash + \frac{L}{c} \tag{2.5}$$

where tof is the arrival time of the recorded signal in the detector.

In a more pictorial way, Figure 2.5 demonstrates the sequence of the above mentioned signals that are used for the determination of the neutron energy for each proton pulse, as a function of the time evolution. Before the proton beam impinges on the lead spallation target of n_TOF, a trigger signal is sent to the Data Acquisition System (DAQ) of n_TOF to open the acquisition window of the running measurement. The acquisition window is user-defined based on the characteristics of each experimental area (e.g. flight path) and the experimental set-up (e.g. detectors, type of measurement). A feature of the n_TOF facility worth mentioning is its low duty cycle ($\sim 0.8\,Hz$). This ensures that there is no overlapping of the slowest neutrons of the first proton pulse that are recorded with the fastest neutrons of the following proton pulse.

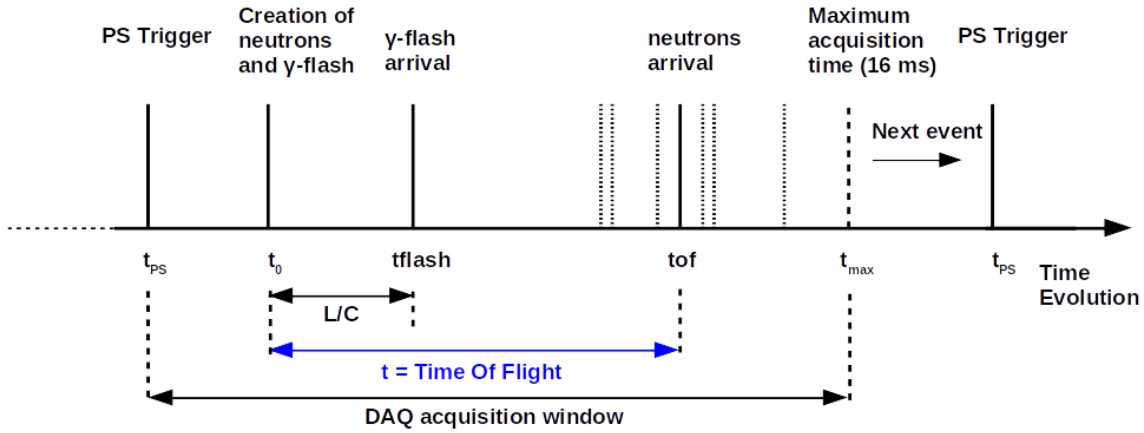

Figure 2.5: Schematic illustration of the sequence of the time signals for each proton pulse that are used in the time-of-flight measurement at the n_TOF facility at CERN. In the experimental campaign of ^{241}Am(n,f), the acquisition window of DAQ in EAR-2 was chosen to be $16\,ms$, therefore covering neutron pulses ranging from meV up to the MeV energy region.

Even though the conversion from the time-of-flight to neutron energy seems a rather simple procedure, it is not at all explicit. What is still missing from the equation is the length that the neutron travels inside the spallation lead target as well as the various materials that the particle meets on its way to the experimental area such as the moderator. As a result, the neutron will be detected at a later time-of-flight and therefore its energy will be underestimated using the so far known conversion. This unknown path of the neutron is called "moderation length λ" of the neutron. Although it cannot be measured experimentally, it can be estimated via Monte Carlo simulations. To address this necessary calculation, a transport code was developed within the n_TOF Collaboration. The transport code is based on the FLUKA code [28] and simulates the optical transport of particles (neutrons and photons) that are created in the lead spallation target up to the experimental areas. For EAR-2, this optical transport begins at a scoring plane of $37.2\,cm$ above the spallation target up to a desired flight path length in EAR-2 experimental hall.

The distribution of the neutron transport inside the target-moderator assembly is generally referred to as the "resolution function (RF)" and it is a unique characteristic of each time-of-flight facility and each experimental area. Figure 2.6 depicts an example of the distribution of the moderation length λ with respect to the measured time-of-flight of the neutrons for EAR-2 at a distance of $19.5\,m$ with respect to the spallation target. It is evident that there is a probability distribution of the moderation length for the neutrons arriving in the experimental

area which depends on their measured time-of-flight. This means that even for the neutrons that are recorded within the same time-of-flight bin, there is not a unique value for λ that can be considered. For the proper interpretation of the resolution function, neither the average nor the most probable value of the λ distribution should be adopted for the time-of-flight to energy conversion. Instead, in order to mimic nature, each recorded neutron should be free to choose a λ value following the corresponding distribution in its recorded time-of-flight. The treatment of the resolution function will be discussed in the following chapter in detail. In addition to the moderation process, within the same simulation the transport code treats the time spread of the primary proton pulse (7 ns RMS) which induces a small uncertainty in the time-of-flight of the detected events mainly affecting the high energy neutron spectrum.

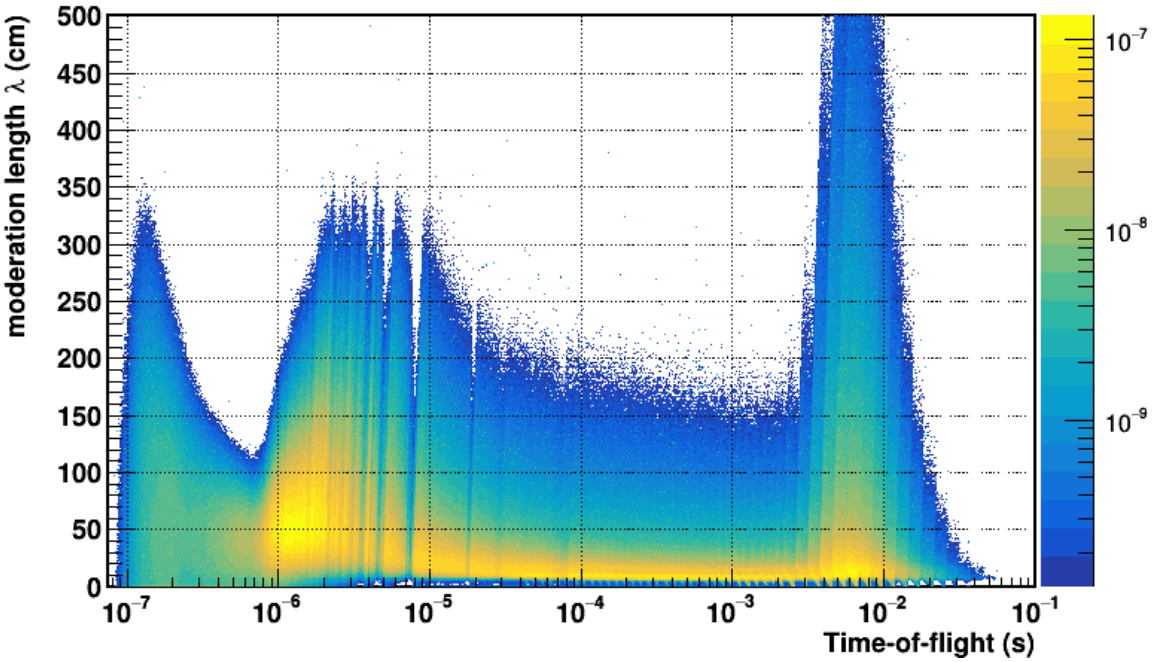

Figure 2.6: Moderation length λ distribution of neutrons in EAR-2 with respect to the measured time-of-flight for a fixed vertical geometrical distance of 19.5 m from the spallation target, as extracted from the transport code. The time-of-flight in the x-axis is given in an isolethargic binning of 100 bins per energy decade, whereas the moderation length λ in the y-axis is given at a linear binning of 1 mm.

In order to include the effect of the resolution function in the determination of the true neutron energy, a new flight path length is introduced called "effective length L_{eff}". The "effective length L_{eff}" is described as:

$$L_{eff} = L_{geom} + \lambda(tof) \tag{2.6}$$

where L_{geom} is a fixed geometrical flight path distance and $\lambda(tof)$ is the moderation length of the neutron assigned from the resolution function distribution.

Combining equations 2.1, 2.5 and 2.6, the neutron energy in classical terms can be expressed as:

$$E_n = \frac{1}{2} M_n \left(\frac{L_{geom} + \lambda(tof)}{tof - tflash + \frac{L}{c}} \right)^2 \tag{2.7}$$

or using the relativistic expression as:

$$E_n = M_n c^2 \left(\frac{1}{\sqrt{1 - \left(\frac{L_{geom} + \lambda(tof)}{(tof - tflash + \frac{L}{c})c} \right)^2}} - 1 \right) \tag{2.8}$$

2.3 Fission foils

The fission foils of the ^{241}Am(n,f) experimental campaign were manufactured and provided by the European Commission Joint Research Center in Geel, Belgium (JRC-Geel). For the realization of the measurement, in total six samples of ^{241}Am (99.98% purity) in oxide compound form were used with a total mass of $0.78\,mgr$ ($\sim 4.6\,\mu gr/cm^2$ per sample) and a total activity of $\sim 0.1\,GBq$ (Table 2.1). In addition to the americium samples, two ^{235}U ($0.26\,mgr$, $0.30\,mgr$) and two ^{238}U ($2.07\,mgr$, $2.21\,mgr$) samples were used as reference foils for the determination of the neutron flux (Table 2.2).

In all cases, the samples were produced by means of molecular plating (also called electrodeposition technique). The actinide material was electrodeposited on a spot of $60\,mm$ in diameter, on top of a $0.025\,mm$ thick aluminum backing foil. The diameter of the actinide deposit was not measured directly but instead the diameter of the aluminum mask was measured with a calliper at room temperature. The total activity of the actinide samples was measured by low-geometry alpha-particle counting (LGA), whereas the isotopic composition was determined by thermal ionization mass spectrometry (TIMS). In addition, the mass and areal density of the samples were derived from the measured activity.

For radioprotection purposes, all the actions concerning the handling of the targets and the mounting/dismounting inside the fission chamber, were performed inside a glovebox in a Class-A lab at the ISOLDE facility at CERN, under the constant supervision of a radioprotection officer. In order to ensure that the risk for contamination during the operation procedures was kept at acceptable levels, constant measurements and smearing tests of the working surface, used equipment, actinide containers and gloves were performed.

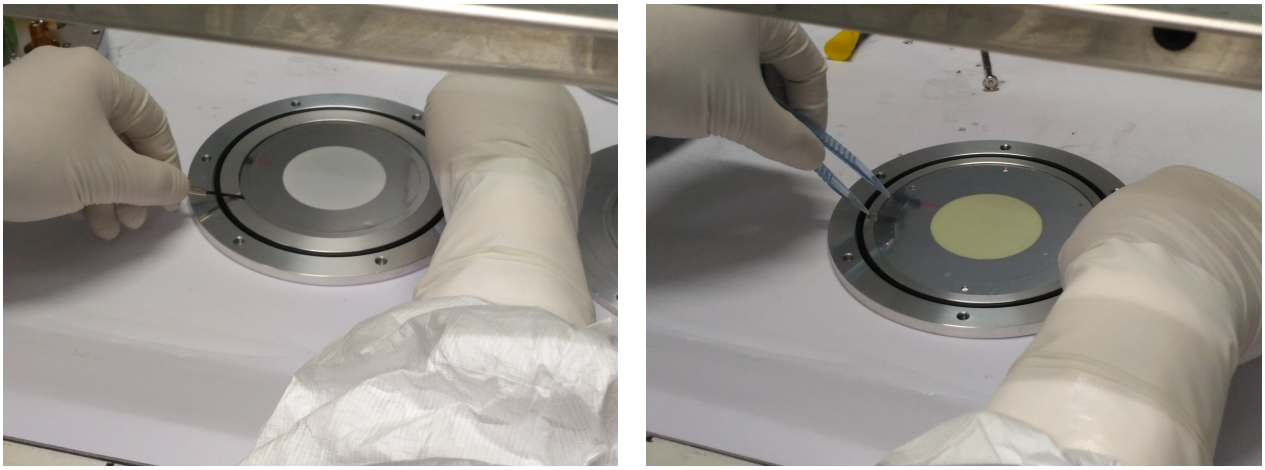

Figure 2.7: *Left Panel:* The 6 cm diameter ^{241}Am deposit is visible on an aluminum backing 11 cm in diameter attached to an aluminum ring 2 mm thick and with 11/10 cm external/internal diameter. *Right Panel:* The 6 cm diameter ^{235}U deposit is visible on an aluminum backing 12 cm in diameter attached to an aluminum ring 1 mm thick and with 12/10 cm external/internal diameter. In both photographs, the samples are still in their containers.

Sample	Reference Number	Activity (MBq)	Mass (μgr)	Areal Density ($\mu gr/cm^2$)	Atomic Abundances (%)
^{241}Am	TP2017-003-03	18.89(8)	148.9(22)	5.27(12)	^{241}Am :0.9998380(10)
	TP2017-003-04	16.73(7)	131.9(19)	4.67(10)	^{242}Am :0.000162(10)
	TP2017-003-05	15.17(6)	119.6(17)	4.23(9)	^{243}Am<0.000002
	TP2017-003-07	18.83(8)	148.4(21)	5.25(12)	
	TP2017-003-08	15.39(6)	121.3(18)	4.29(9)	
	TP2017-003-09	14.59(6)	115.0(17)	4.07(9)	
Total		**99.6**	**785.1**	**27.78**	

Table 2.1: List of the main characteristics and stated impurities of the ^{241}Am samples as reported in the JRC-Geel sample data-sheets. The isotopic composition results for the ^{241}Am enriched samples (lot 2034) were extracted in December 2017, while the activity measurement was performed in January 2018.

Sample	Reference Number	Activity (Bq)	Mass (μgr)	Areal Density ($\mu gr/cm^2$)	Atomic Abundances (%)
^{235}U	TP2017-005-12	20.9(6)	261(7)	9.24(3)	^{234}U :0.00035973(75)
					^{235}U :0.999336(14)
	TP2017-005-15	23.80(17)	297.7(22)	10.53(19)	^{236}U :0.00009629(53)
					^{238}U :0.0002073(14)
Total		**44.7**	**558.7**	**19.77**	
^{238}U	TP2017-004-02	25.70(25)	2067(21)	73.1(11)	^{234}U :0.00000000592(18)
					^{235}U :0.000004668(14)
	TP2017-004-07	27.5(3)	2209(24)	78.1(13)	^{236}U :0.00000009266(42)
					^{238}U :0.999992233(15)
Total		**53.2**	**4276**	**151.2**	

Table 2.2: List of the main characteristics and stated impurities of the ^{235}U and ^{238}U samples as reported in the JRC-Geel sample data-sheets. The isotopic composition results for the ^{235}U enriched samples (lot 680) were extracted in December 2009, while the activity measurement was performed on May 2018. For the ^{238}U actinide samples (lot 2677), the results from TIMS were extracted on November 2009 while the alpha activity was measured on May 2018.

Special care was taken from JRC-Geel for the ^{241}Am samples during their transportation. On top of each and every Americium deposit, inside their individual container, a protective aluminum lid was placed so as to avoid the contamination of the entire container. The lid was placed in a way that was not touching directly the radioactive deposit, but yet acted as shield against ablation of the radioactive material. The protective lid is shown in Figure 2.8.

For the mounting of the radioactive samples in the set-up inside the fission chamber, a special support was designed in order to hold the samples in a fixed position during the entire measurement. The configuration that was designed can be seen in Figure 2.9 and is composed of two aluminum supports that hold the sample in place only by mechanical pressure, therefore avoiding the use of any tape or glue.

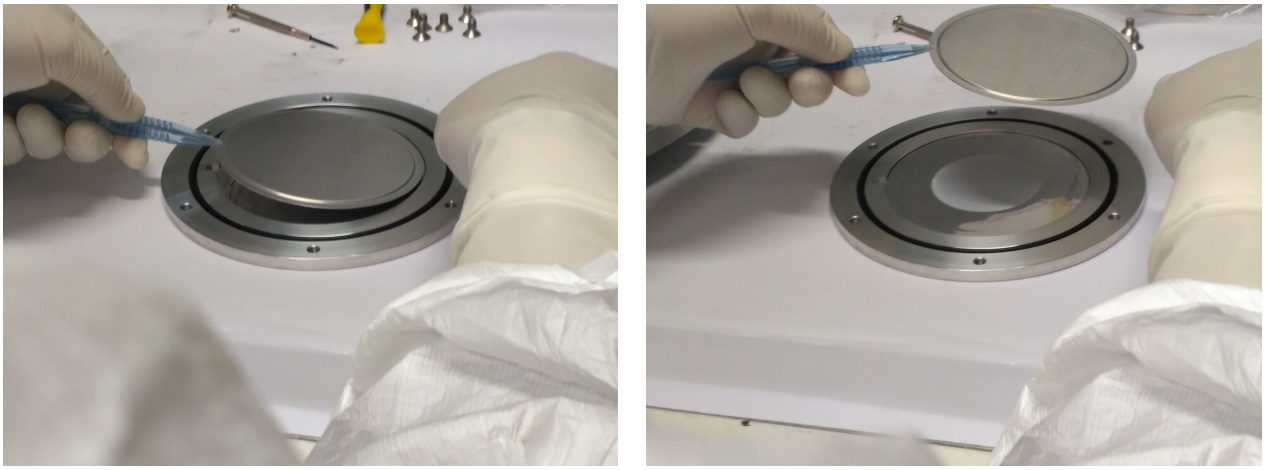

Figure 2.8: Protective aluminum lid covering the deposit of a ^{241}Am sample and held with a tweezer in the right photograph.

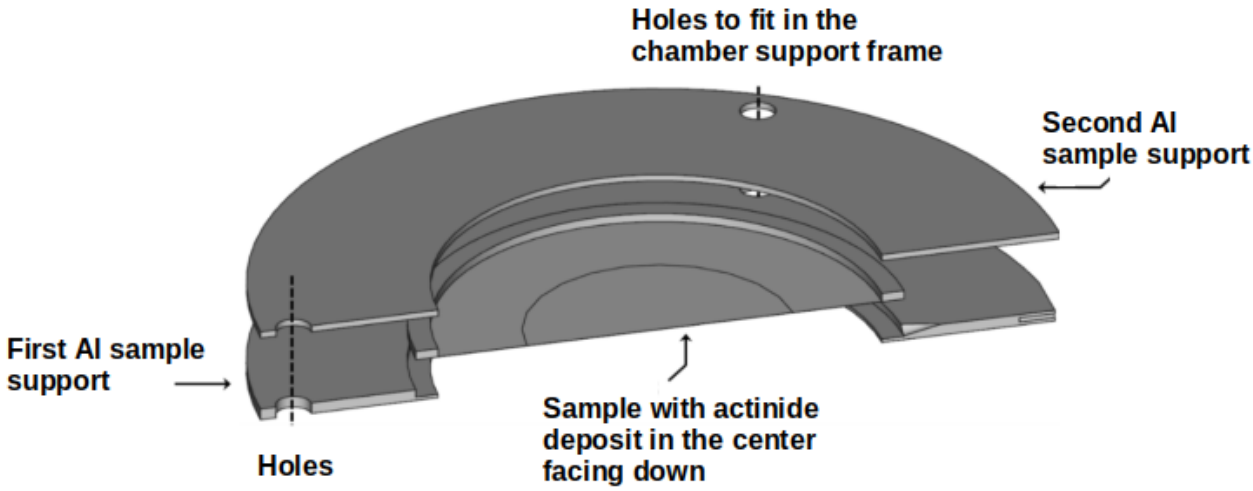

Figure 2.9: Illustration of the sample holders used in the experiment. The firm mounting of the samples inside the fission chamber was established by pressing the support ring of the radioactive sample between two aluminum rings.

2.4 Micromegas detectors

The measurement was carried out using an array of Micromegas detectors (**MICRO**-**ME**sh **GA**seous **S**tructure) which are part of the family of micro-pattern gas detectors (MPGDs). These detectors are parallel plate avalanche gaseous detectors that consist of two regions: the conversion region whose width ranges from several hundreds of μm to a few cm and the narrow amplification region with a width of some tens of μm [29]. In the conversion region, which is also referred in literature as drift region, the ionization takes place and charge carriers are directed towards the amplification region where an avalanche multiplication occurs due to the applied high electric field, inducing a signal. The two regions are separated by a thin micro-mesh foil, $9.5\,cm$ in diameter with $60\,\mu m$ holes on its surface (Figure 2.10). This is the active area of the detector which is by far larger than the samples' diameter ($6\,cm$) that were used in this experiment, so as to avoid efficiency losses.

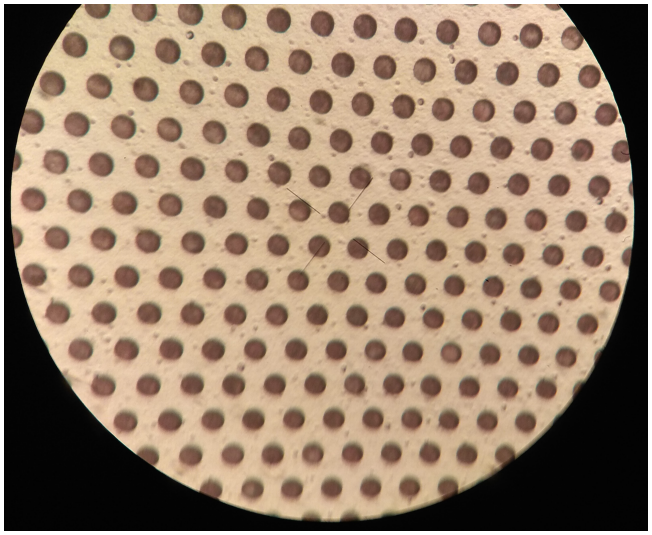

Figure 2.10: Photograph of the mesh of a Micromegas detector used in the experiment obtained with a microscope. The micromesh consists of $60\,\mu m$ diameter holes on its surface with a pitch of $120\,\mu m$ (pitch is the distance between the centers of the holes).

In particular, the Micromegas detectors of the "microbulk" variant that were used in the ^{241}Am(n,f) measurement were manufactured within CERN and are composed of $5\,\mu m$ copper micromesh layer, $50\,\mu m$ thick Kapton pillars that define the amplification region and a $3\,\mu m$ copper layer that corresponds to the anode of the detector (pad). In a more pictorial way, Figure 2.11 outlines the Micromegas structure with the corresponding material geometries. In neutron measurements, it is of particular importance to minimize the amount of material present in the beam. This is instrumental, in order to reduce the background related to scattered neutrons and avoid the perturbation of the neutron flux. The advantages of the detector also include its high efficiency ($\sim 100\%$), the fact that it is easy to manipulate, shows stability during the measurement and can be operated with an appropriate gas at atmospheric pressure.

The principle of operation of a Micromegas detector in fission experiments is the following: an ionizing particle (that could be one of the fission fragments that are generated (heavy or light) or an alpha particle coming from the decay of the radioactive sample) enters the gas volume of the conversion region, leaving part of its energy and ionizing the gas molecules. From the ionization, electrons and ion pairs are created. The weak electric field ($\sim 1\,kV/cm$)

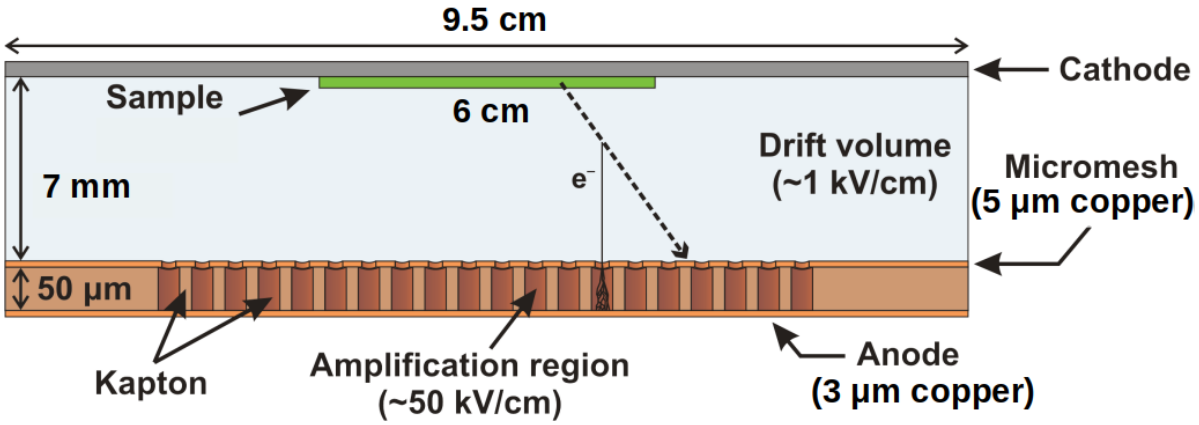

Figure 2.11: Illustration of structure and basic principle of operation of a Micromegas detector.

applied to the drift region causes acceleration of the electrons towards the micromesh. As the electrons reach and go through the holes of the mesh, they experience strong electric fields in the amplification region ($\sim 50\,kV/cm$) giving rise to an avalanche process which increases the number of electrons exponentially. Again due to the potential difference of the narrow amplification region, the electrons are collected in the anode plate (or else pad) while the ions are collected in the mesh plate inducing the corresponding signals.

Even though the electric fields in the conversion and amplification regions are quite uniform, around the micromesh holes, the electric field lines exhibit a funnel like shape (Figure 2.12). This is attributed to the large difference between the two fields applied. For the effective operation of the detector, the knowledge of the field shape around the holes of the micromesh is of prime importance, because from that depends the efficient transmission of the electrons through the holes as well as the fast evacuation of the positive ions in the mesh.

In order to achieve the optimum conditions for the detector function, before the experiment the electron transparency curve for each Micromegas detector is fully characterized. The electron transparency T which is one of the main intrinsic properties of the Micromegas detector, is described by the following ratio:

$$T = \frac{\#\, e^{-} \text{ amplified}}{\#\, e^{-} \text{ approaching the mesh}} \tag{2.9}$$

For the purpose of the characterization of the detector, an ^{241}Am source is attached in the Micromegas drift facing the mesh. For the deduction of the transparency curve for each detector, the mesh voltage is kept constant while the drift voltage is changing. For the transparency characterization of each detector, an integrated pocket ADC-MCA AMPTEK MCA8000D was used, along with the typical preamplifier - amplifier pulse shape electronics. The changes of the centroid of the deposited energy of the alpha particles was recorded. In this way the transparency curve was obtained. A typical electron transparency curve is shown in Figure 2.13, where the values were normalized to the maximum of the curve. In the plot, the electron transmission is shown as a function of the ratio of the electric fields, highlighting that for specific field ratios, the electron transparency reaches a plateau, close to value 1. Therefore, for the given mesh voltage, if the corresponding drift voltages are applied, the micromesh becomes almost 100% transparent to the drifting electrons. From this curve, the operational drift voltage was chosen to lie within the range of the plateau.

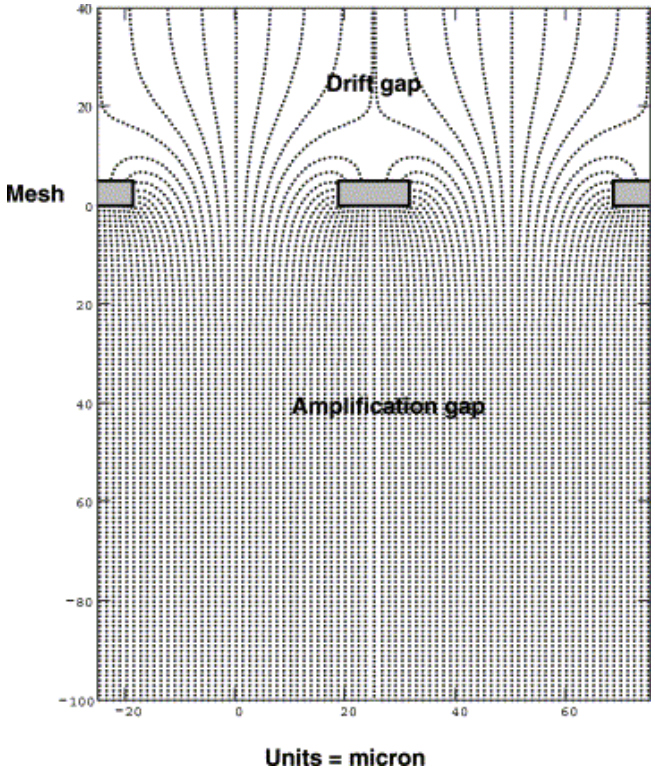

Figure 2.12: The electric field lines around the holes of the micromesh [30].

In order to complete the characterization of the Micromegas detector and verify its good behaviour, it is equally important to obtain its gain curve. In general, the gain in the Micromegas depends on many factors such as the chemical composition and pressure of the gas, the applied voltages and the amplification gap. The gain G can be expressed with the following formula:

$$G = e^{ad} \tag{2.10}$$

where d is the length of the amplification gap and a is the 1^{st} Townsend coefficient that represents the mean free path of the electron between two ionizations. Moreover, an approximation of this coefficient is given by the Rose and Korff formula:

$$a = pAe^{-BpE} \tag{2.11}$$

where p is the pressure of the gas, E is the electric field while A and B are parameters depending on the gas mixture.

Although the final mesh voltage of the detector cannot be chosen a priori, the knowledge of the gain curve is quite useful since it allows the estimation of the change of the mesh voltage that is needed to obtain a desired variation of the gain during the actual experiment. To obtain such a curve, the voltage of the drift was kept constant and the mesh voltage was varying. In Figure 2.14 a typical gain curve can be seen. In practice, it is desirable to set the mesh voltage to large values in order to suppress the alpha background on the one hand and record as clearly as possible the fission signals on the other hand.

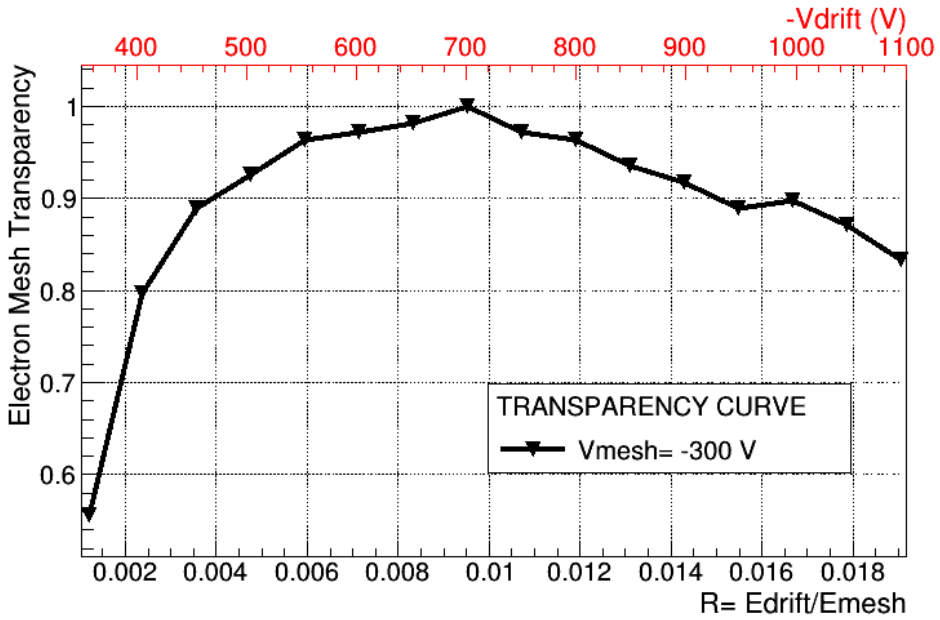

Figure 2.13: Characteristic electron transparency curve of a Micromegas detector used in the experiment with 50 μm amplification gap and 7 mm drift gap, as a function of the ratio of the electric fields in the drift and amplification region E_{drift}/E_{mesh} on the bottom x-axis and the applied drift voltage V_{drift} on the top x-axis. From this curve, the drift voltage in the experimental set-up was chosen to be -700 V (value within the above mentioned plateau).

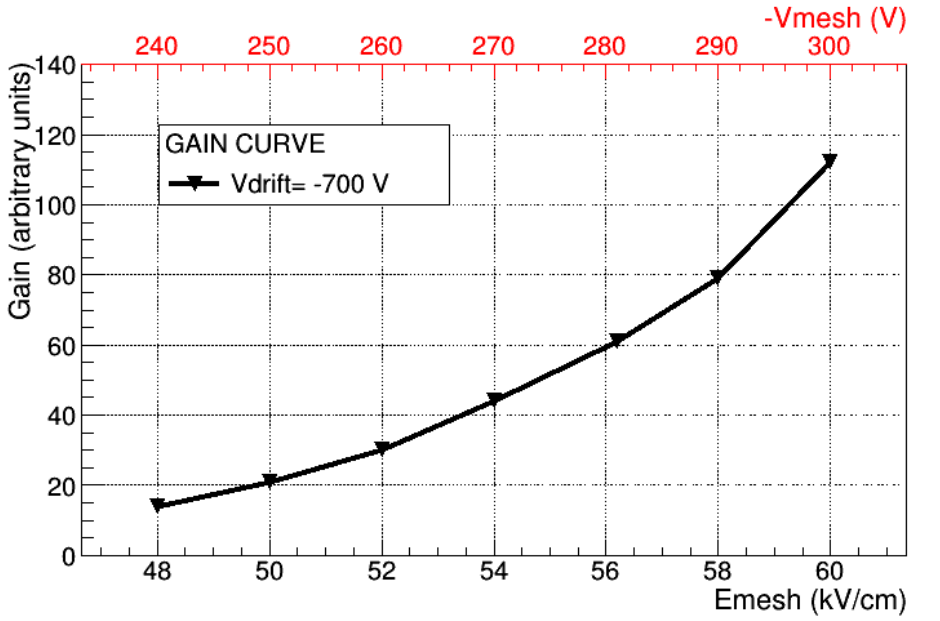

Figure 2.14: Characteristic gain curve of a Micromegas detector used in the experiment with 50 μm amplification gap and 7 mm drift gap, as a function of the electric field in the amplification region E_{mesh} on the bottom x-axis and the applied mesh voltage V_{mesh} on the top x-axis. From this plot, the exponential behaviour of the detector is verified.

To summarize, the adopted detector configuration was as follows: the amplification gap was $50\,\mu m$, the drift gap was chosen to be $7\,mm$, the operational drift and mesh voltages were $-700\,V$ and $-200\,V$ respectively, while the anode was grounded directly on top of the detector with a termination resistance of $50\,\Omega$. The drift gap, as well as rest of the distances inside the fission chamber, were fixed using spacers made of fiberglass and teflon. In addition, as will be mentioned later, the detectors were operated using a gas mixture of Ar:CF_4:isoC$_4$H$_{10}$ (88:10:2) at atmospheric pressure. By adopting the above mentioned configuration and passing the mesh signal of the Micromegas through the appropriate electronic chain (see Section 2.6), the obtained typical fission fragment electrical pulses had $\sim 250\,ns$ full width and FWHM of approximately $\sim 120\,ns$.

In the measurement, each fission foil was paired with a Micromegas detector facing its mesh, so in total ten detectors were employed. Four of them (batch FIMG-2016) were used also in a previous n_TOF measurement, that of ^{237}Np(n,f) , while the rest six (batch FIMG-2018) where newly produced and used in the ^{241}Am(n,f) experiment for the first time. The detectors had a total diameter of $18\,cm$ and an active area (mesh) of $9.5\,cm$. A minor difference between the two batches is that the old ones had also the same diameter in their anode, while the anode of the new ones had a diameter of $10\,cm$ (see Figure 2.15). In practice, this small difference did not play a significant role in the data analysis since the signals were collected from the mesh in all cases, and the ^{241}Am deposits have a much lower diameter of 6 cm.

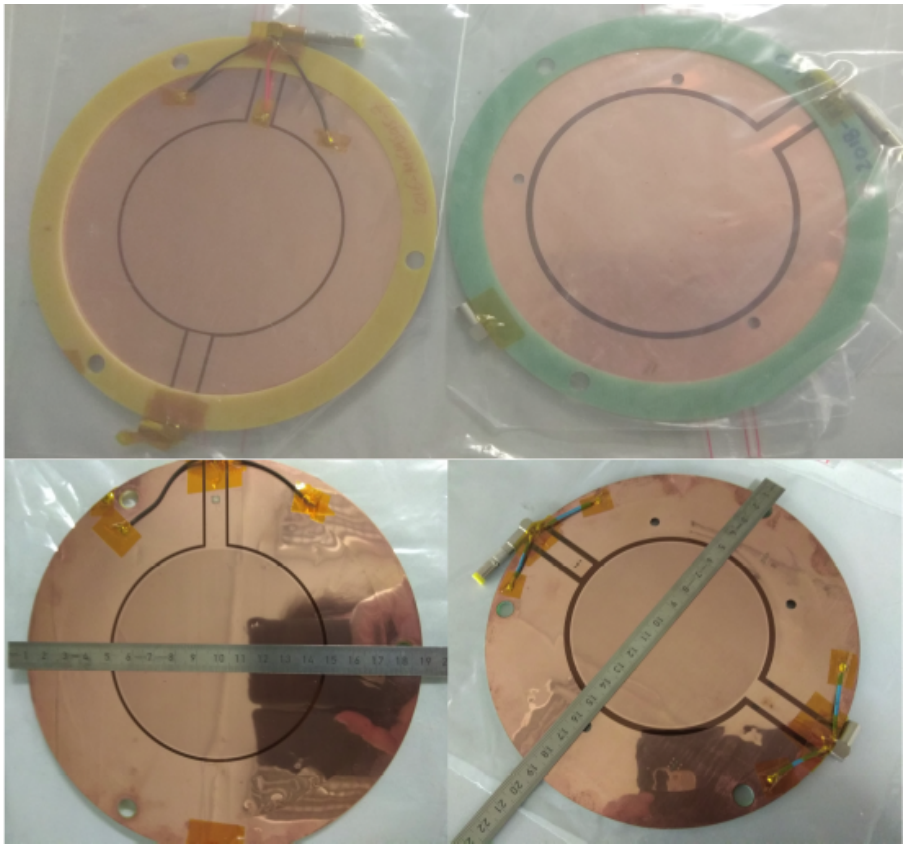

Figure 2.15: The left pictures correspond to FIMG-2016 Micromegas batch and the right ones to the FIMG-2018 batch. In both cases, the top picture corresponds to the anode side, where the detectors are supported with a 2.142 mm thick ring made of fiberglass (yellow and green ring accordingly) and the bottom picture corresponds to the mesh of each Micromegas batch respectively.

2.5 Fission chamber

The Micromegas detectors along with the actinide samples were placed in pairs in a cylindrical 30 cm long aluminum fission chamber. The chamber had entrance and exit windows made of 25 μm thick Aluminized Kapton with a diameter of 15 cm, which is large enough to cover the neutron beam spatial profile of any collimator set-up. The fission chamber was filled with a gas mixture of Ar:CF_4:isoC$_4$H$_{10}$ (88:10:2) at atmospheric pressure. During the measurement, the gas flow and pressure were monitored and controlled with a dedicated flow regulator system by applying two micro-controller valves to the Micromegas gas line, prior to and after the chamber respectively. In this way, the gas pressure was kept constant ensuring stable gain during the whole data-taking period.

The final configuration of sample-detector modules is shown in Figure 2.16. For the soldering of the detectors, following the practice that was applied in the previous fission measurement (^{237}Np(n,f)), in order to minimize the noise present in EAR-2, for the transferring of the mesh signal as well as for the grounding of the anode plate, LEMO cabling was adopted. For the drift voltage supply, a common single core (spaghetti) cable was soldered so as to distribute the voltage to each drift plate.

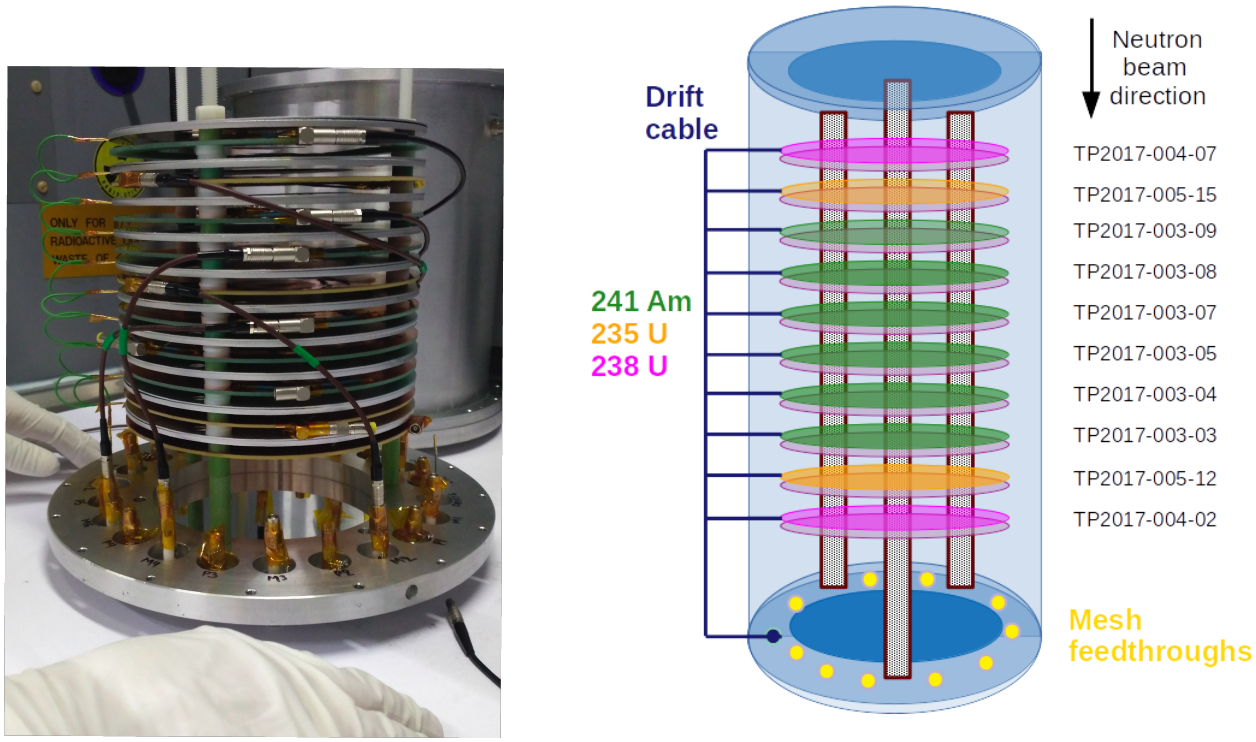

Figure 2.16: *Left Panel:* The measurement set-up consisting of ten Micromegas detectors coupled with the actinide samples, before inserting into the fission chamber. The photograph was taken in the ISOLDE Class-A lab during the mounting procedure.
Right Panel: Schematic illustration of the configuration of the actinide samples inside the fission chamber with respect to the direction of the neutron beam. For the determination of the cross section, the "sandwitch" configuration was adopted, where the isotope under study is placed in the middle of isotopes with a well known cross section that serve as flux monitors.

2.6 Electronics and data acquisition

For the ^{241}Am(n,f) experiment, new preamplifier modules manufactured by INFN-Bari were employed. Even though the main circuit of the current sensitive preamplifiers remained the same compared to previous fission measurements with Micromegas detectors performed at n_TOF, significant upgrades were made with respect to the housing of the modules. The multi-channel modules used in the ^{242}Pu(n,f) , ^{240}Pu(n,f) and ^{237}Np(n,f) measurements, were replaced by single channel Printed Circuit Boards (PCBs) avoiding in this way any cross-talk between the detectors. In addition, each single channel PCB which was coupled with a unique Micromegas detector, was shielded in a separate aluminum box, leading to a significant reduction of electronic noise. The improvement of the quality of the recorded data is depicted in Figure 2.17.

The low voltage power supply of the preamplifiers ($\pm 12\,V$) was applied by means of two CAEN N5424 4-channel NIM modules, provided by the Nuclear Physics Laboratory of Ioannina and one home made unit from n_TOF that served the same purpose (Figure 2.21). These units

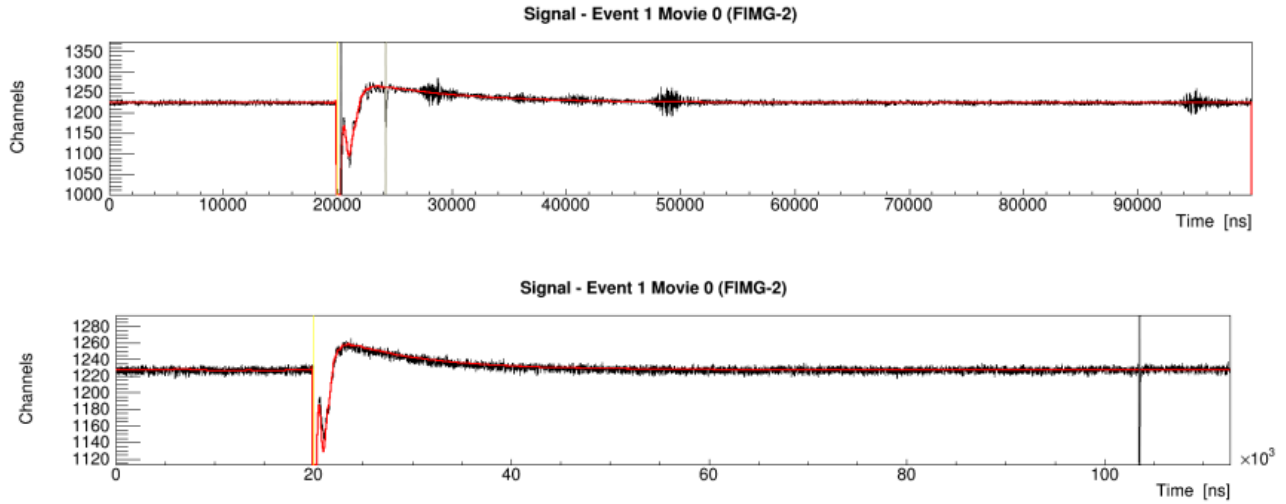

Figure 2.17: Top-panel: Example of a signal movie display from the ^{237}Np(n,f) campaign using the old preamplifier modules. Bottom-panel: Example of a signal movie display from the ^{241}Am(n,f) campaign using the new single channel PCB preamplifiers. In both cases, a ^{235}U sample is employed.

were plugged in a NIM crate which was placed inside the experimental hall in EAR-2. The preamplifiers were used to provide with voltage the mesh electrodes of the Micromegas detectors and to read-out the analogue induced signals.

At n_TOF the detector signals are digitized and stored as waveforms. In this way, the characteristics of interest such as the amplitude, the timing information, the risetime and the full width of the signals can be extracted. The signals from the preamplifiers were fed to the flash Analog-to-Digital Converters (ADC's) of n_TOF in EAR-2, with 12 bit resolution (Teledyne SP Devices, model: ADQ412DC [31]) for digitization. The raw-data for each detector were recorded using a digital acquisition system [32] that was operated with a 112.5 MHz sampling rate (one sample per 8.9 ns) and a full scale range of 5 V. The n_TOF DAQ system is triggered by the PS telegram signal, that corresponds to the extraction of the PS beam towards to the n_TOF spallation target. Following each trigger signal, the acquisition time window was 16 ms long. Taken into account the flight path of EAR-2, this time interval corresponds roughly to a minimum neutron energy of $\sim 0.008\,eV$.

In order to minimize the recording of unnecessary data, a zero-suppression algorithm was applied to the raw-data. After the $\gamma - flash$, the first 100 μs of data were written intact, due to the oscillation of the baseline induced by the $\gamma - flash$ itself. After this time interval, the signals are recorded only if the amplitude of the signal exceeds the amplitude threshold value, set for each individual detector. In order to save the full waveform of the recorded signals, a fixed number of waveform samples is recorded before and after the signal threshold crossings, the so-called pre- and post-samples.

After the digitization, the data were temporarily saved on a local disk. Along with the information concerning the characteristics of the signal itself and the ID of the detector, additional details extracted from beam monitors that follow the intensity of the proton beam bunch by bunch and are located before the spallation target, were also stored. These monitors are the **B**eam **C**urrent **T**ransformer (BCT) which is designed to provide the number of protons impinging on the spallation target provided by the PS and the **P**ic**K**-**UP** Wall Current Monitor

(PKUP) which provides a signal whose amplitude and area are related to the intensity of the proton bunch. Every twenty bunches (equals to twenty events), a segment was created which was moved to the **C**ERN's **A**dvanced **STOR**e manager (CASTOR) for storage on tape for off-line processing and analysis.

2.7 Experimental set-up in EAR-2

The fission chamber was aligned with respect to the neutron beam in EAR-2 in a two step procedure. Firstly, the chamber was aligned roughly using a laser system available in the experimental hall and afterwards, two EBT^3 Gafchromic foils were fixed in contact with the top and bottom window of the fission chamber (Figure 2.18). After a few hours of exposure to the neutron beam, the foils were removed to be scanned and be post processed using the ImageJ toolkit (**Image** processing toolkit written in **J**ava) [33]. The fine-tuning of the placement of the fission chamber was done according to the visualization of the beam spot in the Gafchromic foils.

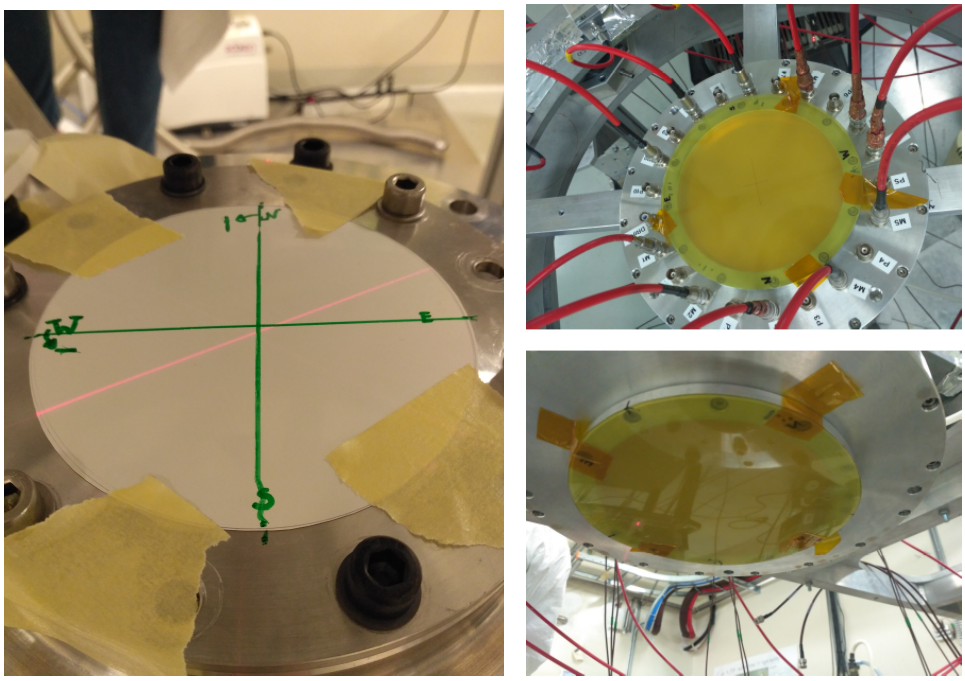

Figure 2.18: Alignment of the fission chamber in EAR-2 with respect to the neutron beam using the laser system (left panel) and the EBT^3 Gafchromic foils on top and bottom of the fission chamber (right panels).

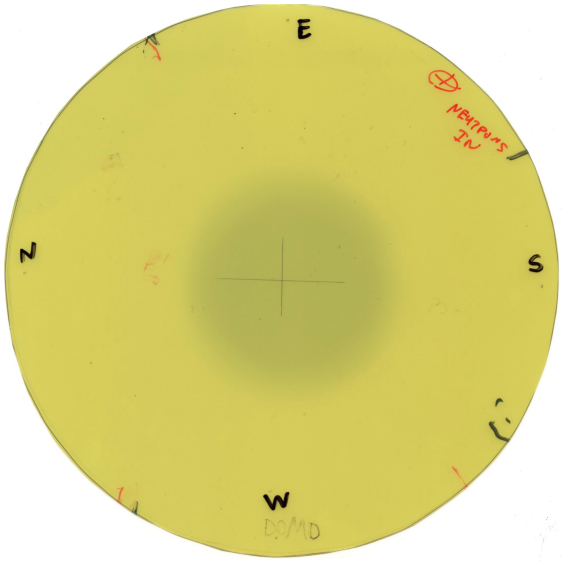

Figure 2.19: A scanned image of an EBT^3 Gafchromic self-developing dosimetry film, confirming the centrality of the fission chamber with respect to the neutron beam spatial profile. The image corresponds to a few hours of exposure in front of the neutron beam, using the fission collimator in EAR-2 at the beginning of the ^{241}Am(n,f) campaign.

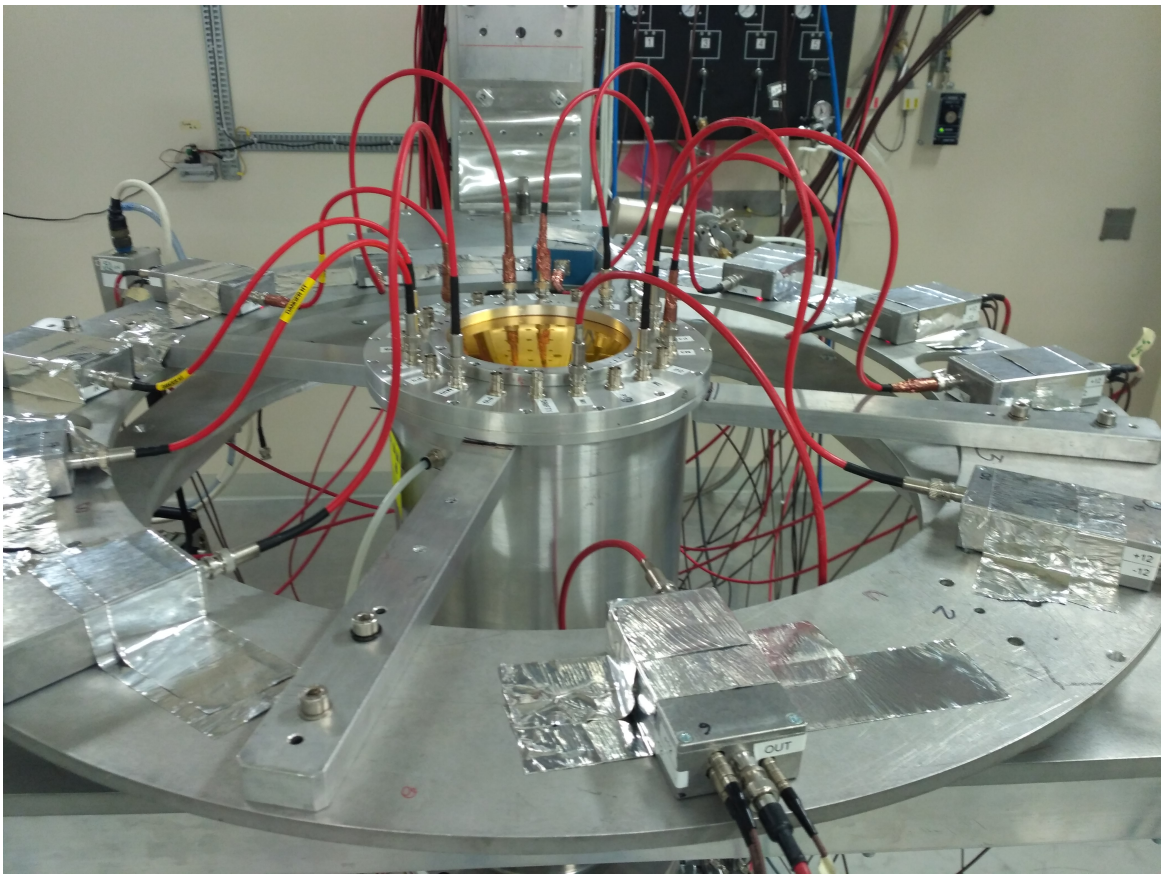

Figure 2.20: The adopted experimental set-up of the ^{241}Am(n,f) measurement in EAR-2 consisting of the fission chamber and the array of the Micromegas preamplifiers that were used.

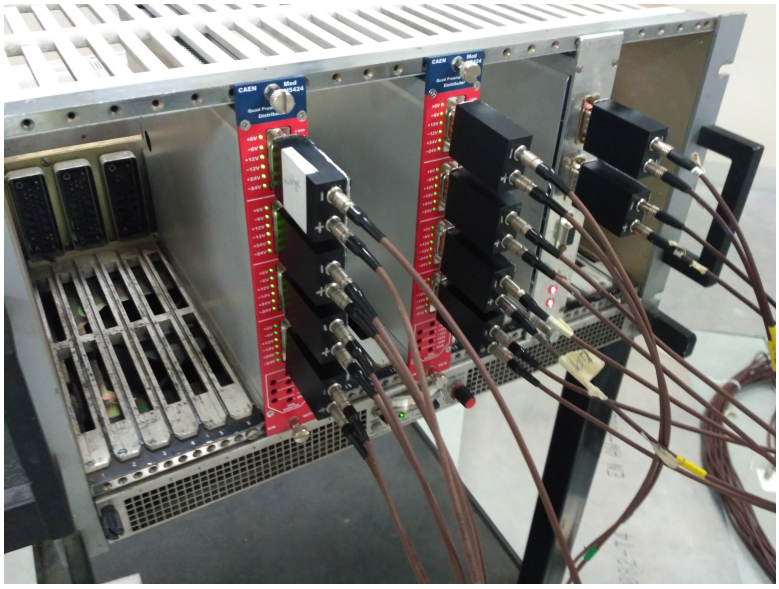

Figure 2.21: Photograph from the experimental hall in EAR-2, showing the NIM modules used for the low voltage power supply of the Micromegas preamplifiers, along with the custom made DB9-to-lemo adapters that were built in the Nuclear Physics Laboratory in Ioannina to provide the $\pm 12\,V$ for the operation of the preamplifiers.

Chapter 3

Data Analysis

The steps of the data analysis process begin from the study of the signals of each detector, the so-called "raw data", which are processed with a dedicated Pulse Shape Analysis code. Next, the quality of the data is evaluated appropriately and those that do not meet the required standards are discarded from the analysis procedure. Finally, the cross section is calculated after applying the necessary correction factors derived from the analysis.

3.1 Analysis of RAW data

3.1.1 Pulse shape analysis

The data transferred to CASTOR are called RAW data and were stored in binary files that could be converted to another format for off-line analysis. The binary files have the following structure. Each waveform, produced by a single proton bunch (trigger), that exceeds the zero-suppression threshold, is digitized and recorded in one of the so-called "movies" for a certain time period. The first movie, in case of presence of neutron beam (beam-on), contains always the $\gamma - flash$ pulse along with other fission and alpha particle signals. In the present experiment, the duration of the first movie had a predefined duration of $100\,\mu s$. The rest of the movies are stored in the files following a chronological order. Every 20 triggers (i.e. proton pulses), a segment is created and many segments compose a run file. Each run is identified by its unique number (RunNumber) and is composed of a predefined number of triggers. In case of absence of the neutron beam (beam-off), data were stored in a similar way, except there was no $\gamma - flash$ pulse recorded. In this case, the DAQ trigger was internal and periodic. The trigger frequency and the time duration of the digitization of the beam-off data depends on the expected activity. Depending on the requirements of each experiment and the volume of data of each measurement, the duration of the run and/or the number of triggers was adjusted accordingly, so that the final volume of the files was as manageable as possible for the next stages of the analysis procedure.

In order to convert the RAW data to ROOT format, a Pulse Shape Analysis code (PSA) was developed within the n_TOF collaboration by P. Žugec et al. [34]. This code was designed for baseline calculation, pulse recognition and pulse shape fitting by adjusting some external input parameters based on the characteristics of the type of detector used.

The algorithm is based on the calculation of the derivative of the signal which is used for the

pulse recognition. Each signal is integrated on both sides of the selected point reducing in this way the noise and smoothing the result. Once the derivative is calculated, the recognition of the pulse takes place. A signal is recognized if its derivative crosses four times a certain threshold value or in case of pile up events the previous condition is relaxed and two consecutive crosses, below or above the mean of the derivative are accepted. The threshold is determined from the RMS (Root Mean Square) of the part of the derivative that corresponds to the signal baseline. The default threshold is set as 3.5 x RMS unless selected otherwise. In case of close unresolved pile up events, the step size for calculating the derivative can be reduced up to the point where the dip between the pulses is able to trigger at least one of the threshold crossings. The reduction of the step size of the derivative is performed gradually and in a controlled way, as it brings a simultaneous reduction of the signal-to-noise ratio, thus making it difficult to distinguish the latter from each other.

After the calculation of the derivative and the recognition of the pulses, the routine locates the $\gamma - flash$ pulse. At this point, a preliminary elimination of the recognized pulses takes places by adjusting some parameters in the UserInput file concerning the pulse width, namely the signal's low and high width threshold. As a next step, the baseline is calculated. The treatment of the baseline is different close to the $\gamma - flash$ region, where many methods are available to treat the oscillations and the rebound caused by the $\gamma - flash$ pulse. At longer time periods after the $\gamma - flash$, the baseline becomes smooth and therefore a constant baseline is calculated taking into account the points between the reported pulses. In the present analysis, for the baseline line in the $\gamma - flash$ region, an average shape of the $\gamma - flash$ signal along with its following rebound, was provided within the UserInput file, therefore calculating an adaptive baseline.

Once the baseline is defined, it is subtracted from the rest of the waveform and the clear signal is revealed. An illustration of the most significant steps that are followed by the Pulse Shape Analysis routine is shown in Figure 3.1, in a region where the baseline is smooth.

One of the most important elements of the pulse shape analysis routine is the determination of the pulse height and the pulse area. This is a very crucial point, since based on these results, certain elimination conditions are applied in order to distinguish the noise and false pulses from the clear signals. The elimination algorithm includes an amplitude threshold and an area/amplitude low and high threshold. Within the analysis routine, three methods are available to calculate the final amplitude of the pulse. These options include a) the search of the maximum of the pulse, b) the activation of the parabolic fitting to the top of the pulse and c) the pulse shape fitting where pulse shape waveforms need to be provided by the user in the UserInput file, so that the final amplitude and area will be determined from the fitted pulse. In the last case, which is actually the one adopted for the analysis of the present work, the routine selects among the provided pulse shapes, the one that provides better χ^2 value for each recognized pulse and then performs the corresponding fitting procedure.

In addition to the amplitude and area of the pulse, the routine takes care of its timing properties. The timing is determined from the signal crossing a fixed fraction of the pulse amplitude. The arrival time of a pulse (tof) is calculated when the pulse crosses a fraction of 30% of its amplitude. With the same logic, the arrival of the $\gamma - flash$ pulse (tflash) is calculated. Furthermore, the peak time information is also reported which corresponds to the peak position of the fitted pulse (peak tof). Moreover, the rise time of the pulse (risetime) is calculated as the time needed for the leading edge of the pulse to rise from 10% to 90% of its amplitude. Finally, the full width at half maximum (fwhm) and the full width at the tenth

maximum (fwtm) are obtained from the time difference of the signal crossing 50% and 10% of the amplitude respectively. All these very significant parameters of each recognized pulse are saved into the ROOT files and are valuable for the data selection during the next steps of analysis.

The created ROOT files have a Tree structure for each type of detector used for the data acquisition. The parameters extracted from the PSA routine, constitute the Tree's branches. The most important branches along with a short explanation are listed below:

- RunNumber: run ID number
- segment: segment number of a specific run
- BunchNumber: counter of the events for the whole run
- event: counter of the proton bunches for each segment
- movie: part of the event where a signal is located
- PSpulse: flag that describes the type of proton beam (dedicated or parasitic)
- PulseIntensity: proton pulse intensity (from BCT)
- date: date of measurement
- time: time of measurement
- detn: detector ID number
- tflash: $\gamma - flash$ timestamp measured at 30% of the signal's amplitude
- tof: neutron's time-of-flight measured at 30% of the signal's amplitude
- peak_tof: neutron's time-of-flight measured at the highest point of the signal's amplitude
- amp: amplitude of the fitted signal
- area: area of the fitted signal
- fwhm: FWHM of the signal
- fwtm: FWTM of the signal
- risetime: rise time of the signal from 10% to 90% of the amplitude
- pulseshape: ID of the provided pulse shape waveform for the fitting of the identified pulse
- chi2: minimal reduced χ^2 of the performed fit of the pulse for a selected pulse shape (the closest the value of χ^2 is to unity the better the fit)
- area_0: area of the identified pulse before fitting assuming a square pulse equal in height
- amp_0: amplitude of the identified pulse before fitting

As a following step in the analysis, the correlation of the above mentioned parameters with each other, as well as the visualization of the data, are primary ingredients for the derivation of the cross section. For this purpose, the most important parameters are graphically represented in the form of histograms that aim to assist in the data quality control and selection of fission events. The data selection was realized with dedicated routines written in the C++ programming language. By looping over the entries of the Micromegas detectors, essential cuts were applied to discard artificial or background pulses. In this way, the fission events were carefully selected and identified, along with the necessary correction factors needed for the ^{241}Am(n,f) reaction cross section determination.

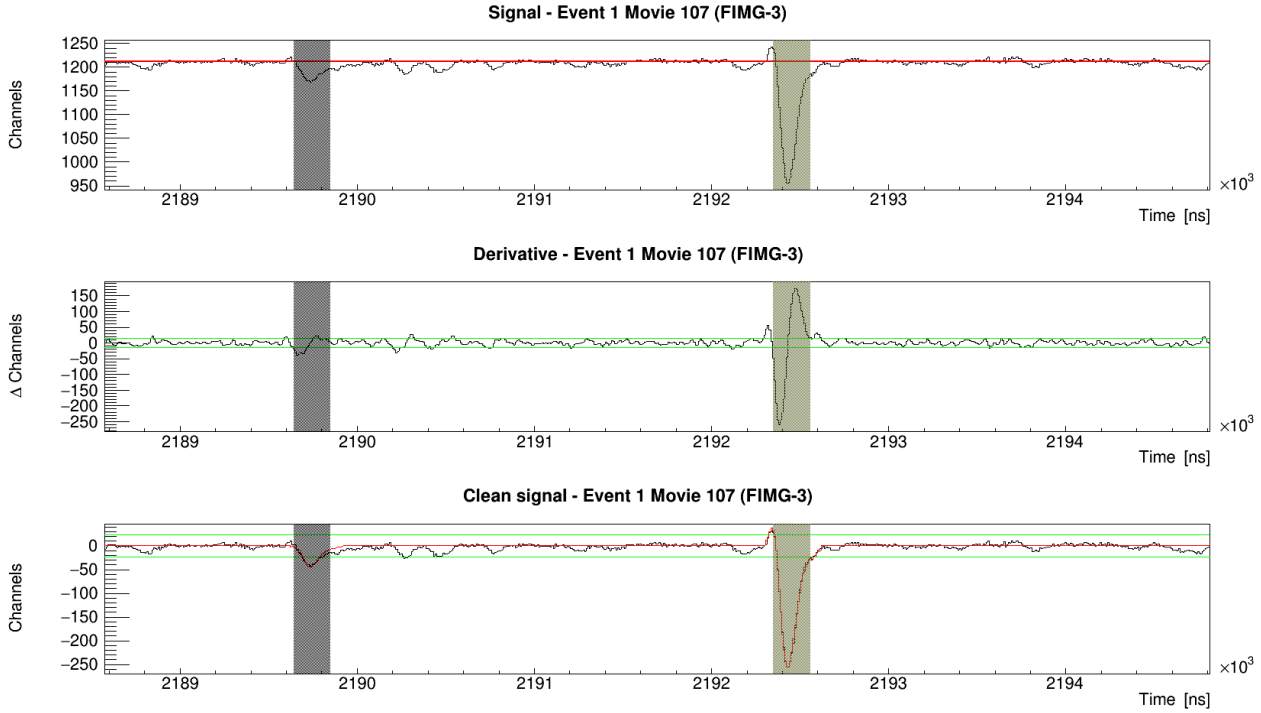

Figure 3.1: Pulse Shape Analysis routine: The first derivative (middle panel) of the raw movie (top panel) is calculated. The green lines represent the positive and negative threshold applied to the derivative. After the identification of the pulses, the calculated baseline is subtracted and finally the signals are reconstructed (bottom panel). The depicted pulses are typical signals of an alpha particle and fission event respectively, from a ^{241}Am sample.

3.1.2 Treatment of fission signals

For the recognition of the pulses in the movies, two pulse shape waveforms were provided to the PSA code for each Micromegas detector that was employed in the experimental fission set-up. A characteristic example of these signals normalized to the same amplitude is visible in Figure 3.2. As can be seen, the fall time of the signals is identical, since this characteristic timing property is related to the constant of the associated electronics. The rise time of the signals on the other hand, is different. The differences on the rise time of the pulses can be interpreted by considering both the geometry of the sample-detector and the mechanism of charge collection.

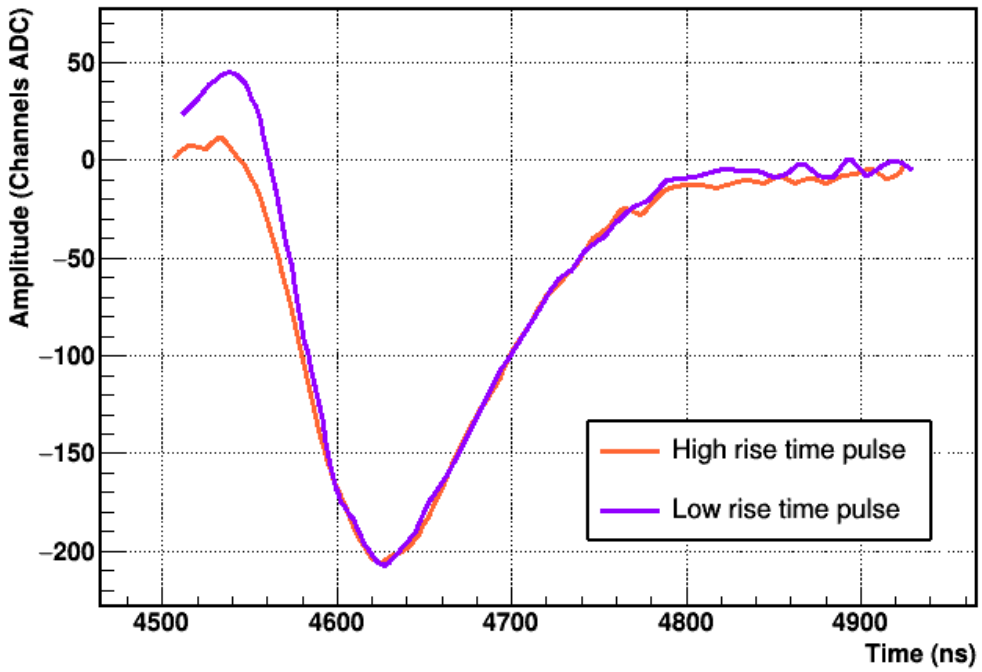

Figure 3.2: Characteristic signals of the same Micromegas detector with a fwhm of 120 ns.

When a fission event occurs, two fission fragments are generated inside the radioactive sample and due to the kinematics of the reaction they travel in opposite directions. One of the fission fragments (heavy or light) will enter the gas volume of the detector and will deposit part of its initial energy along its path. Generally, the larger the amount of the deposited energy, the higher the amplitude of the detected fission signal that is created from the movement of the charge. The rise time of the signal depends on the emission angle of the fission fragment in the drift region of the Micromegas detector. A fission fragment that is emitted in the forward direction, almost at 0° vertical to the detector's surface, leads to the creation of electrons in the drift region that move towards the mesh but entering the amplification region in different times due to the the fact that are created in a different depth of the drift volume. As a consequence, the charge collection starts as soon as the nearest electron to the micromesh goes through the amplification region and ends when the most distant one reaches the micromesh. Therefore, the forward emission of the fission fragments implies a faster charge collection mechanism and high rise time values. On the contrary, a fission fragment that is emitted from the sample at large angle (lateral direction), almost parallel to the detector plane at 85°, creates electrons that have to travel the same distance ($\sim 7\,mm$) to reach almost simultaneously the micromesh. As a result, it takes longer for the charge collection procedure to start but as a duration is faster and this leads to signals with lower rise time values. The extreme above mentioned cases, including also the case that the fission fragment is emitted with an intermediate angle, are visualized in Figure 3.3.

The two pulse shapes with the different rise times were introduced to the PSA code, so that for each detected signal the routine selects the one that better reproduces the recorded waveform. As a proof of principle, in Figure 3.4, a plot of the rise time of the detected signals from a ^{235}U sample as a function of their amplitude, demonstrates that the pulses fitted with the

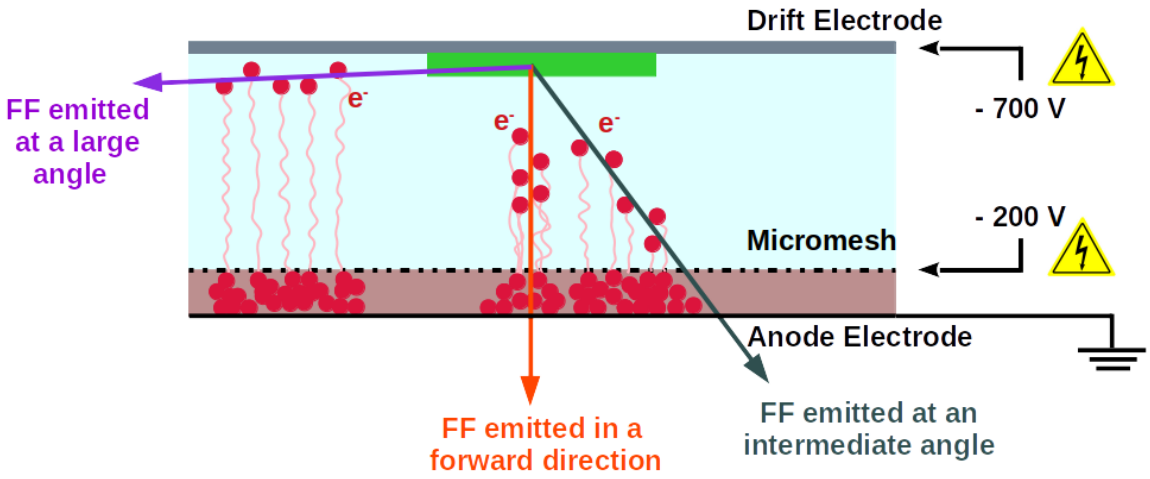

Figure 3.3: Charge collection mechanism depending on the emission angle of the fission fragment.

pulse shape that is suitable for fission fragments emitted at large angles (purple distribution) have been identified with lower rise time values. In addition, the signals fitted with the pulse shape of fission fragments emitted in the forward direction (orange distribution) have been reported with higher rise time values. Of course, an overlapping region of the two distributions exists where pulses emitted in the intermediate angles can be reconstructed using both pulses shapes.

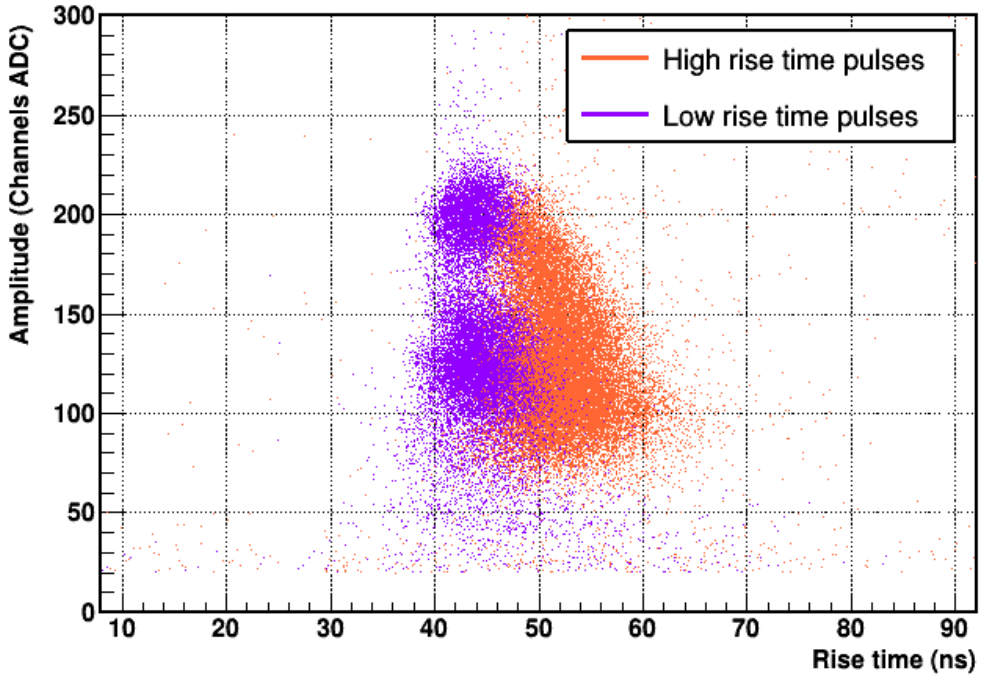

Figure 3.4: Characteristic rise time distributions of the detected signals from a ^{235}U sample in comparison with their amplitude. The rise time of a pulse is calculated as the time needed for the leading edge to rise from the 10% to 90% of its amplitude.

Another interesting remark extracted from this plot concerns the slightly higher preference of small amplitude pulses towards the forward emission direction. This experimental observable has a logical explanation if the following hypothesis is taken into account based on the adopted sample-detector geometry (7 mm drift gap, 9.5 cm micromesh diameter). Assuming that a fission fragment is emitted from the center of the sample with an angle for instance of 45°, it will have a path up to 4.8 cm to deposit part of its energy. On the contrary, a fission fragment that is emitted from the center of the sample in the forward direction, will have less than 7 mm available distance to deposit its energy and therefore can be considered that its energy deposition will be lower resulting in a pulse of smaller amplitude.

Furthermore, inside sample material the energy degradation of the fission fragments emitted vertically to the detector's surface is smaller than those emitted in the lateral direction. For this reason, the kinetic energy of these fission fragments in the active detector volume is higher and therefore the energy deposition is smaller (lower stopping power). For the same reason, for those events emitted vertically to the detector's surface, the heavy fission fragments are better identified due to the smaller energy straggling of those events.

3.1.3 Treatment of the γ-flash

In the first movie of each event for every detector, the routine recognizes the $\gamma - flash$ pulse when a certain set of conditions is satisfied. The proper identification of the start pulse is of prime importance, since the time-of-flight of the recorded signals is measured relative to the $\gamma - flash$. The $\gamma - flash$ pulse is accompanied by a baseline oscillation and a rebound that has to be treated with a special procedure. In order to subtract the $\gamma - flash$ instabilities, the average $\gamma - flash$ pulse along with the accompanied oscillations were deduced for each detector by averaging more than 2200 $\gamma - flash$ signals.

Indeed, as can be seen in Figures 3.5 and 3.6, the main $\gamma - flash$ signal shape scales with the pulse intensity whereas the oscillatory rebound has a more steady shape. This fact is extremely helpful, since an average shape of the $\gamma - flash$ can be subtracted from each individual first movie of each event where the $\gamma - flash$ is present. The subtraction of this waveform intends to lead to a proper reconstruction of the baseline close to the $\gamma - flash$ region, extending in this way the energy region where fission signals of higher neutron energy can be properly analyzed.

To validate the method, the average $\gamma - flash$ waveform from each detector was subtracted from the individual raw movies and the reconstruction of the baseline was examined. Two examples of this procedure, namely a ^{235}U and ^{241}Am case can be observed in Figures 3.8 and 3.9 respectively, where the residuals from this subtraction after a certain time-of-flight correspond to high energy fission events. The resulted residuals confirmed the validation of the method since they fluctuate around zero amplitude. This, in turn is the proof that the $\gamma - flash$ rebound between separate neutron bunches is consistent enough to be subtracted from the raw signals. Of course, a result of this subtraction that is actually the drawback of the method, is the generation of false pulses that can be parsed into the analysis ROOT files and can be mixed up with true events.

As mentioned in the previous chapter, in the present experiment signals were recorded by adopting a sampling rate of 112.5 MHz. This means that the waveform was sampled every 8.9 ns.

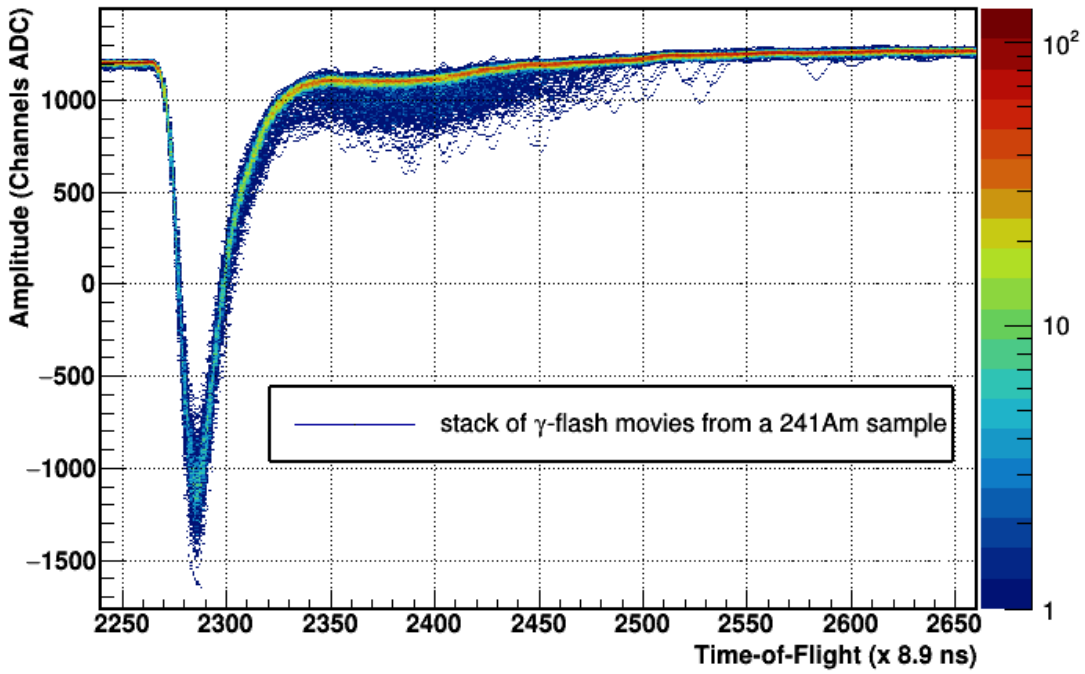

Figure 3.5: Stack of $\gamma - flash$ signals from a ^{241}Am sample. The main $\gamma - flash$ pulse scales with the pulse intensity whereas the following oscillatory rebound shows a consistent behaviour independently of the $\gamma - flash$ amplitude.

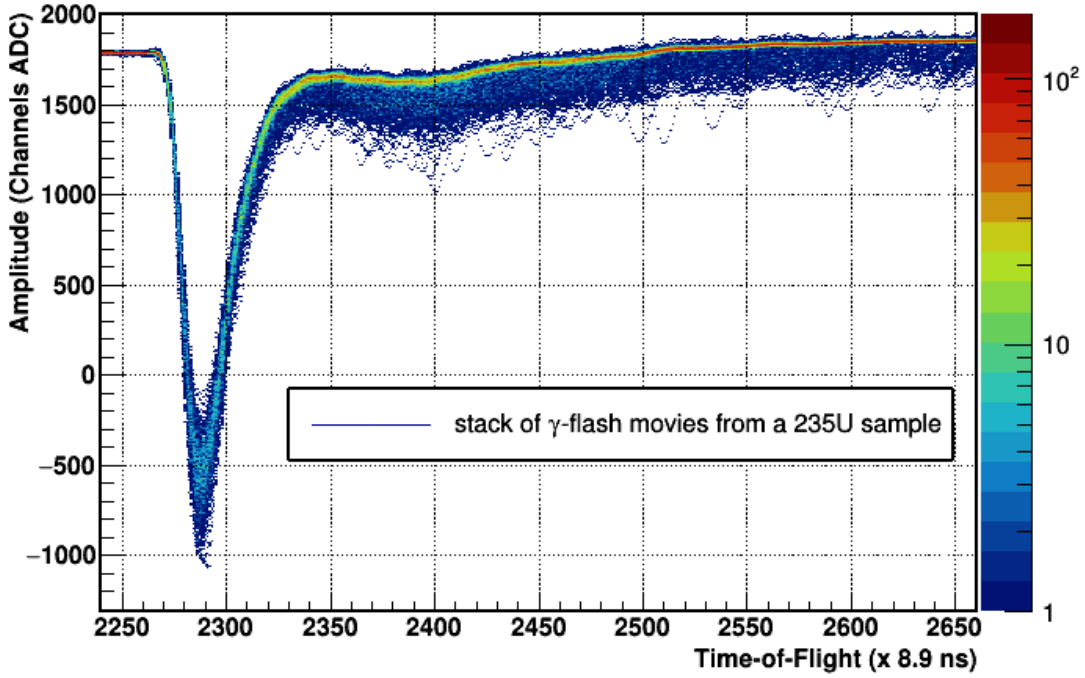

Figure 3.6: Stack of $\gamma - flash$ signals from a ^{235}U reference sample.

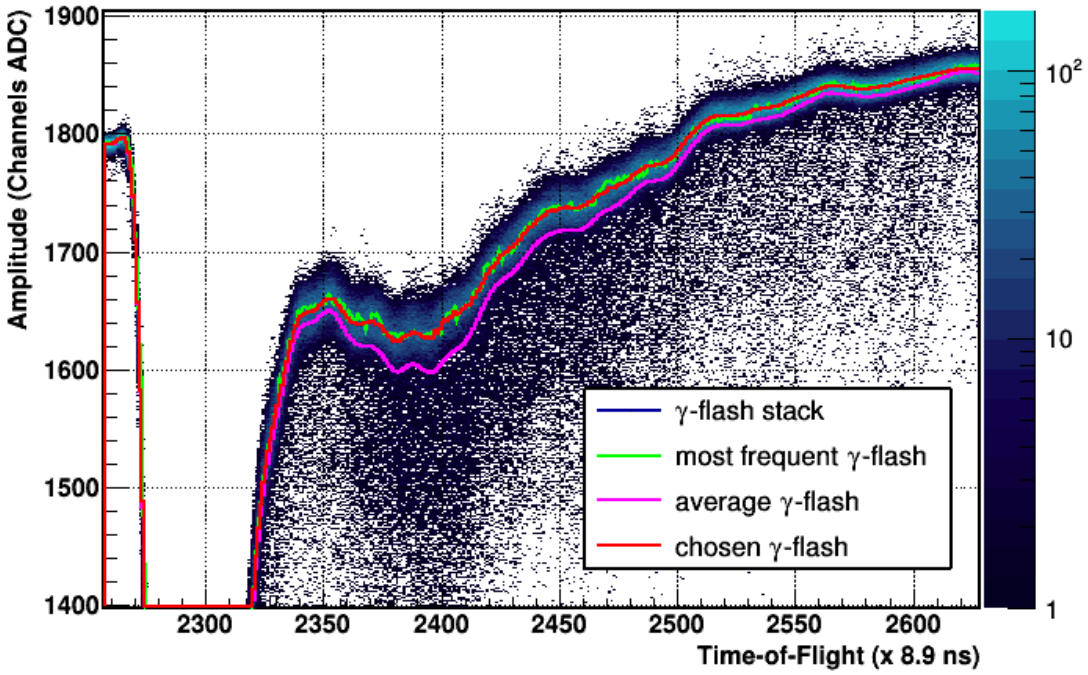

Figure 3.7: Close look to the rebound region of the stack of $\gamma - flash$ signals from a detector with a ^{235}U sample. The final shape of the $\gamma - flash$ is estimated accordingly to the most frequent value of the stack so that the reconstructed baseline will fluctuate around zero, as will be discussed below.

For each detector, the extracted average shape of the $\gamma - flash$ was estimated separately for proton bunches of full intensity (dedicated) and proton bunches of half of the nominal intensity (parasitic). The two shapes were compared with a proper normalization to the amplitude of the $\gamma - flash$ and it turned out to be a perfect match. An example of this comparison, is visible in Figure 3.10. The pulse shape of $\gamma - flash$ that is illustrated in Figure 3.10 was provided inside the UserInput file of the PSA routine to be used for the $\gamma - flash$ signal recognition. The routine aligned the pulse shape to the actual raw signal by fitting the leading edge of the initial pulse along with a small portion of its falling edge as defined by the user. Then the provided pulse shape waveform was scaled according to the multiplication factor obtained from the fitting and finally subtracted from the raw signal.

This whole procedure for the $\gamma - flash$ subtraction is vital for the measurement of ^{241}Am(n,f) in EAR-2 especially with the use of the fission collimator. The experimental set-up in EAR-2 is situated only 19.5 m from the center of the lead spallation target and as a result the very fast neutrons are detected at close times-of-flight between them. In other words, in terms of neutron energy the spectrum is quite compressed. In addition, the shape of the $\gamma - flash$, meaning its huge amplitude covering almost 2500 channels in the dedicated mode, originated from the large fission collimator and its width at the base of the signal which is $\sim 500\,ns$, cause a limitation on the maximum energy of fission signals that can be reconstructed. In Figure 3.11, the matching of the fission signals to neutron incident energies is noticeable. Fission signals can be detected in the rebound of the $\gamma - flash$ as well as in the falling edge.

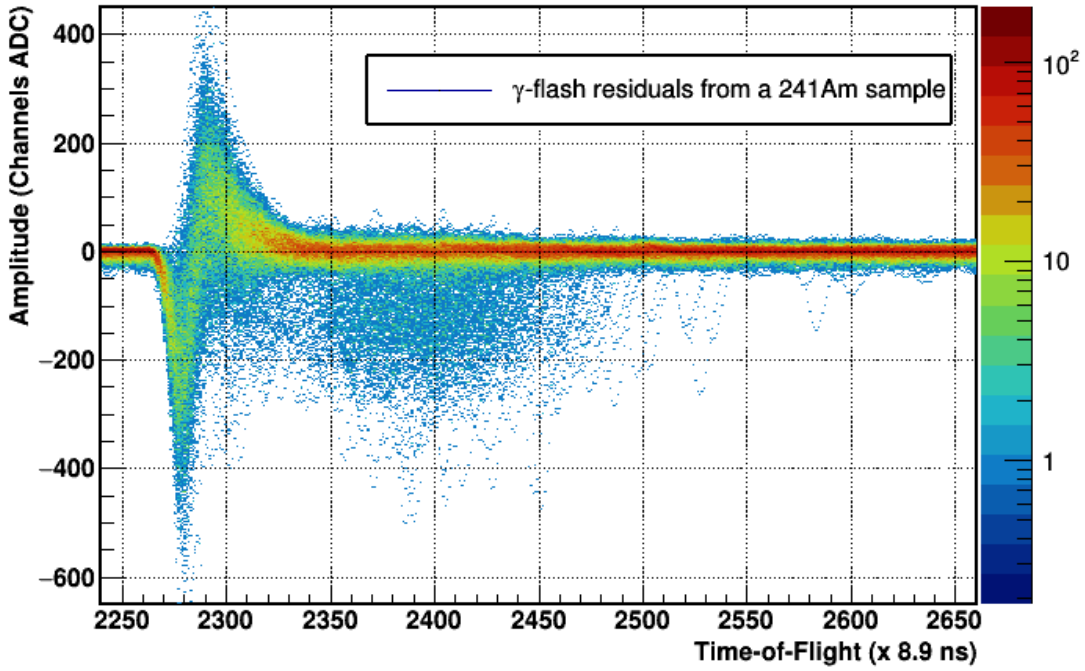

Figure 3.8: Residuals from the subtraction of the average $\gamma - flash$ shape from the raw movies for an ^{241}Am sample.

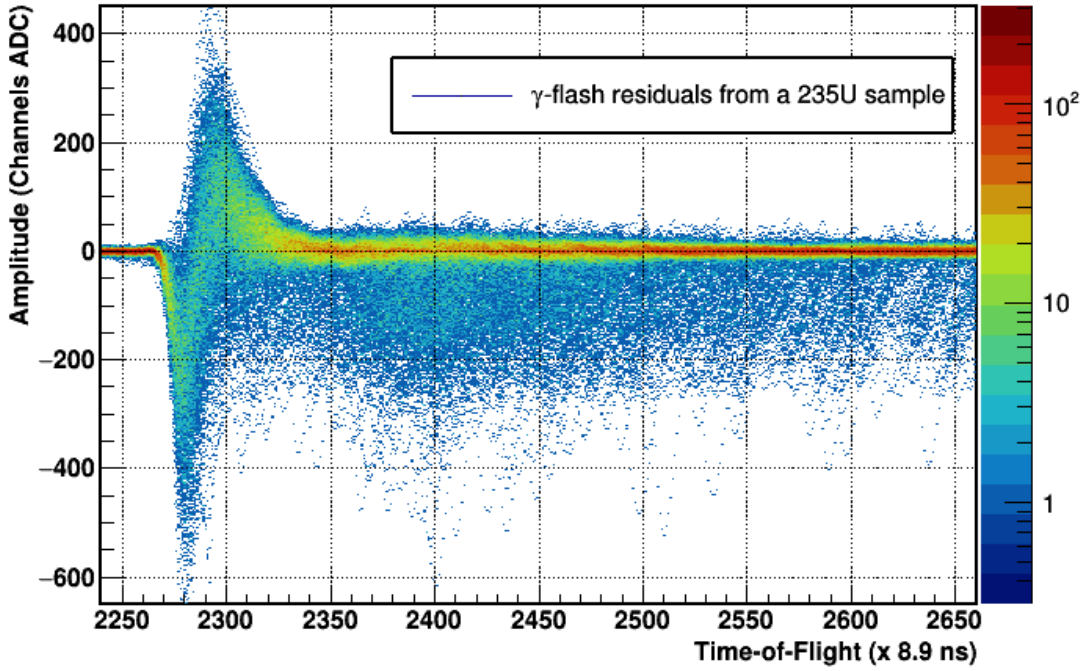

Figure 3.9: Residuals from the subtraction of the average $\gamma - flash$ shape from the raw movies for a ^{235}U sample.

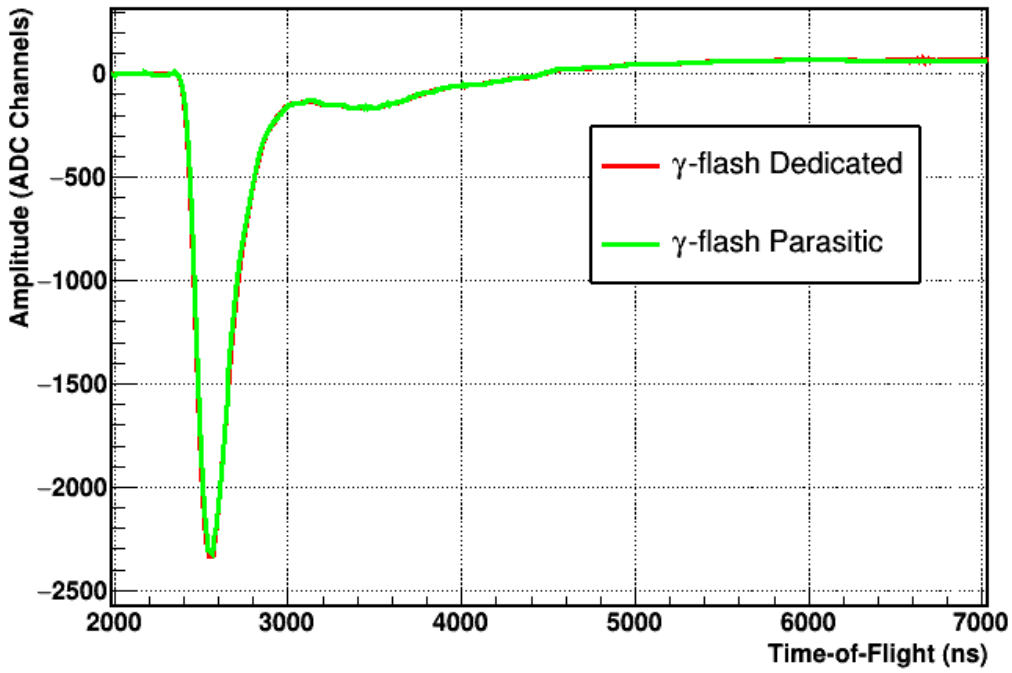

Figure 3.10: Comparison of the average dedicated and parasitic $\gamma - flash$ pulse after a normalization to the amplitude for the same Micromegas detector.

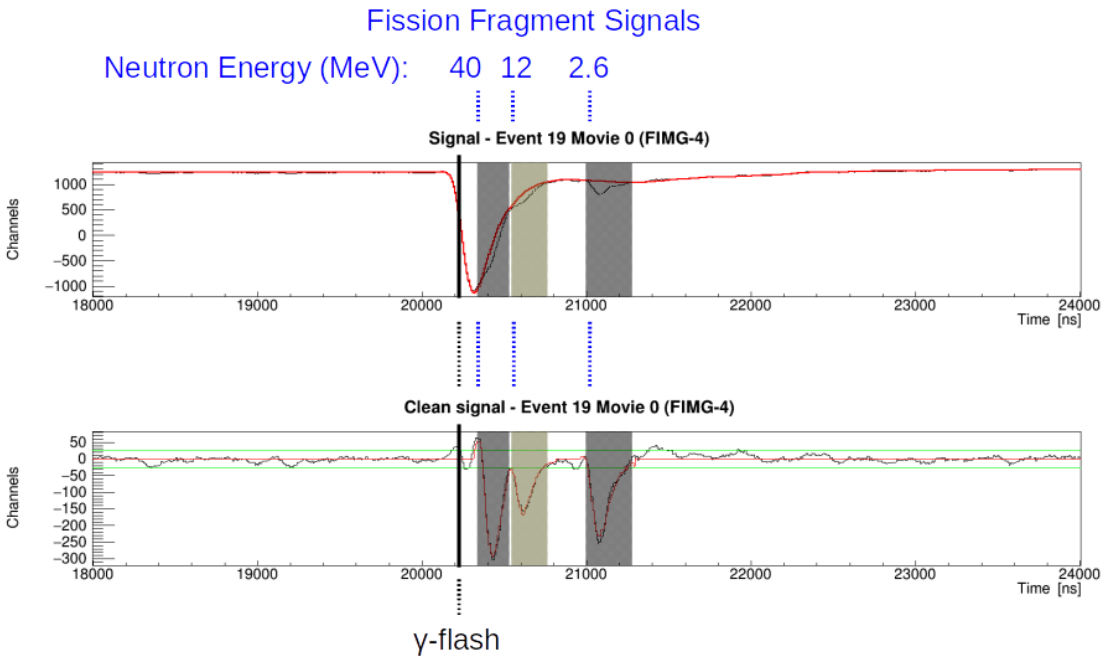

Figure 3.11: Conversion of the time-of-flight of identified fission signals to incident neutron energies calculated at a flight path of $19.5\,m$ in EAR-2 for an Americium sample. The measurement of the fission cross section of ^{241}Am is performed literally on top of the $\gamma - flash$ signal adding several degrees of straitness to the recognition of fission events in the MeV region, which is actually the region of interest for the given measurement.

3.2 Data quality checks

3.2.1 Gain stability of Micromegas detectors

In order to validate the stability of the gain of the Micromegas detectors, a common practice is to compare the pulse height spectra along the duration of the measurement. For this particular experiment, this stage of control of the data was extremely critical since a dedicated gas regulation system, as discussed in the previous chapter, was designed in order to ensure stable gain conditions during the whole duration of the measurement in EAR-2. This was one of the improvements that occurred with respect to the previous experimental fission campaigns. A possible gain shift issue becomes more important when highly radioactive samples, such as ^{241}Am, are considered. This comes from the fact that the safe and consistent separation of alpha particles pulses and fission fragments pulses is based on stable gain conditions.

For the case of ^{241}Am the acquired spectra without the presence of the beam, the so called beam-off spectra, served a dual purpose. Firstly, it defines the high end of the alpha-induced background that corresponds to single or multiple piled-up alpha pulses. Secondly, it provides a second order confirmation of the stability of the detector. For the reference samples, namely ^{235}U and ^{238}U , due to their significantly lower activity, beam-off spectra were almost empty. Instead, their gain stability was confirmed by amplitude spectra acquired with the presence of the beam (beam-on). A characteristic example of the comparison of amplitude spectra from the beginning until the end of the measurement, for each detector family, is depicted in Figure 3.12.

3.2.2 γ-flash distributions

The correct estimation of the arrival time of the $\gamma - flash$ signal is of prime importance since it is used as the start signal for the time-of-flight determination. Consequently, the wrong identification of the $\gamma - flash$ will lead to inaccurate timing properties of the recorded fission signals. This is the reason why the $\gamma - flash$ distributions are indicative of the correct identification and subtraction of the start signal of the measurement. In Figure 3.13, the distributions of the $\gamma - flash$ pulses for all the Micromegas detectors are visualized. The two main identified distributions, follow narrow peaks, as expected and correspond to the $\gamma - flash$ arrival in the parasitic (left) and dedicated (right) pulse intensity respectively. Even though the time-of-flight technique is a relative method, the neutron bunches (BunchNumbers) where the $\gamma - flash$ was identified outside from the aforementioned distributions, were excluded of the analysis.

In the same framework, the $\gamma - flash$ arrival distribution, as recorded from the PKUP, was also studied. In Figure 3.14, again two main narrow distributions are dominant along with some $\gamma - flash$ timestamps that are divergent. Although these events do not constitute a large fraction of the overall identified events, could potentially be the result of the incorrect recognition of the true $\gamma - flash$. For this reason, these neutron bunches are also discarded from all the Micromegas detectors by gating only the events that are close to the two main distributions, following the same logic of the parasitic and dedicated neutron pulses.

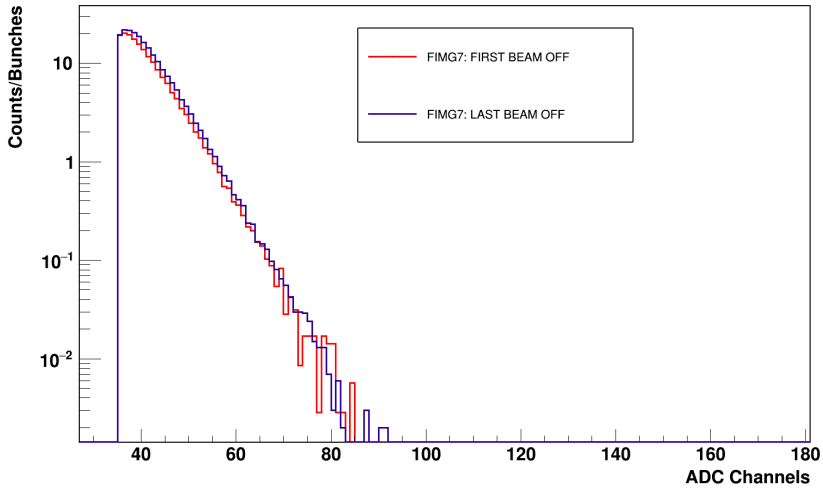

(a)

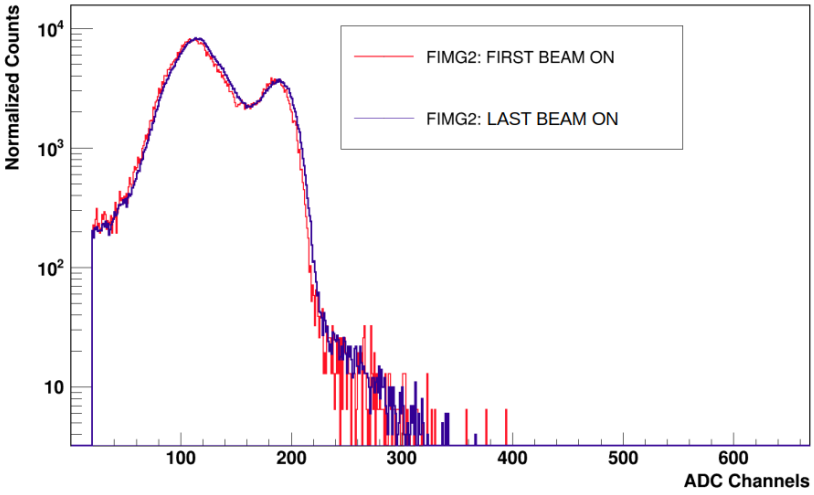

(b)

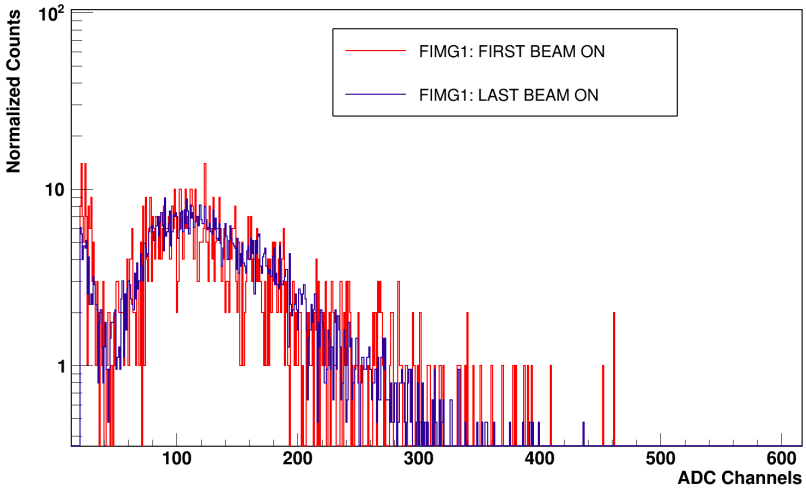

(c)

Figure 3.12: (a) ^{241}Am beam-off spectra (b) ^{235}U beam-on spectra (c) ^{238}U beam-on spectra In all cases, no gain shift was observed from the beginning until the end of the measurement.

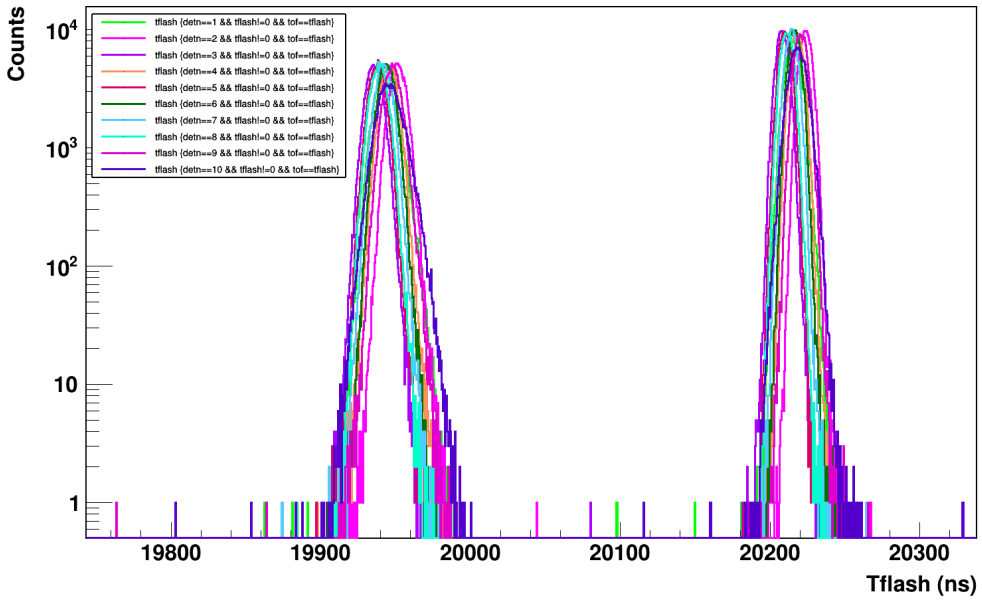

Figure 3.13: Distributions of the $\gamma - flash$ for all the Micromegas detectors used in the measurement. The right distribution corresponds to the arrival of the $\gamma - flash$ from the parasitic neutron pulses whereas the left distribution to the $\gamma - flash$ arrival from the dedicated neutron pulses.

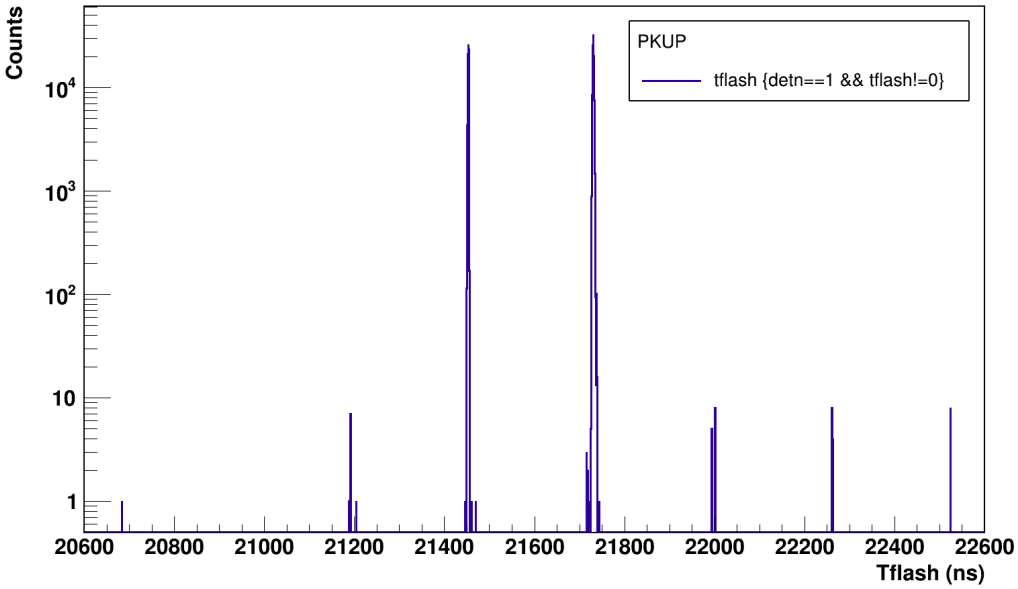

Figure 3.14: Distribution of the $\gamma - flash$ as recorded from the PKUP.

3.2.3 Noise rejection

Along with the useful fission signals, during the various steps of the analysis procedure, electronic noise can be also recorded. During the recognition of the fission pulses in the PSA routine, noise is eliminated by applying certain constraints in the parameters. The constraints can be an amplitude threshold for the identified signals, an area to amplitude ratio and a lower

limit for the FWHM of the pulse. All the pulses that are recorded as fission signals and are used for the cross section determination should be identified of course in times after the $\gamma - flash$ pulse, otherwise they are disregarded from the analysis.

There are cases where noise was introduced in the Micromegas detectors giving rise to pulses at times larger than the $\gamma - flash$ and of extremely high amplitude. These events were easily located and discarded from all the detectors. Such a case is visualized in Figure 3.15, where at the same event simultaneously four out of ten detectors recorded noise and as a result very high amplitude pulses were falsely recorded by the routine. The source of this noise is attributed to the low voltage supply power unit since all four detectors were plugged in the same unit. Lickily, these events were rare and easily noticeable from the obtained distributions of the ROOT files.

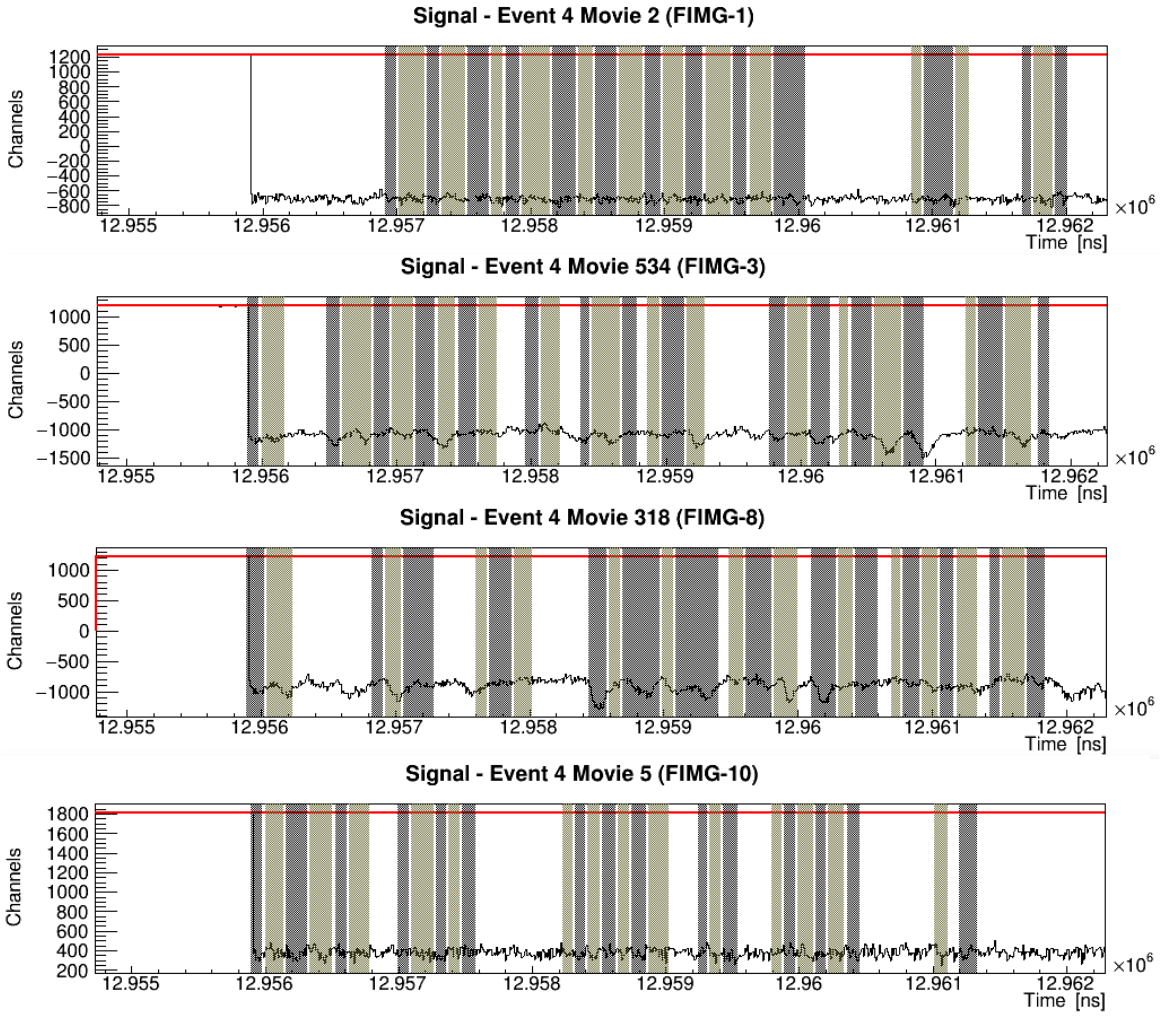

Figure 3.15: Noise that appeared simultaneously in four detectors and resulted in the recognition of extremely high amplitude pulses (more than 1000 ADC channels). These events were rejected from all the detectors and the analysis was not affected.

3.2.4 Rejection of pre-pulses

Another case that the rejection of whole events is crucial, can be seen in Figure 3.16. The small amplitude pulses that look like satellites next to a much higher in amplitude pulse, are the proton pre-pulses coming from the PS accelerator at CERN. The satellite proton pulses are recorded with a time difference of $\sim 260\,ns$ and correspond to the extraction frequency of the proton beam of the PS. The proton losses have an impact on the time-of-flight measurement not only in the Micromegas detectors but in all the detection systems in general.

As can be seen in the bottom panel of Figure 3.16, in the Micromegas detectors the problem does not lie in the pulses that are identified before the $\gamma - flash$, since these, as mentioned before, are anyhow excluded from the analysis. The issue is about the fission signals that are recorded after the $\gamma - flash$ that could be caused from the satellite neutron pulses meaning that a wrong TOF can be assigned. For this reason, these events are also excluded from the analysis. In order to identify and discard these events, a scan in the PKUP movies is necessary. Normally in the PKUP movie, only one pulse should be present which in addition is identified by the routine as the $\gamma - flash$. Therefore, in the scenario that even one additional pulse is identified except from the $\gamma - flash$ (tof!=tflash), it is an indication of the existence of proton pre-pulses. When this is the case, this the particular event is rejected from all the Micromegas detectors.

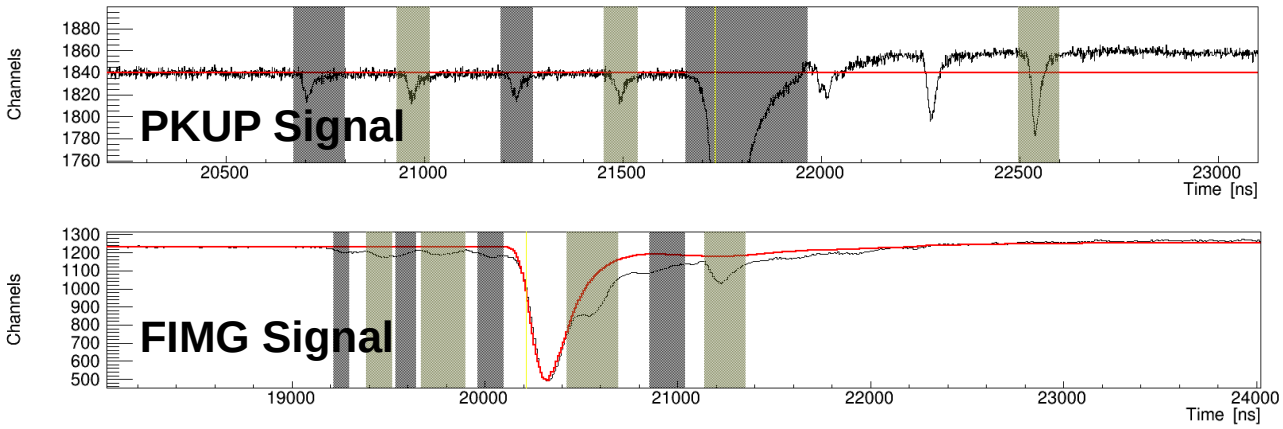

Figure 3.16: Proton satellite pulses that arrive with a time difference of $\sim 260\,ns$ (upper panel). These can lead to signals appearing even before the $\gamma - flash$ (bottom panel).

3.2.5 Rejection of alpha particles in Americium samples

In the analysis of the Americium samples, due to their high natural radioactivity, it is of prime importance to have a well defined separation point between the alpha particles and the recorded fission fragments. In order to estimate the high end of the alpha particles energy distribution in the recorded pulse height spectrum above which it is safe to measure the fission fragments, the beam off and beam on spectra are drawn together for comparison. Figure 3.17 shows such an example for a single Americium sample.

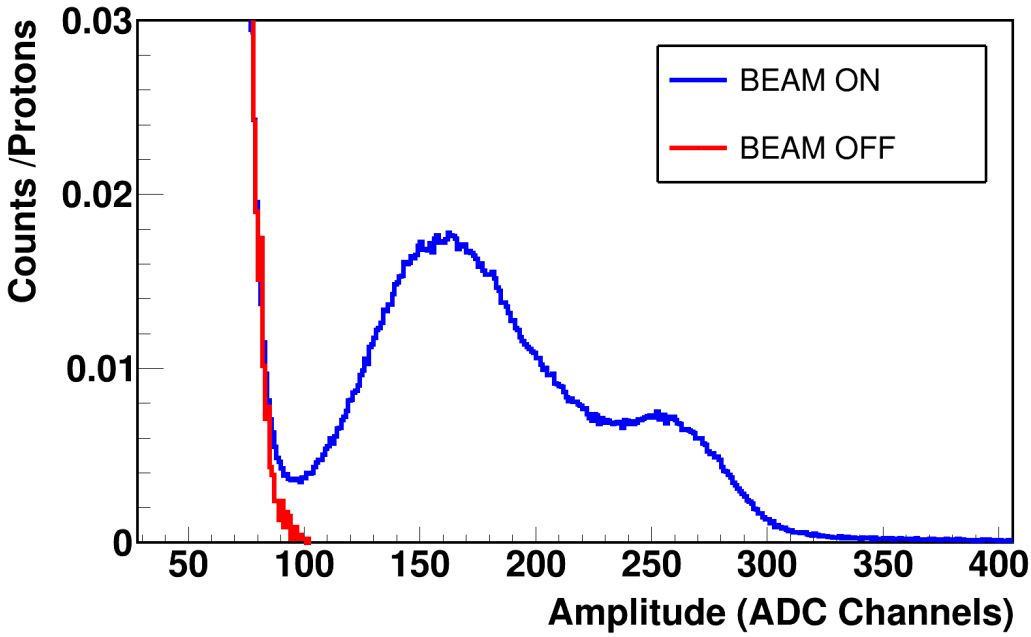

Figure 3.17: Comparison of a beam off and beam on pulse height spectrum for an Americium sample. Above channel 100, it is safe to set an amplitude threshold to distinguish the fission fragments in the analysis. On top of that, the separation point of alpha particles and fission fragments is well defined.

3.2.6 Characteristic time-of-flight distributions

A convenient method for the representation of the time-of-flight data is the study of 2D distributions of the time-of-flight vs amplitude or equivalently neutron incident energy vs amplitude of the recorded pulses. In this way, a map is created where signals are placed on top of it according to their measured time-of-flight and their amplitude. The z-axis in this case, is indicative of the statistics of the pulses. A characteristic representation like this is visualized in Figure 3.18, where at high TOFs the pulse height of the alpha particles from the alpha decay of ^{241}Am (red triangle) goes up to channel 100. At low TOFs, the pulse height of the $\gamma - flash$ residuals (yellow triangle) shadows the distribution of fission fragments in the MeV region. By looking at the triangle-like distribution of alpha particles, an illusion is created that the radioactivity of the sample is reduced in lower TOFs (and higher neutron energies). This is just a false impression. The radioactivity is always the same. In reality this effect occurs because as we move from higher TOFs (lower energies) to shorter TOFs (higher energies), the time binning is reduced. Assuming a sample of ^{241}Am with an activity of 17 MBq, this means 17 million of alpha particle decays per second. For instance, for a given flight path of 19.5 m, the time difference between 1 to 2 eV corresponds to 400.000 ns, whereas the time difference between 1 to 2 MeV corresponds to 400 ns. This is a factor of 1000 which is directly linked to 1000 times more alpha particle decays. Therefore this is exactly what is seen in Figure 3.18, if one looks at the 10^6 ns and 10^3 ns respectively.

For the reference samples ^{235}U and ^{238}U the same distributions are visible in Figures 3.19, 3.20. The significantly lower activity results in the absence of alpha particle recording. In Figure 3.19, the high statistics in an extended time-of-flight region is indicative of the fissility of the ^{235}U sample. On the other hand, Figure 3.20 illustrates the case of the ^{238}U fissionable

isotope with a reaction threshold around 1 MeV which, in combination with its significantly lower cross section, justify the absence of fission signals in the thermal region.

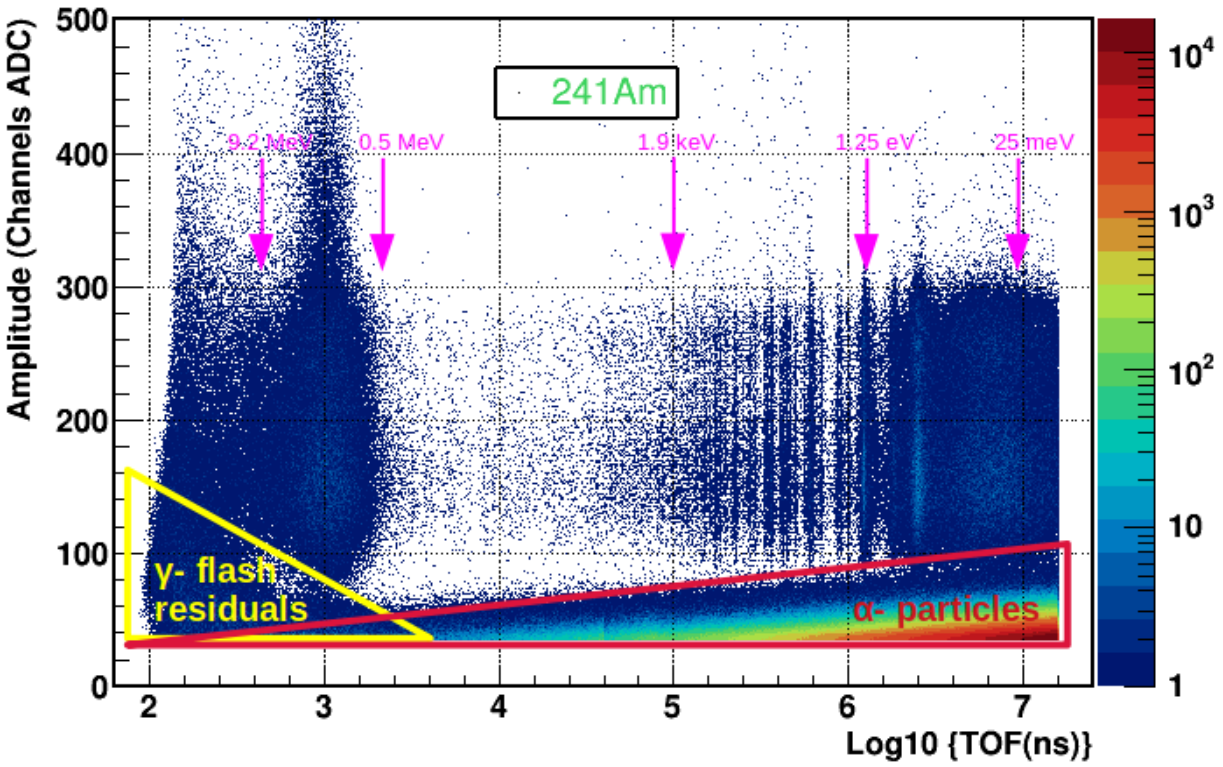

Figure 3.18: Amplitude vs Time-of-Flight distribution for a ^{241}Am sample with an adopted binning of 1000 bpd in the x-axis. The dominant alpha activity at large TOFs that correspond to the thermal region is visible. On the other hand, at small TOFs and higher neutron energies appear $\gamma - flash$ residuals which are false pulses created from the subtraction of the $\gamma - flash$.

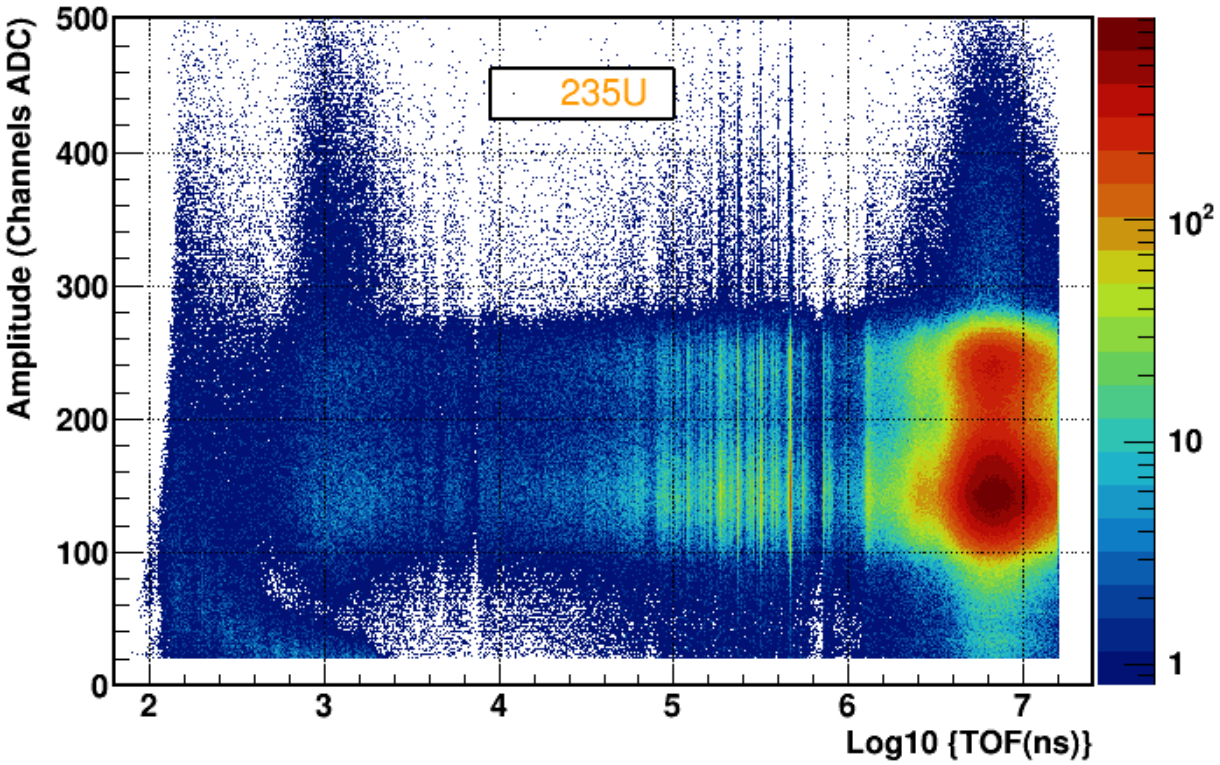

Figure 3.19: Amplitude vs Time-of-Flight distribution for a ^{235}U sample with an adopted binning of 1000 bpd in the x-axis. The high statistics in the whole TOF range is an indication that the ^{235}U isotope is fissile. The clusters in the TOF range between 10^5 to 10^6 ns are attributed to the resonances of ^{235}U.

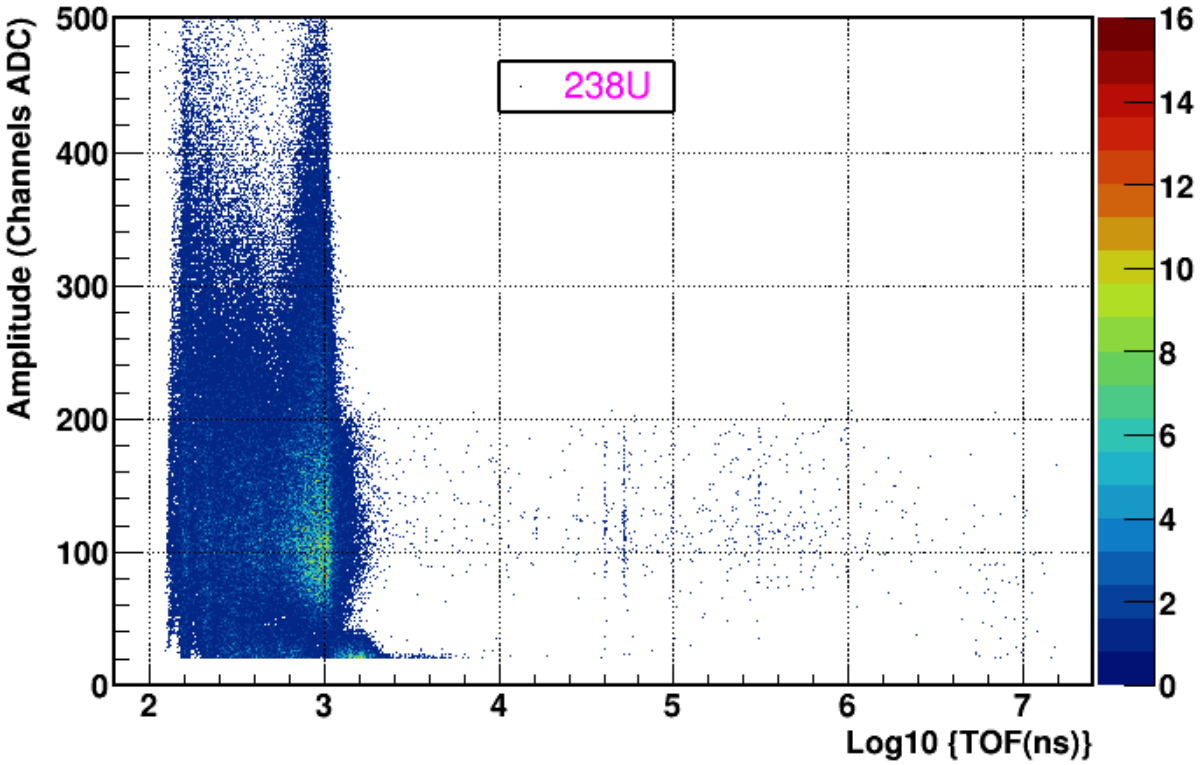

Figure 3.20: Amplitude vs Time-of-Flight distribution for a ^{238}U sample with an adopted binning of 1000 bpd in the x-axis. The lack of signals in the low energy region is attributed to the fact that the ^{238}U isotope is fissionable and the ^{238}U(n,f) reaction has a threshold at $1\,MeV$.

3.2.7 Comparison of pulse height spectra

One more significant data quality check is based on the comparison of pulse height distributions between dedicated and parasitic bunches. As mentioned before, two beam modes are available at n_TOF, the dedicated pulses with the nominal proton intensity and the parasitic ones with approximately half of the nominal intensity. In any case, the pulse intensity of each proton bunch is recorded along with the rest of the pulses' parameters and is used to verify the statistical agreement of the dedicated and parasitic data.

Driven by the above assumption, a common practice is to compare the pulse height spectra of both beam modes after normalizing the distributions to the number of protons. Given that the proton beam hits the spallation target of n_TOF at the same point, after the normalization it is expected that both distributions will match. This is not the case for the whole neutron energy range given that due to the expected fluctuations of the neutron flux and the reaction cross section, the observed counting rates are also fluctuating significantly. The reason lies in the fact that both the cross section and the neutron flux fluctuate and as a result the counting rate is varying significantly between different neutron energy regions. In order to benchmark the analysis procedure after the $\gamma - flash$ subtraction as well as to estimate the necessary correction factors concerning the amplitude cut and pile up of fission events per incident neutron energy, the pulse height spectra of dedicated and parasitic pulses were compared. The comparison of

the pulse height spectra for a variety of neutron energies is illustrated in Figures 3.21, 3.22 and 3.23 for a Micromegas detector from each isotope.

For ^{235}U, when scaling the parasitic distributions to the number of protons in the low neutron energies, it seems that the statistics of the dedicated pulses are higher than the parasitic ones (Figure 3.21a). This effect was observed in the thermal region in all the detectors of the ^{241}Am fission campaign but also in other experiments during Phase III of the n_TOF in 2018. This observation leads to the indication that the proton beam's impact point on the lead spallation target was not identical for both beam modes, resulting in a slightly different neutron flux production. Consequently, in order to match both distributions, the application of an extra normalization factor is required, which is not more than 10% only for this region (Figure 3.21b) and remains the same for the rest of the detectors as well. In the MeV region (Figure 3.21e), due to the high counting rates, pile up losses are expected. Therefore, the respective correction factors have to be applied.

For ^{241}Am, apart from the above mentioned 10% extra normalization factor that is needed, the general agreement between the dedicated and parasitic pulse height spectra is better. In the MeV region, where the higher counting rate is expected and observed, after the normalization of the parasitic pulses to the number of protons, the dedicated ones are slightly lower in statistics again due to counting losses.

For ^{238}U, due to its very low, practically unmeasured experimentally cross section in the thermal neutron spectrum, there are no recorded data to show the comparison in such low energy regions. At the threshold of the reaction however just below $1\,MeV$ as depicted in Figure 3.23a, the comparison between dedicated and parasitic pulses is almost perfect. For higher neutron energies, as illustrated in Figures 3.23b, 3.23c and 3.23d, the scaling of the parasitics to the number of protons resulted in an unpleasant discovery. In the dedicated pulse height spectra, the once observed double bumps are not seen anymore and a significant amount of pulses have been recorded with higher amplitude values creating a long tail and covering almost twice the region in channels ADC of the previously recorded distribution. This extreme distortion of the pulse height spectrum is translated, as will be discussed in the next sections, in counting losses up to 50%. The calculation of experimental counting rate as illustrated in Figure 3.24, highlight that the mass of ^{238}U samples was not properly optimized and in fact was 10 times higher than the one really needed for the specific experimental conditions.

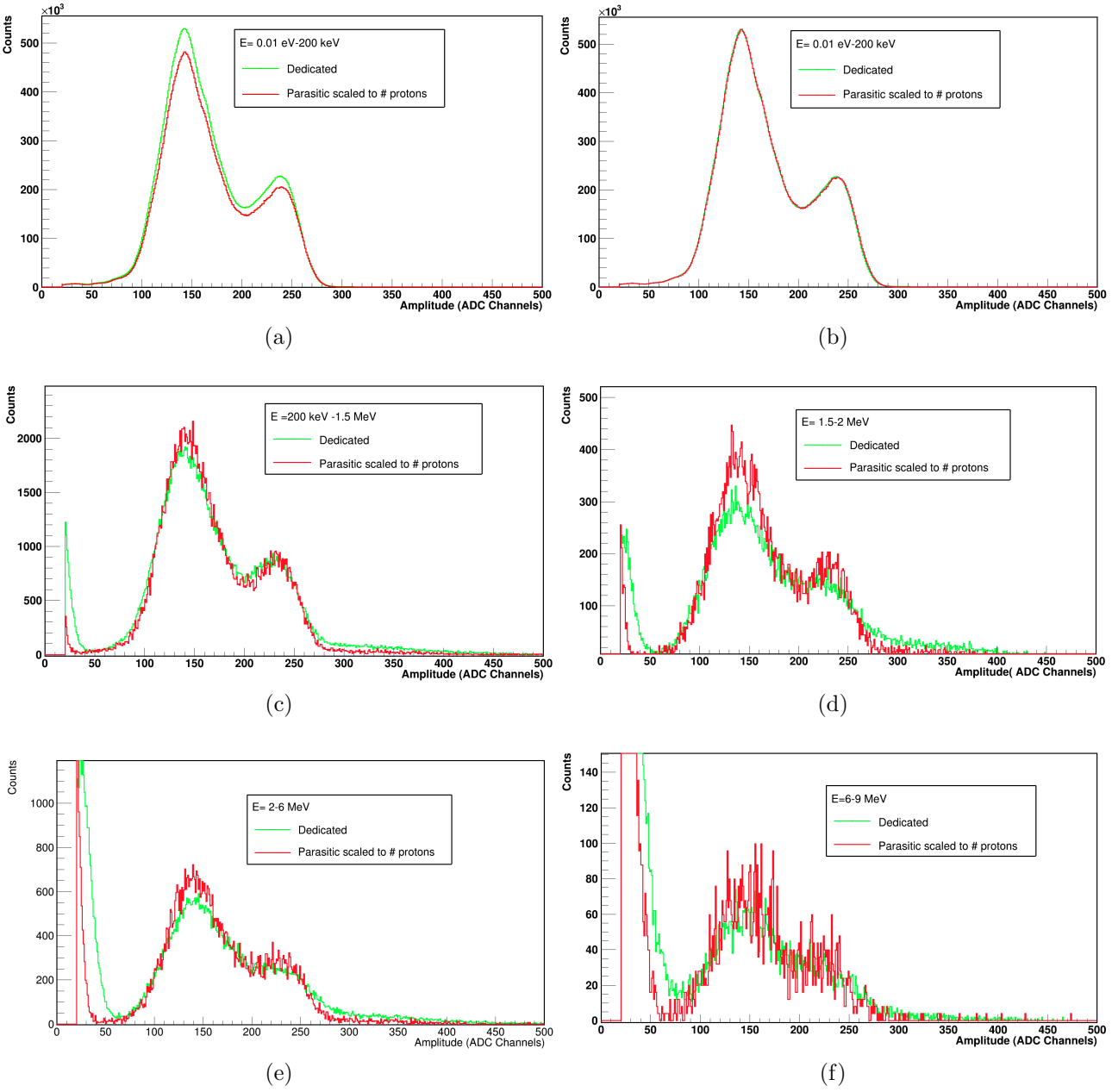

Figure 3.21: Comparison of pulse height spectra for a ^{235}U sample for a variety of incident neutron energies.

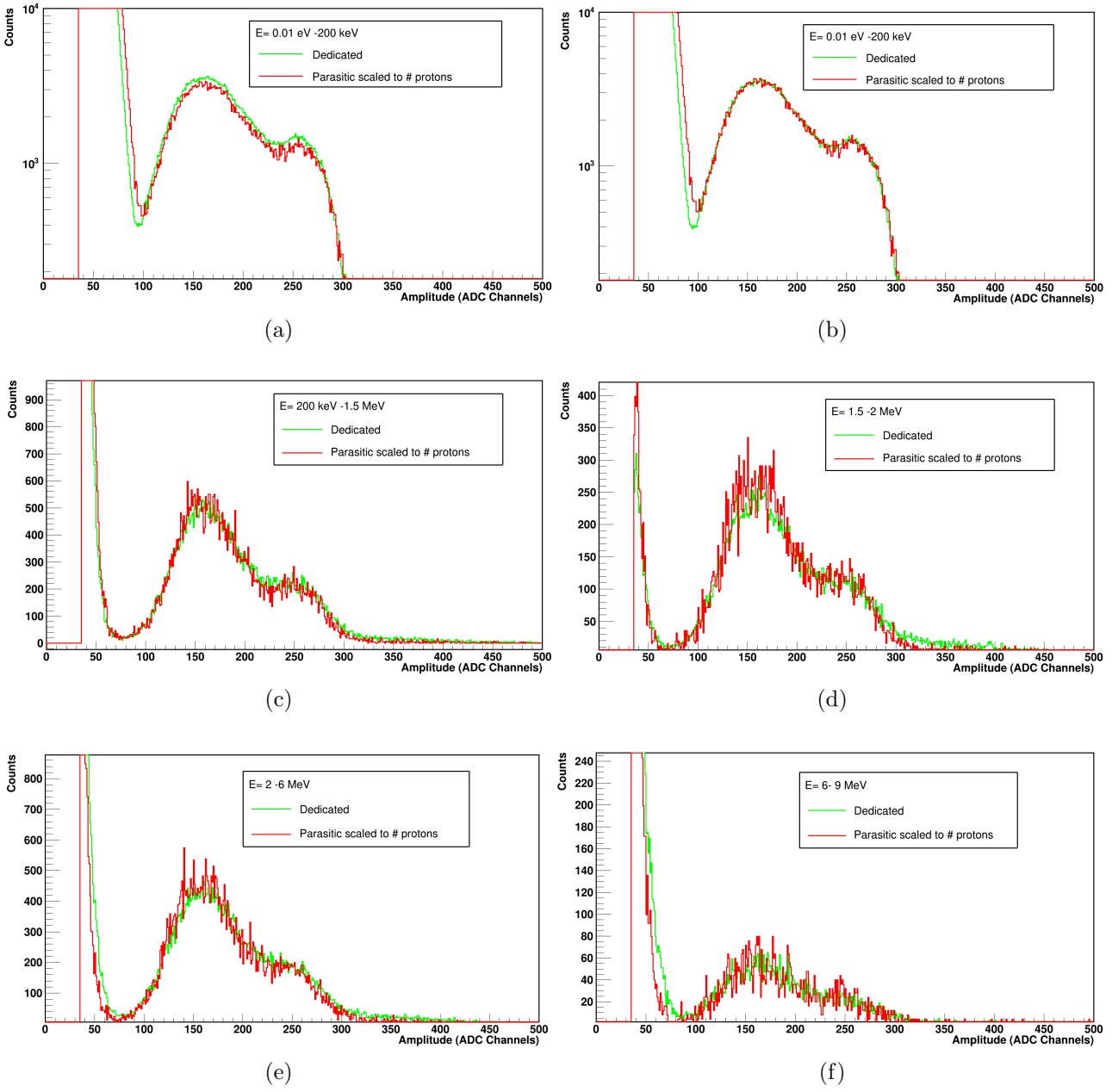

Figure 3.22: Comparison of pulse height spectra for an ^{241}Am sample for a variety of incident neutron energies.

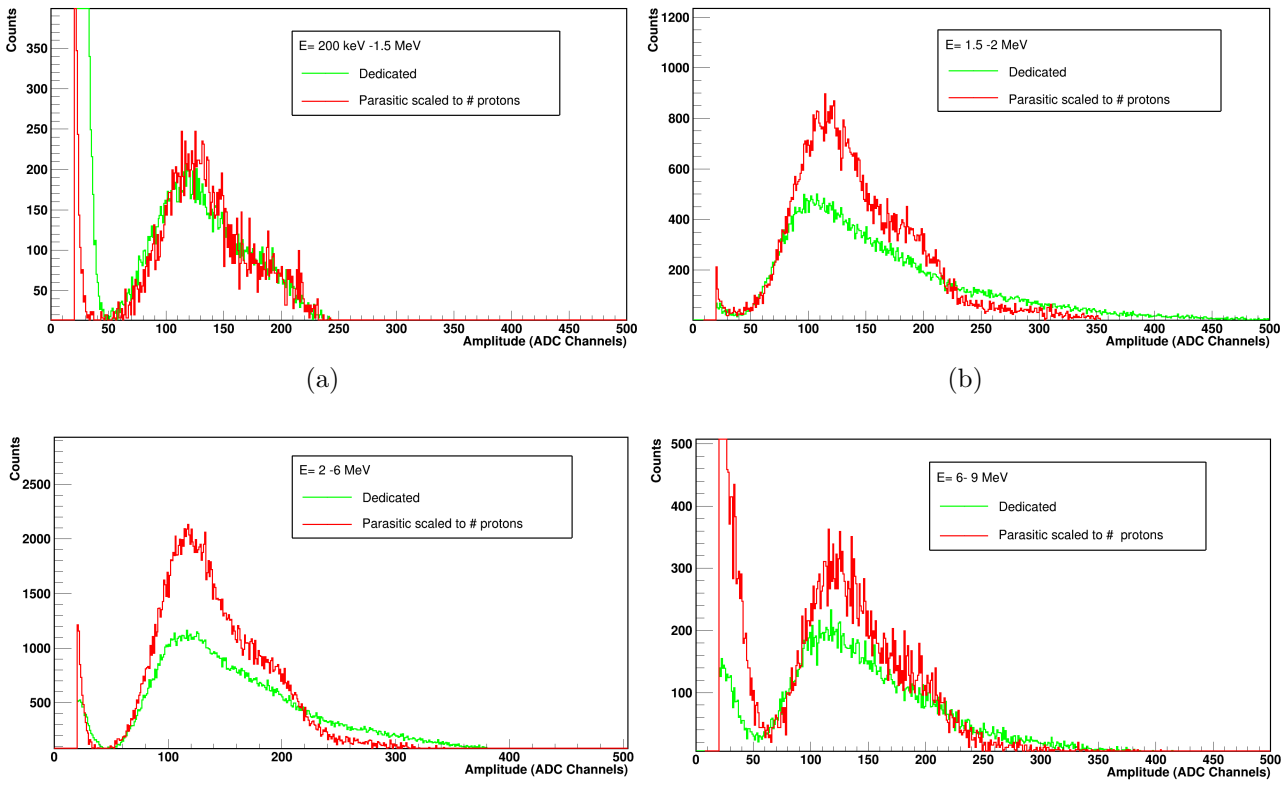

Figure 3.23: Comparison of pulse height spectra for a ^{238}U sample for a variety of incident neutron energies.

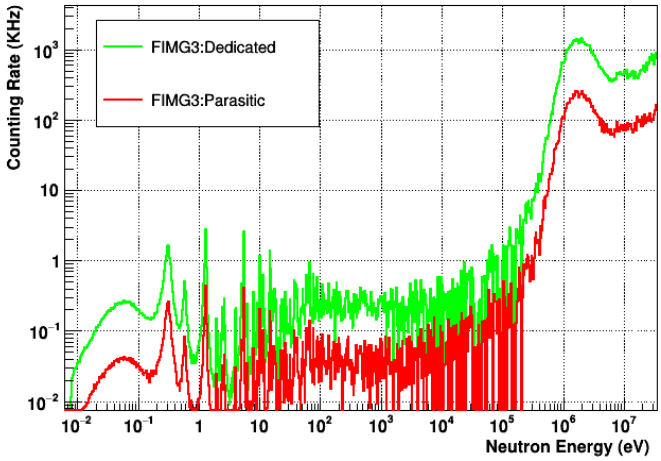

(a)

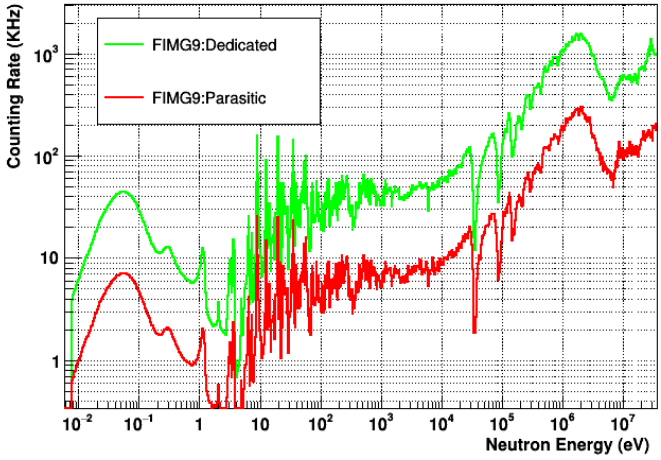

(b)

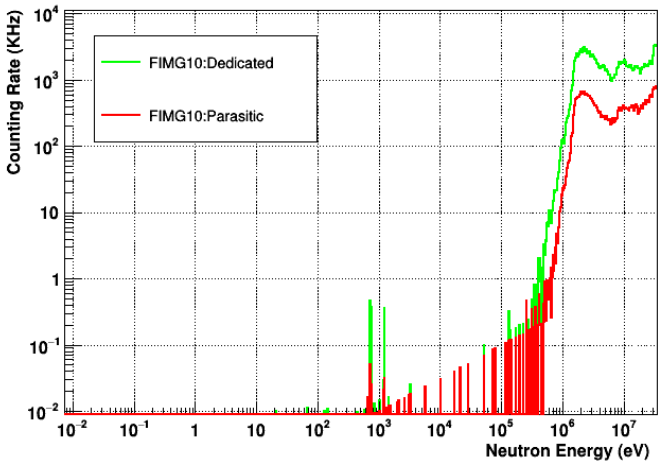

(c)

Figure 3.24: (a) ^{241}Am (b) ^{235}U and (c) ^{238}U counting rates for the two pulse modes of the n_TOF facility in EAR-2 with the fission collimator. In the energy region between 1 and 3 MeV for the dedicated pulses the maximum counting rate locally for ^{241}Am is 1.4 MHz, for ^{235}U is 1.5 MHz and for ^{238}U is 3 MHz. In the Micromegas detectors when the counting rate exceeds 1 MHz, pile up events are observed in the pulse height spectrum along with the so called "pile up tail". In this case, the piled up pulses are recorded at higher positions (channels ADC) than the original pulses would have been stored.

3.2.8 Comparison of fission fragment yields

In order to assess the efficiency of the parameters used within the PSA routine and evaluate at first approach the selection of the fission events, it is instrumental to inspect the resulting fission fragment yields. Accordingly, the calculated yields were normalized to the mass of each isotope used and the results are shown in Figure 3.25. The yield spectra of each isotope family seem to agree with each other up a few MeV in neutron energy. It has to be pointed out that very small deviations are expected to be observed even for the isotopes of the same family, since not all the detectors were operated with the same mesh voltages. The reason lies in the fact that in some detectors the $\gamma - flash$ was saturated and the gain had to be reduced. In reality, the gain in the Micromegas detectors for the ^{241}Am(n,f) campaign was set to avoid the saturation of $\gamma - flash$ on the one hand and on the other hand to achieve an acceptable separation point between the alpha particles and the fission fragments in the case of Americium but also an acceptable signal to noise ratio for the rest of the reference detectors.

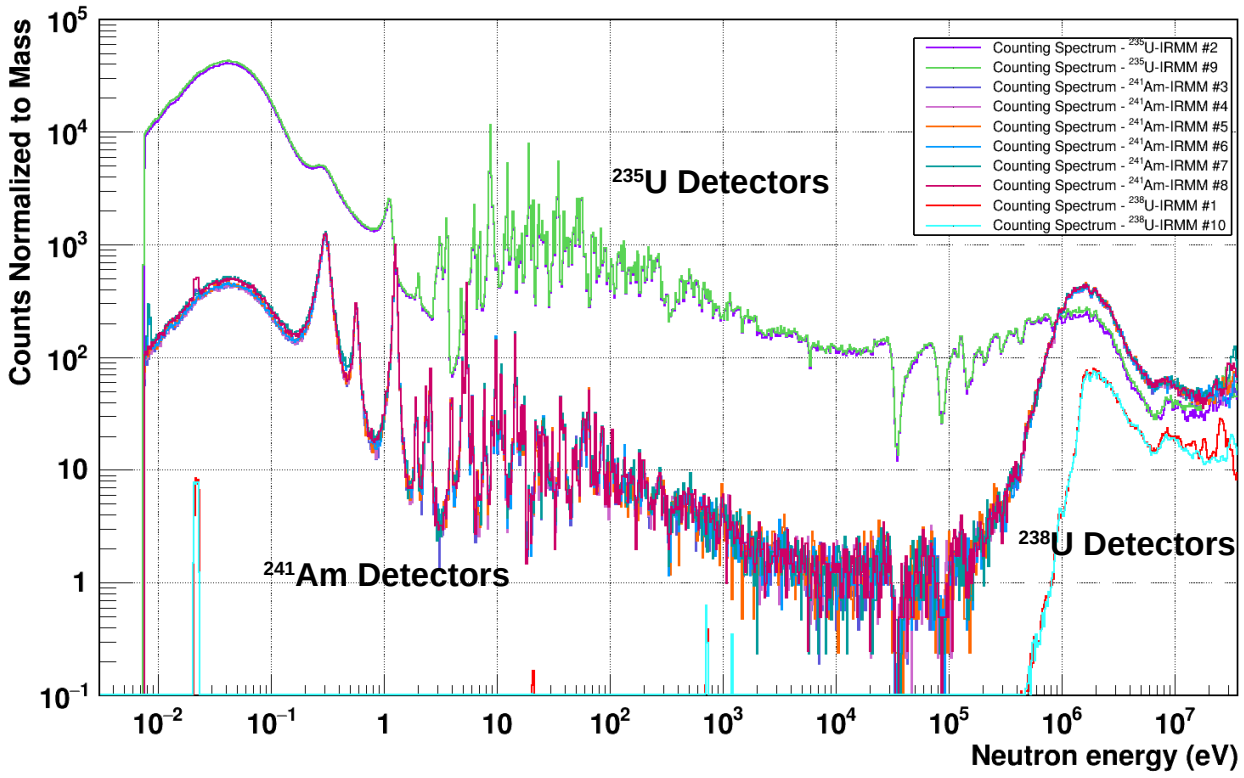

Figure 3.25: Fission fragment yields normalized to mass for all the Micromegas detectors used in the ^{241}Am(n,f) campaign.

3.3 Basic corrections

3.3.1 Geometrical flight path length of neutrons

The first step towards the conversion of the time-of-flight to neutron energy is the determination of the geometrical flight path length of neutrons (L_{geom}). The method for finding the appropriate L_{geom} for each radioactive sample is to compare the experimental TOF spectrum with various candidate distances from the transport code, until a matching between both distributions of the resonance peaks is achieved. The best isotope to start with, is ^{235}U , since the statistics acquired due to its high cross section especially in the region of resonances is quite satisfactory. On top of that, the fissile nature of ^{235}U allows the matching of the resonance peaks with the flux dips in the keV neutron energy region with a single L_{geom} value. Figure 3.26, demonstrates a reproduction of the TOF spectrum of a reference ^{235}U sample, including the position of resonances in the low energy part and the dips from the materials in front of the neutron beam in the keV energy region. This type of comparison is performed using the TOF distributions because both spectra carry the information of the resolution function (RF) of EAR-2 of the n_TOF facility.

Once the L_{geom} for the two ^{235}U samples is fixed from the reproduction of the experimental spectra with the transport code and is verified that their intermediate distance is in accordance with their true relative geometrical distance, then the next step is to reproduce the geometrical flight paths for the rest of the samples (^{241}Am and ^{238}U isotopes) using the known relative distances inside the fission chamber.

3.3.2 Resonance investigation of Americium samples

During the process of evaluating the geometrical flight path L_{geom} for the ^{241}Am samples, it was observed that in the experimental spectra, the first strong resonance displays more broadened characteristics compared to the corresponding resonance structure from the transport code, while the very next resonances are in accordance with the experimental recorded fission yield (Figure 3.27a). In addition, some additional resonance clusters are noticed that do not match with the ones expected from the ^{241}Am(n,f) reaction according to the JEFF-3.3 evaluated library (Figure 3.27b).

Searching for other contaminant candidates except from the already reported Americium impurities from JRC-Geel, namely ^{242}Am and ^{243}Am , it was crucial to search in the experimental yield for fingerprint resonances. This study pointed towards ^{239}Pu as the main identified contributor in the resonance region. By distinguishing in the recorded data a unique resonance of ^{239}Pu at 75 eV, in a region where no other contribution from the ^{241}Am isotope was expected (Figure 3.28b), it was possible to quantify the amount of ^{239}Pu present in the provided samples. From the purity check of americium samples approximately 0.45% of ^{239}Pu contamination was identified and eventually subtracted later on in the analysis.

As a final confirmation of the new estimated isotopic composition, all reported impurities including the ^{239}Pu contamination, were also considered. As can be seen in Figure 3.29, after including 0.45% of ^{239}Pu, the reproduction of the experimental yield is more accurate.

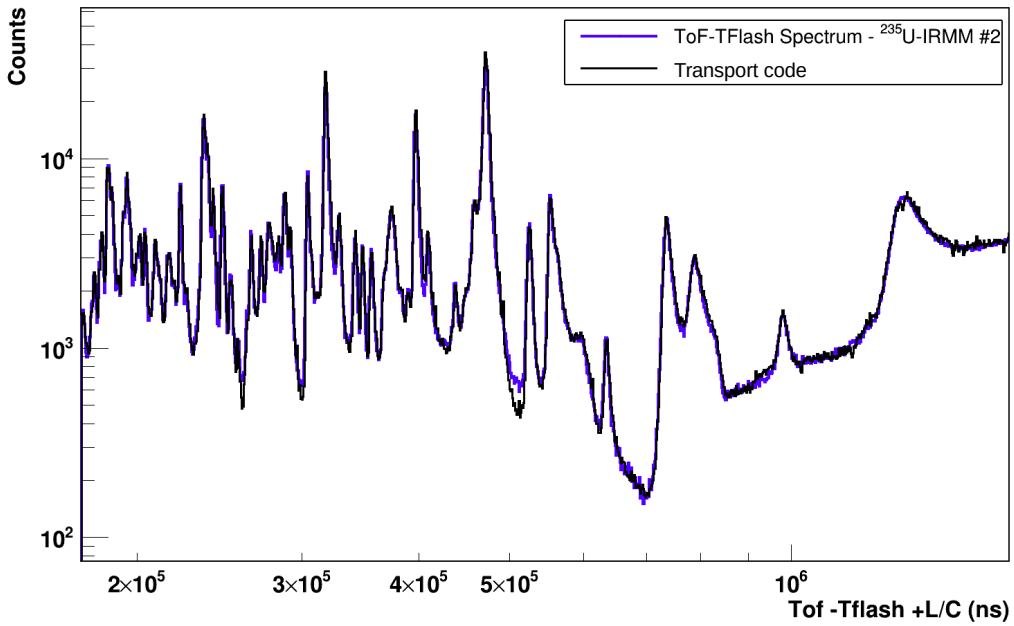

(a)

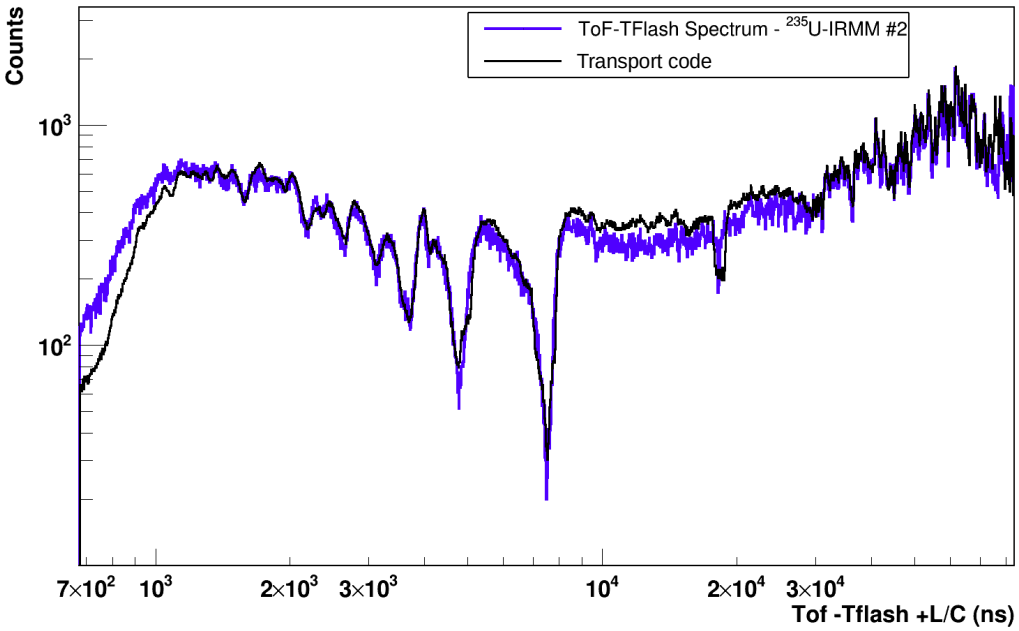

(b)

Figure 3.26: Reproduction of the experimental TOF distribution from the transport code with a single L_{geom} for a ^{235}U sample that was used in the experiment (a) in the region of resonances and (b) in the region of the expected neutron flux dips.

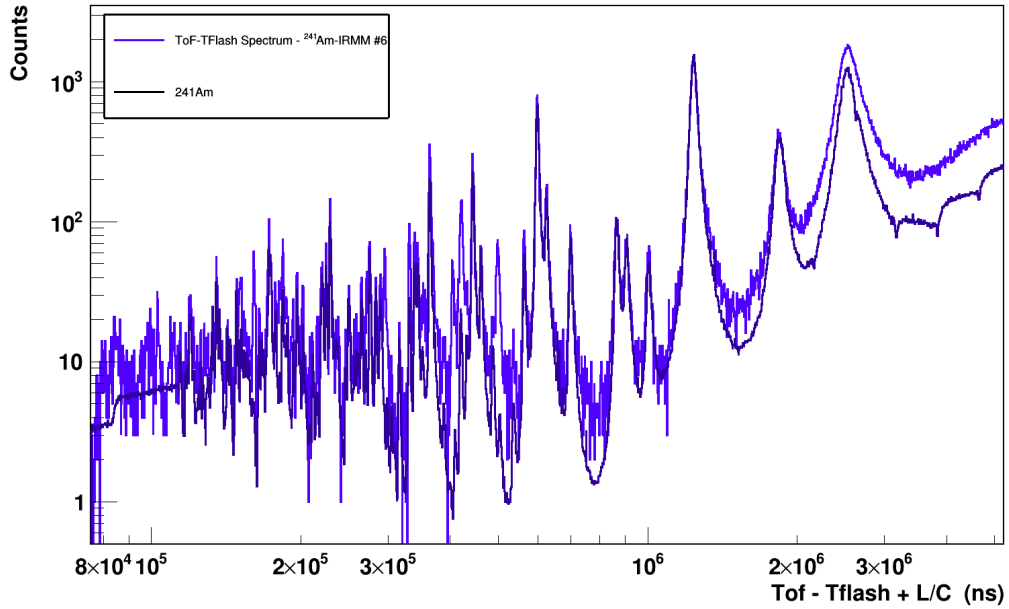

(a)

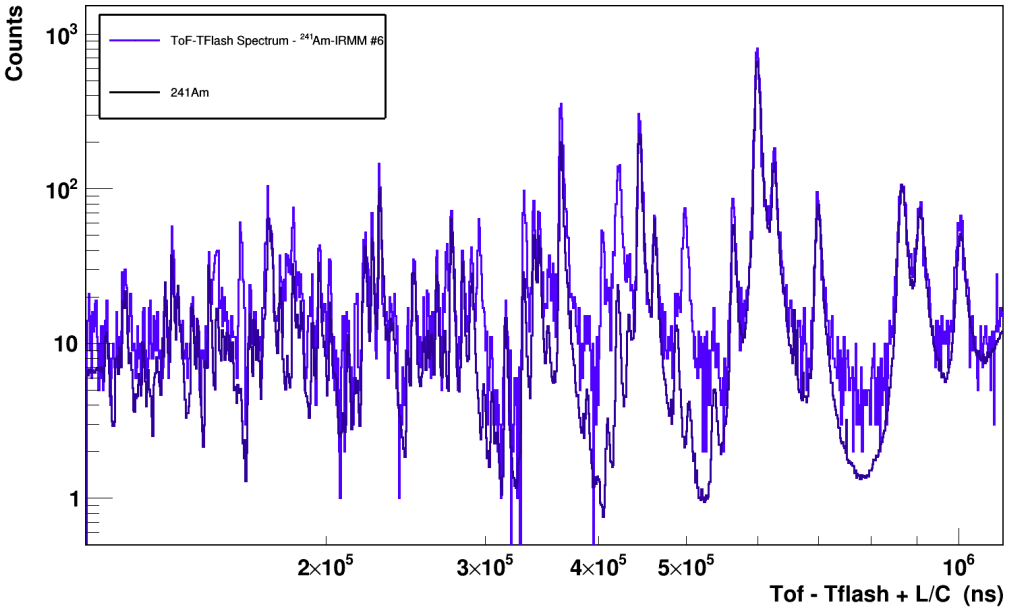

(b)

Figure 3.27: Comparison of the experimentally recorded TOF spectrum from an ^{241}Am sample with the transport code. Indicative of the existence of unreported contaminants is (a) the mismatch of the first strong resonance (from the right side of the plot) and (b) the appearance of resonance clusters that cannot be attributed to the neutron-induced cross section of ^{241}Am .

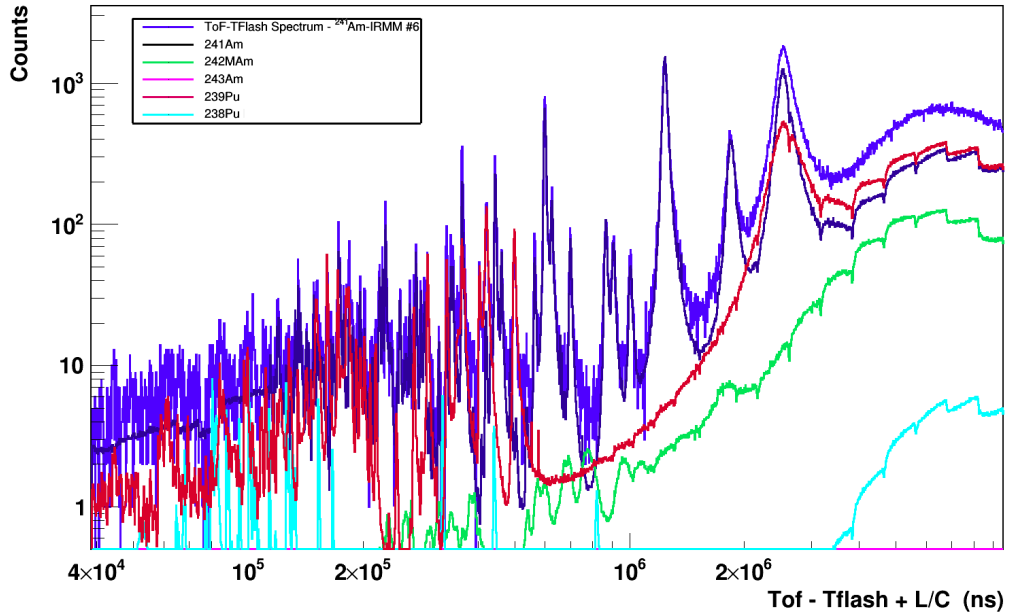

(a)

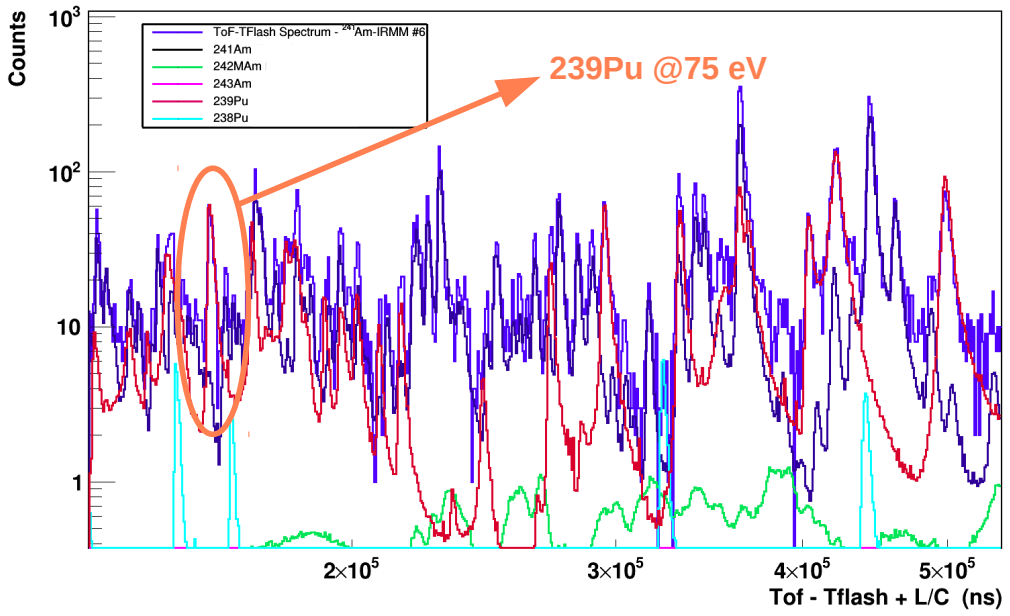

(b)

Figure 3.28: (a) Contribution of Americium impurities and ^{239}Pu contamination in the resonance region (b) Quantification of the ^{239}Pu based on the "fingerprint" resonance at 75 eV.

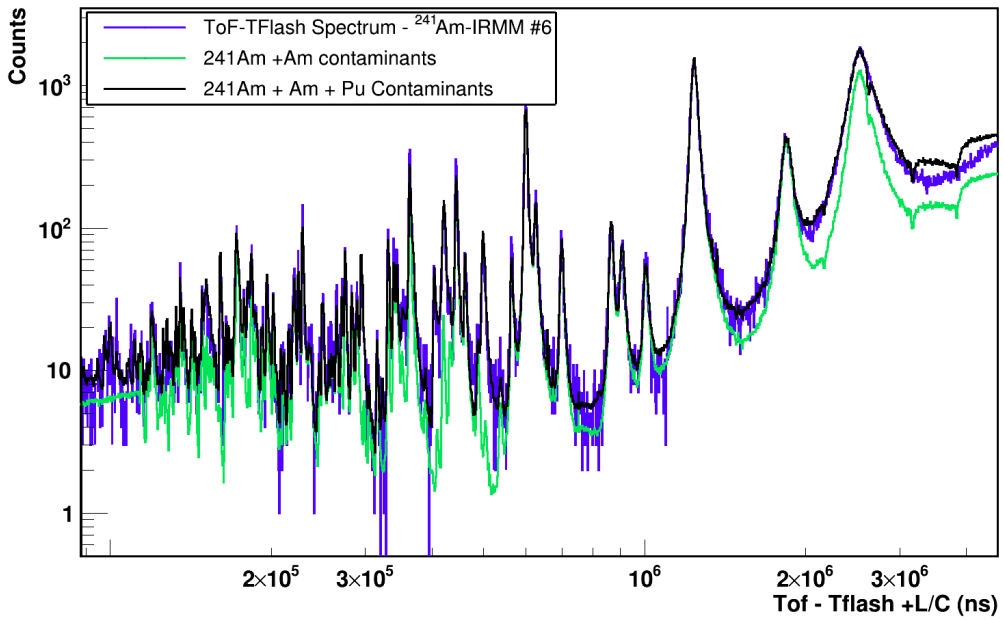

(a)

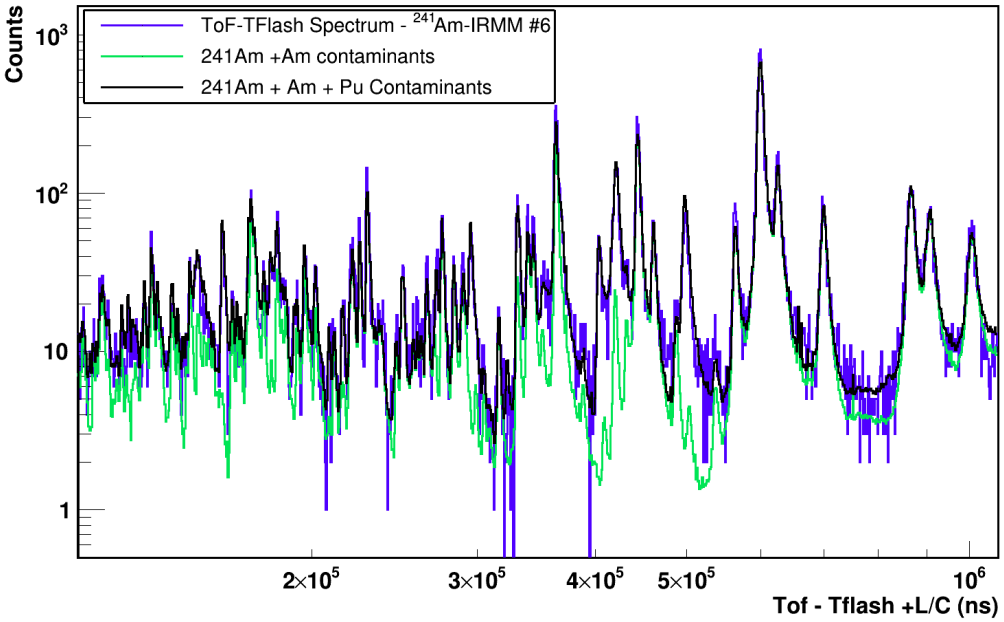

(b)

Figure 3.29: Reproduction of the experimental fission fragment TOF yield considering the contributions of the reported from the JRC-Geel Americium impurities and the unreported 0.45% ^{239}Pu contamination extracted from the purity investigation of Americium samples.

3.3.3 Contaminants overview

Even though the ^{241}Am samples used were 99.98% pure, reported impurities had to be taken into consideration and the recorded fission fragment yield had to be corrected accordingly. In addition, an amount of ^{239}Pu of the order of 0.45% that was discovered during the resonance investigation of the Americium samples was added to the list of the already known contaminants. The neutron-induced fission cross sections of the main contaminants that were present in the samples are illustrated in Figure 3.30 after correcting for the actual composition.

More specifically, in the case of ^{241}Am samples (Figure 3.30a), the contribution of contaminants and especially of ^{239}Pu is significant at low neutron energies in the resonance region. On the contrary, for neutron energies above the fission threshold, the contribution from the contaminants is more than two orders of magnitude lower than the reaction under study. The impressive aspect of this plot is that it shows that even a very small portion of percentage from a fissile isotope such as ^{239}Pu can contaminate a large region of interest for the main reaction under study and accordingly can contribute to the recorded fission fragment yield. For the ^{235}U samples (Figure 3.30b), the contribution of the contaminants is negligible. Also for the ^{238}U samples (Figure 3.30c), above the threshold of the fission reaction, which is the only region of interest for this isotope, again the contaminants' contribution is of minor importance.

3.3.4 Characterization of Americium samples

The ^{241}Am samples were measured in the Target Preparation Laboratory in JRC-Geel, Belgium, with the alpha spectrometer LG2. Due to the high activity of the targets ($\sim 18\,MBq$ per sample), the alpha peaks from the Plutonium contaminants could not be distinguished clearly in the spectrum. As can be seen in Figure 3.31, the main alpha peak from the ^{241}Am contribution covered a wide number of channels.

In order get a better understanding of the experimental spectrum, a simple exercise was performed to evaluate whether or not it is feasible to trace a small amount of ^{239}Pu contamination of the order of 0.45%, since this was the indication from the analysis of resonances from the experimental TOF spectrum of ^{241}Am. Initially, the activity of a single ^{241}Am target was used to calculate the alpha particle emissions for a duration of 10 minutes. Then, these events were shared among the so far known isotope composition of the Americium target (^{241}Am : 99.4838%, ^{242}Am : 0.0162%, ^{243}Am : 2.E-4%) plus an estimation of ^{239}Pu contamination (^{239}Pu : 0.45%). Finally, using the most dominant alpha lines for each isotope, the calculated events were used to reproduce an alpha spectrum using the corresponding intensities of the alpha peaks and sampling random numbers from a standard Gaussian distribution. In the Gaussian distribution, the mean matches with the alpha peak in MeV and the standard deviation emulates the alpha resolution of silicon barrier detectors and was calculated as follows:

$$\sigma = \frac{\text{FWHM} \quad \text{(MeV)}}{2.35} \tag{3.1}$$

A typical alpha resolution value for these detectors is 20 keV FWHM but also the same exercise was performed with a much worse resolution of 40 KeV FWHM for comparison purposes.

In Figures 3.32a, 3.32b, the results are highlighted for the scenario of 20 keV and 40 keV FWHM alpha resolution respectively. Although these figures cannot be directly compared with the experimental spectrum of Figure 3.31, it is obvious that such small amounts of contaminants cannot be distinguished with α -spectroscopy.

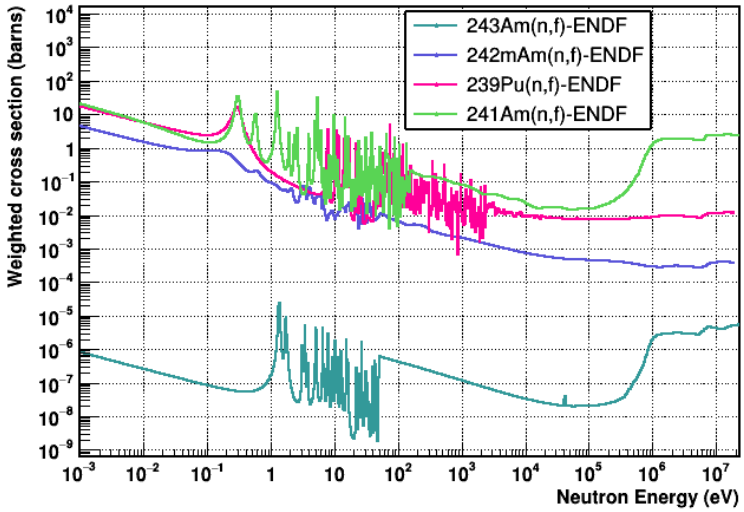

(a)

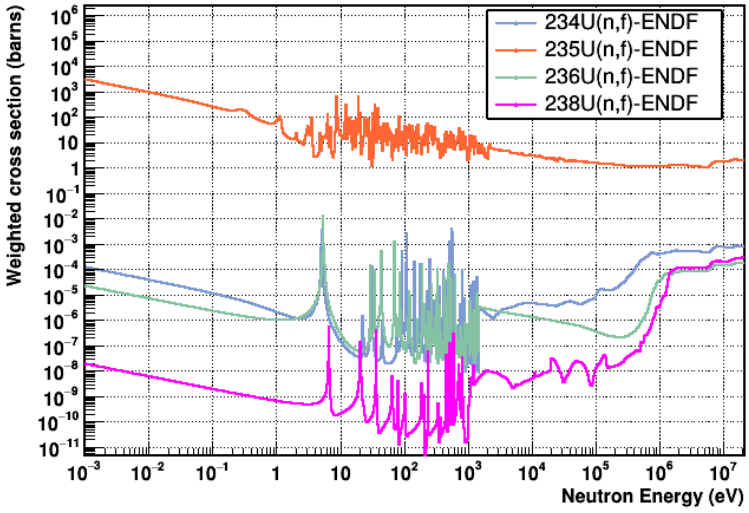

(b)

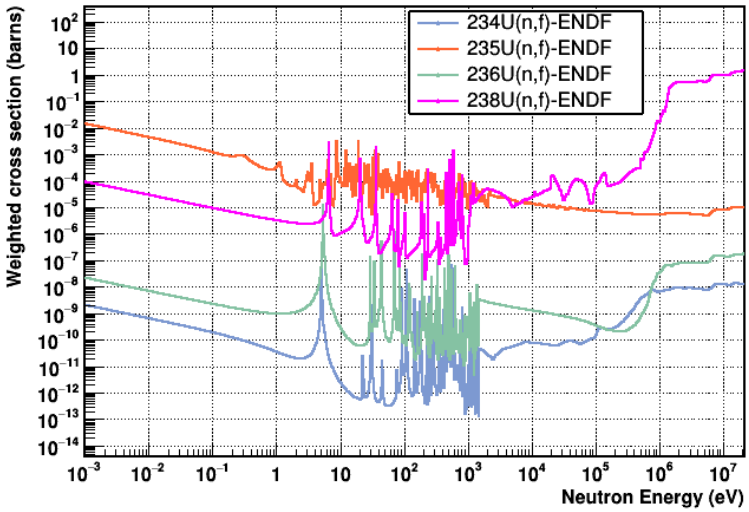

(c)

Figure 3.30: Weighted according to the sample composition fission cross sections in 100bpd for the (a) ^{241}Am (b) ^{235}U and (c) ^{238}U samples from the ^{241}Am(n,f) campaign using the ENDF/B-VIII.0 evaluated library.

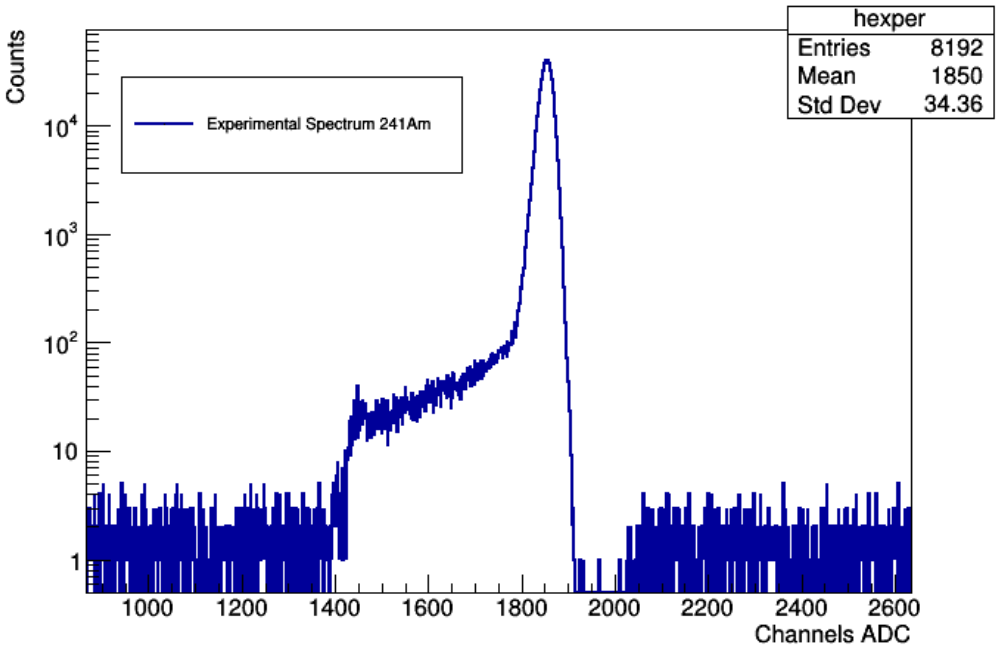

Figure 3.31: Alpha spectrum of a single ^{241}Am target measured at the LG2 station in the Target Preparation Laboratory of JRC-Geel.

In front of this situation, the samples were placed in a specially designed station on top of a broad energy and High Purity Germanium detector (HPGe) of 45% relative efficiency, in order to perform γ -spectroscopy. Each ^{241}Am target was scanned in detail using a $4\,mm$ lead collimator that was placed between the window of the detector and the target. By measuring a specific gamma line in the spectrum ($E_\gamma = 59.54\,keV, I_\gamma = 35.9\%$) which is attributed to the decay of the ^{241}Am isotope, it was possible to perform relative measurements and acquire the profile of the actinide deposit for all the ^{241}Am samples covering the total diameter ($6\,cm$) of each target (Figure 3.35). The results demonstrated that the distribution of the material during the electrodeposition technique in some targets is not homogeneous.

In order to validate the results acquired with γ -spectroscopy, the homogeneity of the targets was also studied by means of autoradiography. In this technique, the radioactive targets were exposed in front of a phosphor screen, the so-called imaging plate. The ^{241}Am targets, were put in direct contact with the imaging plate for approximately 2 minutes. The imaging plates trapped the radiation energy and at a latter stage were scanned with a laser beam resulting in an energy release in the form of luminescence. From the luminescence which is proportional to the exposed radiation, it was possible to acquire information about the homogeneity of the target layer. The results from the comparison of the autoradiography method and the γ -spectroscopy scanning, for three ^{241}Am targets, are illustrated in Figures 3.36, 3.37 and 3.38.

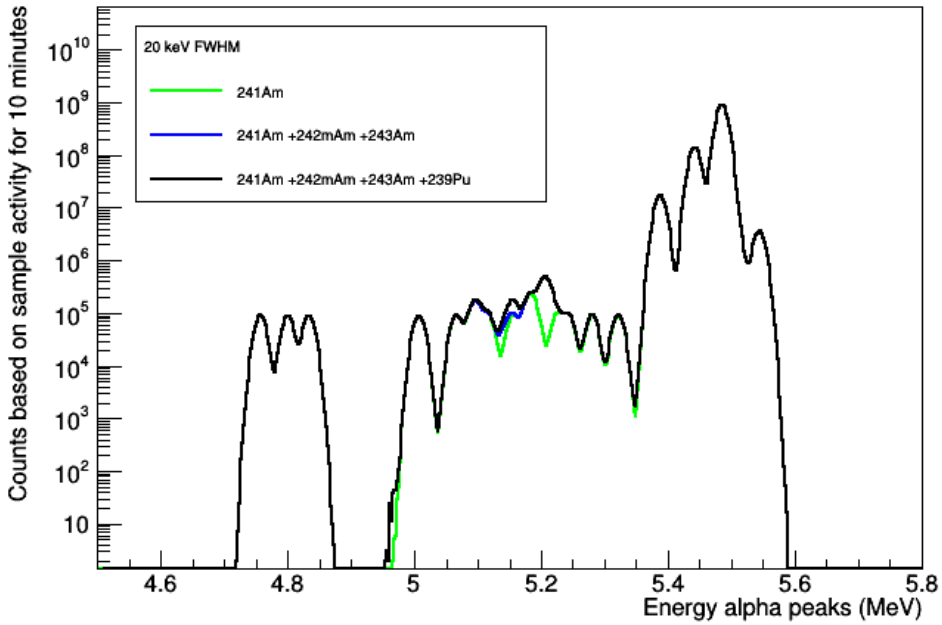

(a)

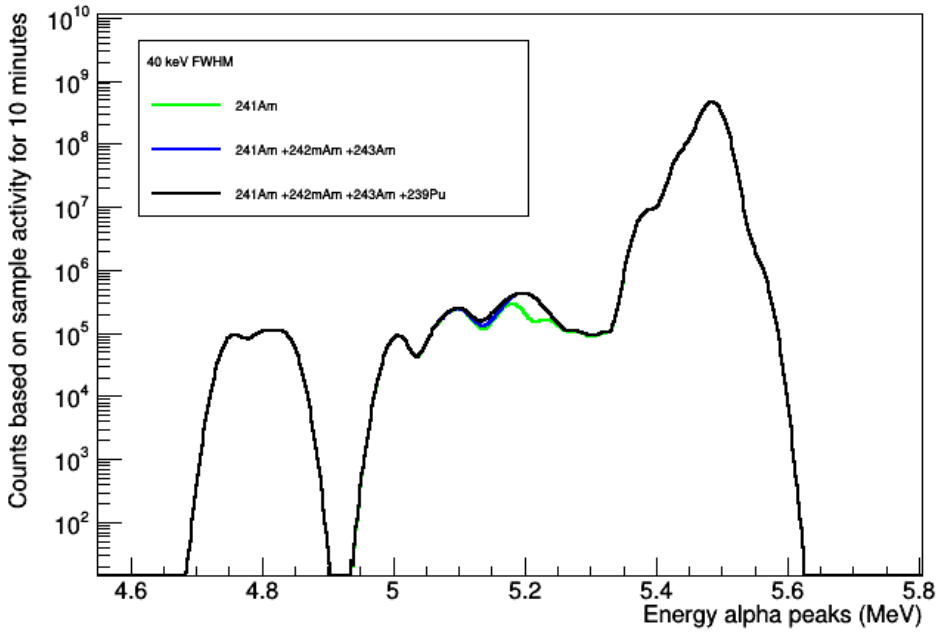

(b)

Figure 3.32: (a) 20 keV FWHM alpha resolution (b) 40 keV FWHM alpha resolution

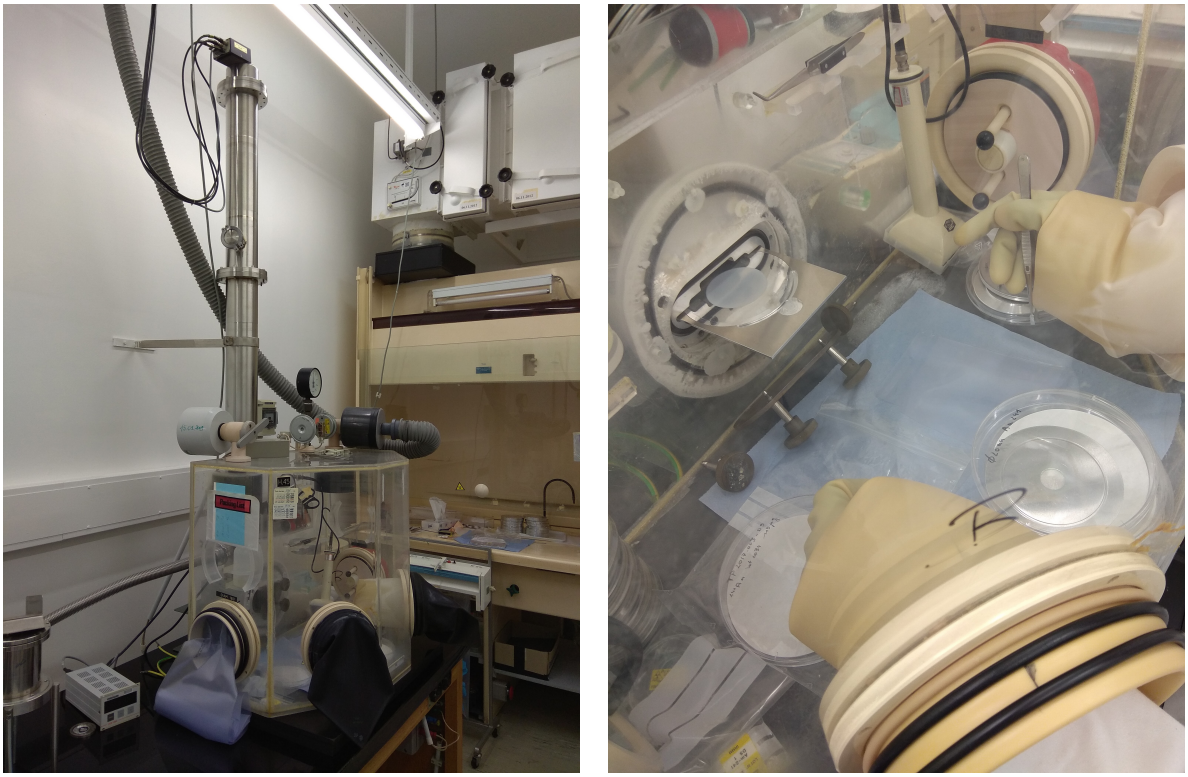

Figure 3.33: Set-up for the characterization of actinide targets by low geometry alpha particle counting in the Target Preparation Laboratory of JRC-Geel (left panel). The silicon surface barrier detector has a diaphragm of 34 mm in diameter and is located at a distance of 1.635 m from the actinide target. On the right panel, a picture taken from the outside of the safety glovebox during the mounting of an ^{241}Am target in the measurement position.

Figure 3.34: Set-up in the γ-spectroscopy station of the Target Preparation Laboratory in JRC-Geel. The picture was taken during the scanning measurement of an ^{241}Am target.

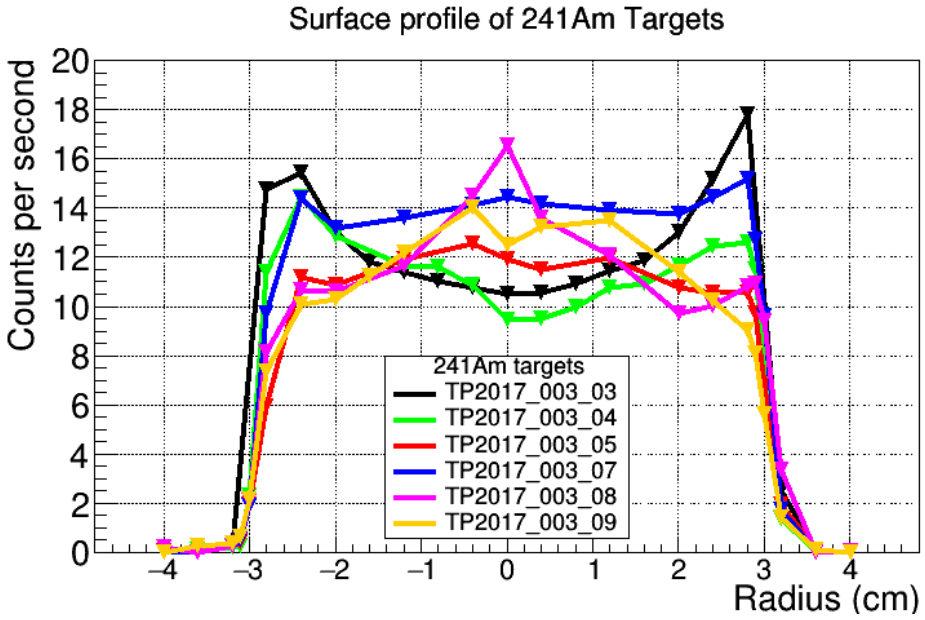

Figure 3.35: Surface profile of all ^{241}Am targets acquired by γ-spectroscopy scanning.

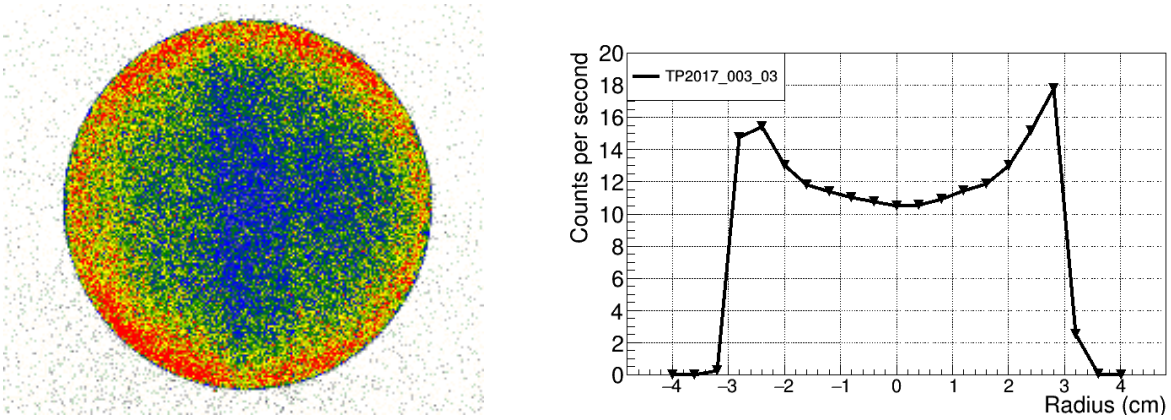

Figure 3.36: Surface profile investigation of the TP2017-003-03 ^{241}Am target using autoradiography and γ-spectroscopy scanning.

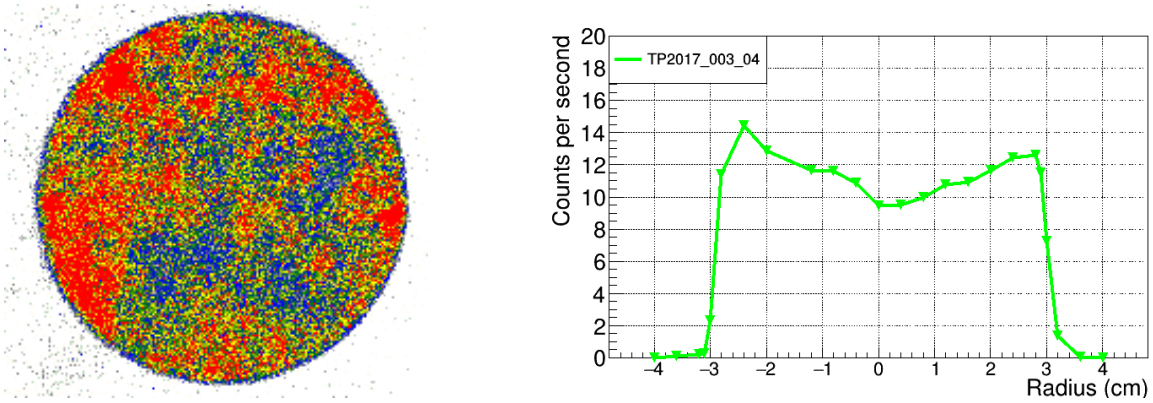

Figure 3.37: Surface profile investigation of the TP2017-003-04 ^{241}Am target using autoradiography and γ-spectroscopy scanning.

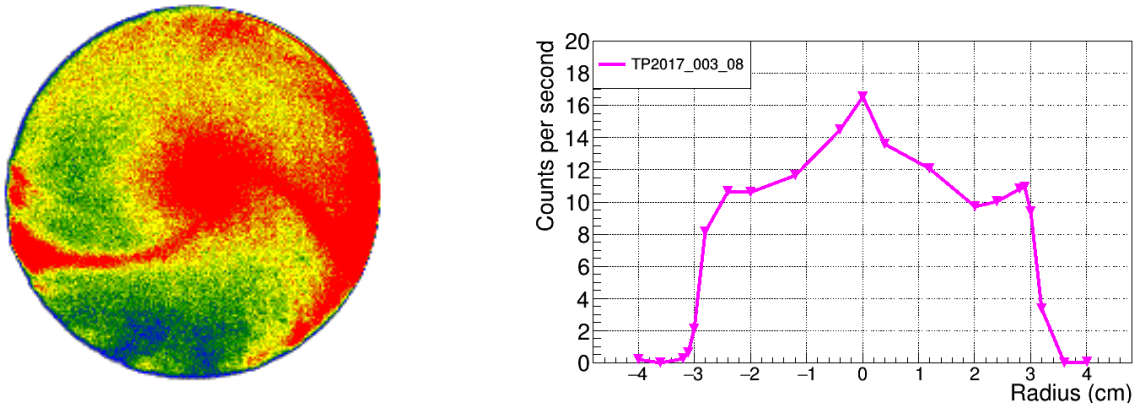

Figure 3.38: Surface profile investigation of the TP2017-003-08 ^{241}Am target using autoradiography and γ-spectroscopy scanning.

3.3.5 Spontaneous fission

The branching ratio for spontaneous fission (a nucleus spontaneously splits into fragment nuclides) in ^{241}Am is $3.6\times10^{-10}(9)\%$ [35]. Taking into account an ^{241}Am sample with the highest activity among the available ones, for example $18.89\,MBq$ and considering the ratio of the primary decay mode of ^{241}Am, which is via alpha particle emission over the spontaneous fission branching ratio ($\alpha/s.f = 3.6\times10^{-12}$), it turns out that 1.088×10^{-6} spontaneous fission events per bunch are expected. Given that one run was composed approximately of 4000 bunches, the expected spontaneous fission rate per single run is estimated to be $4.35\times10^{-3}\,events$, which is a practically negligible contribution to the overall statistics.

The same calculations were also performed for the reference samples, namely ^{235}U and ^{238}U. Table 3.1, shows the results of this study using the branching ratios of spontaneous fission as reported from [36], [37]. In all cases, the spontaneous fission contribution is negligible.

Sample	Highest Activity (Bq)	Decay Modes and Branching Ratios (%)	Total decays per bunch	SF events per bunch	SF events per run
^{241}Am	18.89(8)	a:100 SF: 3.6E-10(9)	302240	1.088E-6	4.35E-3
^{235}U	23.80(17)	a:100 SF: 7.E-9(2)	0.3808	2.67E-11	1.07E-7
^{238}U	27.5(3)	a:100 SF: 5.45E-5(2)	0.44	2.4E-07	9.59E-4

Table 3.1: Investigation of the spontaneous fission contribution for Americium and reference samples. As can be seen, the spontaneous fission component is practically negligible, and the same conclusion is deduced from the beam off spectra of ^{235}U and ^{238}U samples, which are empty in the region (in ADC channels) that normally is expected to record fission events.

3.3.6 Resolution function of EAR-2

As can be seen in Figure 3.39, for neutrons that arrive within the same time-of-flight bin in the experimental area, there is a distribution for the moderation length. In other words, not all the neutrons of the same TOF or equivalently neutron energy have traveled the same distance inside the target-moderator assembly. Additionally, there is no way to know experimentally the moderation length for each single neutron that arrives in the experimental area other than the Monte Carlo simulations that provide the resolution function by calculating this probability, but still cannot benchmark each detected neutron in the actual experiment.

From the 2-dimensional probability distribution of the moderation length as a function of the time-of-flight, the average and most probable values for λ can be extracted per TOF bin. As illustrated in Figures 3.40a and 3.40b respectively, the distributions are quite conflicting and on top of that there is no specific reason to use any of these single λ valued distributions for the TOF to energy conversion. Ideally, for the TOF to energy conversion the full information of the resolution function as provided by the Monte Carlo simulations has to be considered.

In the frame of the ^{241}Am(n,f) reaction study, a new method was developed in order to include the effect of the resolution function in the experimental data of the EAR-2 of the n_TOF. A code written in C++ was created, according to which for every recorded pulse, the code allocates on an event-by-event basis randomly a λ value which is sampled from the distribution of the corresponding time-of-flight bin. Then, this random λ value is stored as an extra branch inside a new Tree along with the rest of the characteristic quantities of the pulse for further analysis. With this method it is evident that neutron pulses detected with the same time-of-flight will be allocated with a different random λ value that follows the distribution of the moderation length distribution λ of the given TOF bin.

As a proof of principle, Figure 3.40 illustrates the implementation of the random λ distribution method for the three isotopes of this measurement. The 2-dimensional distributions are populated according to the conventional TOF yield that is expected for each isotope by considering its mass, neutron flux and cross section. As a general observation, the better the statistics are, the easier is to see the formation of the original resolution function that is used (Figure 3.39). This is actually the case of the fissile ^{235}U sample that can be seen in Figure 3.41b.

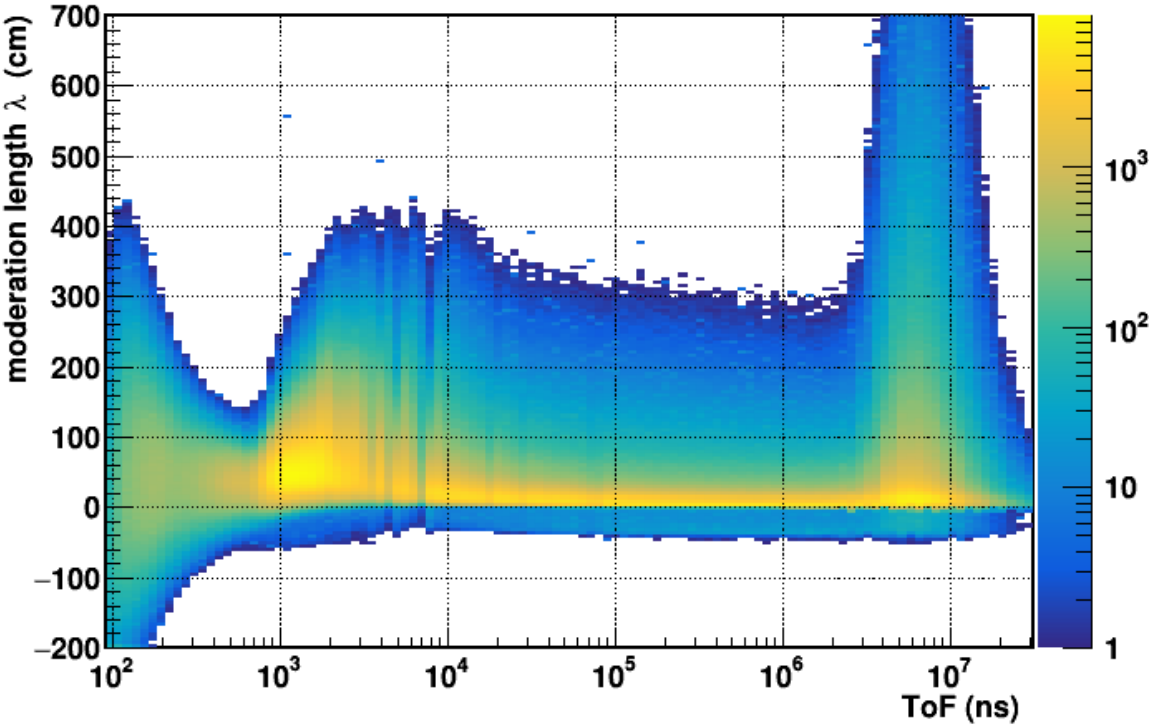

Figure 3.39: Full moderation length λ distribution as a function of the time-of-flight for a geometrical flight path of 19.5 m in EAR-2 for the fission collimator. The negative λ values are related to the scoring plane of the Monte Carlo simulation which for EAR-2 was set 37.2 cm above the center of the spallation target. Furthermore, the spread of the λ distribution at small times-of-flight (high neutron energies) is attributed to the proton beam width (7 ns RMS).

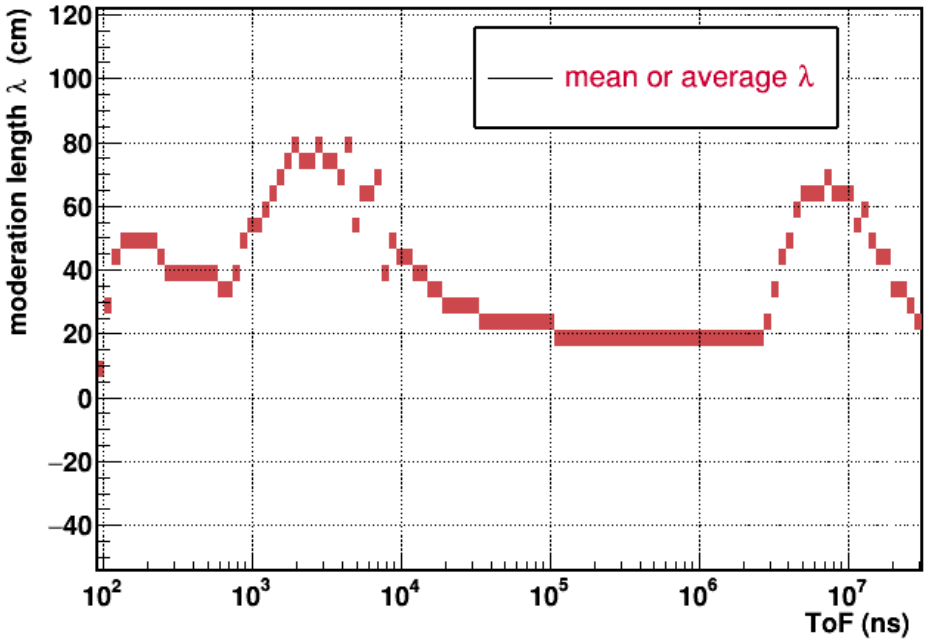

(a)

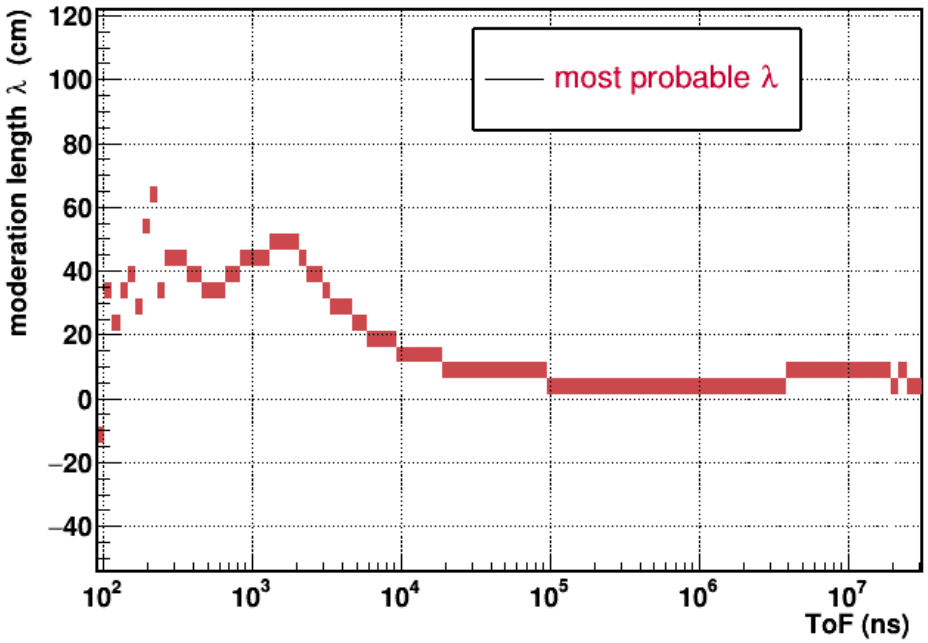

(b)

Figure 3.40: (a) Average and (b) most probable λ value distribution as a function of the time-of-flight for a geometrical flight path of 19.5 m in EAR-2.

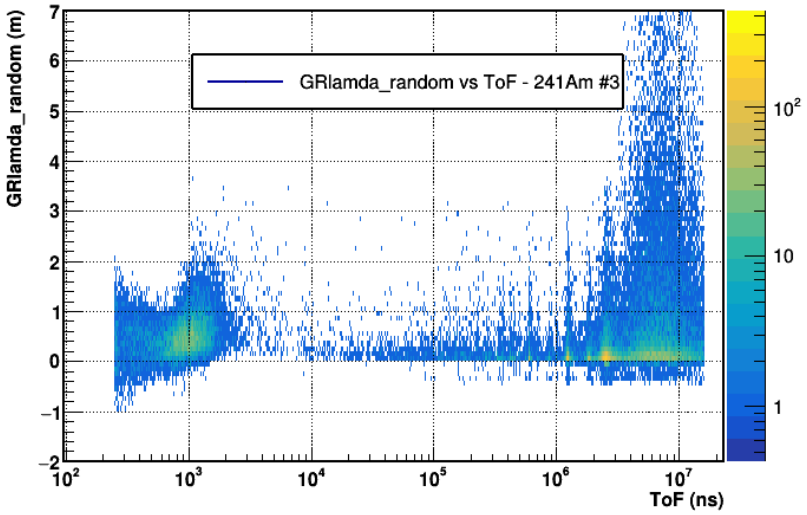

(a)

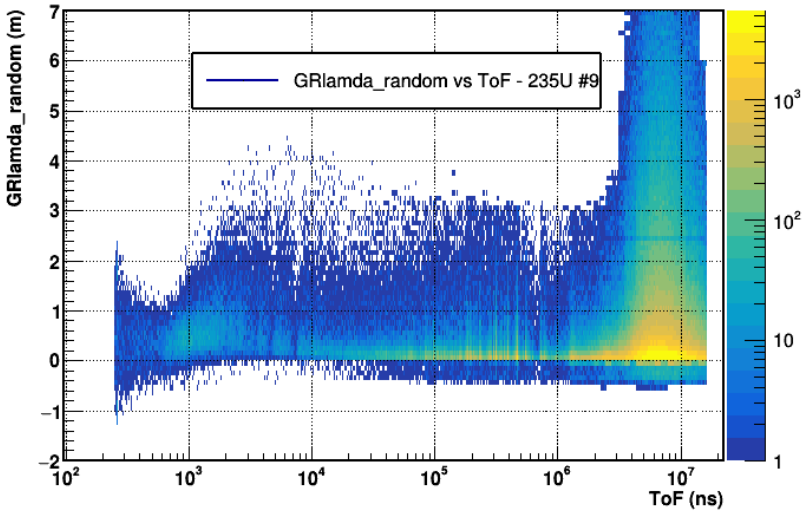

(b)

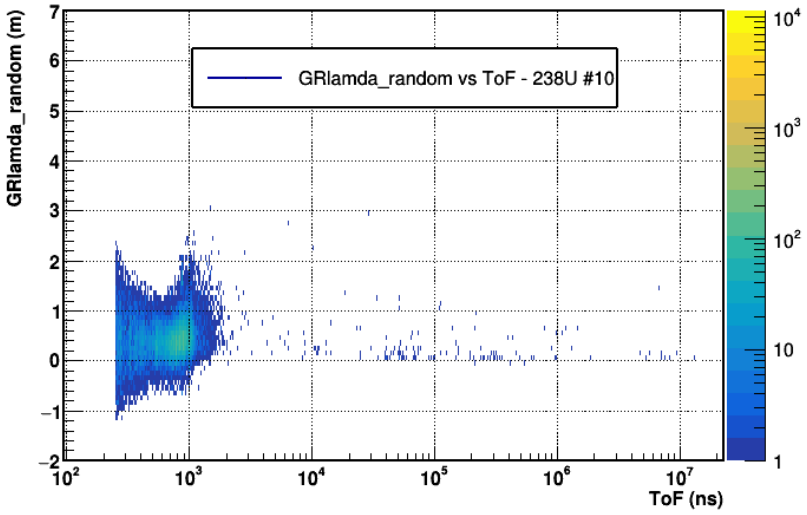

(c)

Figure 3.41: EAR-2 resolution function on an event-by-event implementation for a sample of (a) ^{241}Am (b) ^{235}U and (c) ^{238}U detector family.

3.3.7 GEF code as fission fragment event generator

The GEneral description of Fission model (GEF) code [38] is a computer code that simulates the nuclear fission process using the Monte Carlo method. GEF, among others, predicts fission observables with a rather good agreement with the experimental data. Within the framework of the present study, GEF was used as a fission fragment event generator for the nuclear reactions under study and its output was provided as input to a simulation that handles the transportation of particles which was performed with the GEANT4 tooklit [39] [40] [41]. The goal was to study the energy deposition of the fission fragments inside the volume of the Micromegas detector using the same geometry that was adopted in the ^{241}Am(n,f) experiment.

GEF provided on an event-by-event basis, the atomic (or charge) and total mass distributions for the produced light and heavy fission fragments along with their total kinetic energy in MeV. The fission fragments are emitted from the compound fissioning nuclei of ^{236}U, ^{239}U and ^{242}Am respectively. In Figures 3.42, the distributions of the total yield of fission fragments is shown as a function of the mass and atomic number, for the created compound nuclei assuming monoenergetic incident neutrons of $1\,MeV$. For the light fission fragments, the heavier the compound nucleus is, the heavier are the produced light fragments. The trend of shifting in the mass distribution of the light fission fragments in Figure 3.42a, indicates that the heavier the compound nucleus is, the extra nucleons are absorbed almost exclusively from the lighter fission fragments. For the heavy fragments, as illustrated in Figure 3.42b, the low edge of the atomic distribution remains nearly constant independently of the compound nucleus. The reason for this lies in the fact that in this region exists the "doubly magic" nucleus ^{132}Sn with Z=50 and N=82. According to the shell model, in the nucleus, magic numbers are the number of either protons or neutrons at which a shell is closed. As a result, nuclei with a "magic" number of protons or neutrons are more stable than other nuclei. The seven first most widely recognized magic numbers are 2, 8, 20, 28, 50, 82 and 126. Since there is no overlap of the light fission fragments with these numbers, their distribution is not affected by shell closures and therefore no such effect is observed there.

The output of GEF in addition to the Z and A of the produced fission fragments provides also their total kinetic energy after the prompt-neutron emission. In order to calculate the kinetic energy of each fission fragment independently, the principle of conservation of the kinetic energy and momentum is taken into account. The momentum of the incident neutrons is considered negligible and therefore the application of the conservation laws can be expressed as follows:

$$KE_{Total} = KE_{LF} + KE_{HF} \tag{3.2}$$

$$\vec{0} = \vec{P}_{LF} + \vec{P}_{HF} \tag{3.3}$$

where the notation LF and HF stands for the light and heavy fission fragments respectively. By solving the simple equations 3.2, 3.3, the kinetic energy of the fission fragments is given as:

$$KE_{LF,HF} = \frac{A_{HF,LF}}{A_{LF} + A_{HF}} \cdot KE_{Total} \tag{3.4}$$

where A_{LF} and A_{HF} are the total post neutron emission masses of the light and heavy fission fragment respectively. From equation 3.3 is straightforward that the fission fragments are emitted in opposite directions since the conservation of momentum implies that:

$$\vec{P}_{LF} = -\vec{P}_{HF} \tag{3.5}$$

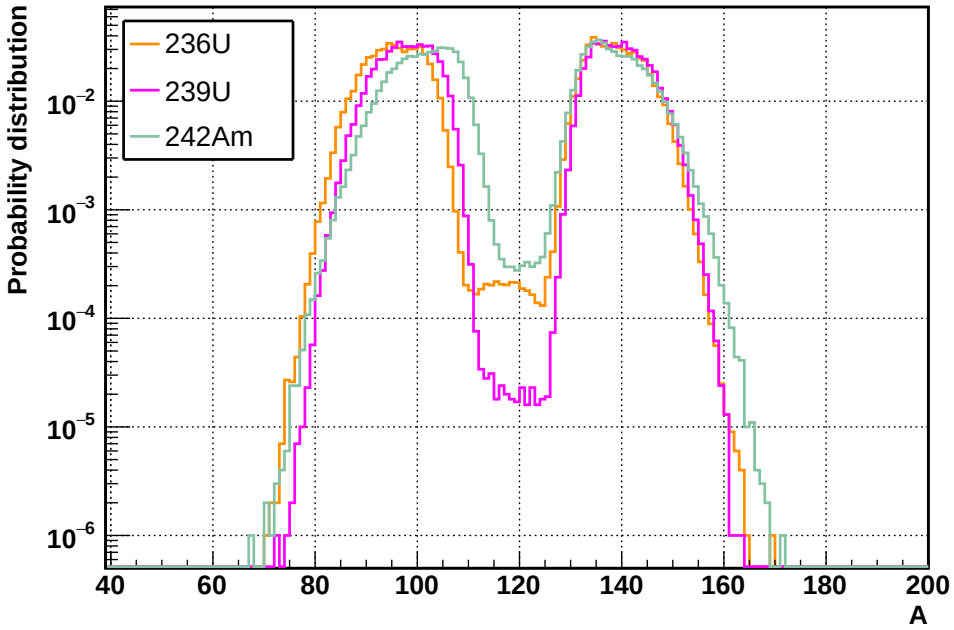

(a)

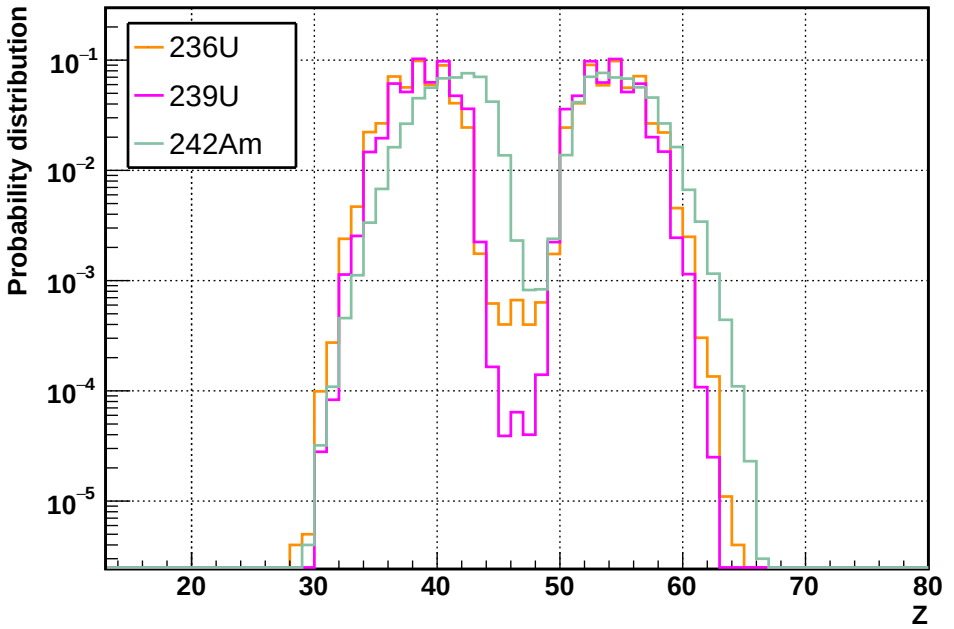

(b)

Figure 3.42: (a) Mass and (b) atomic number fission fragment distributions for the fissioning nuclei under study calculated with the GEF code assuming monoenergetic incident neutrons of 1 MeV.

The kinetic energy of fission fragments that emerged from the compound nucleus ^{242}Am is illustrated in Figure 3.43a, where the contributions from the heavy and light fission fragments are also highlighted. In the 2-dimensional plot of Figure 3.43b, the kinetic energy of the fission fragments is correlated with their mass number. This is a characteristic distribution and is widely referred to as "fission fragment lungs" due to the association suggested by the shape of the corresponding structure.

Having already for each compound nucleus a list of the produced fission fragments along with their properties (Z, A, KE), the next step is to initialize their position (x0, y0, z0) and momentum (px0, py0, pz0) within the radioactive target, to be used as fission event generator in the GEANT4 simulation. Initially, for each fission event, due to the kinematics of the reaction as already mentioned above, only one of the produced fission fragments (light or heavy) will eventually enter the gas volume in the direction of the Micromegas detector. Consequently, for each fission event only one of the fragments was chosen, giving a 50-50 probability for that to be light or heavy. The fission fragments were generated randomly inside the volume of the actinide target, ensuring in this way uniform distribution of the radioactive material. To achieve this, the (x,y) coordinates were assigned to random numbers that were generated within the surface of the actinide target with radius $R = 3\,cm$, according to the following condition:

$$x^2 + y^2 < R^2 \tag{3.6}$$

Then, the z coordinate was also randomly chosen inside the frames of the thickness of the target. The uniform fission fragment generation within the cylindrical volume of the actinide target is better visualized in Figure 3.44. In addition to the randomization of the starting coordinates, a uniform distribution was adopted concerning the momentum direction of the fission fragments. The selected fission fragments were propagated isotropically in a 2π emission angle towards the gas volume in the direction of the Micromegas detector. Figure 3.45 illustrates the 2π uniform momentum that was randomly assigned to the fission fragments. The fission fragments along with their properties as calculated with the GEF code were used as primary particles at the GEANT4 simulation in order to study their energy deposition in the active volume of the Micromegas detector and to estimate the efficiency of the detection set-up.

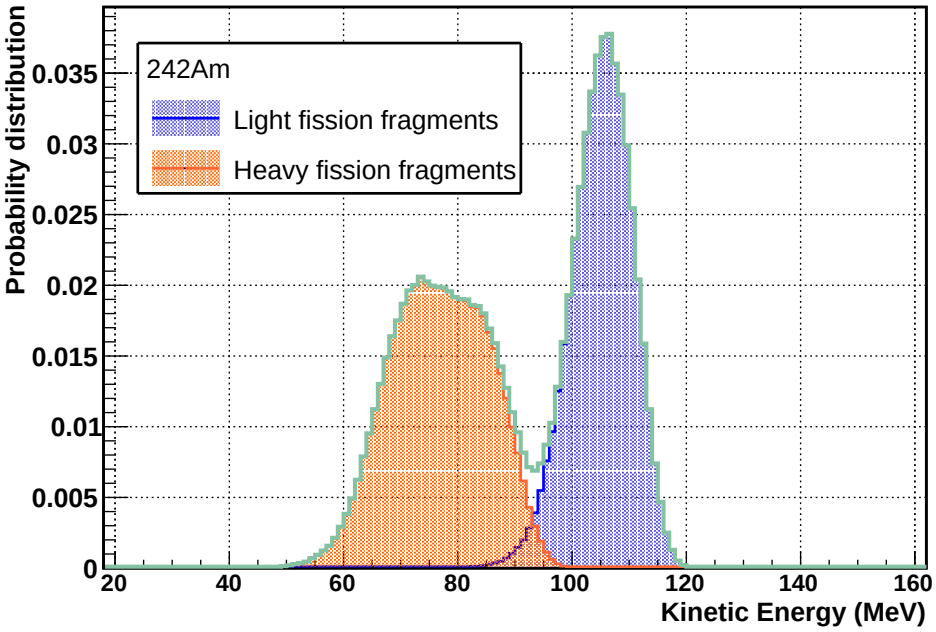

(a)

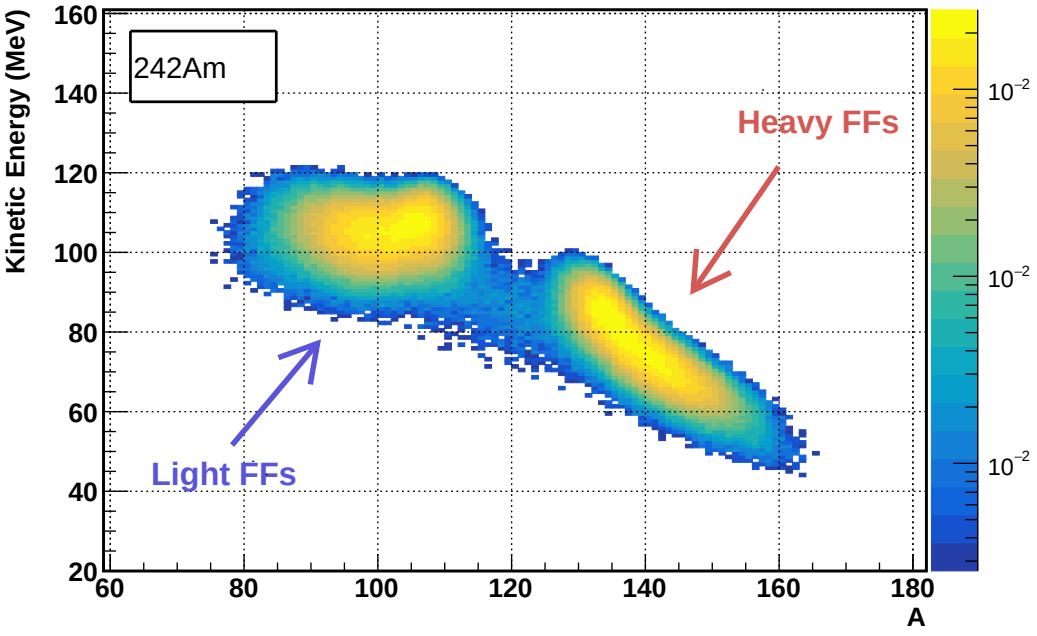

(b)

Figure 3.43: (a) Probability distribution of the kinetic energy and (b) Mass number versus kinetic energy for the light and heavy fission fragments calculated with the GEF code for the compound nucleus ^{242}Am and considering incident neutrons of 1 MeV.

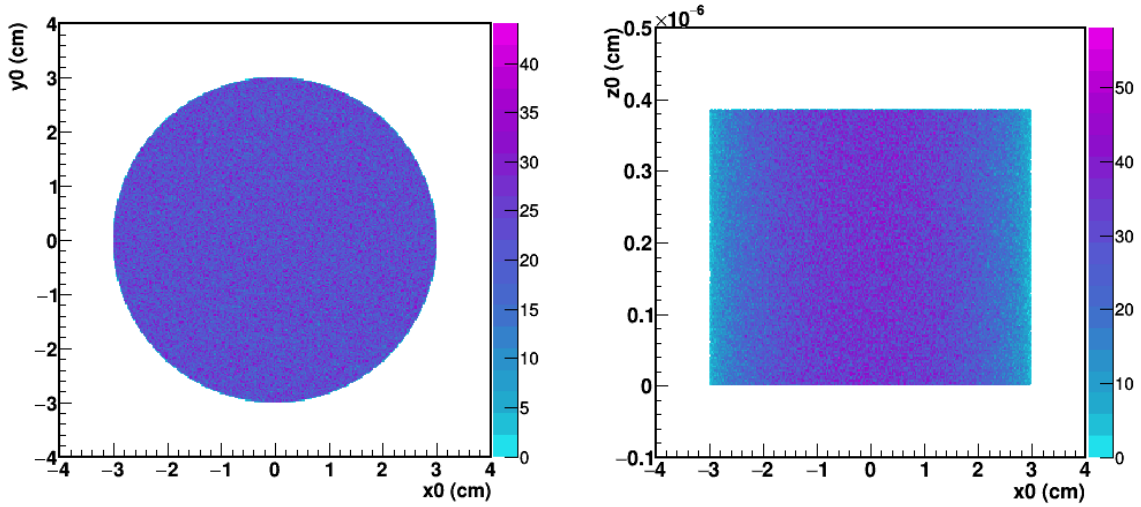

Figure 3.44: Random generation of the fission fragments in the cylindrical volume of an Am target shown in the x-y plane (left panel) and in the x-z plane (right panel).

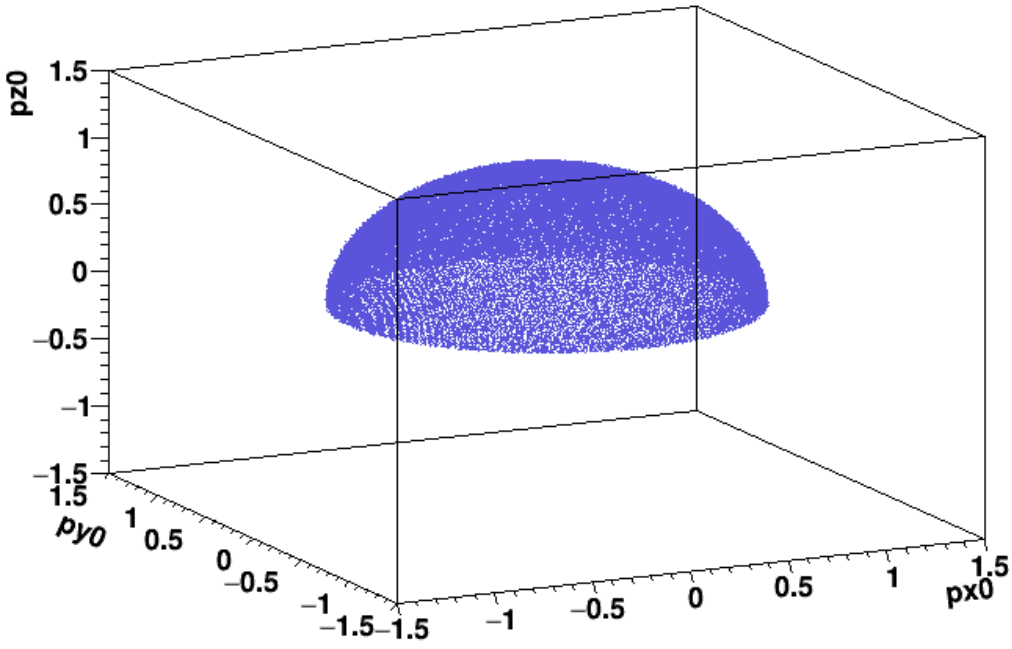

Figure 3.45: Propagation of the fission fragments along the z-axis towards the direction of the Micromegas detector by adopting a 2π isotropic emission. The x-y plane coincides with the surface layer of the actinide material.

3.3.8 GEANT4 geometry simulation

Within GEANT4, a simple geometry of the fission chamber including the actinide sample and the Micromegas detector was implemented, as illustrated in Figure 3.46. A cylindrical aluminum chamber with dimensions 30 cm x 30 cm x 1.5 cm (length x diameter x thickness) was filled with a gas blend of Ar:CF_4:isoC_4H_{10} (88:10:2) at atmospheric pressure with a volume density of 1.88 mgr/cm^3. In addition, the two chamber's kapton windows of 25 μm thickness and 15 cm diameter placed at the entrance and exit of the fission chamber respectively were also included in the simulation. The cylindrical volume of the actinide sample which was placed at the center of the inner volume of the fission chamber had a diameter of 6 cm and a thickness that was properly adjusted to match the areal density and the total mass of the actual actinide sample. Finally, the active gas volume in front of the Micromegas detector was simulated as a separate cylindrical gas volume with 9.5 cm diameter, to match the micromesh active surface, and 7 mm thickness which corresponds to the drift gap distance that was adopted in the actual ^{241}Am experiment. This was actually the scoring volume in the GEANT4 simulation for the recording of the energy deposition from the transportation of the fission fragments in the active gas volume of the Micromegas detectors.

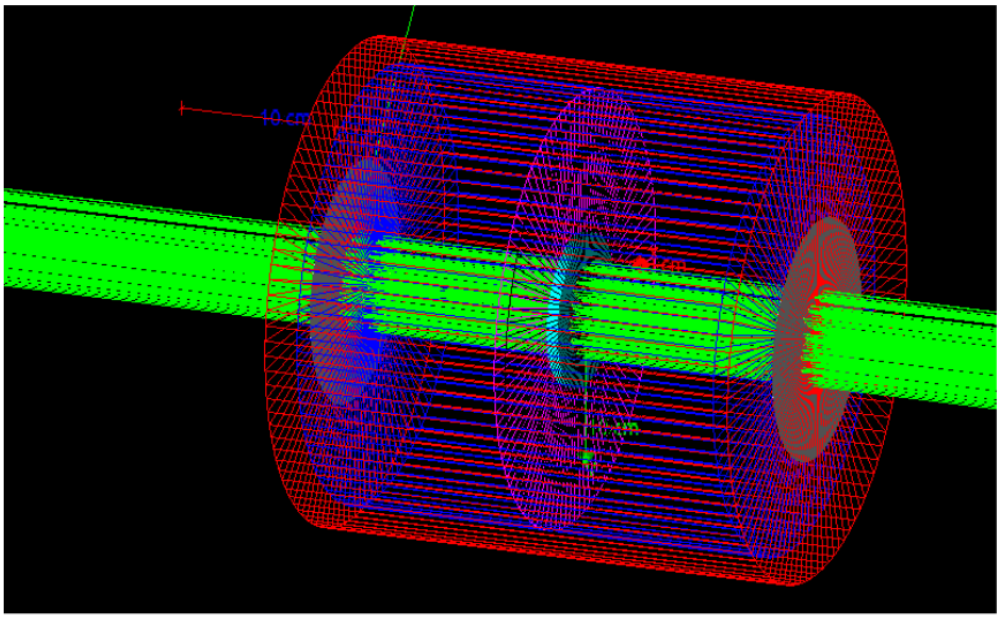

Figure 3.46: Visualization of the fission chamber geometry.

An example of the output of the GEANT4 simulation is visualized in Figure 3.47. In this plot, the total energy deposition of the fission fragments generated from the ^{236}U fissioning compound nucleus in the active gas volume of a Micromegas detector is presented. In addition, the individual contributions of the light and heavy fission fragments are also highlighted with different colours. Furthermore, in Figure 3.48, a comparison is made concerning the total energy deposition of the fission fragments, for various actinide samples used in the experiment, taking into account the masses, material densities and their estimated thicknesses.

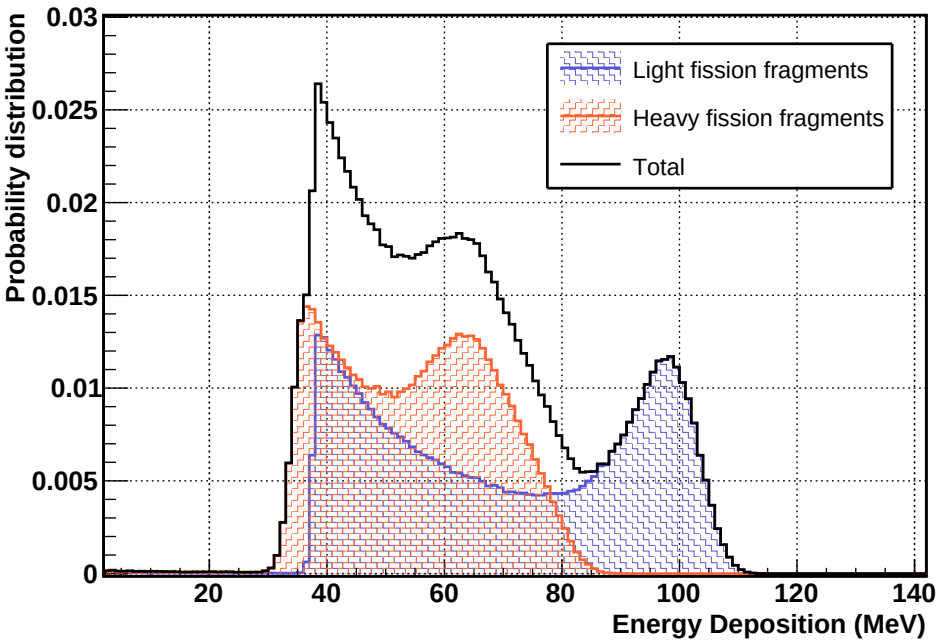

Figure 3.47: Simulated energy deposition of heavy and light fission fragments from the ^{235}U(n,f) reaction.

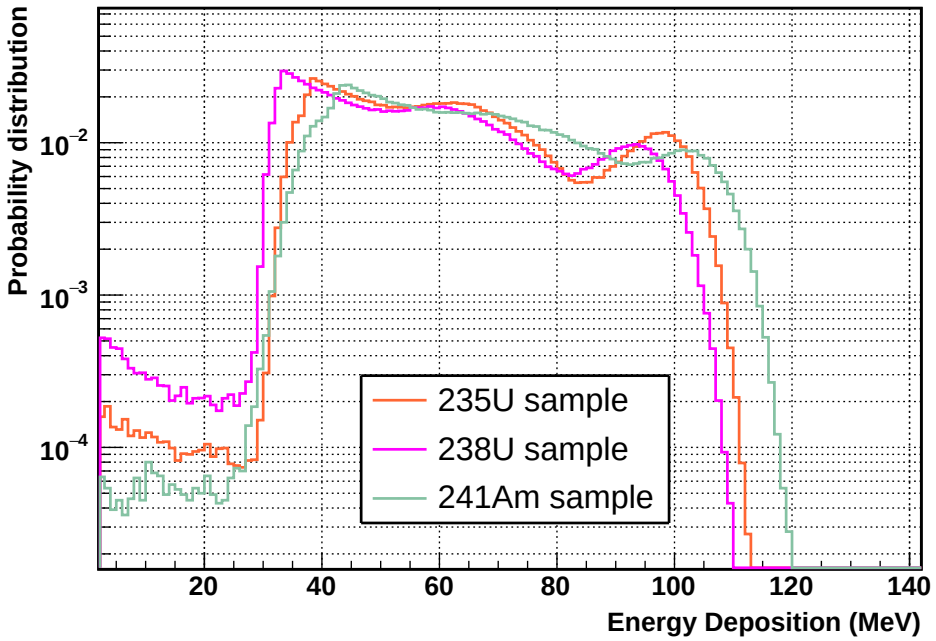

Figure 3.48: Comparison of the simulated energy deposition of the fission fragments for the different (n,f) reactions, considering incident neutrons of the MeV region and taking into account the real thicknesses of the actinide samples used in the experiment. The significant higher probability distribution of the ^{238}U sample below 30 MeV is directly related to its larger thickness compared to the rest of the actinide family samples used in the experiment.

Since the exact chemical composition of the actinide targets prepared with the electrodeposition technique, is not accurately known, a sensitivity study was performed in order to compare the energy deposition of the fission fragments considering various chemical oxide compounds. For this purpose, various simulations with GEANT4 were performed, each time by adopting a different chemical composition in the volume of the cylindrical target under study. Based on the available information for the value of the volume densities of the isotopic as well as oxide compounds [42], the thickness of the actinide was adjusted accordingly in each simulation, ensuring at the same time the homogeneous generation of the imported from GEF fission fragments inside the actinide's volume.

In Figures 3.49 and 3.50, the energy deposition of fission fragments induced by thermal neutrons for different actinide compound scenarios is depicted for an ^{241}Am and ^{235}U target respectively. For the proper interpretation of the results, Tables 3.3 and 3.5 show the estimated thicknesses of the actinides for the adopted chemical compositions. As a general observation, the general shape of the total energy deposition is not significantly affected by considering different scenarios for the chemical composition of the compounds, therefore the exact knowledge of the latter is not crucial for the simulations. Nonetheless, it is worth mentioning that the thickness of the actinide sample slightly affects the low energy part of the energy deposition below 30 MeV. For example in the case of ^{241}Am (Figure 3.49), this low energy part is almost the same in all scenarios because the corresponding thicknesses are also very much alike. On the other hand, in the case of ^{235}U (Figure 3.50), the higher is the low energy part, the thicker is the target. At the end of the day, the selection of the adopted chemical composition is a free choice based on the better agreement with the experimental data but also keeping in mind that as the thickness of the target increases, the efficiency also changes as well. For the present work, it was assumed that the targets are purely isotopic with no oxide impurities.

From the GEF/GEANT4 simulations, the efficiency ϵ of the Micromegas detector is estimated, which in reality is a correction factor that is indicative of the fission fragments that are lost inside the volume of the actinide target and therefore do not enter the active gas volume of the Micromegas detector. The detection efficiency ϵ is calculated according to the following formula:

$$\epsilon = \frac{\text{FFs entering the gas volume}}{\text{FFs emitted from the actinide volume}} \tag{3.7}$$

In all cases, considering the different geometric effects of each target case (^{241}Am, ^{235}U, ^{238}U), which are basically the various thicknesses, over one million fission fragments that were emitted towards the direction of the gas volume of the Micromegas detector in each Monte Carlo simulation, the efficiency was found to be $\epsilon = 0.999$. This means that only 0.1 % of the fission fragments were absorbed inside the actinide deposit, a number that is indicative of how thin the fission foils were.

Am isotope mass	**Target Abundance (%)**	**Weighted mass**
241.056827413	99.9838	241.018
242.059547428	0.00162	0.004
243.06137994	0.002	0.005
Total	**99.98742**	**241.027**
O isotope mass	**Natural Abundance (%)**	**Weighted mass**
15.9949146196	99.757	15.956
16.99913175664	0.038	0.006
17.99915961284	0.205	0.037
Total	**100**	**15.999**

Table 3.2: Weighted mass calculation for a case of ^{241}Am sample used in the experiment. The atomic masses are taken from [43].

Chemical formula of compound	**Am**	**AmO_2**	**Am_2O_3**
Atomic/Molecular weight	241.027	273.025	530.051
Am (%)	100	88.3	90.9
O (%)		11.7	9.1
d (gr/cm^3)	13.67	11.68	11.77
total mass (gr)	0.0001489	0.0001687	0.0001637
target thickness (nm)	3.85	5.11	4.92

Table 3.3: Thickness calculation of ^{241}Am target assuming different compound chemical composition. The compound volume densities were retrieved from ref. [42].

U isotope mass	**Target Abundance (%)**	**Weighted mass**
234.04095037	0.035973	0.084
235.04392819	99.9336	234.888
236.045566201	0.009629	0.023
238.050786996	0.02073	0.049
Total	**99.99993**	**235.044**
O isotope mass	**Natural Abundance (%)**	**Weighted mass**
15.9949146196	99.757	15.956
16.99913175664	0.038	0.006
17.99915961284	0.205	0.037
Total	**100**	**15.999**

Table 3.4: Weighted mass calculation for a case of ^{235}U sample used in the experiment. The atomic masses are considered from [43].

Chemical formula of compound	**U**	**UO_2**	**U_3O_8**
Atomic/Molecular weight	235.044	267.043	833.128
U (%)	100	88	84.6
O (%)		12	15.4
d (gr/cm^3)	18.97	10.95	8.39
total mass (gr)	0.0002977	0.0003382	0.0003517
target thickness (nm)	5.55	10.93	14.83

Table 3.5: Thickness calculation of ^{235}U target assuming different compound chemical composition. The compound volume densities were retrieved from ref [42].

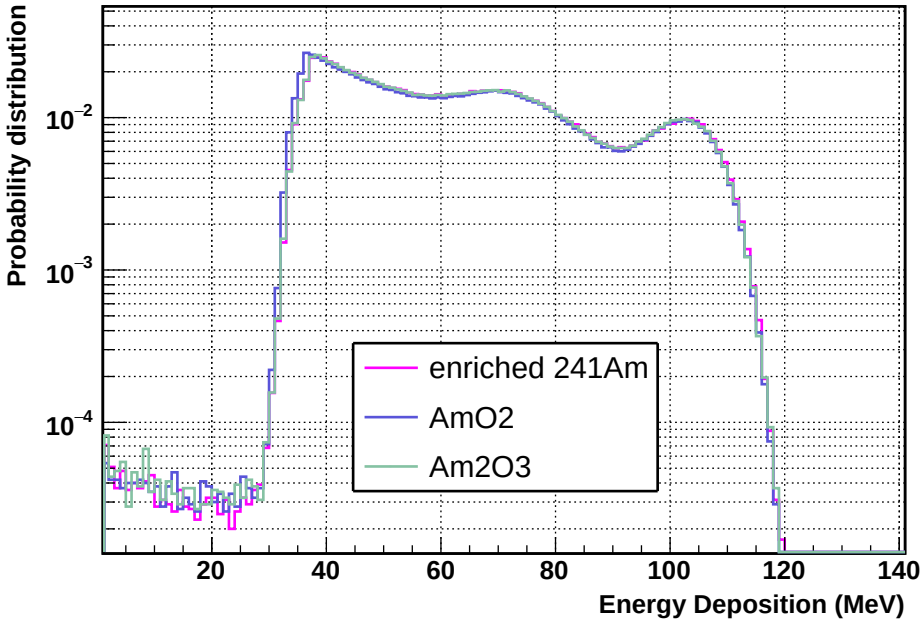

Figure 3.49: Energy deposition of fission fragments induced by thermal neutrons considering different chemical composition compounds for the case of a ^{241}Am target. The extremely good agreement of the energy deposition in the low energy part is related to the similar thicknesses of the adopted compounds.

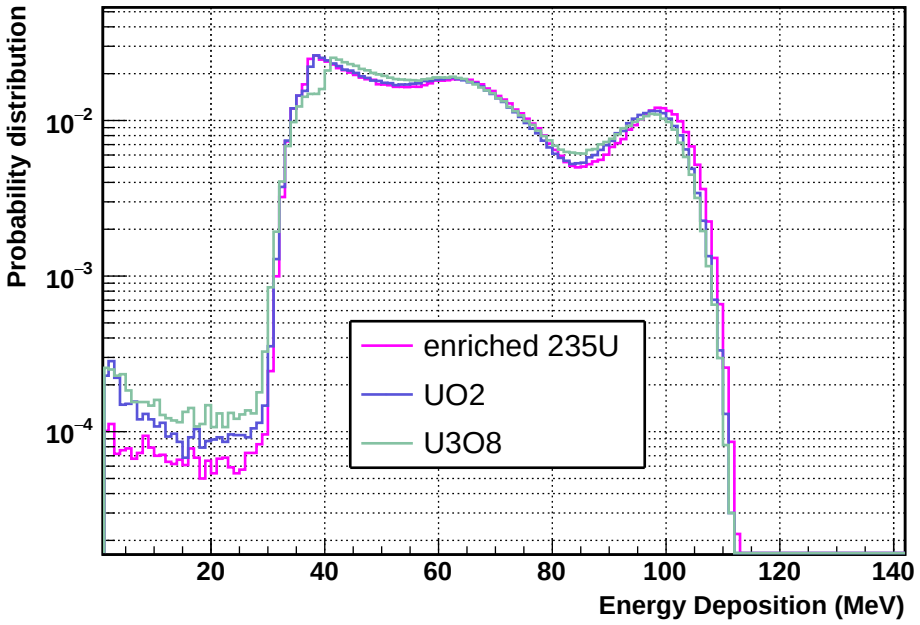

Figure 3.50: Energy deposition of fission fragments induced by thermal neutrons considering different chemical composition compounds for the case of a ^{235}U target. The small discrepancy in the low energy part is a result of the different thicknesses of the adopted compounds.

3.3.9 Response function of the Micromegas detector

The energy deposition of the fission fragments inside the active gas volume of the detector, as extracted from the Monte Carlo simulations, is used for the estimation of two main corrections: (a) The amplitude cut correction factor, which is applied in the experimental amplitude spectrum to achieve the distinction of the fission signals from the rest of the recorded signals which are mainly attributed to alpha particles and "$\gamma - flash$" residuals and (b) The pile-up correction factor, which dominates the high energy neutron spectrum and is expected to be significant when signals are overlapping with each other due to an inflated counting rate, therefore leading to counting losses.

The reproduction of the experimental pulse height spectra is achieved by the conversion of the simulated energy deposition of fission fragments in MeV, to ADC Channels via the following formula:

$$ADC\ Channels = A + B \cdot Gauss(E_{dep}, \sigma(E_{dep})) \tag{3.8}$$

where the A,B parameters of the linear transformation are related to the gain of each Micromegas detector and the resolution broadening is accomplished by using a Gaussian-like distribution with the energy deposition value as mean and a randomized energy deposition dependent response function as standard deviation. For a satisfactory reproduction of the experimental spectra, practically any kind of response function may be used, provided that no distinction is made in the treatment of convolution of the energy deposition between the light and heavy fission fragments. In the present work, the response function that was adopted is given in the following formula:

$$\sigma(E_{dep}) = C \cdot (\frac{D}{\sqrt{E_{dep}}} + \frac{E}{E_{dep}}) \tag{3.9}$$

where the C, D, E parameters are adjusted individually for each Micromegas detector until a realistic reproduction of the experimental pulse height spectra is achieved.

3.3.10 Amplitude Cut

In order to account for the fission fragments that are lost due to the applied cut in the experimental pulse height spectrum, the simulated spectrum is used to estimate the portion of fission fragments that lies below the amplitude cut threshold. This is the reason that the comparison of the simulated and experimental spectrum or else the reproduction of the experimental spectrum with the simulated one is needed. An illustration of this comparison is visualized in Figure 3.51 for the three actinide families, where a very satisfactory agreement is achieved between the experimental and simulated spectrum in each case. In these Figures, the percentage of the rejected fission fragments for different typical amplitude cut channels, is also indicated on top of each plot. It is important to mention that in each simulation the integral of the high energy part of the experimental spectrum is equal to the simulated one for the equivalent region of ADC Channels. Furthermore, the final choice of the amplitude cut channel is based on the adequate separation of the alpha particles with the fission fragments for low neutron energies, as well as the rejection of the "$\gamma - flash$" residuals in the high energy region of the neutron spectrum.

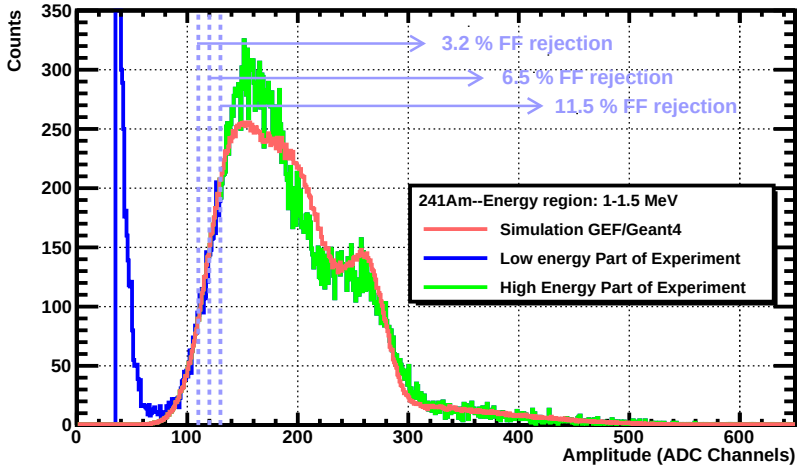

(a)

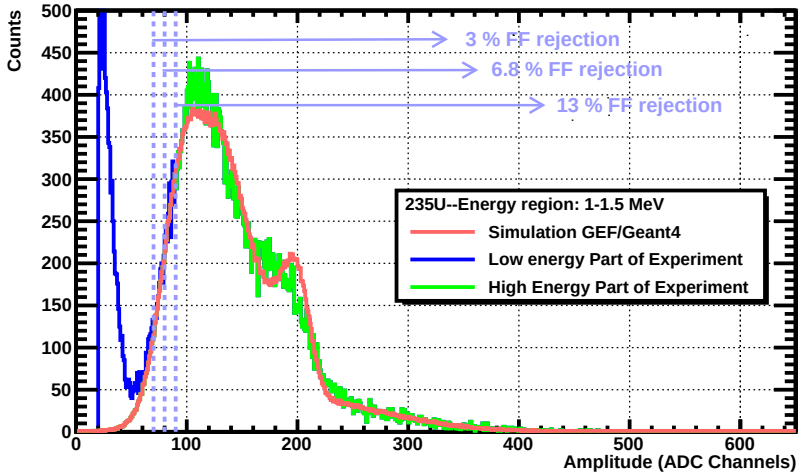

(b)

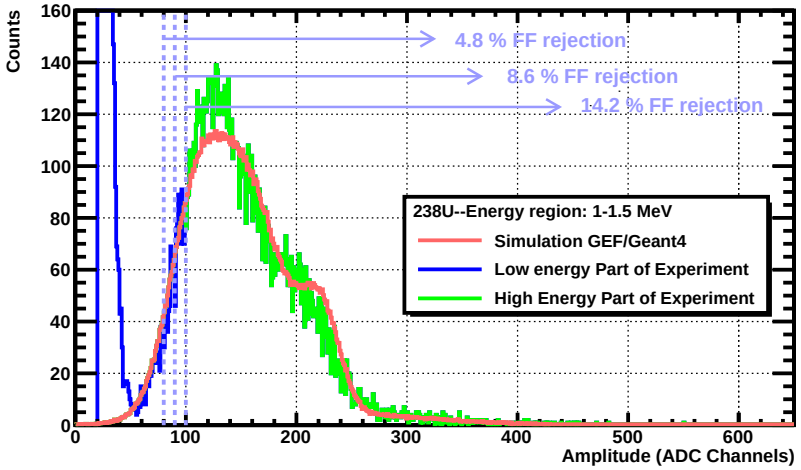

(c)

Figure 3.51: Estimation of the amplitude cut correction factor for a case of (a) ^{241}Am (b) ^{235}U and (c) ^{238}U sample by comparing the experimental spectra with the simulated ones.

3.3.11 Pulse pile-up

At extremely high counting rates ($\sim MHz$), possible counting losses may occur [44]. Counting losses are subject to dead time and pile-up physical phenomena. It has to be underlined that these are two different phenomena [45]. Dead time or resolving time of a counting system is characterized as the minimum time of separation for the proper detection of the pulses and is mainly attributed to the instrumentation part of the detection system and the electronic pulse processing. The phenomenon of pile-up is observed when two or more pulses arrive too close to each other, practically when they overlap and therefore the production of a combined pulse of summed amplitude takes place. The identification between dead time and pile-up is not always clear, it is nonetheless necessary in order to understand the origin of counting losses (or else the physics of the phenomena) and to be able to properly account for these counting losses during the data analysis procedure. Briefly and very generally, in the case of pile-up, a summed pulse is produced when e.g. two pulses are combined leading simultaneously to energy resolution degradation in addition to count loss. On the other hand, in the case of dead time, the second pulse is lost without any energy degradation of the first pulse. Keeping the latest definitions in mind, it is legitimate to consider the source of counting losses in the case of Micromegas detectors which belong to the category of proportional gas counters.

For this purpose, the examination of the pulse height spectra of the Micromegas detectors is quite educational as well as of prime importance. In Figure 3.52a, the pulse height spectrum of a ^{235}U sample can be seen. Through the comparison of the dedicated pulse height spectrum with the parasitic one scaled to the number of protons for the same neutron energy region, it is observed that at higher counting rates (moving from parasitic to dedicated bunches), pulses that once were expected to lie around the two dominant humps are now recorded at higher amplitude channels. The same phenomenon is also observed in Figure 3.52b, for the case of a ^{238}U sample where the pulse height spectrum from the dedicated bunches is in fact distorted to a higher degree than in the case of ^{235}U sample. The reason lies in the higher counting rate, leading to a degradation of the resolution of the spectrum and a long tail of piled-up pulses. From this, it is understood that for the experimental condition of the present work (Micromegas coupled to Flash ADC), the pulse losses are attributed to the pile-up phenomenon.

To correct for the piled-up pulses in the analysis, a prototype method was developed based on the post-processing of spectral information and deconvolution of pile-up events, using the simulated energy deposition of the fission fragments from the GEF/GEANT4 Monte Carlo simulations. The systematic study of the experimental pulse height spectrum was focused into three individual amplitude ADC channel regions, as illustrated in Figure 3.53. In particular, in the first (I) region, the agreement of the experimental and simulated spectrum in these lower ADC channels is important, mainly for the determination of the amplitude cut correction factor. To achieve a nice reproduction of the low part of the amplitude spectrum, three control points were used to ensure that the final reconstructed integral of the spectrum is the same independently of the choice of the channel for the amplitude cut correction and that the possible differences in the integrals between these channel points are kept below 1%. The second (II) region is defined as the intermediate region from the end of the amplitude cut control points up to approximately the channel where the experimental spectrum ends in the absence of piled-up pulses. Even though in this region the simulation does not follow exactly the experimental distribution on a channel-by-channel basis, once more, the overall integral in both cases is kept the same. There are two main possible reasons that can explain this discrepancy. The first one is that the response function that was used for the conversion of the energy deposition of the

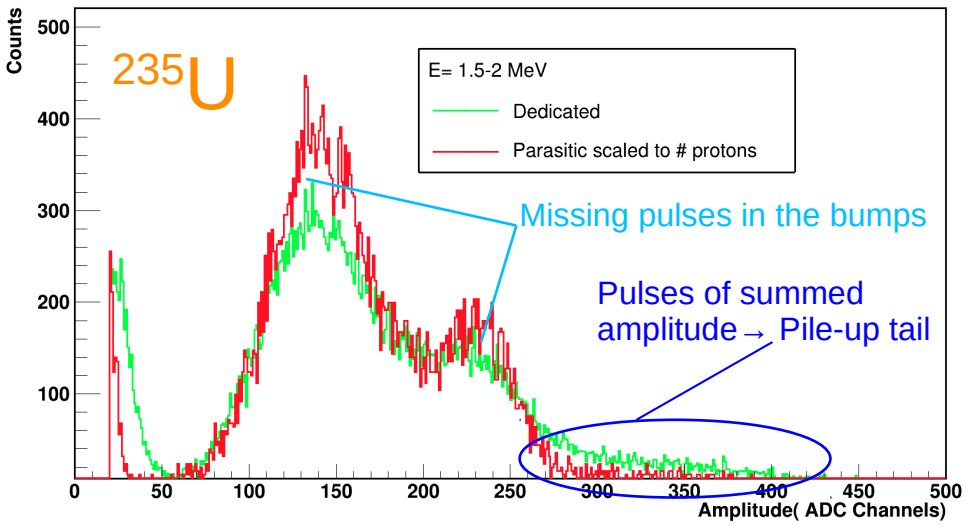

(a)

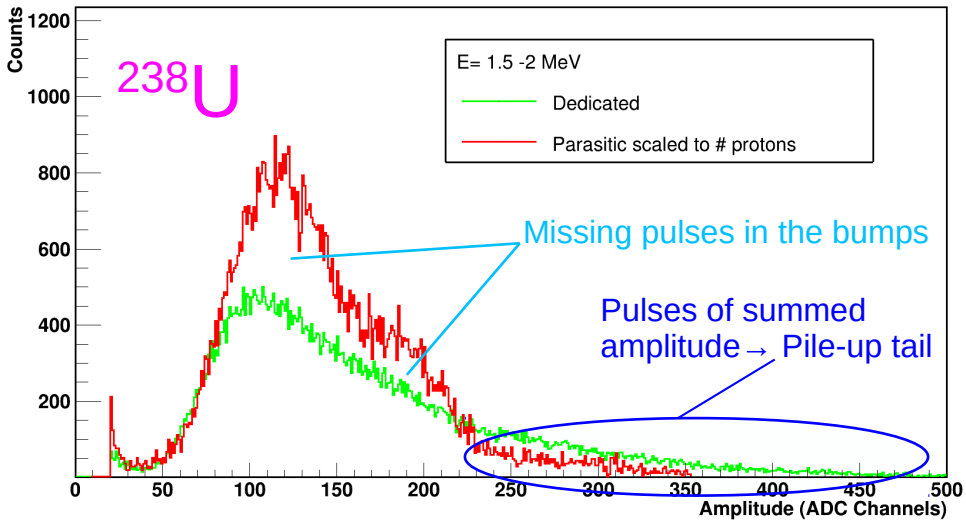

(b)

Figure 3.52: Experimental pulse height spectra of dedicated and parasitic bunches in the region of MeV for a case of (a) ^{235}U and (b) ^{238}U sample. The degradation of the energy resolution in the higher amplitude ADC channels is evident. At higher counting rates (dedicated bunches), the effect of the pile-up, appears as the moving of pulses from lower to higher ADC channels, therefore giving rise to a pile-up tail of pulses.

fission fragments to amplitude ADC channels is maybe not the ideal one, and the second reason lies in the fact that in the simulations the recombination of electrons during the transportation of ions through matter is not taken into account.

The third (III) and last region of study starts from the end of the second region and extends up to the end of the pulse height spectrum, covering the entire area of the overlapped pulses, otherwise known as "pile-up tail". In the third region, the integral between the simulated and experimental spectrum is kept the same as well. The overall goal is to actually estimate how many pulses have been piled-up and not just to calculate the simple integral below the "pile-up tail". The reproduction of the experimental spectrum with the simulation is considered successful when the shape of the lower part of the spectrum matches with the simulated one, the integrals of the individual above mentioned regions of study are almost identical and the "pile-up tail", if it exists, is nicely followed.

In practice, the technical overlapping of pulses in the simulated spectra requires the use of the distribution of the time difference of consecutive pulses, as recorded during the experiment. Prior to the conversion of the energy deposition to ADC channels, the simulated events are given a timestamp from a time distribution like the one that is illustrated in Figure 3.54. The simulated fission events are timestamped with random numbers that follow the above mentioned time distribution, in the time interval between [0,dt]. The dt value stands for the TOF bin width measured in ns, of the neutron energy region of the pulse height spectrum under study. Then, using a pile-up threshold value, the effect of pile-up is artificially created on an event-by-event basis by comparing the timestamps of the simulated fission events. Practically, this pile-up threshold value, which is set in the time interval between [0,dt), has no physical meaning, nonetheless the critical number is the ratio of the pile-up threshold value over the TOF bin width. In the comparison process, if the difference of the timestamp of two consecutive events is larger than the pile-up threshold value, then the two events are considered separate, as is their energy deposition in the simulated spectrum. If on the other hand, the difference of the timestamp of the two consecutive events is lower than the pile-up threshold value, then the events are considered as one and their energy deposition is summed, using a uniform distribution, before converting to ADC channels. Additionally, by observing the end of the "pile-up tail" in the experimental spectrum, multiple pile-up threshold values can be defined in order to mimic 1^{st}, 2^{nd} and 3^{rd} order degree of pile-up. Therefore, meaning to have an already piled-up pulse, piled-up with an other one and goes on. As expected, the higher the counting rate in an experimental spectrum of a specific energy range, the higher the degree of pile-up that should be adopted for a better reproduction of the spectrum.

With this method, the actual number of fission events that have been piled-up were estimated and finally the corresponding neutron energy dependent correction for the counting losses was retrieved. An example of this whole process for the case of an ^{238}U sample, is demonstrated in Figures 3.55 and 3.56, where the simulated spectra are compared with the experimental ones in an extended neutron energy range spanning from 0.5 to 6.5 MeV.

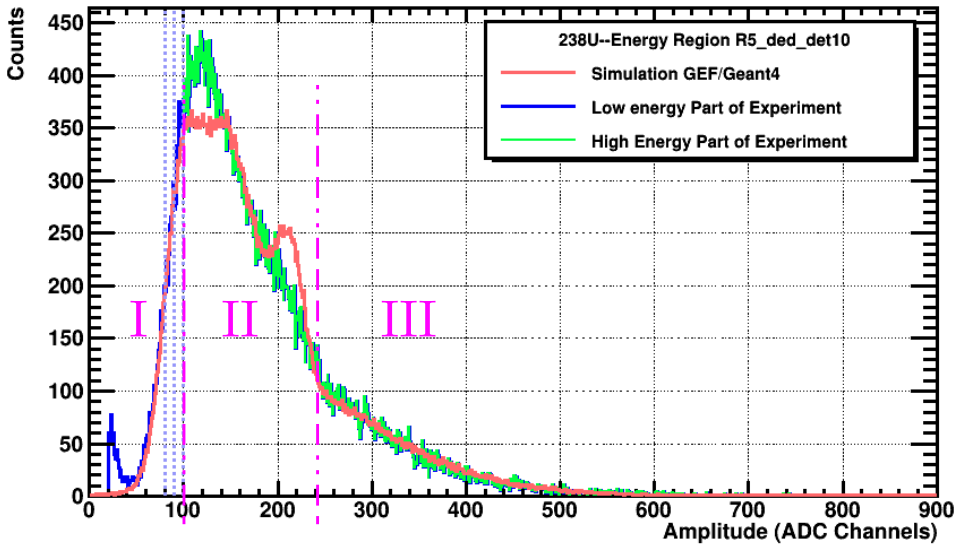

(a)

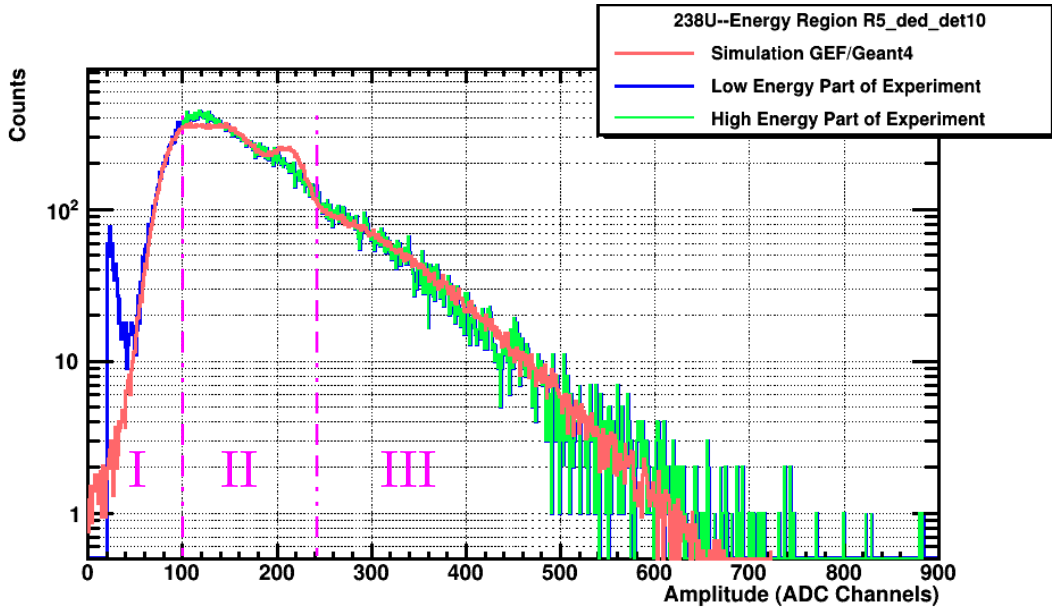

(b)

Figure 3.53: (a) Linear and (b) logarithmic view of the same pulse height spectrum divided in three regions of study.

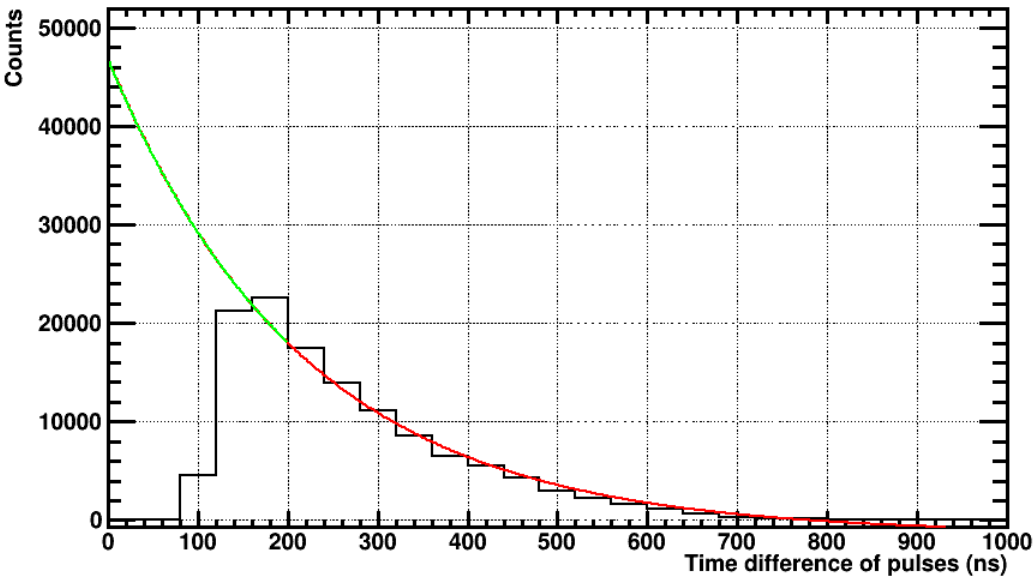

Figure 3.54: Time difference of consecutive pulses for the range from 200 keV to 10 MeV neutron energy.

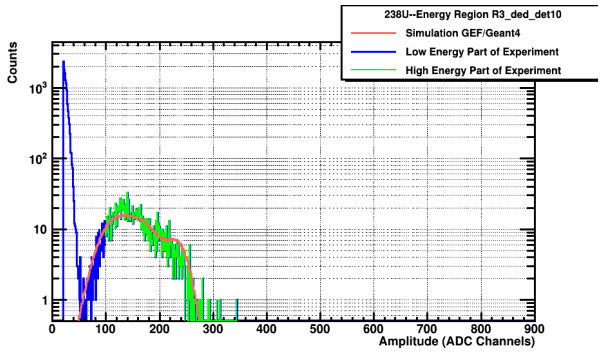

(a) $E_n = 0.5 - 1\,MeV$, Pile-up = 0%

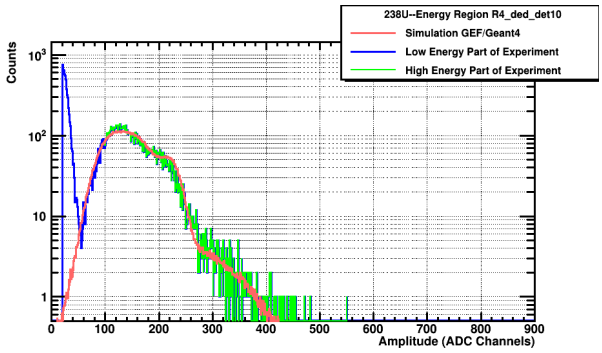

(b) $E_n = 1 - 1.5\,MeV$, Pile-up = 7%

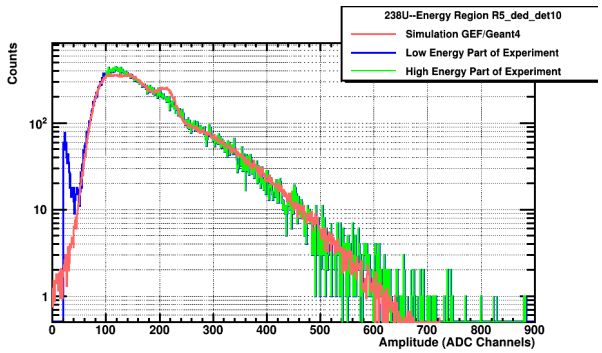

(c) $E_n = 1.5 - 2\,MeV$, Pile-up = 37%

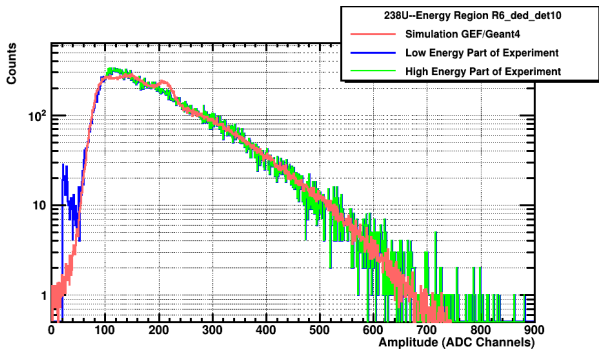

(d) $E_n = 2 - 2.5\,MeV$, Pile-up = 49%

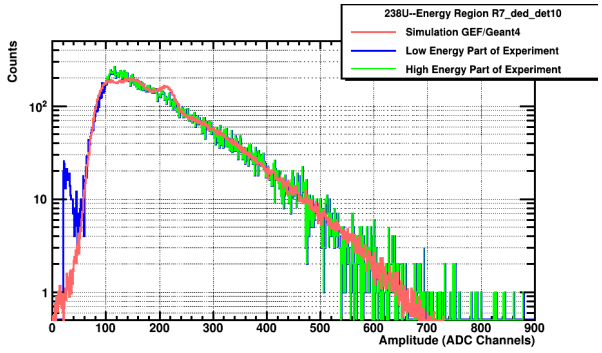

(e) $E_n = 2.5 - 3\,MeV$, Pile-up = 46%

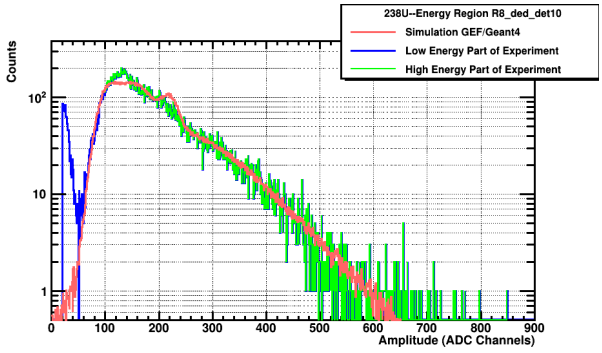

(f) $E_n = 3 - 3.5\,MeV$, Pile-up = 38%

Figure 3.55: Simulated pile-up reconstruction in pulse height spectra of ^{238}U for various neutron energies spanning from 0.5 to 3.5 MeV.

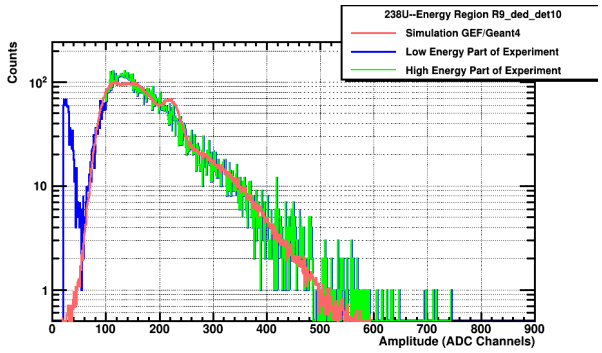

(a) $E_n = 3.5 - 4\,MeV$, Pile-up = 31%

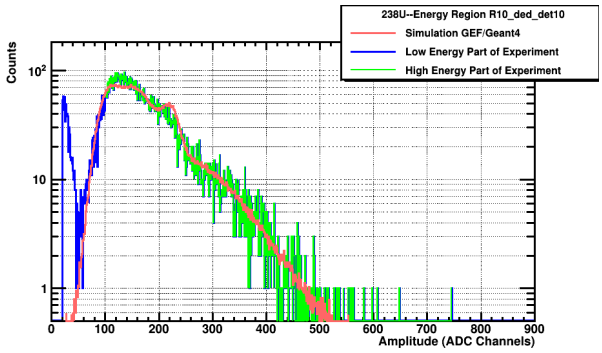

(b) $E_n = 4 - 4.5\,MeV$, Pile-up = 29%

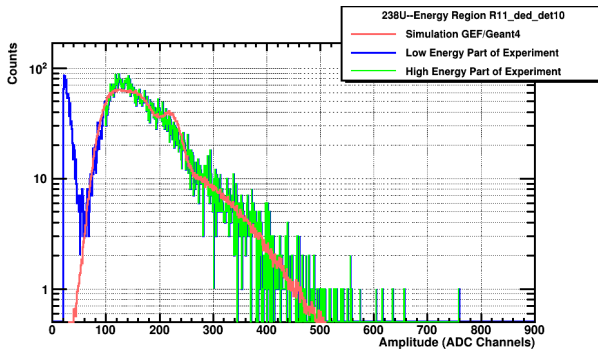

(c) $E_n = 4.5 - 5\,MeV$, Pile-up = 26%

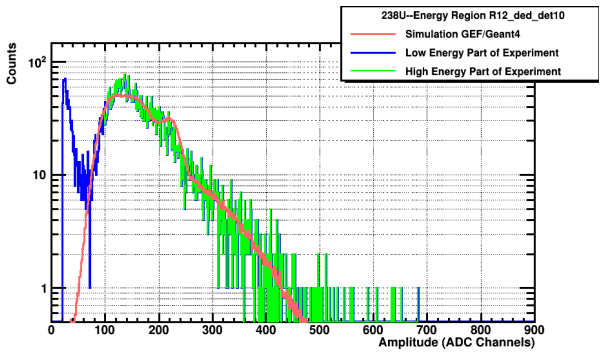

(d) $E_n = 5 - 5.5\,MeV$, Pile-up = 25%

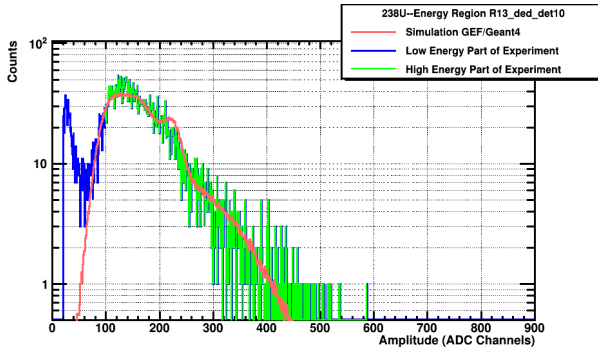

(e) $E_n = 5.5 - 6\,MeV$, Pile-up = 24%

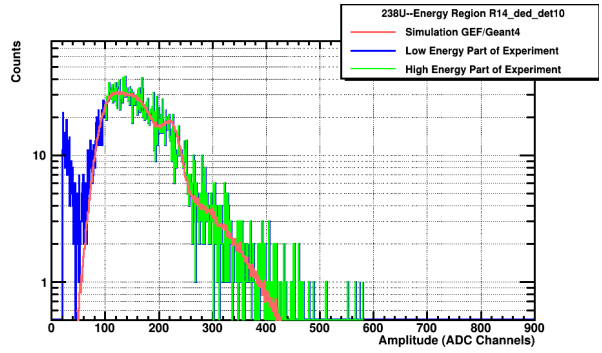

(f) $E_n = 6 - 6.5\,MeV$, Pile-up = 21%

Figure 3.56: Simulated pile-up reconstruction in pulse height spectra of ^{238}U for various neutron energies spanning from 3.5 to 6.5 MeV.

Chapter 4

Experimental Results

After the detailed analysis procedure described in the previous chapter, the cross section of the reaction under study is calculated by applying the necessary corrections to the measured fission fragment yields.

4.1 Cross section calculation

The ^{241}Am(n,f) cross section is calculated relative to the ^{235}U(n,f) cross section for each energy bin, according to the formula:

$$\sigma(E_n) = \frac{N(E_n)}{N^{ref}(E_n)} \cdot \frac{\epsilon}{\epsilon^{ref}} \cdot \frac{f_{amp}(E_n)}{f^{ref}_{amp}(E_n)} \cdot \frac{f_{pu}(E_n)}{f^{ref}_{pu}(E_n)} \cdot \frac{f_{cont}(E_n)}{f^{ref}_{cont}(E_n)} \cdot \frac{n^{ref}}{n} \cdot \sigma^{ref}(E_n) \tag{4.1}$$

In Equation 4.1, N are the recorded counts in the fission fragment yield distributions, ϵ is the Micromegas efficiency which takes into account the fraction of fission fragments that do not manage to enter the Micromegas gas volume, f_{amp} is the correction factor for the amplitude cut, f_{pu} is the correction factor for pile-up, f_{cont} is the contribution for the contaminants in the samples and n are the areal densities of the samples. The quantities corresponding to the reference sample, which in this case is ^{235}U, are referred to with the subscript "ref". Additionally, the number of nuclei per barn in the samples is calculated from the following equation:

$$n\left[\frac{nuclei}{b}\right] = 10^{-24}\frac{N_A \cdot \rho_A}{A_r} \tag{4.2}$$

where N_A is the Avogadro number, ρ_A is the known areal density in gr/cm^2 and A_r is the atomic weight.

4.2 Results

The cross section determination of the ^{241}Am(n,f) reaction was performed relative to the ^{235}U(n,f) reference reaction for the neutron energy region of 9 meV up to 6 MeV. Unfortunately, the ^{238}U samples could not be used as reference due to the extreme counting rate that caused issues both in the systematic identification and subtraction of the γ-flash pulse, as well as in the accurate detection of the fission signals in the MeV neutron range. The results of the fission measurement performed in EAR-2 of the n_TOF facility at CERN are presented in Figure 4.1. In Figure 4.2 the comparison of the experimental cross section data with the evaluated libraries ENDF/B-VIII.O [46] and JEFF-3.3 [47] is displayed. The data are presented using an isolethargic binning of 100 bpd in the axis of neutron energy.

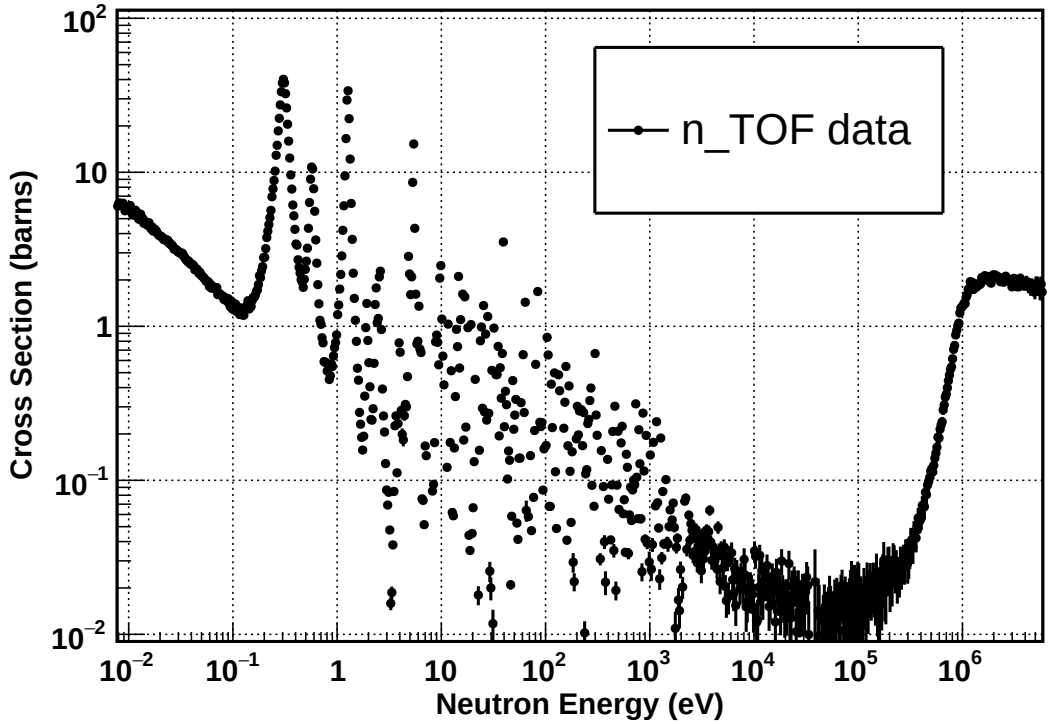

Figure 4.1: Experimental cross section data of the present work for the ^{241}Am(n,f) reaction spanning from 9 meV up to 6 MeV. The data are plotted in isolethargic binning of 100 bpd in the energy axis. The errors shown in the figure are attributed only to the statistical uncertainty.

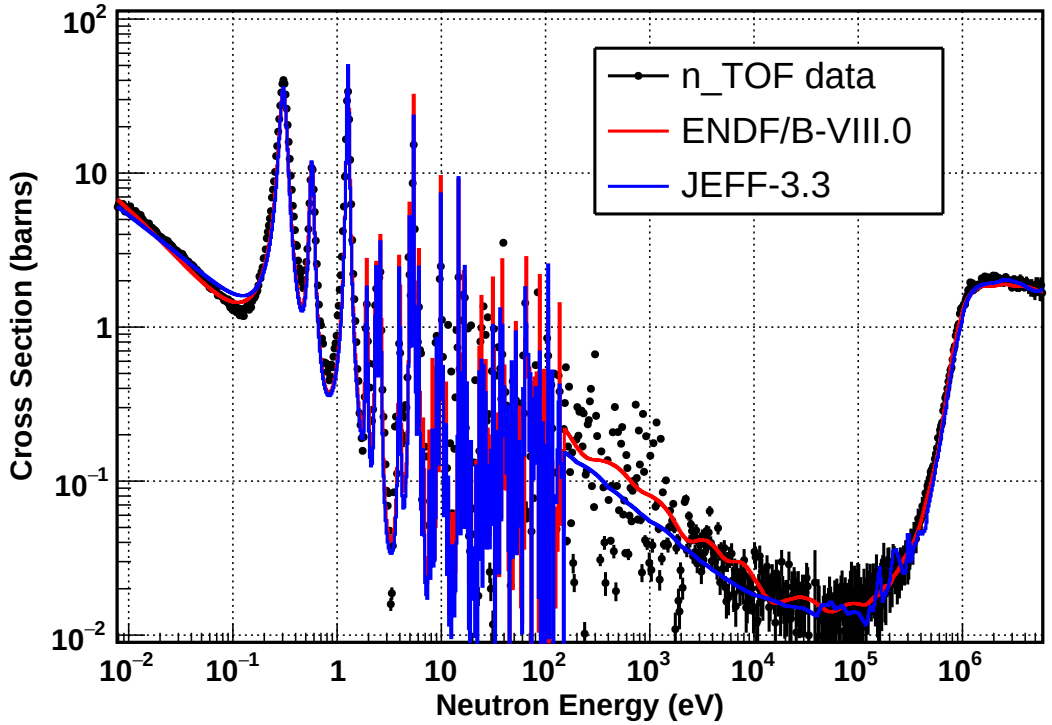

Figure 4.2: Comparison of the experimental cross section data of the present work for the ^{241}Am(n,f) reaction with the evaluated libraries ENDF/B-VIII.O and JEFF-3.3. The data are plotted in isolethargic binning of 100 bpd in the energy axis. The errors shown in the figure are attributed only to the statistical uncertainty.

The experimental cross section data in the first three resonances of the ^{241}Am(n,f) reaction against the above mentioned evaluated libraries are presented in Figure 4.3. The n_TOF data seem to follow the general shape of the resonance structures. The broadening of the first resonance may be attributed to the quality of simulations for the resolution function of EAR-2 during Phase-III of n_TOF. Additionally, the cross section data at the threshold of the reaction are in agreement with the evaluations, while in the fission plateau, the maximum deviation of the data with respect to the evaluations is $< 10\%$ in the energy range 1.2 to 2.5 MeV. Figure 4.4 illustrates the cross section of ^{241}Am fission reaction from 0.1 to 6 MeV incident neutron energy.

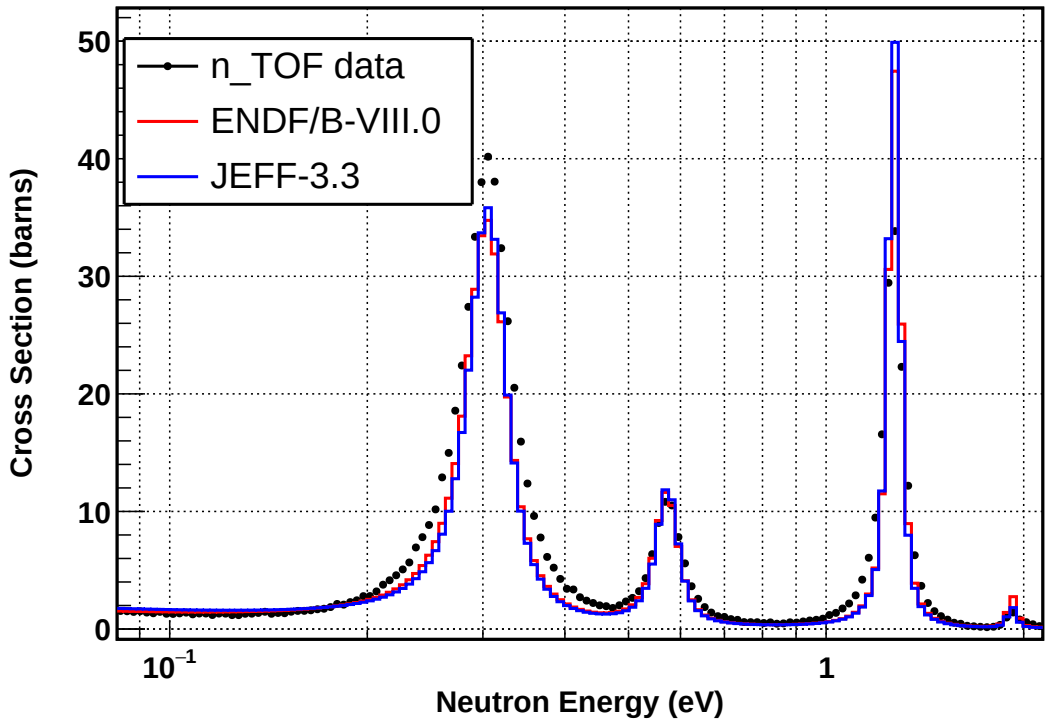

Figure 4.3: Comparison of the experimental cross section data of the present work for the ^{241}Am(n,f) reaction with the evaluated libraries ENDF/B-VIII.O and JEFF-3.3, showing the first three dominant resonances above the neutron separation energy. The errors shown in the figure are attributed only to the statistical uncertainty.

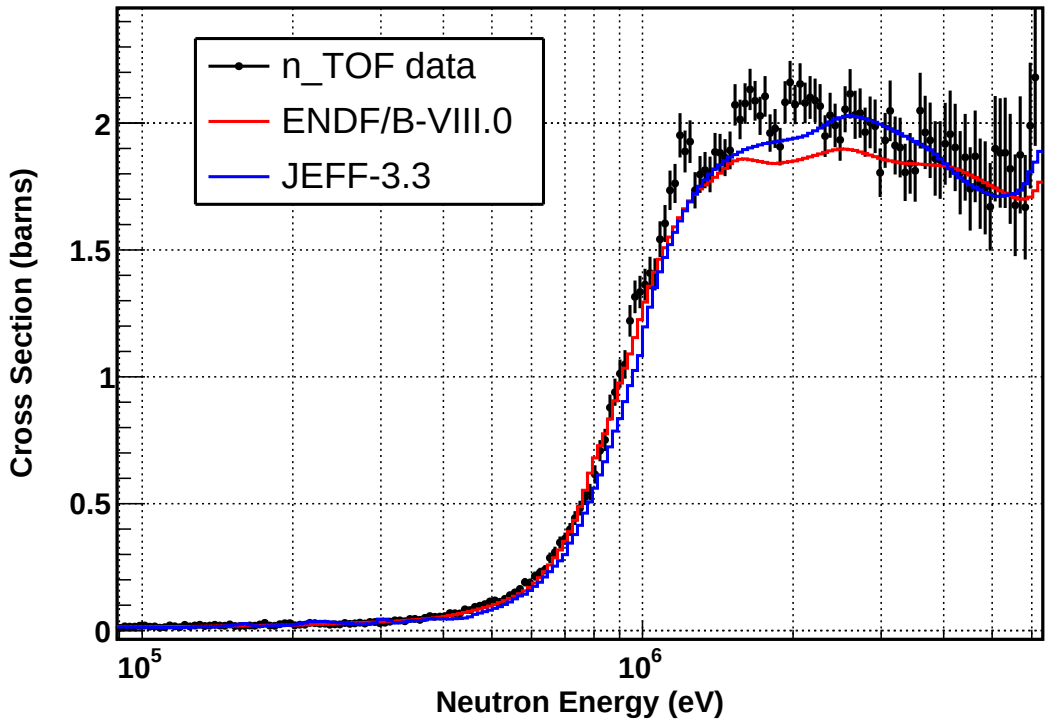

Figure 4.4: Comparison of the experimental data of the present work for the ^{241}Am(n,f) nuclear reaction with the evaluated libraries ENDF/B-VIII.O and JEFF-3.3, in the threshold and plateau of the reaction covering the neutron energy region from 100 keV up to 6 MeV. The data are plotted in isolethargic binning of 100 bpd in the energy axis. The errors shown in the figure are attributed only to the statistical uncertainty.

In the resonance region, the cross section results of the ^{241}Am(n,f) reaction of this work along with previous data sets are presented in Figure 4.5. In the threshold and the plateau of the fission reaction, the same comparison is depicted in Figure 4.6. The data of this work nicely follow the cross section values of the previous works in the threshold of the reaction. In the plateau, the largest deviation from the previous data is observed between 1.5 and 2.5 MeV and is less than 10%. Following the onset of second-chance fission, as can be seen in Figure 4.7, due to the lack of experimental data, the evaluations show significant discrepancies between them.

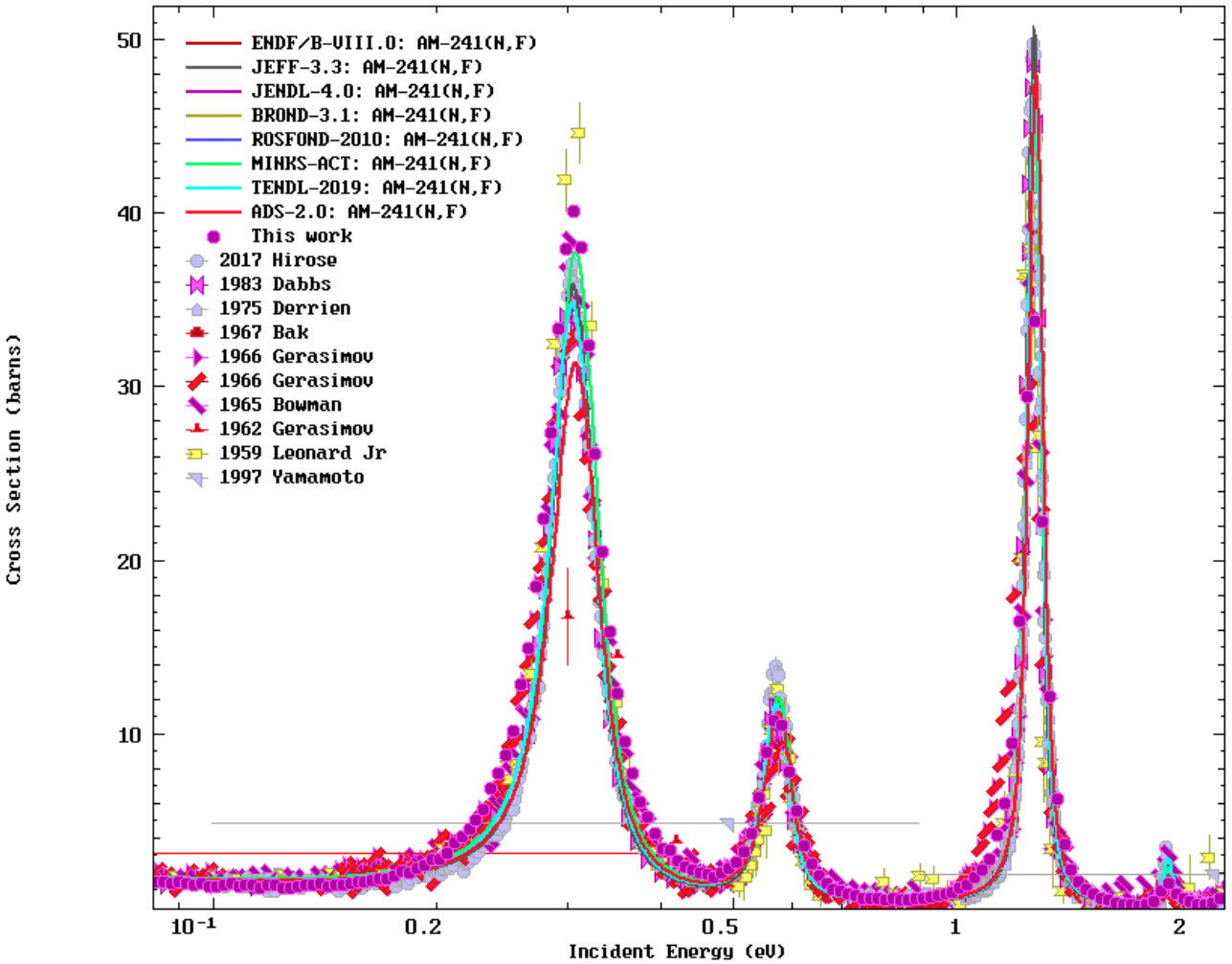

Figure 4.5: Comparison of the experimental data of the present work (magenta circle) for the ^{241}Am(n,f) nuclear reaction with other experimental data retrieved from the EXFOR database, for the first three resonances.

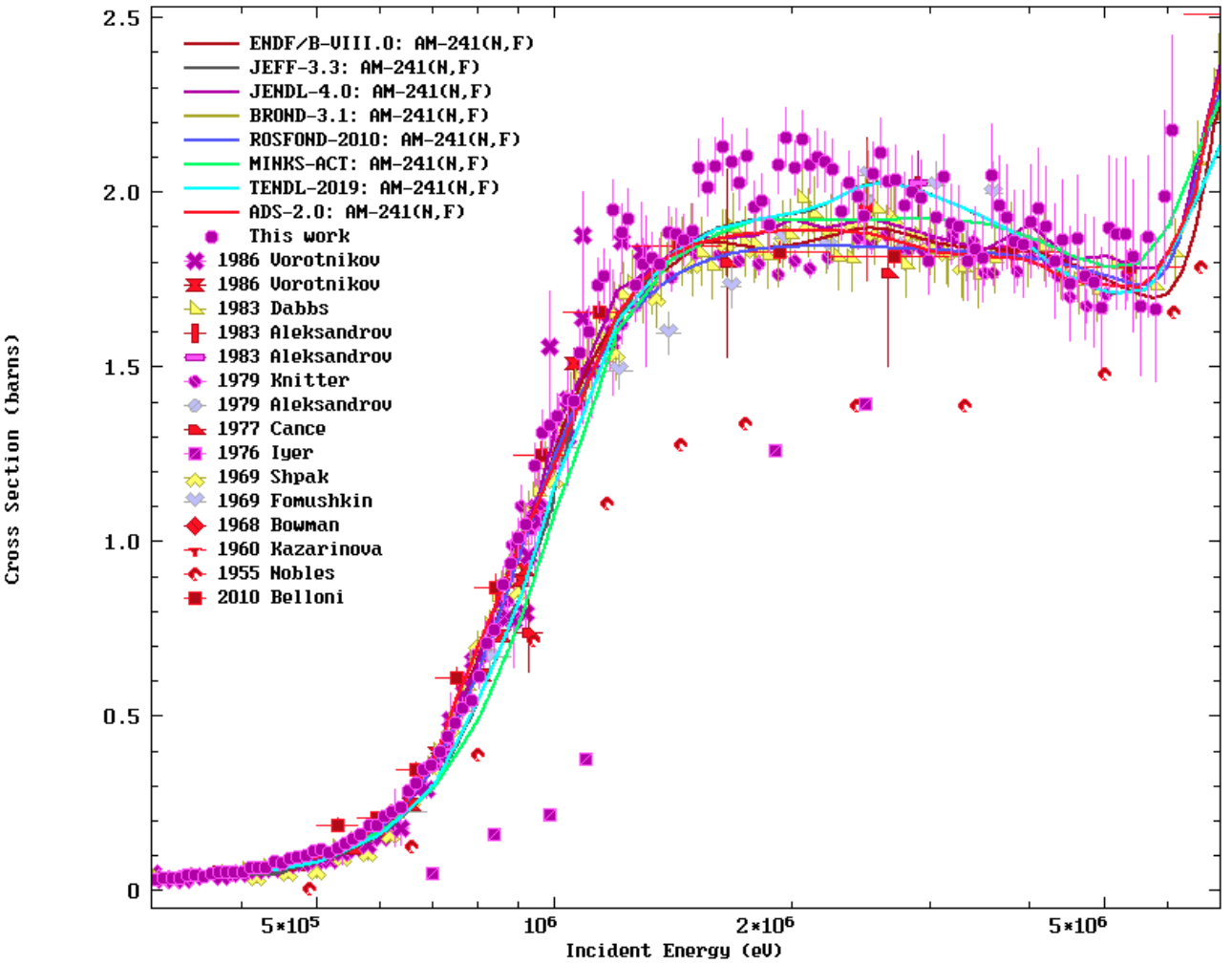

Figure 4.6: Comparison of the experimental data of the present work (magenta circle) for the ^{241}Am(n,f) nuclear reaction with other experimental data retrieved from the EXFOR database, in the threshold and plateau of the fission reaction.

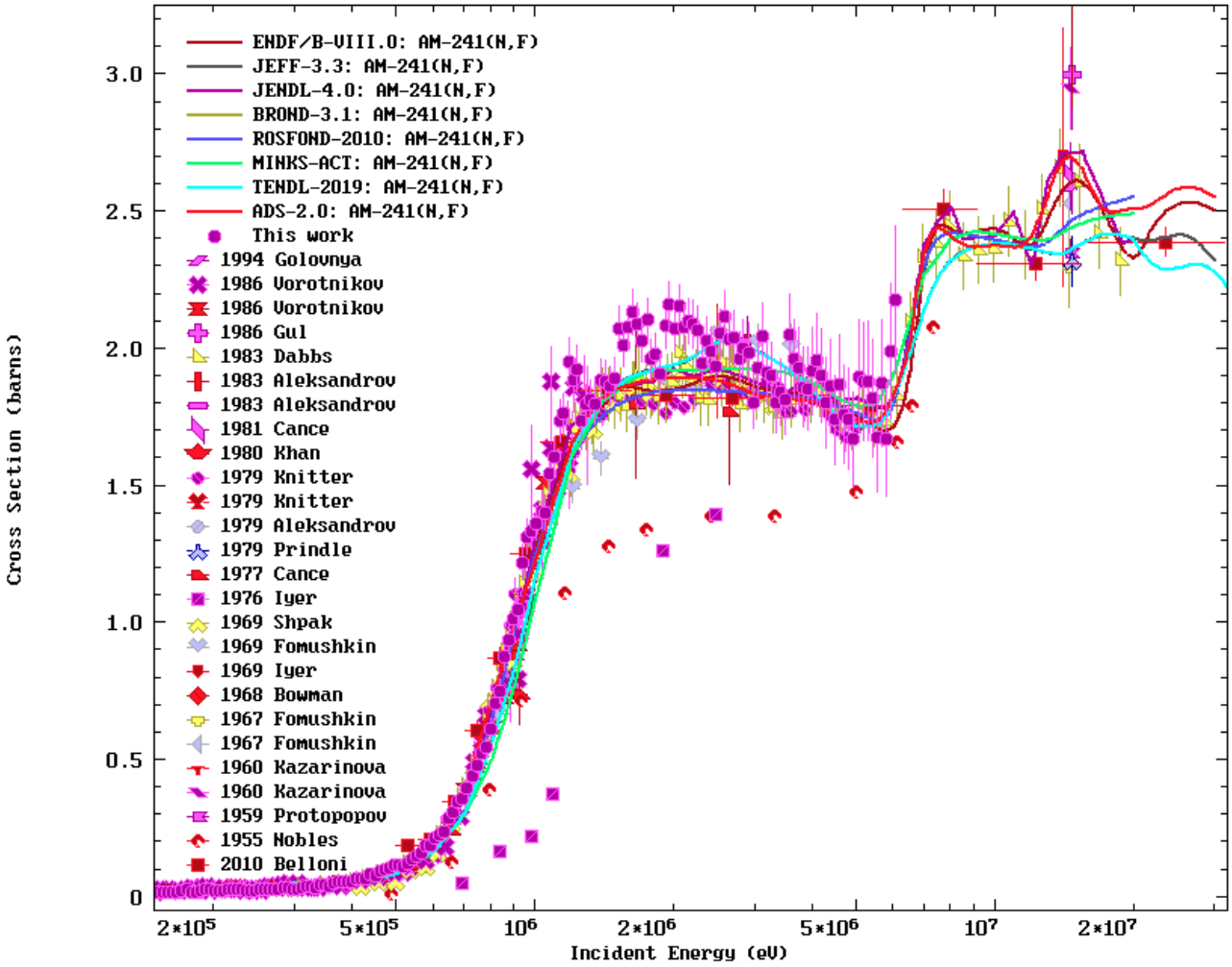

Figure 4.7: Experimental data retrieved from the EXFOR database, covering the neutron energy region from 0.4 to 30 MeV along with the available evaluated libraries.

The statistical uncertainty of the ^{241}Am(n,f) cross section is shown in Figure 4.8 for the neutron energy range of $0.2 - 6\,MeV$ which was the region of interest for this experimental work. The results are related to the binning choice of the energy axis which is 100 bpd. With the selection of a coarser energy bin, the statistical uncertainty would improve with a price paid in the energy resolution. The systematic uncertainties of the measurement are listed in Table 4.1 and include the uncertainty in the samples' mass as reported from the manufacturers, the detector efficiency calculated from the simulations performed with the combination of GEANT4 and GEF, the amplitude cut and pile-up corrections and the uncertainty in the fission cross section of ^{235}U that was used as reference reaction and was retrieved from the ENDF/B-VIII.0 evaluated library. The uncertainties in the amplitude cut corrections were estimated with sensitivity studies by altering the response function used for the conversion of the fission fragments' energy deposition to ADC amplitude channels, while the pile-up correction uncertainty was estimated by changing the multiplicity of the pile-up in the simulations so as to achieve a reasonable fit with the recorded experimental spectra.

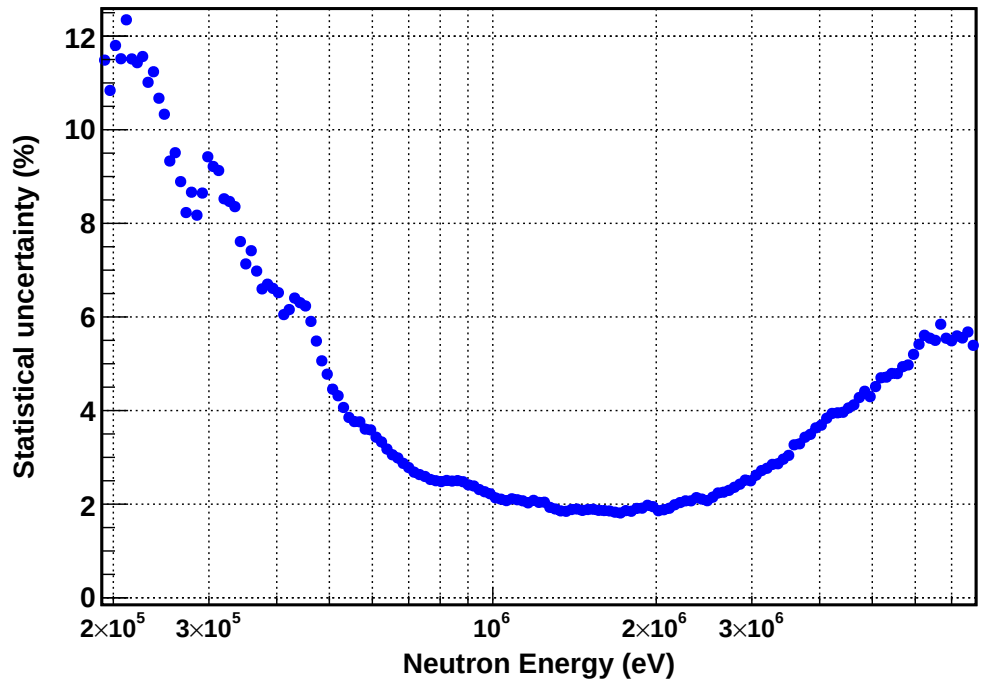

Figure 4.8: Statistical uncertainty of the ^{241}Am(n,f) cross section measurement for energies higher than 0.2 MeV in isolethargic binning of 100 bpd.

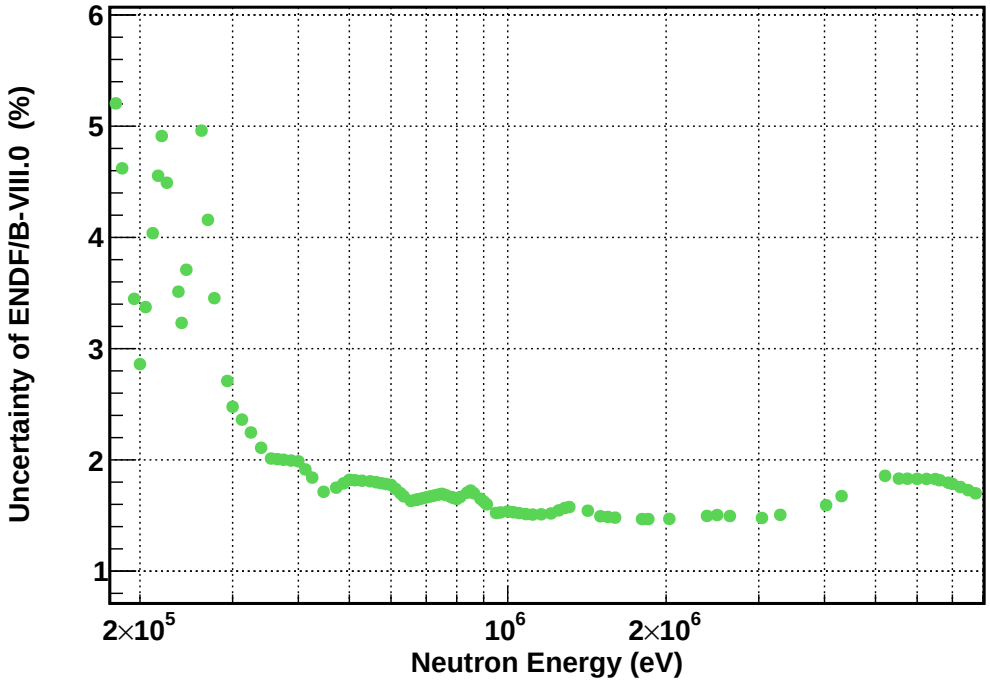

Figure 4.9: Uncertainty in the ^{235}U(n,f) reaction's cross section from ENDF/B-VIII.0 [46], which was used as reference for the calculation of ^{241}Am(n,f).

Contribution	**Uncertainty** (%)	
	^{241}Am	**^{235}U**
Sample mass	< 1.5	< 3
Detector efficiency	negligible	
Amplitude cut correction	< 3	
Pile-up correction	< 4	
^{235}U cross section	< 2	

Table 4.1: Systematic uncertainties of the cross section calculation of ^{241}Am(n,f) reaction for the neutron energy range $0.2 - 6\,MeV$.

Chapter 5

Theoretical Fission Cross Section Calculations

In this chapter, an overview of the theory of nuclear fission process is given, aiming to achieve a smoother transition to the theoretical framework in which the ^{241}Am(n,f) reaction was studied. A theoretical investigation of the ^{241}Am(n,f) reaction cross section was performed using the TALYS code in order to reproduce the experimental results of the present work in addition to the previous experimental data. Accordingly, in the theoretical calculations various fission parameters of Americium isotopes were adjusted, such as the fission barriers and widths along with the level density parameters of the corresponding nuclei.

5.1 Nuclear fission

5.1.1 Discovery of fission

In 1938, a group of scientists proved the Greek philosophers wrong, by dividing the atom, that originates from the Greek word "άτομο", meaning "that which cannot be divided". The discovery of fission owes much to the discovery of neutron by James Chadwick [48] back in 1932. In the following period, neutrons were used as a probe to bombard natural Uranium with the aim of producing heavier elements. In 1943, Enrico Fermi [49] after a series of such experiments, produced what he believed that were the first transuranic elements after Uranium. At that time, it was thought that hitting a large nucleus like Uranium with a neutron, could induce only minor changes. Following Fermi's work, in 1938, the radiochemists Otto Hahn and Fritz Strassmann, also bombarded Uranium and other elements with neutrons and began identifying the series of decay products. After careful chemical analysis, they concluded that they detected radioactive barium isotopes, which have an atomic number 56, and other fragments of Uranium itself. Their discovery raised vigorous doubts since it hinted that Uranium nucleus was deformed greatly and ended up splitting into roughly two equal pieces.

Hahn shared their findings with his former physicist colleague Lise Meitner, who together with Otto Frisch, her nephew and also a physicist, explained the nuclear process involved. Meitner and Frisch, suggested that the nucleus resembles a liquid drop, following the idea of the Russian physicist George Gamow [50] that was also embraced by Niels Bohr. As a proposed mechanism, it was assumed that as the Uranium nucleus becomes elongated, it starts to pinch in the middle up to the point where it eventually splits into two smaller "drops". Meitner calculated that the product nuclei of Hahn and Strassmann would have less mass, as their

experimental findings also indicated that the daughter nuclei weighted less than the initial Uranium, and that due to their mutual repulsion they would carry approximately 200 MeV. Her calculations were confirmed using the famous formula $E = mc^2$ of Albert Einstein, that showed that the detected mass loss from the splitting process should have been converted into kinetic energy of the new fragments. Frish, borrowing the term of cell division from biology "binary fission", named the newly discovered nuclear process "fission". Meitner and Frish [51, 52] published their paper in Nature in January of 1939, while the two radiochemists published their findings separately [53]. After the discovery of fission, the scientific community focused on exploiting the potential of the particular nuclear reaction. Considering the fact that through the splitting of heavy nuclei additional neutrons were emitted along with the release of enormous amounts of energy, the idea of a controlled "self-sustained chain reaction" would make it possible to generate tremendous amounts of energy for heat and power while on the other hand an "uncontrolled reaction" would lead to a destructive violent energy release, known as "atomic bomb". The scientific community of 1944 awarded solely Otto Hahn the Nobel Prize in Chemistry, "for his discovery of the fission of heavy nuclei", without recognizing Meitner's contribution and her tremendous role in the discovery of fission.

Following the discovery of fission, Niels Bohr and John Archibald Wheeler [54] formulated the theoretical description of fission, based on the Liquid-Drop Model (LDM), which until today remains the basis for understanding the fission mechanism. The nuclear fission process is discussed in depth by Robert Vandenbosch and John Robert Huizenga [55] and Cyriel Wagemans [56], while fission in the context of statistical models is discussed by Andrew John Cole [57].

5.1.2 The nuclear fission mechanism

Nuclear fission in heavy nuclei results from the competition between the nuclear and Coulomb forces. As a physical process, fission can either occur as a natural decay spontaneously or be induced through the absorption of a light particle, for instance a neutron or a photon. In the latter scenario, excited states in the created compound nucleus can be reached, overcoming or penetrating the Coulomb barrier to fission, as long as the excitation energy of the system is high enough. As illustrated in Figure 5.1, for a heavy nucleus like ^{238}U the binding energy is about 7.6 MeV per nucleon, whereas for two fragments in the mass region around $A = 119$ the binding energy is approximately 8.5 MeV per nucleon. Therefore, it is energetically preferable for the Uranium nucleus to fission since the system will move to a more strongly bound condition. Additionally, the difference from the binding energy of the above mentioned systems, as will be discussed latter, is expressed as a release of energy that accompanies any nuclear fission reaction.

The binding energy can be expressed through a semiempirical mass formula that includes contributions from the liquid-drop model that treats gross collective characteristics of nuclei considering the latest as a drop of liquid, as well as the shell model which deals with individual nucleons. The semiempirical formula of nuclear binding energy is:

$$\begin{aligned} E_B =& E_V + E_S + E_C + E_{SYM} + E_{PAIR} \\ =& \alpha_V \cdot A - \alpha_S \cdot A^{2/3} - \alpha_C \cdot Z(Z-1) \cdot A^{-1/3} - \alpha_{sym} \cdot \frac{(A-2Z)^2}{A} + \delta \end{aligned} \tag{5.1}$$

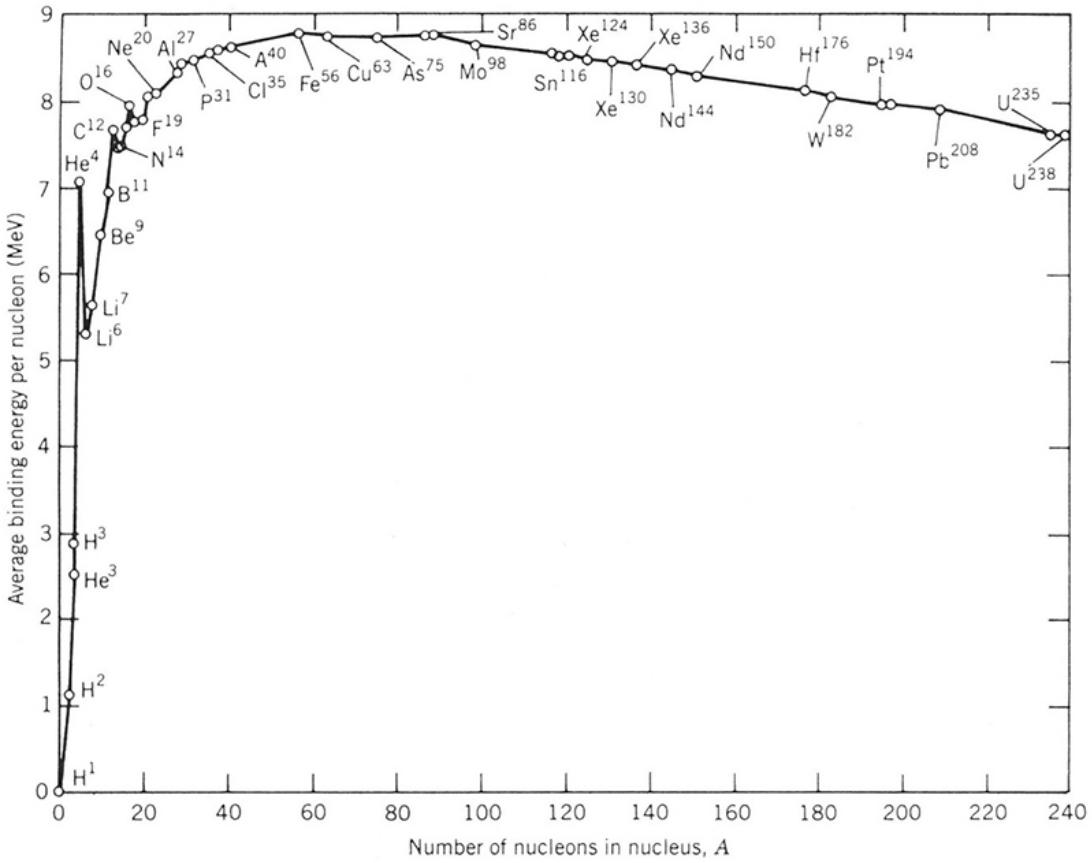

Figure 5.1: Binding energy per nucleon as a function of the mass number A.

where the pairing energy δ is expressed as:

$$\delta = \begin{cases} +\alpha_P \cdot A^{-3/4} & \text{, for Z and N even} \\ -\alpha_P \cdot A^{-3/4} & \text{, for Z and N odd} \\ 0 & \text{, for A odd} \end{cases} \tag{5.2}$$

A set of constants that reproduces with a good agreement the experimental data lies in the choice of $\alpha_V = 15.5\,MeV$, $\alpha_S = 16.8\,MeV$, $\alpha_C = 0.72\,MeV$, $\alpha_{sym} = 23\,MeV$ and $\alpha_P = 34\,MeV$ [58]. In the formula of the binding energy, the first term is called "volume term" and suggests that each nucleon attracts only its closest neighbors and not all of the other nucleons. The second term is called "surface term" and accounts for the nucleons on the surface of the nucleus that are surrounded be fewer neighbors than the nucleons on the center and therefore are less tightly bound. This is the reason that this term has a negative sign. The third term introduces the Coulomb repulsion of the protons and implies a reduction in the binding energy as well. The fourth term is called "symmetry term" and tends to make the nucleus symmetric in neutrons and protons favoring nuclei with $Z = A/2$. This term is meaningful for light nuclei whereas its importance is reduced for heavier nuclei since due to the Coulomb repulsion, the number of neutrons required increases rapidly in order to achieve nuclear stability. The last term of the binding energy formula is the "pairing term" and treats the tendency of nucleons to couple pairwise to specially stable configurations. The pairing term is of significant importance for explaining the extreme differences that are observed in the fissionability of Uranium and

actinides, since the excitation energies can be raised or lowered when the effect of pairing is taken into account.

A nucleus ready to fission can be considered as an initially spherical nucleus that is gradually stretched. Even though the total volume of the deformed nucleus remains constant through this stretching procedure, on the contrary the surface and Coulomb terms will definitely be affected. The stretched nucleus can be represented as an ellipsoid with a volume $V = 4/3\pi\alpha\beta^2$, where the semimajor axis α and semiminor axis β can be expressed as a function of the spherical radius R and the eccentricity of the ellipse ϵ as follows:

$$\alpha = R(1+\epsilon) \tag{5.3}$$

$$\beta = R(1+\epsilon)^{-1/2} \tag{5.4}$$

Additionally, the surface area of an ellipsoid using the two above mentioned axes of symmetry can be written as:

$$S \approx 4\pi \sqrt[p]{\frac{2\cdot\alpha^p\beta^p + \beta^p\beta^p}{3}} \tag{5.5}$$

with $p = 8/5$. Combining equations 5.3, 5.4 and 5.5 and performing a Taylor expansion to keep terms up to the second order, the following result is obtained concerning the distortion of the initial sphere into an ellipsoid:

$$S = 4\pi R^2(1 + \frac{2}{5}\epsilon^2 - ...) \tag{5.6}$$

Similarly but through a more complicated procedure, it can be shown that the Coulomb term of the binding energy formula is expanded as $(1 - \frac{1}{5}\epsilon^2 + ...)$. Consequently, the decrease in the binding energy between a spherical nucleus and an ellipsoid of the same volume is calculated as:

$$\begin{aligned}\Delta E =& B(\epsilon) - B(\epsilon = 0)\\ =& -\alpha_S \cdot A^{2/3}(1 + \frac{2}{5}\epsilon^2 - ...) - \alpha_C \cdot Z(Z-1)\cdot A^{-1/3}(1 - \frac{1}{5}\epsilon^2 + ...)\\ &+ \alpha_S \cdot A^{2/3} + \alpha_C \cdot Z(Z-1)\cdot A^{-1/3}\\ =& (-\frac{2}{5}\alpha_S \cdot A^{2/3} + \frac{1}{5}\alpha_C \cdot Z(Z-1)\cdot A^{-1/3})\epsilon^2\end{aligned} \tag{5.7}$$

If the second term is larger than the first one then the nucleus gains energy through deformation. It is therefore considered unstable against stretching and it will eventually fission spontaneously. The critical value above which fission occurs instantly (when $E_C/2E_S > 1$) is calculated as:

$$\frac{Z^2}{A} > 47 \tag{5.8}$$

In the case of ^{241}Am the value of $\frac{Z^2}{A}$ is 37.5. Subsequently, the parameter that defines the "fate" of a nucleus with respect to the fission probability shortly after its creation is the "fissility parameter x" that is defined accordingly as:

$$x = \frac{E_C}{2E_S} \tag{5.9}$$

5.1.3 Double-humped fission barrier

The macroscopic approach of the liquid-drop model (LDM) fails to describe various related observables, such as the observed asymmetric mass distributions of fission fragments, the correct prediction of experimental barrier heights and the existence of fission isomers, which are all connected with shell effects. In 1966, Vilen Mitrofanovich Strutinsky [59–61] introduced a shell correction to the liquid-drop model, resulting in a hybrid macroscopic-microscopic approach. According to Strutinsky's shell correction method (SCM), the semiempirical mass formula of Equation 5.1, can be expanded as follows:

$$E_B = E_{LMD} + E_{SHELL} \tag{5.10}$$

with

$$E_{SHELL} = \delta U = U - \tilde{U} \tag{5.11}$$

where U is the sum of the single-particle energies for a given deformation β of an average potential and $\tilde{U}$ is calculated under the assumption of a uniform distribution of level densities. The added shell correction term modified the potential dependency with respect to the deformation evolution of the nucleus, introducing oscillations that result in the formation of a "double-humped fission barrier".

The concept of the double-humped fission barrier of actinide nuclei is discussed in detail by Bjørnholm and Lynn [62]. The double potential well that appears in the Strutinsky picture of the deformation energy is graphically illustrated in Figure 5.2b, while for comparison purposes Figure 5.2a shows a liquid-drop model single-humped barrier without shell corrections. In Figure 5.2b, states in the first well that correspond to the ground state are called "Class-I" states and are dense and narrow, whereas states in the second well that belong to the "fission isomeric (or metastable) excited states" are called "Class-II" states and are broader and more widely spaced. Furthermore, the states on the top of the barriers are called "intrinsic" or "transition" states. A significant difference of the double-humped fission barrier compared to the liquid-drop model picture, is that nuclear fission can take place even if the nucleus is not excited above the fission barrier. In the case where the nucleus is excited above the bottom of the well between the two humps, fission can occur through the penetration of the corresponding fission barriers. Additionally, the double-humped fission barrier offered a theoretical explanation of the experimentally observed fission isomeric states, which are long-lived vibrational excited states that also undergo fission with a higher fission probability compared to the ground states. These states of the second potential well that are found typically at excitation energies around $2 - 3\,MeV$, have the possibility to either decay by fission through a relatively thin barrier or by γ-emission back to the ground state.

Furthermore, the picture of the double-humped fission barrier decoded the appearance of fission resonances that tend to cluster in well-separated groups. Fission resonances occur when states from the first well match in energy and in spin-parity with states from the second well and as a result the fission probability escalates. This effect on the cross section of ^{241}Am is depicted in Figure 5.3, where resonance structures in the energy region between 0.1 and $100\,eV$ are shown. The individual resonances that emerge up to approximately $2\,eV$ are attributed solely to excited states from the first potential well (Class-I states) since the second well is not so deep as the first one. Later on, the observed resonances in the fission excitation function are formed as a result of the coupling of the dense Class-I states and the narrower Class-II states. The

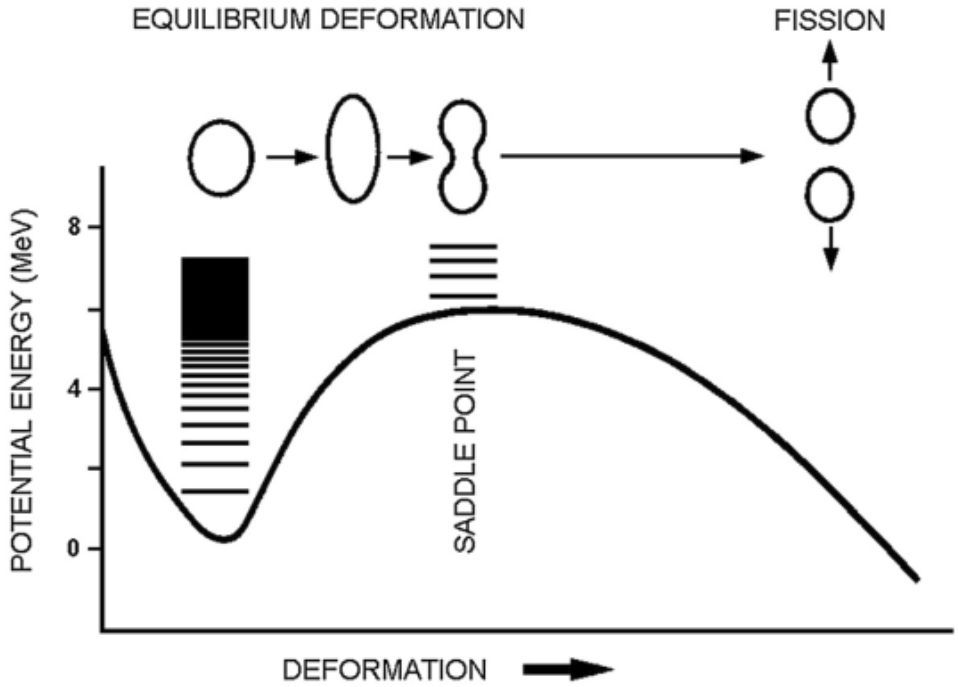

(a)

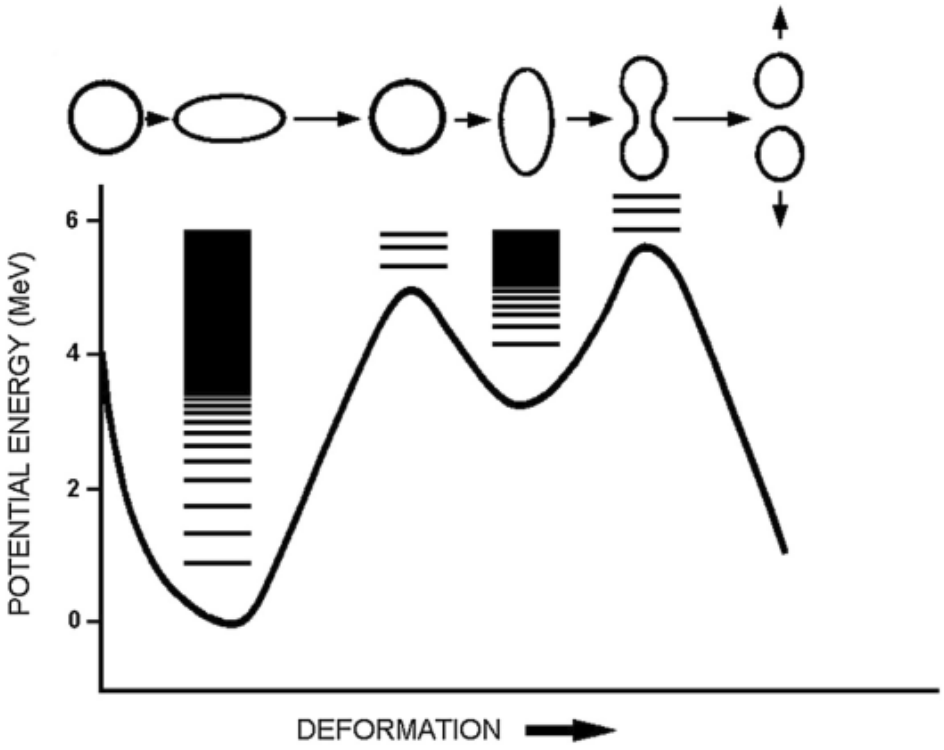

(b)

Figure 5.2: (a) The liquid-drop model potential well and (b) the double-humped fission barrier modified by shell corrections [63].

distance between the observed clusters corresponds to the spacing of Class-II states, whereas the spacings within each cluster reflect the spacing of Class-I states.

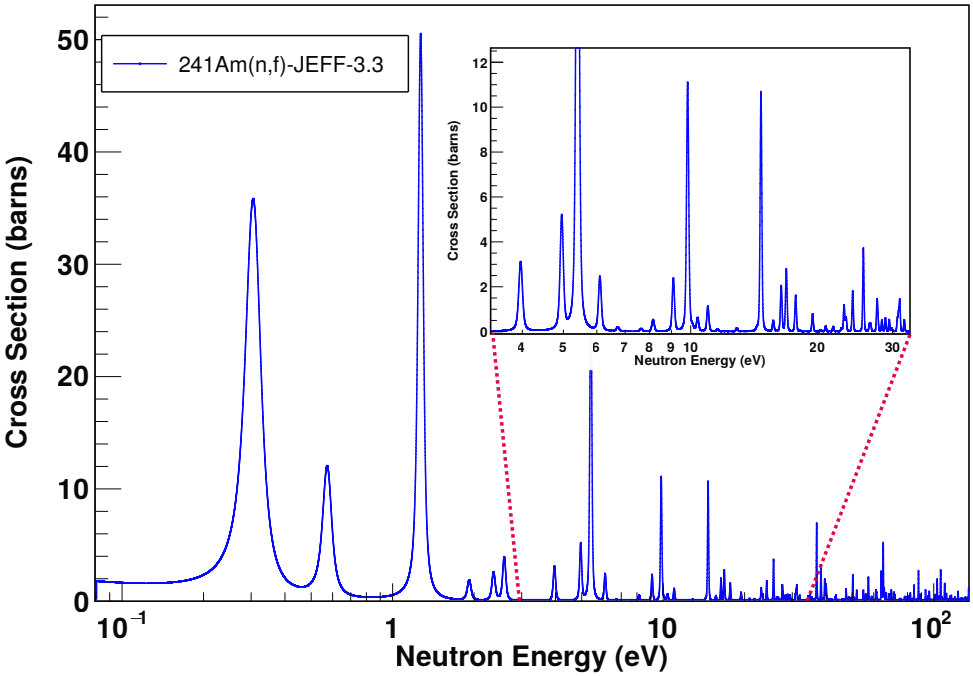

Figure 5.3: Individual resonances and clusters of resonances in the fission cross section of ^{241}Am. The first single strong resonances are attributed solely to Class-I states, while the following clusters of resonances emerge from the coupling in energy and spin-parity of Class-I with Class-II states.

The density of states in the compound nucleus depends on the excitation energy. The higher the excitation energy above the ground state is, the closer the states are located. This means that the average spacing of resonances decreases as the incident neutron energy increases. Notably, the low-lying nuclear levels that are shown in Figure 5.3 display a width that is small compared to their average energy spacing which is $\sim 0.5eV$. The width of each resonance structure is related to its lifetime according to the following formula:

$$\Gamma_\alpha = \frac{\hbar}{\tau_\alpha} \tag{5.12}$$

where Γ_α is the width of the state α and τ_α is its lifetime. An example of a single resonance structure width is illustrated in Figure 5.4. The low-level discrete levels in the compound region have high probability of formation (large cross section) and their widths are small compared to their average spacing distance, because at low incident energies the state that is formed usually has only two available options to decay. It can either re-eject the incident particle, similarly to elastic or inelastic scattering or it can decay through γ-emission. As the excitation energy increases, so do the available modes of decay. In addition, at highly excited energies, the states are so frequent that they overlap with each other since their spacing is shorter than the widths of individual states. As a consequence of the mixing of states, the compound-nucleus continuum is formed.

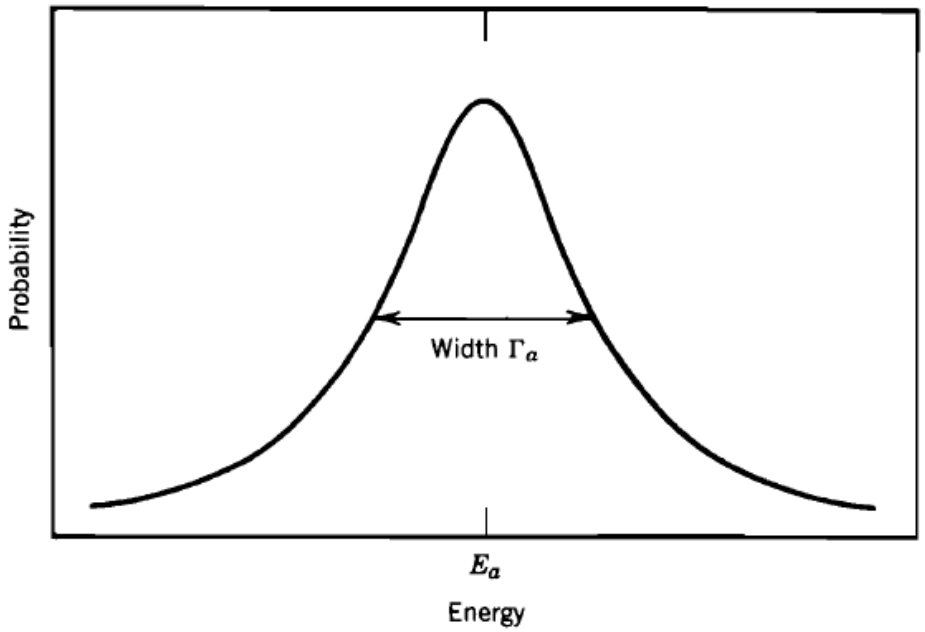

Figure 5.4: Probability to observe the energy of a single unstable state of width Γ_α [58].

Regarding the fission barriers, performed calculations indicate that for the main range of actinides the height of the inner (or first) barrier is practically the same and on average fluctuates between $5 - 7\,MeV$. Nonetheless, close to the Thorium region it has been observed that its value falls rapidly below the above mentioned value. In addition, the secondary well which is noted at increased deformation, is placed $\sim 2 - 3\,MeV$ shallower than the well of the ground state for all actinides. Furthermore, the outer (or second) barriers, display the tendency to fall quite strongly when moving from lighter actinides $(6 - 7\,MeV)$ to heavier actinides $(2 - 3\,MeV)$. A characteristic example for the trend of fission barriers height for typical actinides is illustrated in Figure 5.5.

Finally, some experimental evidence, such as narrow resonances close to the fission threshold region in the neutron-induced fission cross section of light isotopes of ^{230}Th and ^{232}Th, known as the "thorium anomaly", indicate that a triple-humped fission barrier could be possible. Under this assumption, the second hump of the former picture of the double-humped fission barrier, splits into two barriers that are separated by a shallow well, giving rise to Class-III vibrational states [64] [65].

5.1.4 Energy distribution of fission

Nuclear fission as a process can either occur naturally as a spontaneous decay process of heavy nuclei or can be induced through the bombardment of light particles, such as neutrons (neutron-induced fission) or protons (proton-induced fission) or even photons (photo fission). In any case, fission is the outcome of the disruption of the delicate balance between the attractive nuclear force and the repulsive Coulomb force within a heavy nucleus that is powered by the fact that the nuclear binding energy is maximized for medium mass nuclei.

During the evolution of nuclear fission, the fissionable nucleus is deforming constantly through elongation up until the scission point, where it splits into two or more lighter fragments

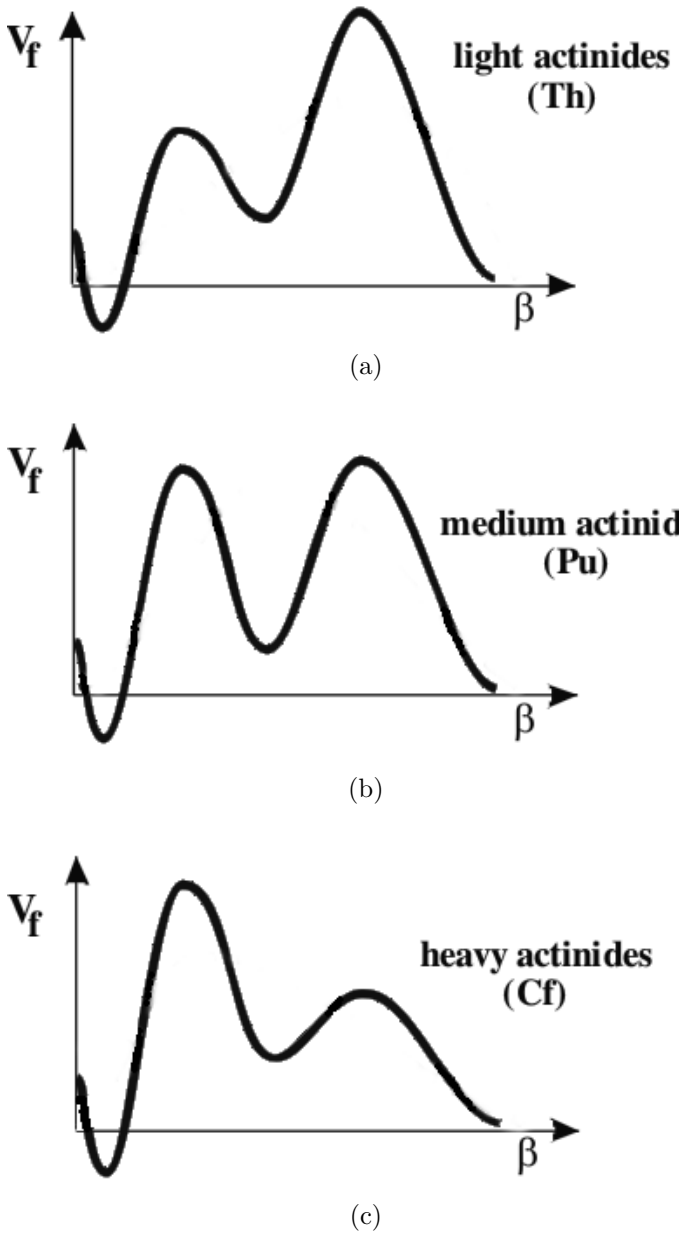

Figure 5.5: Inner and outer fission barrier heights on (a) light, (b) medium and (c) heavy actinides.

with simultaneous emission of "prompt neutrons" and a large energy release. These "prompt neutrons" are emitted instantly when fission occurs and are classified as fast neutrons with an average energy of $\sim 2\,MeV$. Since the fission fragments produced follow a mass distribution as discussed in the previous chapter, the number of prompt neutrons that are emitted in this stage of the fission process have a distribution as well which depends on the specific masses of fission fragments that are created in each fission event. To simplify fission energy calculations, an average number of 2.5 neutrons per fission is considered. This is based on experimental data concerning the Poisson multiplicity spectrum of prompt neutrons emitted during fission of Uranium and various actinide isotopes.

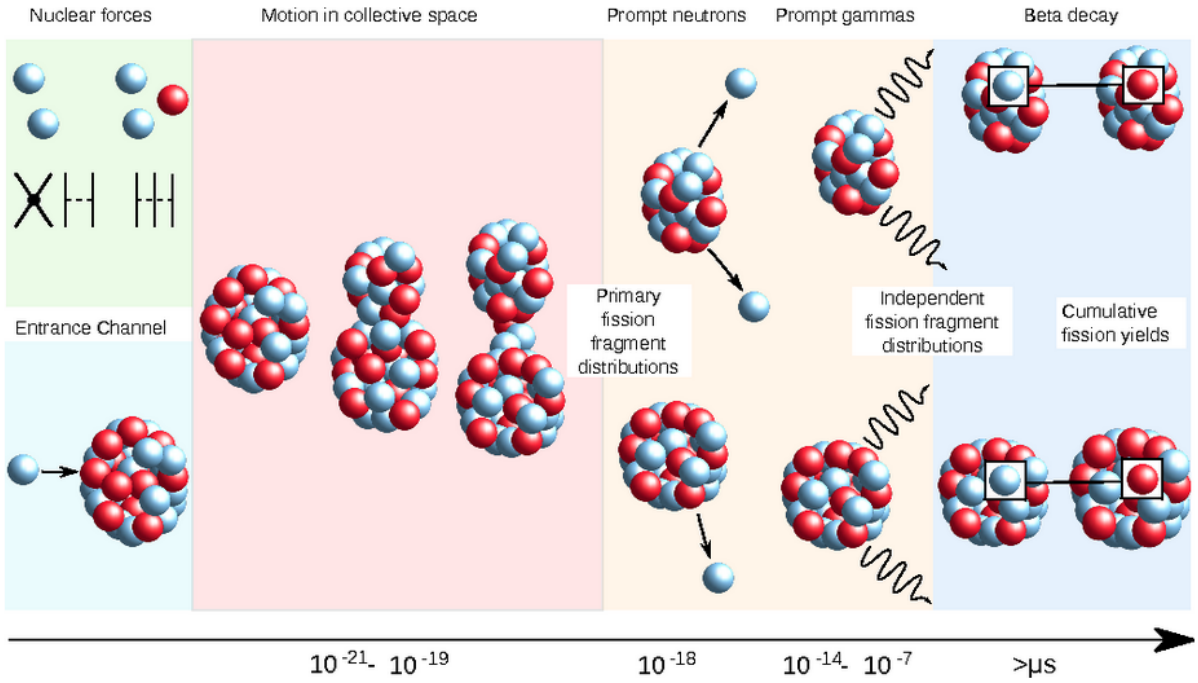

Figure 5.6: Different stages of neutron-induced fission process along with a characteristic time scale evolution [66].

Following a fission event, the originally created fission fragments may undergo $\beta - decays$ that result in the production of "delayed neutrons". "Delayed neutrons" are observed at much longer time scales compared to "prompt" ones, which is characteristic of the lifetime of the decaying nucleus. The intensity of emitted "delayed neutrons" is estimated to be approximately 1 over 100 fission events. Although this number sounds small enough, "delayed neutron emission" is crucial for the operation of fission reactors. The majority of thermal fission reactors are designed to be subcritical to prompt neutrons and use the delayed neutrons to take it to critical mode in order to achieve a steady energy release.

Figure 5.6 presents a schematic illustration of the evolution of the fission process, starting from the creation of a compound nucleus after the absorption of a neutron, moving to the elongation of the compound nucleus up to the scission point where two fission fragments are created with simultaneous emission of prompt neutrons and γ-rays. Then the originally created fission fragments may undergo subsequent β-decays followed by delayed neutron and γ-emission ending with two product nuclei in their isomeric or ground state. The corresponding time scales of the fission process are also indicated in the horizontal axis of Figure 5.6, highlighting the

time dependent evolution character of the fission process.

From each fission event, approximately 200 MeV are released. The kinetic energy of fission fragments accounts almost for 80% of the total fission energy. Table 5.1 summarizes in more detail the partitioning of fission energy per single fission event of ^{235}U induced by thermal neutrons.

	Energy (MeV)
Prompt Energy	$\mathbf{176.5 \pm 5.5}$
kinetic energy of fission products	164.6 ± 4.5
kinetic energy of 2.5 prompt neutrons	4.9 ± 0.5
γ-energy	7.0 ± 0.5
Delayed Energy from fission product decay	$\mathbf{23.5 \pm 5.0}$
β-decay	6.5 ± 1.5
neutrino radiation	10.5 ± 2.0
γ-energy	6.5 ± 1.5
Total	$\mathbf{200.0 \pm 6.0}$

Table 5.1: Energy distribution in thermal fission of ^{235}U [63].

5.1.5 Neutron-induced fission cross sections

In the context of the present thesis, neutron-induced fission cross sections of ^{241}Am and Uranium isotopes were studied. In general, Uranium and actinide isotopes are classified into two categories based on whether or not their excitation energy is sufficient in order to fission after absorbing an incident neutron with theoretically zero energy. Heavy nuclei are categorized accordingly as:

- **Fissile nuclei** that can absorb thermal neutrons or even neutrons of nearly zero kinetic energy and reach an excitation energy already above the fission barrier (i.e. ^{235}U)
- **Fissionable nuclei** that need to reach a threshold in order to fission and require the capture of incident neutrons with additional kinetic energy of the order of MeV, so as to overcome the fission barrier (i.e. ^{238}U, ^{241}Am)

Figure 5.7, depicts evaluated neutron-induced fission cross sections for various isotopes. The comparison reveals two dominant trends in the shape of fission excitation function, between the keV and MeV neutron energy region. In the case of fissionable isotopes, the cross section shows a step-like behaviour before reaching a plateau in the MeV region. On the other hand, the fission cross section of fissile isotopes, which in general has a higher value in the thermal region, has a smoother behaviour and the formed compound nucleus after the neutron capture does not have a threshold to overcome in order to fission with fast neutrons.

The observed difference of the high energy part in the excitation function of fission among a variety of isotopes can be explained by taking into consideration the pairing effects of term δ in the binding energy for the ground state of the target nucleus and the excited state of the compound nucleus after the absorption of the neutron. For the majority of Uranium isotopes

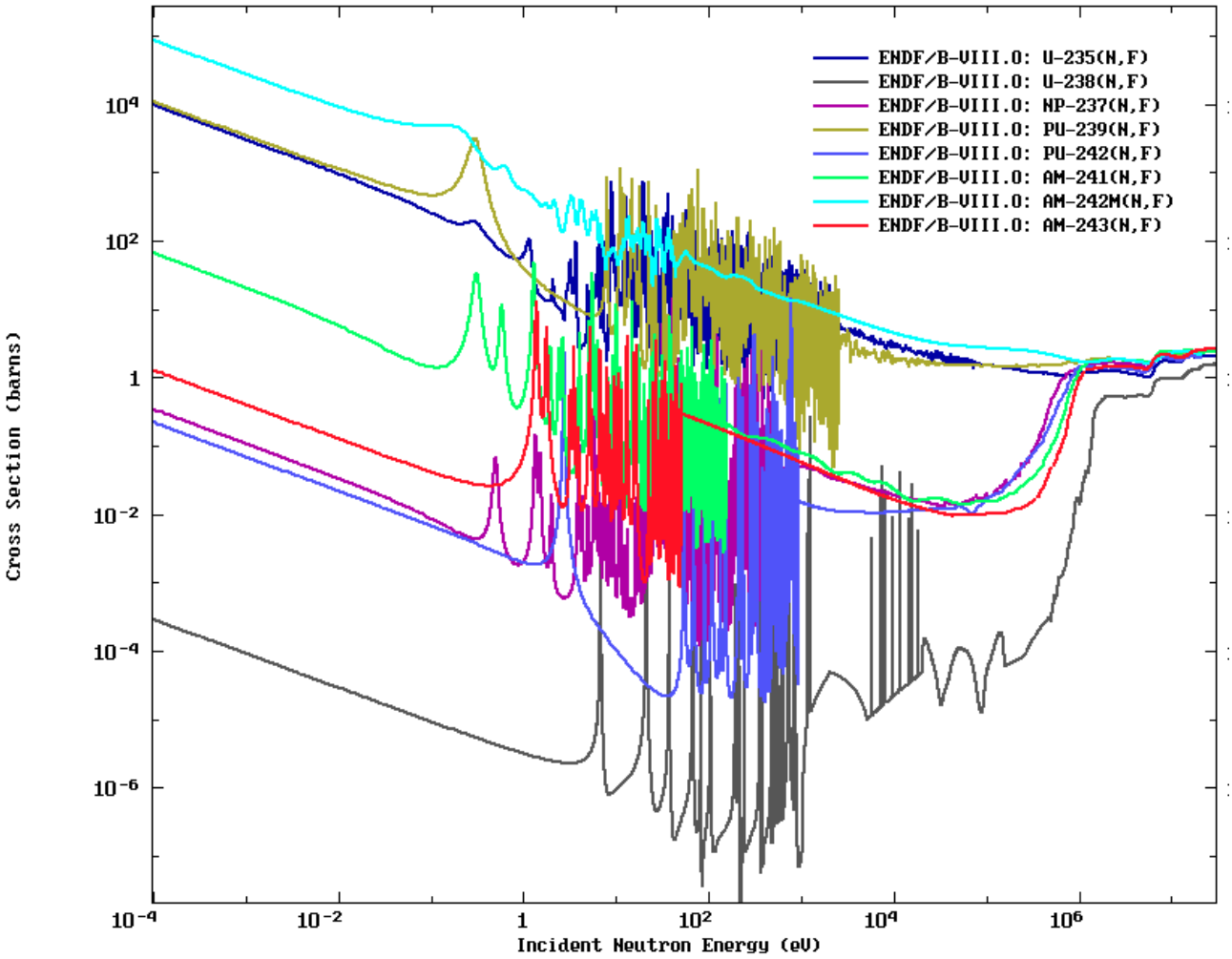

Figure 5.7: Neutron-induced fission cross sections of various fissile and fissionable isotopes, retrieved from the ENDF/B-VIII.0 evaluated library.

and actinides, in principle, the activation energy, which is the energy needed to overcome the fission barrier, is approximately the same and ranges between $6 - 7\,MeV$. Nonetheless, the neutron separation energy S_n, which is the minimum excitation energy E_{ex} when neutrons have nearly zero kinetic energy, is strongly affected by the pairing effects of nuclei. As can be seen in Figure 5.8, the difference in the neutron separation energy for the formed compound isotopes with odd and even number of neutrons, corresponds to the needed energy to overcome the fission barrier. In this way, it can be naturally explained why ^{238}U and ^{241}Am are not fissile (compound nucleus with odd neutron number) while ^{235}U and ^{242}Am are fissile (a compound nucleus with even number of neutrons is formed).

Returning to the features of the neutron-induced cross sections as can be observed in Figure 5.7, in the lower energy part of the spectrum the excitation function of all isotopes display similar structures. In the thermal region, the dependence of the cross section is proportional to the incident neutron energy following the "$1/u$ law". This can be intuitively explained by considering that the probability for a neutron to be captured and a compound nucleus to be formed is proportional to the needed time for the neutron to traverse the nucleus. Therefore, the dependence of the cross section from the neutron energy can be expressed as follows:

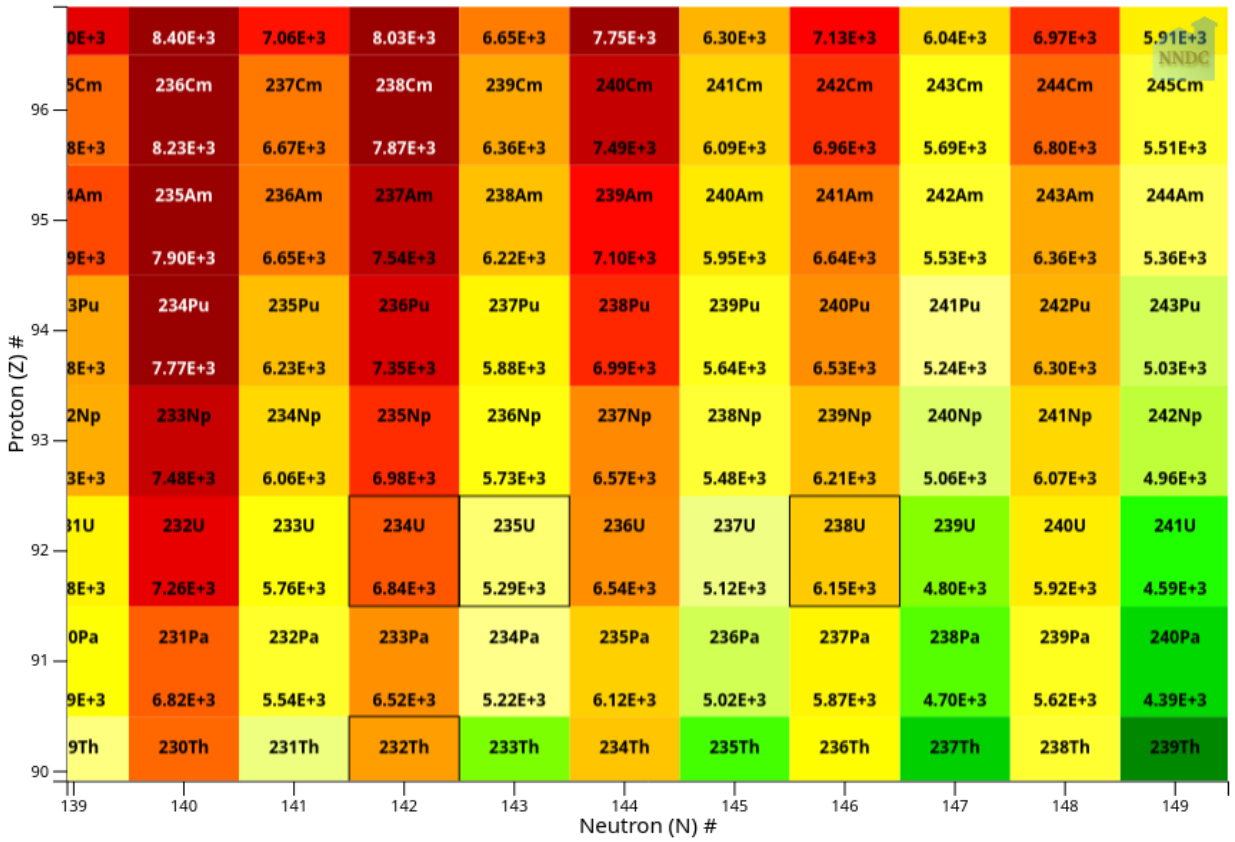

Figure 5.8: Separation energy values in keV for indicative isotopes exported from the NNDC database.

$$\sigma \propto \frac{1}{u} \propto \frac{1}{\sqrt{E}} \tag{5.13}$$

Following the smooth shape of the cross section in the low energy part, between 1 to a few hundred's of eV, peak structures which are called "resonances" are observed. The resonances are in reality excited states of the compound nucleus which are located above the neutron separation energy of the initial nucleus and are reached when the incident neutrons have the proper kinetic energy. At low energies, the energy gap between the compound nucleus states is larger, and as a consequence the observed resonances have a larger distance between them as well. The energy region where these first strong resonances are observed in the range between $1 - 10\,eV$ is called "resolved resonance region" (RRR). At higher excitation energies, when the incident neutron energy increases, the level spacing of the compound nucleus states is becoming narrower due to the higher density of levels. The region between $10 - 10^3\,eV$ is called "unresolved resonance region" (URR), since the compound nucleus is excited into its continuum and the resonances cannot be resolved anymore. Depending on the nucleus, the cross section bears a smooth behaviour from this region up to the threshold of the fission reaction. Especially for ^{241}Am, Figure 5.9 highlights the formation of excited states after the neutron capture in the compound nucleus potential well and their equivalence with the experimentally observed resonances in the cross section of ^{241}Am(n,f).

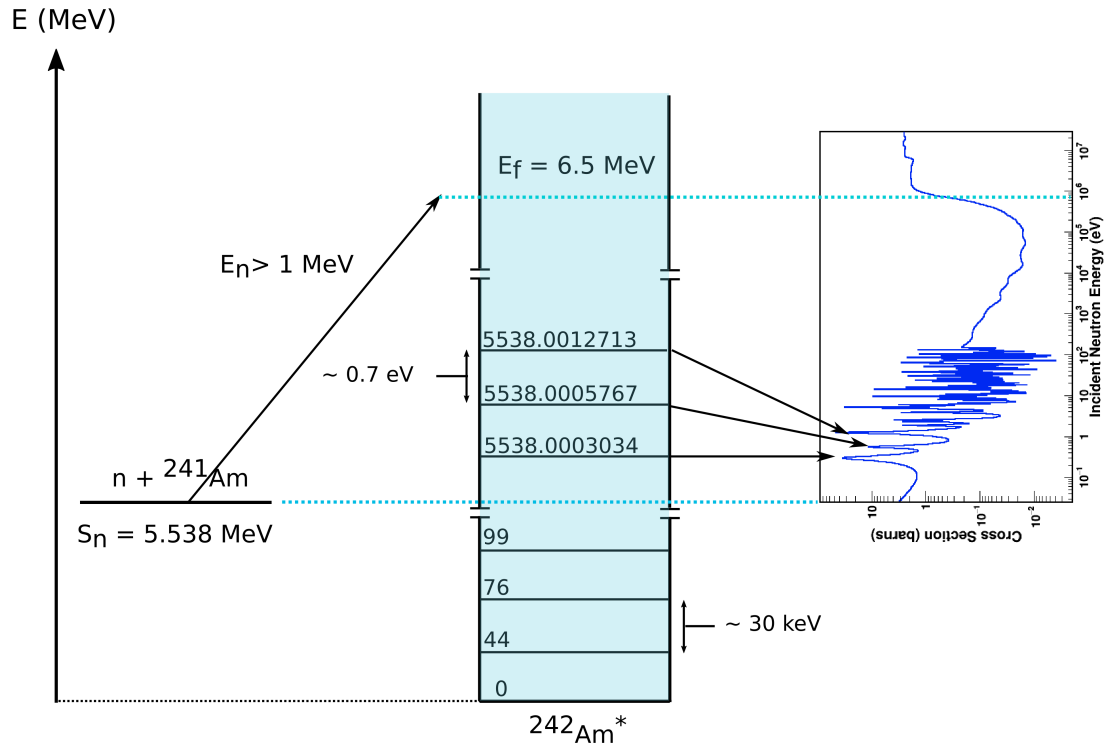

Figure 5.9: Schematic representation of neutron capture from ^{241}Am that results in the formation of the compound nucleus ^{242}Am. In case of neutron absorption with zero kinetic energy, the compound nucleus will be formed in an excited level state approximately $5.538\,MeV$ above its ground state. In the energy diagram, the first four levels of ^{242}Am together with the first three levels that lie just above the neutron separation energy S_n are shown. The levels above the neutron separation energy correspond to the first resonances that are displayed in the neutron-induced fission cross section of ^{241}Am on the right side of the figure. In order to overcome the fission barrier, the compound nucleus ^{242}Am should be excited above $\sim 6.5\,MeV$ by capturing a fast neutron ("neutron-induced fission") with incident energy of the order of MeV. Close to its ground state, the level spacing of the compound nucleus is of the order of $30\,keV$, whereas at higher excitation energies, the resonances of the (n, f) excitation function of ^{241}Am resulting from the matching between class-I and class-II states are formed at a closer level spacing of the order of $\sim 0.7\,eV$. In the figure, the units of the compound nucleus levels are in keV, unless otherwise specified.

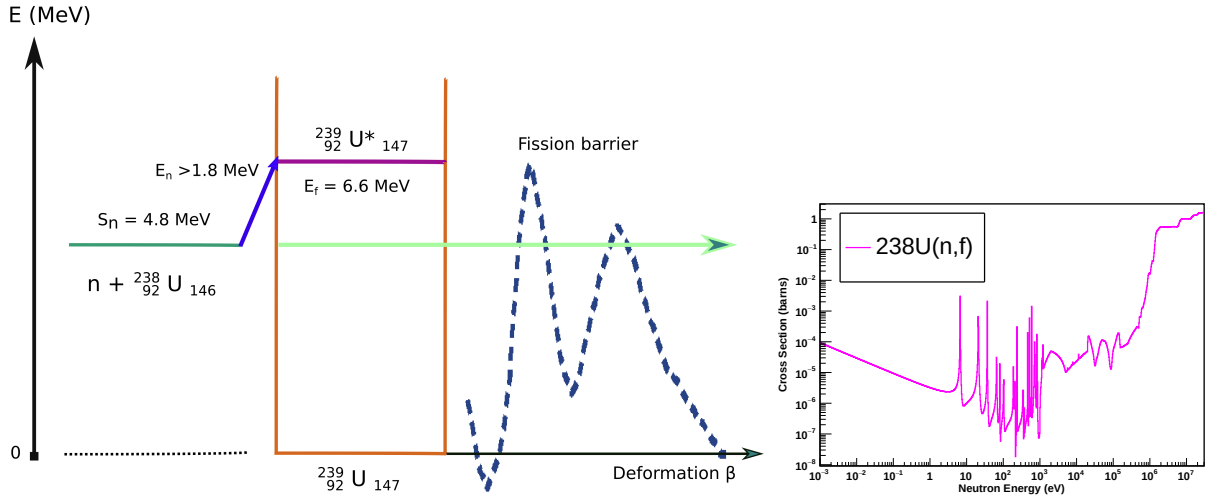

Figure 5.10: Energy diagram of the interaction n + ^{238}U. In order to overcome the fission barrier in the excited level state of the compound nucleus ^{239}U, neutrons from the fast spectrum with energy more than 1.8 MeV are required. On the right, the neutron-induced fission cross section of ^{238}U displays a steep threshold above 1 MeV, which is a common characteristic of fissionable nuclei.

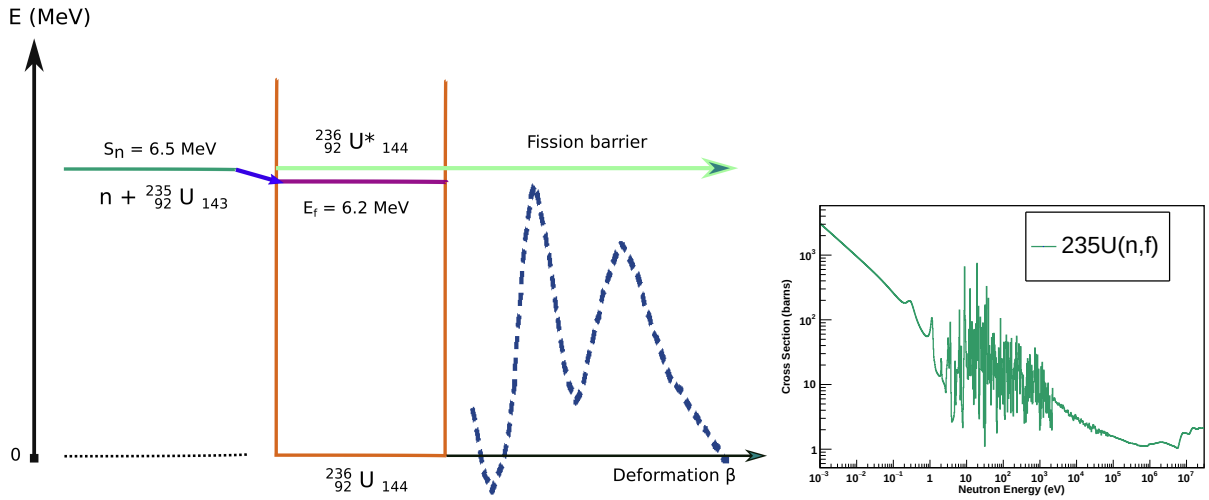

Figure 5.11: Energy diagram of the interaction n + ^{235}U. The neutron separation energy of ^{235}U is only 300 keV higher than the fission barrier, readily enabling fission without the need of additional kinetic energy from incident neutrons. On the right, the neutron-induced fission cross section of ^{235}U highlights the absence of a fission threshold with the smooth shape of the excitation function close to the MeV region.

When the kinetic energy of neutrons is high enough to overcome the fission barrier, just before the MeV region, then the shape of the cross section is increased in case of fissionable nuclei as illustrated for ^{238}U in Figure 5.10, or remains more or less constant in case of fissile nuclei such as ^{235}U in Figure 5.11 respectively. After the "fission threshold", which is different for each nucleus, the observed (n, f) cross section is comparable in all nuclei.

At even higher neutron energies in the MeV region, after the fission threshold, the cross section of Uranium and actinides show similar behaviour. Above the fission threshold, the cross section shows a step-like behaviour as a result of the "multi-chance fission" due to the superposition of various (n, xnf) channel openings. When the compound nucleus acquires large excitation energy, exceeding the sum of the neutron separation energy of the initial energy plus the energy of the fission barrier, then the (n, nf) "second chance fission" occurs around $\sim 6\,MeV$ with the evaporation of one neutron. At $\sim 12\,MeV$ (approximately two times the neutron separation energy), the $(n, 2nf)$ "third chance fission" channel opens and as the excitation energy is further increased, the probability of pre-equilibrium neutron emission prior to the fission process inflates as well.

5.2 Theoretical investigation

5.2.1 The TALYS code

TALYS [67] is a nuclear reaction code that simulates nuclear reactions involving neutrons, protons, γ-rays, deuterons, tritons, helium and alpha particles, in the particle energy region between 1 keV and several hundreds of MeV. The code incorporates all major reaction mechanisms such as direct reactions, compound nucleus reactions, pre-equilibrium reactions and multiple emissions using various optical model parameters. TALYS is widely used for theoretical cross section calculations and data evaluations since it calculates a nuclear reaction's cross section while accounting for the competition between various reaction channels, for the same particle energy region of interest. The probability that a nucleus fissions is estimated by TALYS within the framework of the compound nucleus reaction mechanism using the Hauser-Feshbach statistical model [68]. For the calculations of the present work, version 1.95 of TALYS was used, and the default values for nuclear masses, discrete levels, decay schemes and ground state deformations were adopted. Figure 5.12 illustrates schematically the basic function of the TALYS code.

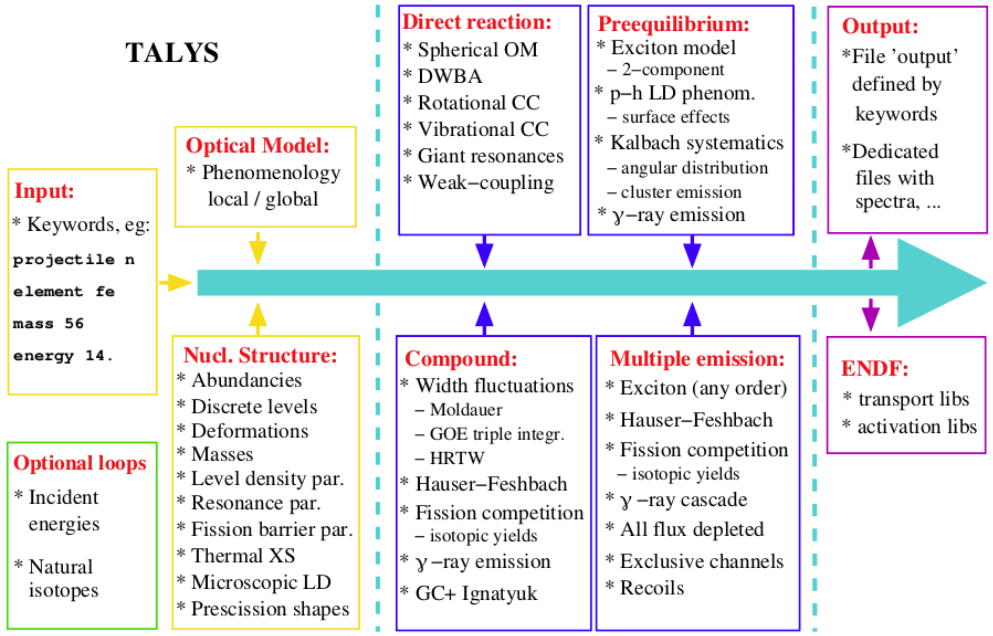

Figure 5.12: A simplified illustration of the function of TALYS code and its integrated models [67].

5.2.2 Hauser-Feschbach theory

The theoretical calculations of the present work were performed within the framework of the Hauser-Feschbach statistical model. In this quantum-mechanical formalism, the cross section calculations of the compound nucleus reactions obey the laws of the conservation of energy, angular momentum and parity as indicated by Equations 5.14.

$$\begin{aligned} E_a + S_a &= E_{a'} + E_x + S_{a'} = E^{tot} \\ s + I + l &= s' + I' + l' = J \\ \pi_0 \Pi_0 (-1)^l &= \pi_f \Pi_f (-1)^{l'} = \Pi \end{aligned} \tag{5.14}$$

As a consequence of the capture of the projectile by the target nucleus, a compound nucleus is formed with a total energy E^{tot} and a range of values for the total spin J and parity Π. According to Bohr's hypothesis, the decay mode of the compound nucleus is independent of the formation mechanism. In other words, due to the delay between the compound nucleus formation and the ejectile emission (typically $10^{-18} - 10^{-16} s$), but also due to the complex motions of nucleons occurring in this time interval, the compound nucleus system has lost memory of the input channel through which it was created. Within this scope, the cross section for the reaction $A + a \rightarrow C^* \rightarrow a^{'} + A^{'}$, is given by Equation 5.15:

$$\begin{aligned} \sigma_{\alpha\alpha'}^{comp} = & D^{comp} \frac{\pi}{k^2} \sum_{J=mod(I+s,1)}^{l_{max}+I+s} \sum_{\Pi=-1}^{1} \frac{2J+1}{(2I+1)(2s+1)} \sum_{j=|J-1|}^{J+I} \sum_{l=|j-s|}^{j+s} \sum_{j'=|J-I'|}^{J+I'} \sum_{l'=|j'-s'|}^{j'+s'} \\ & \times \delta_\pi(\alpha)\, \delta_\pi(\alpha') \frac{T_{\alpha l j}^J(E_\alpha)\, \left\langle T_{\alpha' l' j'}^J(E_{\alpha'}) \right\rangle}{\sum_{\alpha'', l'', j''} \delta_\pi(a'')\, \left\langle T_{\alpha'' l'' j''}^J(E_{\alpha''}) \right\rangle} W_{\alpha l j \alpha' l' j'}^J \end{aligned} \tag{5.15}$$

The symbols used in the above equations, have the following meanings:
E_α is the projectile's energy
s is the spin of the projectile
π_0 is the parity of the projectile
l is the orbital angular momentum of the projectile
j is the total angular momentum of the projectile
$\delta_\pi(\alpha) = 1$, if $(-1)^l \pi_0 \Pi_0 = \Pi$ and 0 otherwise
α stands for the channel designation of the initial system of projectile and target nucleus as: $\alpha = \left\{a, s, E_\alpha, E_x^0, I, \Pi_0\right\}$, where a is the projectile type and E_x^0 is the excitation energy of the target nucleus which is usually zero
l_{max} is the maximum l-value of the projectile
S_α is the separation energy
$E_{\alpha'}$ is the ejectile's energy
s' is the spin of the ejectile
π_f is the parity of the ejectile
l' is the orbital angular momentum of the ejectile
j' is the total angular momentum of the ejectile
$\delta_\pi(\alpha') = 1$, if $(-1)^{l'} \pi_f \Pi_f = \Pi$ and 0 otherwise
α' stands for the channel designation of the final system of ejectile and residual nucleus as: $\alpha' = \left\{a', s', E_{\alpha'}, E_x, I', \Pi_f\right\}$, where a' is the ejectile type and E_x is the excitation energy of the residual nucleus
I is the spin of the target nucleus
Π_0 is the parity of the target
I' is the spin of the residual nucleus
Π_f is the parity of the residual nucleus

Π is the parity of the compound system
J is the total angular momentum of the compound system
D^{comp} is the depletion factor to account for direct and pre-equilibrium effects
k is the wave number of relative motion
T is the transmission coefficient
W is the width fluctuation correction (WFC) factor which considers the correlations between the input and output channels. At low incident energies, this component enhances the elastic channel, however at energies beyond a few MeV, it is negligible. For incident energies higher than the projectile separation energy, the default value in TALYS for W is unity. In such a case, the cross section equation is written as:

$$\sigma_{\alpha\alpha'}^{comp} = \sum_{J=mod(I+s,1)}^{l_{max}+I+s} \sum_{\Pi=-1}^{1} \sigma_{J\Pi}^{CF}\left(E^{tot}\right) \frac{\Gamma_{\alpha'}\left(E^{tot}, J, \Pi \rightarrow E_x, I', \Pi_f\right)}{\Gamma^{tot}\left(E^{tot}, J, \Pi\right)} \tag{5.16}$$

where $\sigma_{J\Pi}^{CF}$ is the cross section for the formation of the compound nucleus per spin and parity that is given through the following formula:

$$\sigma_{J\Pi}^{CF}(E^{tot}) = D^{comp}\,\frac{\pi}{k^2}\frac{2J+1}{(2I+1)(2s+1)} \sum_{j=|J-1|}^{J+I} \sum_{l=|j-s|}^{j+s} T_{\alpha lj}^{J}(E_\alpha)\,\delta_\pi(\alpha) \tag{5.17}$$

The partial decay widths as a function of transmission coefficients are:

$$\Gamma_{\alpha'}\left(E^{tot}, J, \Pi \rightarrow E_x, I', \Pi_f\right) = \frac{1}{2\pi\rho\left(E^{tot}, J, \Pi\right)} \sum_{j'=|J-I'|}^{J+I'} \sum_{l'=|j'-s'|}^{j'+s'} \delta_\pi(a') \left\langle T_{\alpha' l' j'}^{J}(E'_{\alpha'})\right\rangle \tag{5.18}$$

where ρ describes the compound nucleus level density, and the total decay width is expressed as follows:

$$\Gamma^{tot}\left(E^{tot}, J, \Pi\right) = \sum_{\alpha''} \Gamma_{\alpha''}\left(E^{tot}, J, \Pi \rightarrow E_x, I'', \Pi_f\right) \tag{5.19}$$

containing all the possible exit channels allowed by the energy conservation and selection rules, where all the possible states on the residual nuclei are summed through the sum over α''.

In the case where the exit channel is gamma emission, the above mentioned transmission coefficients are replaced by the "γ-ray strength functions". Thereupon, the cross section calculation with the formalism of the Hauser-Feshbach theory directly depends on the optical and level density models, as well as on transmission coefficients and γ-ray strength functions. In this formalism, fission is described as a decay channel of the formed compound nucleus and therefore, it depends on the transmission coefficients through the fission barriers as well as on the nuclear level density of transition states on top of the fission barriers. The fission probability can be estimated by TALYS on the basis of both phenomenological and microscopic grounds, including the cross section calculation for multi-chance fission.

5.2.3 Fission transmission coefficients

The Hill-Wheeler expression and Bohr's transition state hypothesis are the backbones of TALYS's default fission model. As a result, fission transmission coefficients are taken into

account along with the particle and photon transmission coefficients in the Hauser-Feshbach model. For a compound nucleus with excitation energy E_x, the Hill-Wheeler expression provides the probability of tunneling through a barrier with height B_f and width $\hbar\omega_f$ as follows:

$$T_f(E_x) = \frac{1}{1 + \exp\left[-2\pi\frac{(E_x - B_f)}{\hbar\omega_f}\right]} \tag{5.20}$$

Additionally, when the excitation energy ε_i of a transition state is higher than the top of the fission barrier, then the barrier is shifted according to Equation 5.21.

$$T_f(E_x, \varepsilon_i) = \frac{1}{1 + \exp\left[-2\pi\frac{(E_x - B_f - \varepsilon_i)}{\hbar\omega_f}\right]} \tag{5.21}$$

The total transmission coefficient for a compound nucleus with excitation energy E_x, spin J and parity Π, is the sum of the individual transmission coefficients for each barrier that the nucleus may tunnel through. Therefore, it is expressed as:

$$T_f^{J,\Pi}(E_x) = \sum_i T_f(E_x, \varepsilon_i)\, f(i, J, \Pi) + \int_{E_{th}}^{E_x} \rho(\varepsilon, J, \Pi)\, T_f(E_x, \varepsilon)\, d\varepsilon \tag{5.22}$$

In the above equation, the summation traverses all discrete transition states located on top of the barrier, whereas the beginning of the continuum is marked by E_{th}. Moreover, the factor $f(i, J, \Pi)$ is unity in case that the spin and parity of the transition state are the same as the compound nucleus, or is 0 otherwise. Furthermore, $\rho(\varepsilon, J, \Pi)$ accounts for the level density of fission channels with spin J and parity Π for an excitation energy ε.

Of course, for double humped barriers the expression commonly used is subject to an effective transmission coefficient T_{eff} defined as:

$$T_{eff} = \frac{T_A\, T_B}{T_A + T_B} \tag{5.23}$$

where T_A and T_B are the transmission coefficients for barrier A and B respectively, calculated from Equation 5.22. Consequently, if a triple humped barrier has to be considered, the calculated effective transmission coefficient is:

$$T_{eff'} = \frac{T_{AB}\, T_C}{T_{AB} + T_C} \tag{5.24}$$

where T_{AB} is derived from Equation 5.23, so that the final expression implemented within TALYS is:

$$T_{eff'} = \frac{T_A\, T_B\, T_C}{T_A\, T_B + T_A\, T_C + T_B\, T_C} \tag{5.25}$$

As an alternative to the Hill-Wheeler approach, within TALYS there is an option to use the WKB approximation in order to calculate fission transmission coefficients as well. The implementation of this method within TALYS was performed by Michaela Sin and Roberto Capote and is described in detail in [65]. In this approach, the real part of the barriers associated with the discrete transition states is parameterized by smoothly joined parabolas as a function of the quadrupole deformation parameter β along the fission path.

5.2.4 Fission barrier parameters

The shape of the fission cross section and its absolute value make the fission barrier parameters one of the most crucial characteristics in the theoretical cross section estimations. For the calculation of fission barriers, in the context of the present study, two different approaches which are available with the TALYS code were employed.

The first scenario relies on the Hill-Wheeler approximation where the double humped fission barriers are described by independent inverted parabolas with designated fission barrier heights and curvatures or widths. The choice of the fission barrier parameters was based on an experimental compilation performed by V.M. Maslov [69] that includes a collection of a large set of actinide fission barrier heights and curvatures for both the inner and outer barrier based on a fit to experimental data. This set of fission barrier parameters are also included in the Reference Input Parameter Library (RIPLE-3) [70] in the section containing the empirical fission barriers. In order to reproduce the available experimental data including those of the present study, the default fission barrier parameters of the key Americium isotopes were properly adjusted.

The second scenario that was employed for the calculation of the fission barrier parameters, is based on a microscopic calculation using the WKB approximation and the Hartree-Fock-Bogolyubov (HFB) numerical description of the entire fission path. The one-dimensional multihumped fission barrier is described by the optical model for fission, which takes into account potential transmission processes utilizing a complex potential of the form:

$$V_f = V + iW \tag{5.26}$$

The real part of the barriers associated with the discrete transition states is parameterized by smoothly joined parabolas as a function of the quadrupole deformation parameter β along the fission path as follows:

$$V_i(\beta) = E_{fi} + (-1)^i \frac{1}{2} \mu \hbar^2 \omega_i^2 \ (\beta - \beta_i)^2 \tag{5.27}$$

where i is an index running from 1 to 3 for a two-humped barrier. The energies E_{fi} represent maxima of V_i, which in case of humps are equivalent to the barriers' height and minima of V_i which comparably correspond to the wells. Additionally, β_i are the corresponding abscissae, $\hbar\omega_i$ is the curvature of each parabola referring to the barrier's width and μ is the inertial mass parameter which is assumed to be independent of β and is given approximately by the semi-empirical expression $\mu \simeq 0.054 A^{5/3}\, MeV^{-1}$, where A is the mass number.

The discrete transition states are rotational levels built on vibrational or non-collective band-heads. Accordingly, they correspond to a fixed set of quantum numbers including angular momentum J, parity π and angular momentum projection on a nuclear symmetry axis K with excitation energies:

$$E_i(J, K, \pi) = E_{fi} + \epsilon_i(K, \pi) + \frac{\hbar^2}{2I_i} [J(J+1) - K(K+1)] \tag{5.28}$$

where $\epsilon_i(K, \pi)$ are the excitation energies of the band-heads and $\frac{\hbar^2}{2I_i}$ are inertial parameters. The important thing to mention is that each transition state is associated with a different parabolic barrier with height $E_i(J, K, \pi)$ and curvature $\hbar\omega_i$. The discrete part of the transition state spectrum above a specific energy E_{ci} is succeeded by the continuum which is characterized by the level density functions $\rho_i(E, J, \pi)$ at each saddle point.

In the optical model for fission, the negative imaginary part iW in the deformation range is introduced in order to simulate the damping of class II vibrational states. Consequently, this causes an absorption of the incoming flux in the wells. The strength W depends quadratically on deformation and increases with the excitation energy according to the following formula:

$$W(\beta) = -\alpha(E)\,[E - V(\beta)] \tag{5.29}$$

where α is an energy dependent parameter that controls the strength of the imaginary part of the fission potential. Figure 5.13, illustrates an example for the parameterization of fission barriers in the optical model for fission in the microscopic approach for the description of a double-humped barrier.

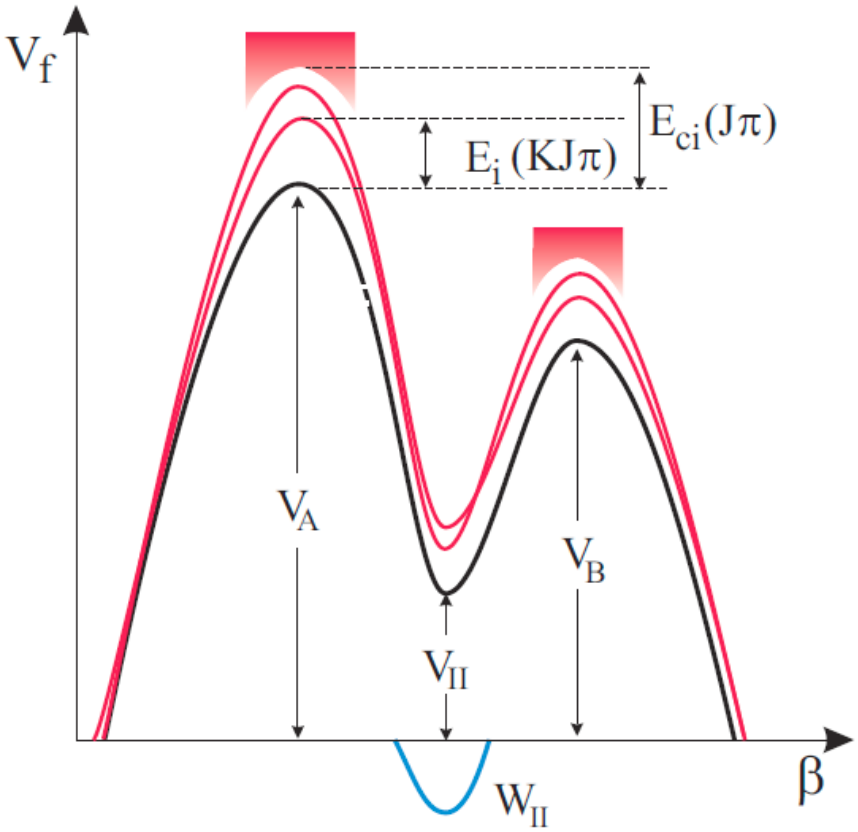

Figure 5.13: Parameterization of double-humped fission barriers for the optical model of fission [71].

A comparison of the two theoretical approaches employed in the theoretical calculations is depicted in Figure 5.14, where the two independent inner and outer barriers of Hill-Wheeler are plotted together with the entire fission path of the microscopic HFB approach against the quadrupole deformation parameter β for the compound nucleus ^{242}Am.

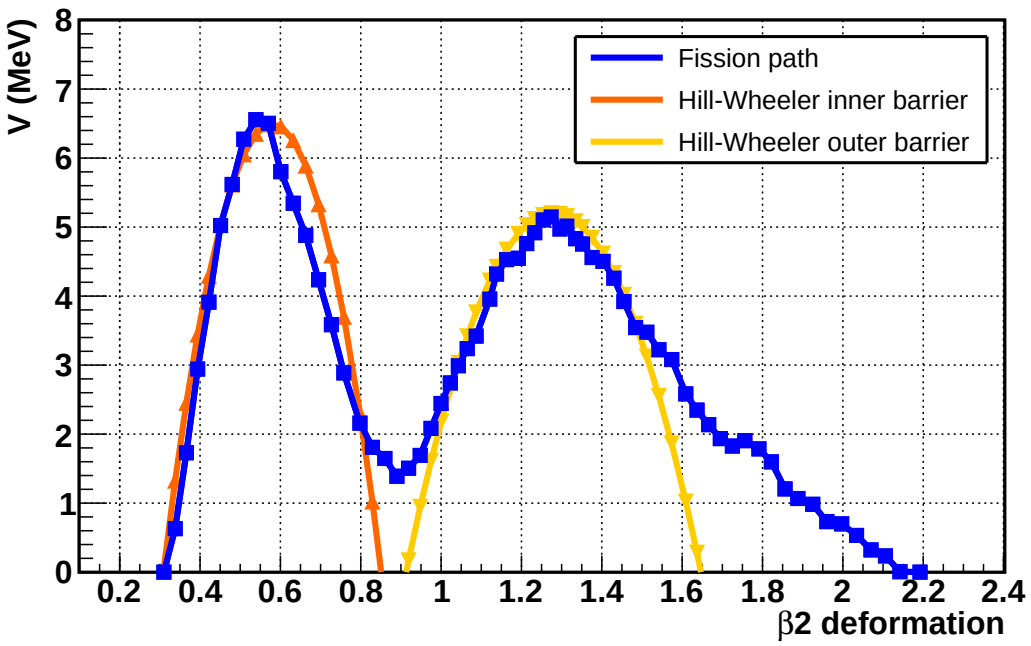

Figure 5.14: Comparison of fission barriers described by decoupled inverted parabolas along with the projection of the entire fission path based on the microscopic HFB approach which is described by smoothly joined parabolas as a function of the quadrupole deformation parameter β for the compound nucleus ^{242}Am.

5.2.5 Calculations and results

For the theoretical calculations of the cross sections for the neutron-induced reactions of ^{241}Am, the TALYS-1.95 code was used. Apart from the fission channel, which is the channel of interest of this study, the rest of open competing channels namely the total, elastic, inelastic, capture and (n, xn) channels, were taken into consideration. Due to the fact that different sets of fission barrier parameters in combination with adjusted level densities can result in the same cross section value for the fission channel, it is also essential to simultaneously observe these changes in the cross section of the aforementioned reaction channels. Consequently, wherever data were available, the outcomes of each theoretical calculation were compared with the experimental cross sections retrieved from the EXFOR database, to ensure an overall satisfactory reproduction for all competing reaction channels simultaneously. In the region of interest for these theoretical calculations no experimental evidence was found for the elastic and inelastic channels, except from one data point for the inelastic channel at 14.7 MeV, which was unfortunate since the latter is the primary competitive channel for fission in the plateau of the reaction. The theoretical calculations were extended in the neutron energy range of 0.1 to 30 MeV.

An optical model designed specifically for actinides by Soukhovitskii et al. [72], which was provided inside the TALYS code, was employed in the theoretical calculations carried out for the present thesis. The default calculation of TALYS uses a phenomenological level density model by combining the Constant Temperature model (CTM) for low excitation energies and the Fermi Gas (FGM) model for higher energies. In this combination, it is necessary to match the formulas for the two level densities at a matching energy E_M, where both their equations and their derivatives are identical. Additionally, the default option for the γ-ray strength function

in TALYS was the generalized Lorentzian form of Kopecky and Uhl [73]. Finally, regarding the fission barrier parameters used, these are experimental parameters based on the double-humped barrier approach, resulting from a fit to experimental data which are also available in the RIPLE-3 library. Figure 5.15 shows the outcome of the default calculation of TALYS based on the above mentioned models. It is evident that apart from the (n, γ) channel, the (n, f) and (n, xn) reaction channels fail to be reproduced.

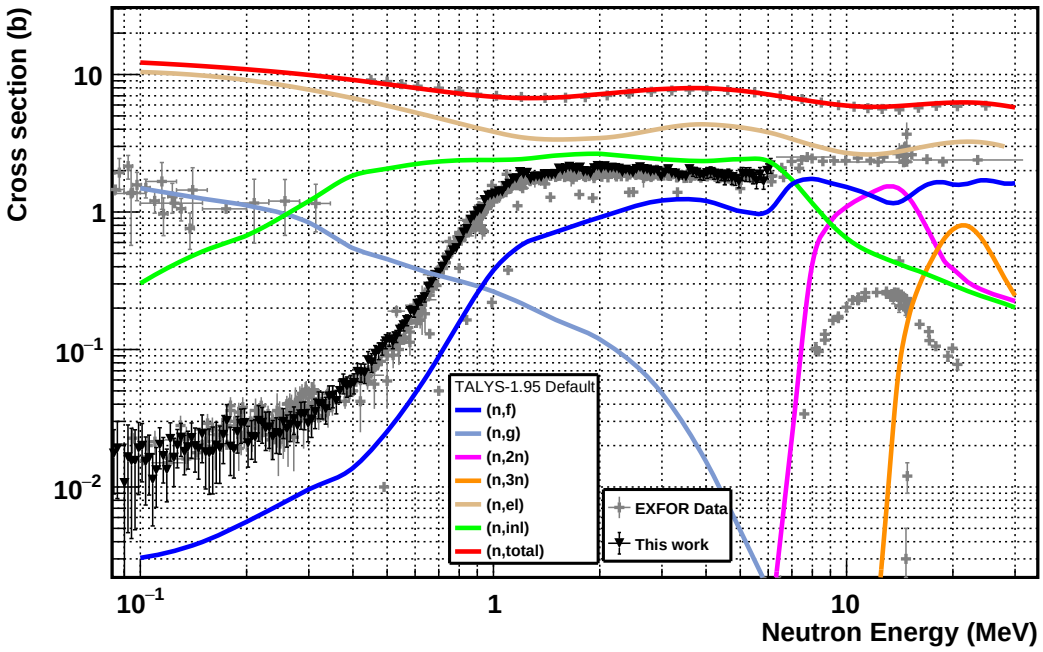

Figure 5.15: TALYS calculation for ^{241}Am for the default parameters and nuclear models for incident neutron energies in the range between $0.1 - 30$ MeV. Along with the theoretical predictions, the available experimental data for all competing channels are plotted, superimposed with the data of the present work for the fission channel.

Inside TALYS there is an option to use the so-called "best files", which is a collection of modified input parameters that are unique for each nuclide. In principle, the collection of best TALYS input parameters aims at the simultaneous high-quality reproduction of decay channels for a particular isotope. The results of the best TALYS parameters are depicted in Figure 5.16, where especially for the fission channel the calculation fails to reproduce the threshold of the reaction together with the beginning of the fission plateau, even though after the $3\,MeV$ it seems to converge with the experimental data.

As a next step, several changes were made to the fission barrier parameters, namely fission barrier heights and widths along with the level density parameters of Americium isotopes, in an effort to improve the agreement between the TALYS calculations and the experimental data. The modification of the fission barrier parameters are visible in the Tables 5.2 and 5.3, where the initial and modified values of the fission barrier heights and curvatures for the Americium isotopes are highlighted. Concerning the level density adjustments, in the case of ^{242}Am isotope no changes were made so that there is a self-consistency with the existing experimental D_0's (average level spacing) which are calculated to be $\approx 0.58\,eV$, extracted from the resonance

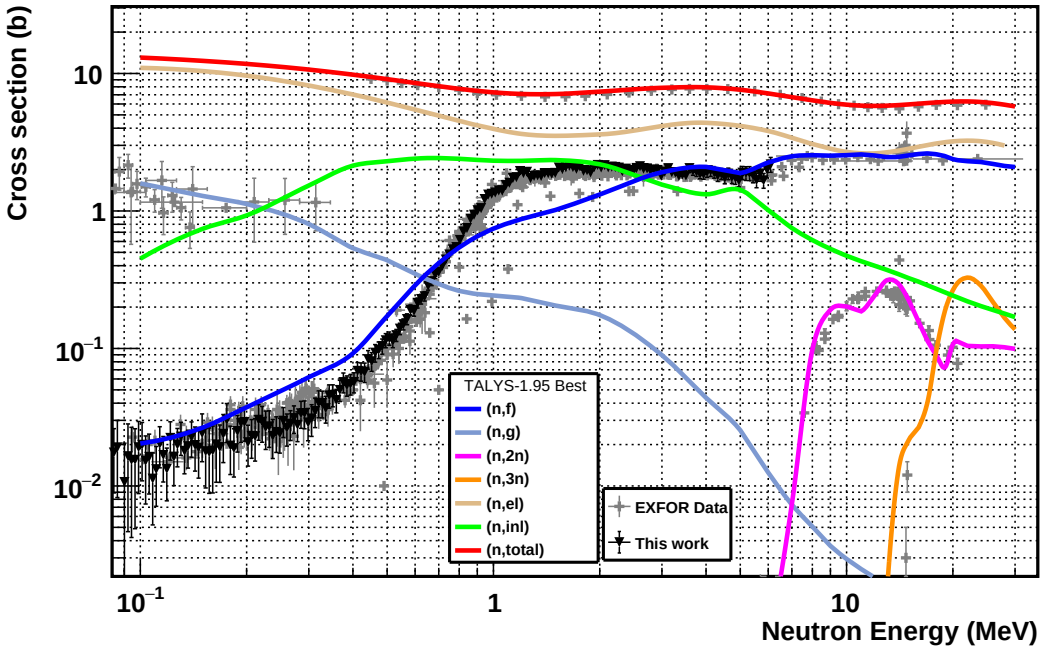

Figure 5.16: TALYS "best files" calculation for ^{241}Am for incident neutron energies in the range between $0.1 - 30$ MeV, along with all the available experimental data.

parameters of the ^{241}Am $+ n$ interaction. The average s-wave level spacing at the neutron separation energy S_n, which is typically determined from the available experimental set of s-wave resonances, can be used in the FGM model to estimate the level density parameter a according to the following formula:

$$\frac{1}{D_0} = \sum_{J=|I-\frac{1}{2}|}^{J=I+\frac{1}{2}} \rho_F\left(S_n, J, \Pi\right) \tag{5.30}$$

where I is the spin of the target nucleus. Moreover, the level density parameter of ^{241}Am was increased only by 3%, whereas the one for ^{240}Am was increased by 15%. Last but not least, the most recent addition by Stephane Goriely and Vladimir Plujko, for the photon strength functions (PSF) (strength 9) available only in the most recent version 1.95 of TALYS, employing the Simplified Modified Lorentzian (SMLO) predictions, was applied for the modified calculation of TALYS, using the combination of the phenomenological CTM and FGM models. The outcomes of these calculations are shown in Figure 5.17, where overall a satisfactory reproduction for all the decay channels is observed. Especially for the fission channel, the theory follows smoothly the experimental data both in shape and absolute cross section value, from the threshold of the reaction up to approximately the second chance fission. Additionally, the $(n, 2n)$ channel which is the main competing channel above the $8\,MeV$, is also in agreement with the experimental cross section observables.

Americium Isotope	**Inner barrier**		**Outer barrier**	
	$\mathbf{V_A}$ **(MeV)**	$\hbar\omega_\mathbf{A}$ **(MeV)**	$\mathbf{V_B}$ **(MeV)**	$\hbar\omega_\mathbf{B}$ **(MeV)**
^{242}**Am**	6.32	0.65	5.78	0.43
^{241}**Am**	6.00	0.69	5.35	0.43
^{240}**Am**	6.00	0.59	4.56	0.43

Table 5.2: Fission barrier heights and widths for the Americium isotopes used in the default calculation of the TALYS code.

Americium Isotope	**Inner barrier**		**Outer barrier**	
	$\mathbf{V_A}$ **(MeV)**	$\hbar\omega_\mathbf{A}$ **(MeV)**	$\mathbf{V_B}$ **(MeV)**	$\hbar\omega_\mathbf{B}$ **(MeV)**
^{242}**Am**	6.15	0.54	5.2	0.8
^{241}**Am**	5.4	0.45	4.35	0.3
^{240}**Am**	5.5	0.9	5.5	0.4

Table 5.3: Fission barrier heights and widths for the Americium isotopes used in the modified calculation of the TALYS code.

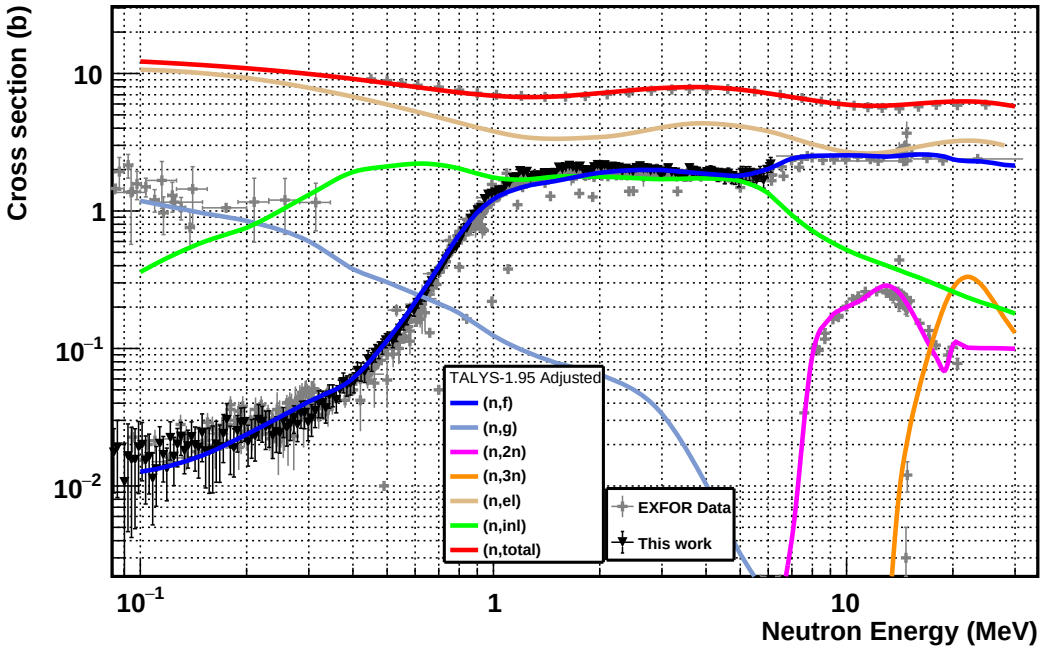

Figure 5.17: TALYS modified calculation using the combination of Constant Temperature + Fermi Gas models, by adjusting the fission barrier parameters and level densities of the Americium isotopes.

For the microscopic theoretical investigation, a separate set of calculations were performed with TALYS as mentioned previously, where the entire fission path is described by smoothly joined inverted parabolas as a function of the quadrupole deformation β in the framework of the Hartree-Fock-Bogolyubov (HFB) model. Again, this microscopic approach was initially tested with the default parameters of TALYS, using a suitable microscopic level density model available, that of Hilaire's combinatorial tables following the deformed Skyrme-Hartree-Fock-Bogolyubov framework in addition to a microscopic γ-ray strength function (strength 8). The results of these calculations are shown in Figure 5.18. Even though the (n, xn) reaction channels are accurately reproduced, the theoretical calculation of the fission channel from the threshold of the reaction up to the beginning of the second chance fission is completely off-track. In order to achieve a reasonable agreement of the microscopic theory with the experimental fission data of the ^{241}Am, a corresponding workflow was followed as in the previous scenario. In particular, necessary adjustments were performed regarding the fission barrier parameters and level densities of the involved Americium isotopes. The results of the modified microscopic calculations with the TALYS code of Figure 5.19 highlight a satisfactory reproduction of the cross section data from EXFOR, wherever available, for all the competing decay channels for the neutron energy range of 0.1 to 30 MeV.

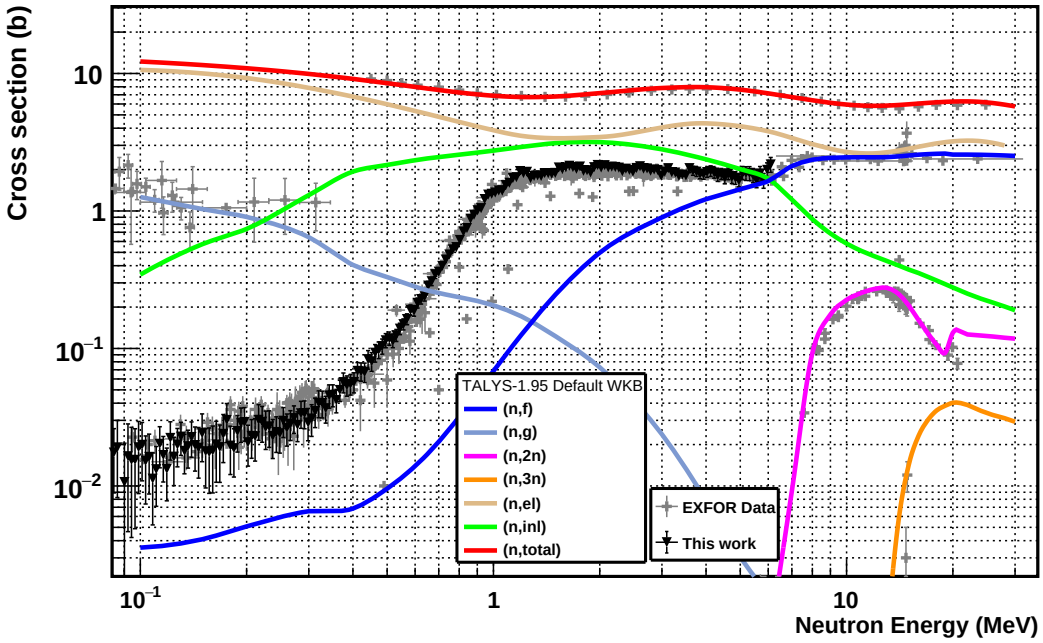

Figure 5.18: TALYS default microscopic calculation for ^{241}Am for incident neutron energies in the range between 0.1 to 30 MeV plotted together with the available experimental data retrieved from the EXFOR database.

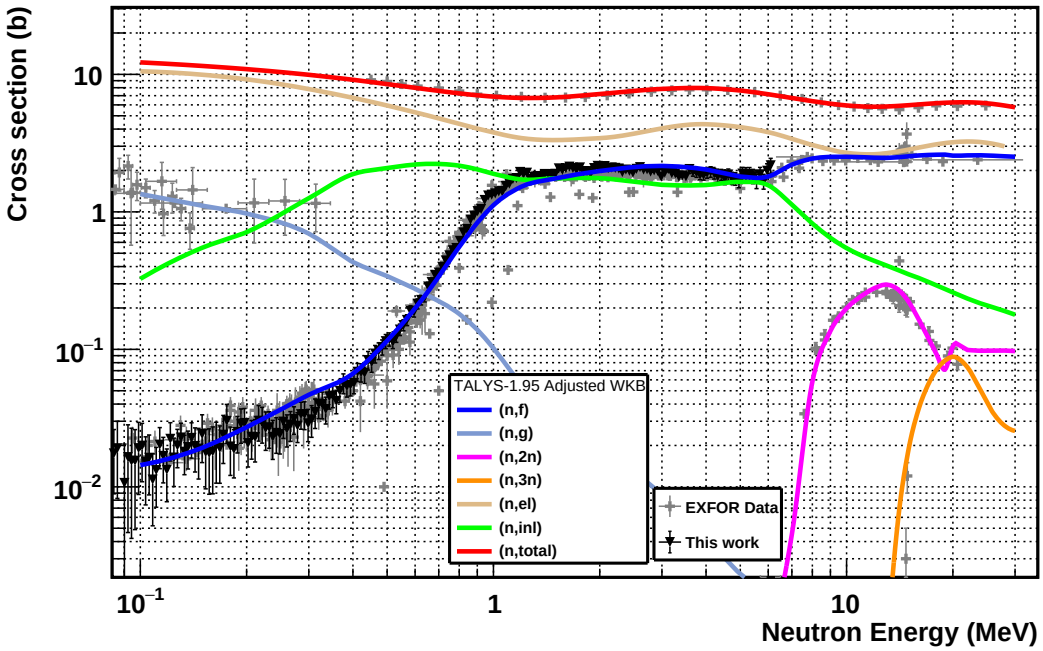

Figure 5.19: TALYS modified microscopic calculation for ^{241}Am for incident neutron energies in the range between 0.1 to 30 MeV plotted together with the available experimental data retrieved from the EXFOR database.

Chapter 6

Conclusions and Future Perspectives

Even though fission was discovered roughly 80 years ago, developing a thorough theoretical explanation with good predictive power is still a work in progress, while nuclear modelling requires a wealth of available experimental data for neutron-induced fission reaction cross sections and other observables. In parallel, the design and sensitivity studies of advanced nuclear systems and Generation IV Fast Neutron Reactors could incinerate/transmutate the existing nuclear waste of aging conventional reactors, producing safer and cleaner nuclear energy, free of greenhouse gas emissions. These systems require high precision cross section data from various neutron-induced fission reactions of minor actinides found in nuclear waste, for neutron energies ranging from thermal up to several tens of MeV. Among the long-lived minor actinides with high radioecological risk for the environment is the isotope ^{241}Am ($T_{1/2} = 433y$) which is present in high percentage in nuclear waste, representing about 1.8% of the mass of actinides in nuclear waste of Pressurised Water Reactors' (PWR) UO_X fuel. The importance of the cross section measurement of the neutron-induced fission of ^{241}Am is highlighted by the fact that the ^{241}Am(n,f) reaction is included by the Nuclear Energy Agency in the "Nuclear Data High Priority Request List".

Within this framework, the ^{241}Am(n,f) reaction cross section was measured using the time-of-flight technique at the vertical experimental beam line (EAR-2) at the n_TOF facility at CERN, located approximately at a neutron flight path of $19.5\,m$ above the Pb neutron spallation target and characterized by a high instantaneous neutron flux and a moderate resolution function. The experimental set-up of the measurement consisted of a stack of low mass Micromegas detectors that offer high efficiency for the detection of the energy deposition of the fission fragments in their active volume, as well as six thin radioactive ^{241}Am samples with a total activity of $0.1\,GBq$. The measurement was quite challenging, since for the first time such highly radioactive samples with a specific activity of $127\,MBq/mg$ were attempted to be measured in EAR-2 with the large aperture diameter "fission" collimator ($6.7\,cm$).

From this work, experimental cross section data of the ^{241}Am(n,f) reaction were obtained relative to ^{235}U, over a broad neutron energy range covering almost 10 orders of magnitude, from $9\,meV$ up to $6\,MeV$. The improvements in the design of preamplifier modules aimed at reducing the baseline oscillations and enhancing the signal-to-noise ratio. Moreover, for the present measurement, a dedicated gas regulation system was used in order to monitor the gas flow and pressure inside the fission chamber. These upgrades significantly improved the experimental conditions and the quality of the recorded data with respect to previous fission measurements carried out with a similar detection set-up at n_TOF.

The data analysis procedure involved many stages. In the initial steps it included the accurate selection of fission signals, a methodology for the "γ-flash" subtraction and the rejection of alpha particles, noise and unwanted pulses. Afterwards, Monte Carlo simulations were performed via GEF/GEANT4 for the study of the efficiency and the energy deposition of fission fragments in the active gas volume of the detector so as to estimate the necessary amplitude and pile-up corrections in the recorded pulse height spectra. Additionally, in order to perform in an accurate way the conversion of time-of-flight to neutron energy, the full 2-dimensional probability distribution of the moderation length λ, as a function of the time-of-flight, was included in the calculations. During the analysis, an unreported contamination of ^{239}Pu in the Americium samples was observed and a "fingerprint" resonance identification technique was followed in order to estimate the quantity of the contamination in the samples under study. Despite the satisfactory precision of the followed experimental investigation, no resonance analysis for the ^{241}Am samples was conducted, because the samples' formal characterization has not been yet completed.

In order to complement the cross section measurement, theoretical cross section calculations were performed with the TALYS-1.95 code. Satisfactory results for the fission cross section of ^{241}Am, as well as for other competitive neutron-induced reactions, namely (n, γ), (n, el), (n, inl), (n, xn) and (n, tot) channels were accomplished in the energy range from 0.1 to 30 MeV. The theoretical agreement with the available experimental data was achieved by adjusting the double-humped fission barrier parameters (heights and curvatures), in addition to level density parameters of the corresponding Americium isotopes, both in phenomenological and microscopic approach.

More precise cross section measurements could be possible, not only by using even faster electronics, but also by employing more sophisticated detectors with better timing characteristics that would expand the possibilities of experimental measurements. For instance, at some point we could think to move from standard to strip Micromegas detectors, in order to have the ability to also measure angular fission fragment distributions, which up to now within the n_TOF facility is only possible to study with Parallel Plate Avalanche Counters (PPACs).

As an extension of the present work, a future experiment was proposed to be conducted at the n_TOF facility during Phase-IV for the cross section determination of ^{243}Am(n,f) reaction [74], taking advantage of both experimental areas available for time-of-flight measurements (EAR-1 and EAR-2). The combination of the above mentioned experimental areas, as well as the implementation of a "hybrid" target configuration consisting of thick and thin samples of ^{243}Am ($T_{1/2} = 7364y$), optimized simultaneously for both areas, will result in the collection of data with satisfactory statistical uncertainty in a wide energy range. More specifically, the part of the measurement conducted in EAR-1 will cover the energy region from the fission threshold up to approximately 300 MeV, whereas in EAR-2 due to the high instantaneous neutron flux, the measurement is expected to profit from increased statistics both in the thermal and resonance region.

Bibliography

[1] http://pubsapp.acs.org/cen/80th/americium.html.

[2] https://periodic.lanl.gov/95.shtml.

[3] R. E. Krebs, *The history and use of our earth's chemical elements: a reference guide*. 2nd edition, Greenwood Press, 2006.

[4] https://www.nndc.bnl.gov/nudat3/.

[5] https://www.cosmos.esa.int/web/ulysses/rtg.

[6] J. S. Dustin and R. Borrelli, "Assessment of alternative radionuclides for use in a radioisotope thermoelectric generator," *Nuclear Engineering and Design* **385** (2021) 111475. https://www.sciencedirect.com/science/article/pii/S0029549321004271.

[7] J. S. Dustin and R. Borrelli, "Modeling of Am-241 as an alternative fuel source in a radioisotope thermoelectric generator," *Nuclear Engineering and Design* **385** (2021) 111495. https://www.sciencedirect.com/science/article/pii/S0029549321004477.

[8] https://inis.iaea.org/collection/NCLCollectionStore/_Public/16/006/16006734.pdf.

[9] https://www.gen-4.org/gif/.

[10] https://pris.iaea.org/PRIS/WorldStatistics/OperationalReactorsByCountry.aspx.

[11] https://pris.iaea.org/PRIS/WorldStatistics/NuclearShareofElectricityGeneration.aspx.

[12] https://chem.libretexts.org/Bookshelves/General_Chemistry/Map%3A_Chemistry_-_The_Central_Science_(Brown_et_al.)/21%3A_Nuclear_Chemistry/21.06%3A_Nuclear_Fission.

[13] *Nuclear Fuel Cycle Simulation System: Improvements and Applications*. No. 1864 in TECDOC Series. International Atomic Energy Agency, Vienna, 2019. https://www.iaea.org/publications/13502/nuclear-fuel-cycle-simulation-system-improvements-and-applications.

[14] R. Wigeland, T. Bauer, T. Fanning, and E. Morris, "Separations and Transmutation Criteria to Improve Utilization of a Geologic Repository," *Nuclear technology* **154** (04, 2006) 95–106.

[15] https://www.tpub.com/doenuclearphys/nuclearphysics50.htm.

[16] https://www.iaea.org/sites/default/files/16/11/np-parisagreement.pdf.

[17] A. Stanculescu, "Accelerator Driven Systems (ADSs) for nuclear transmutation," *Annals of Nuclear Energy* **62** (2013) 607–612. https://www.sciencedirect.com/science/article/pii/S0306454913000820.

[18] https://www.oecd-nea.org/dbdata/hprl/search.pl?vhp=on.

[19] www.nea.fr/html/science/wpec/volume26/volume26.pdf.

[20] I. Shaaban and M. Albarhoum, "A computational study of re-cycling the MTR research reactors with MOX fuel mixed with 241Am, 242Am and 243Am as burnable absorbers actinides using the MCNP4C code," *Annals of Nuclear Energy* **109** (2017) 626–634. https://www.sciencedirect.com/science/article/pii/S0306454916304200.

[21] A. Plompen, "Minor Actinides, Major Challenges, the Needs for and Benefits of International Collaboration," *Nuclear Data Sheets* **118** (2014) 78–84. https://www.sciencedirect.com/science/article/pii/S0090375214000374.

[22] https://publications.jrc.ec.europa.eu/repository/handle/JRC42917.

[23] J. W. T. Dabbs, C. H. Johnson, and C. E. Bemis Jr., "Measurement of the ^{241}Am Neutron Fission Cross Section," *Nuclear Science and Engineering* **83** no. 1, (1983) 22–36. https://doi.org/10.13182/NSE83-A17986.

[24] F. Belloni, M. Calviani, N. Colonna, P. Mastinu, and P. M. Milazzo et al., "Measurement of the neutron-induced fission cross-section of ^{241}Am at the time-of-flight facility n_TOF," *European Physical Journal A* **49** (Jan., 2013) 2.

[25] C. Rubbia, S. A. Andriamonje, D. Bouvet-Bensimon, S. Buono, R. Cappi, P. Cennini, C. Gelès, I. Goulas, Y. Kadi, P. Pavlopoulos, J. P. C. Revol, A. Tzima, and V. Vlachoudis, "A high resolution spallation driven facility at the CERN-PS to measure neutron cross sections in the interval from 1 eV to 250 MeV," tech. rep., CERN, Geneva, May, 1998. http://cds.cern.ch/record/357112.

[26] N. Colonna, A. Tsinganis, R. Vlastou, N. Patronis, M. Diakaki, S. Amaducci, M. Barbagallo, S. Bennett, E. Berthoumieux, M. Bacak, G. Cosentino, S. Cristallo, P. Finocchiaro, J. Heyse, D. Lewis, A. Manna, C. Massimi, E. Mendoza, M. Mirea, and P. Žugec, "The fission experimental programme at the CERN n_TOF facility: status and perspectives," *The European Physical Journal A* **56** (02, 2020) .

[27] C. Weiß, E. Chiaveri, S. Girod, V. Vlachoudis, O. Aberle, S. Barros, I. Bergström, E. Berthoumieux, M. Calviani, C. Guerrero, M. Sabaté-Gilarte, and A. Tsinganis et al., "The new vertical neutron beam line at the CERN n_TOF facility design and outlook on the performance," *Nuclear Instruments and Methods in Physics Research Section A:*

Accelerators, Spectrometers, Detectors and Associated Equipment **799** (2015) 90–98. https://www.sciencedirect.com/science/article/pii/S0168900215008566.

[28] T. Böhlen, F. Cerutti, M. Chin, A. Fassò, A. Ferrari, P. Ortega, A. Mairani, P. Sala, G. Smirnov, and V. Vlachoudis, "The FLUKA Code: Developments and Challenges for High Energy and Medical Applications," *Nuclear Data Sheets* **120** (2014) 211–214. https://www.sciencedirect.com/science/article/pii/S0090375214005018.

[29] Y. Giomataris, "Development and prospects of the new gaseous detector 'Micromegas'," *Nucl. Instrum. Meth. A* **419** (1998) 239–250.

[30] G. Charpak, J. Derré, Y. Giomataris, and P. Rebourgeard, "Micromegas, a multipurpose gaseous detector," *Nuclear Instruments and Methods in Physics Research Section A: Accelerators, Spectrometers, Detectors and Associated Equipment* **478** no. 1, (2002) 26–36. https://www.sciencedirect.com/science/article/pii/S0168900201017132. Proceedings of the ninth Int.Conf. on Instrumentation.

[31] https://spdevices.com/images/stories/press_releases/15-1404-news_release_spd_cern_20150130.pdf.

[32] U. Abbondanno, G. Aerts, F. Lvarez, H. Lvarez, S. Andriamonje, J. Andrzejewski, G. Badurek, P. Baumann, F. Beca, J. Benlliure, E. Berthomieux, B. Betev, F. Calviño, D. Ott, R. Capote, P. Cennini, V. Chepel, E. Chiaveri, N. Colonna, and K. Wisshak, "The data acquisition system of the neutron time-of-flight facility n_TOF at CERN," *Nuclear Instruments and Methods in Physics Research Section A Accelerators Spectrometers Detectors and Associated Equipment* **538** (02, 2005) 692–702.

[33] https://imagej.nih.gov/ij/index.html.

[34] P. Žugec, C. Weiß, C. Guerrero, F. Gunsing, V. Vlachoudis, M. Sabate-Gilarte, A. Stamatopoulos, T. Wright, J. Lerendegui-Marco, F. Mingrone, J. Ryan, S. Warren, A. Tsinganis, and M. Barbagallo, "Pulse processing routines for neutron time-of-flight data," *Nuclear Instruments and Methods in Physics Research Section A: Accelerators, Spectrometers, Detectors and Associated Equipment* **812** (2016) 134–144. https://www.sciencedirect.com/science/article/pii/S0168900215016344.

[35] https://www-nds.iaea.org/relnsd/nubase/nubase_min.html#lastnuc=241AM.

[36] https://www-nds.iaea.org/relnsd/nubase/nubase_min.html#lastnuc=235U.

[37] https://www-nds.iaea.org/relnsd/nubase/nubase_min.html#lastnuc=238U.

[38] https://www.lp2ib.in2p3.fr/nucleaire/nex/gef/.

[39] S. Agostinelli et al., "Geant4—a simulation toolkit," *Nuclear Instruments and Methods in Physics Research Section A: Accelerators, Spectrometers, Detectors and Associated Equipment* **506** no. 3, (2003) 250–303. https://www.sciencedirect.com/science/article/pii/S0168900203013688.

[40] J. Allison et al., "Recent developments in Geant4," *Nuclear Instruments and Methods in Physics Research Section A: Accelerators, Spectrometers, Detectors and Associated Equipment* **835** (2016) 186–225. https://www.sciencedirect.com/science/article/pii/S0168900216306957.

[41] J. Allison et al., "Geant4 developments and applications," *IEEE Transactions on Nuclear Science* **53** no. 1, (2006) 270–278.

[42] R.Kirk and D.Othmer, *Encyclopedia of Chemical Technology, 4th Edition*. John Wiley and Sons, 2004.

[43] http://amdc.impcas.ac.cn/masstables/Ame2016/mass16.txt.

[44] G. F. Knoll, *Radiation Detection and Measurement*. John Wiley and Sons, New York, 2010.

[45] S. Usman and A. Patil, "Radiation detector deadtime and pile up: A review of the status of science," *Nuclear Engineering and Technology* **50** no. 7, (2018) 1006–1016. https://www.sciencedirect.com/science/article/pii/S1738573318302596.

[46] D. Brown, M. Chadwick, R. Capote, A. Kahler, A. Trkov, and M. Herman et al., "ENDF/B-VIII.0: The 8th Major Release of the Nuclear Reaction Data Library with CIELO-project Cross Sections, New Standards and Thermal Scattering Data," *Nuclear Data Sheets* **148** (2018) 1–142. https://www.sciencedirect.com/science/article/pii/S0090375218300206. Special Issue on Nuclear Reaction Data.

[47] A. J. M. Plompen et al. , "The joint evaluated fission and fusion nuclear data library, JEFF-3.3" *Eur. Phys. J. A* **56** no. 7, (2020) 181. https://doi.org/10.1140/epja/s10050-020-00141-9.

[48] J. Chadwick, "Possible Existence of a Neutron," *Nature* **129** (1932) 312. https://www.nature.com/articles/129312a0.

[49] E. Fermi, "Radioactivity Induced by Neutron Bombardment," *Nature* **133** (1934) 757. https://www.nature.com/articles/133757a0.

[50] G. Gamow, "Mass defect curve and nuclear constitution," *Proc. R. Soc. Lond.* **126** (1930) 632–644. https://royalsocietypublishing.org/doi/10.1098/rspa.1930.0032.

[51] L. Meitner and O. Frisch, "Disintegration of Uranium by Neutrons: a New Type of Nuclear Reaction," *Nature* **143** (1939) 239–240. https://www.nature.com/articles/143239a0.

[52] L. Meitner and O. Frisch, "Products of the Fission of the Uranium Nucleus," *Nature* **143** (1939) 471–472. https://www.nature.com/articles/143471a0.

[53] O. Hahn and F. Strassmann, "Über den Nachweis und das Verhalten der bei der Bestrahlung des Urans mittels Neutronen entstehenden Erdalkalimetalle," *Naturwissenschaften* **27** (1939) 11–15. https://doi.org/10.1007/BF01488241.

[54] N. Bohr and J. A. Wheeler, "The Mechanism of Nuclear Fission," *Phys. Rev.* **56** (Sep, 1939) 426–450. https://link.aps.org/doi/10.1103/PhysRev.56.426.

[55] R. Vandenbosch and J. R. Huizenga, *Nuclear fission*. Academic Press, New York, NY, 1973.

[56] C. Wagemans, *The nuclear fission process*. CRC Press, United States, 1991. https://www.osti.gov/biblio/6430419.

[57] A. Cole, *Statistical Models for Nuclear Decay: From Evaporation to Vaporization*. Taylor and Francis, 2000. https://doi.org/10.1201/9781420033472.

[58] K. S. Krane, *Introductory nuclear physics*. Wiley, New York, NY, 1988. https://www.wiley.com/en-ie/Introductory+Nuclear+Physics,+3rd+Edition-p-9780471805533.

[59] V. Strutinsky, "Shell effects in nuclear masses and deformation energies," *Nuclear Physics A* **95** no. 2, (1967) 420–442. https://www.sciencedirect.com/science/article/pii/0375947467905106.

[60] M. Brack, J. Damgaard, A. S. Jensen, H. C. Pauli, V. M. Strutinsky, and C. Y. Wong, "Funny hills: The shell-correction approach to nuclear shell effects and its applications to the fission process," *Rev. Mod. Phys.* **44** (Apr, 1972) 320–405. https://link.aps.org/doi/10.1103/RevModPhys.44.320.

[61] V. Strutinsky, ""Shells" in deformed nuclei," *Nuclear Physics A* **122** no. 1, (1968) 1–33. https://www.sciencedirect.com/science/article/pii/0375947468906994.

[62] S. Bjørnholm and J. E. Lynn, "The double-humped fission barrier," *Rev. Mod. Phys.* **52** (Oct, 1980) 725–931. https://link.aps.org/doi/10.1103/RevModPhys.52.725.

[63] G. Choppin, J.-O. Liljenzin, J. Rydberg, and C. Ekberg, "Chapter 11 - Mechanisms and Models of Nuclear Reactions," in *Radiochemistry and Nuclear Chemistry (Fourth Edition)*, G. Choppin, J.-O. Liljenzin, J. Rydberg, and C. Ekberg, eds., pp. 313–338. Academic Press, Oxford, fourth edition ed., 2013. https://www.sciencedirect.com/science/article/pii/B9780124058972000112.

[64] P. Möller and J. Nix, "Calculation of fission barriers," in *Proceedings of the Third IAEA Symposium on the Physics and Chemistry of Fission*, vol. Physics and Chemistry of Fission 1, pp. 103–143. Rochester, New York, 1974.

[65] M. Sin, R. Capote, A. Ventura, M. Herman, and P. ObložinskÝ, "Fission of light actinides: ^{232}Th(n,f) and ^{231}Pa(n,f) reactions," *Phys. Rev. C* **74** (Jul, 2006) 014608. https://link.aps.org/doi/10.1103/PhysRevC.74.014608.

[66] https://www.fuw.edu.pl/~dobaczew/FoF/S2.html.

[67] A. J. Koning, S. Hilaire, and M. C. Duijvestijn, "TALYS: Comprehensive Nuclear Reaction Modeling," *AIP Conference Proceedings* **769** no. 1, (2005) 1154–1159. https://aip.scitation.org/doi/abs/10.1063/1.1945212.

[68] W. Hauser and H. Feshbach, "The Inelastic Scattering of Neutrons," *Phys. Rev.* **87** (Jul, 1952) 366–373. https://link.aps.org/doi/10.1103/PhysRev.87.366.

[69] https://www-nds.iaea.org/publications/indc/indc-blr-0013/.

[70] R. Capote, M. Herman, P. Obložinský, P. Young, S. Goriely, T. Belgya, A. Ignatyuk, A. Koning, S. Hilaire, V. Plujko, M. Avrigeanu, O. Bersillon, M. Chadwick, T. Fukahori, Z. Ge, Y. Han, S. Kailas, J. Kopecky, V. Maslov, G. Reffo, M. Sin, E. Soukhovitskii, and P. Talou, "RIPL – Reference Input Parameter Library for Calculation of Nuclear Reactions and Nuclear Data Evaluations," *Nuclear Data Sheets* **110** no. 12, (2009) 3107–3214. https://www.sciencedirect.com/science/article/pii/S0090375209000994. Special Issue on Nuclear Reaction Data.

[71] M. Herman, M. Herman, R. Capote, M. Sin, A. Trkov, B. V. Carlson, P. Oblozinsky, C. M. Mattoon, H. Wienke, S. Hoblit, Y. S. Cho, G. P. Nobre, V. Plujko, and V. Zerkin, "EMPIRE-3.2 Malta modular system for nuclear reaction calculations and nuclear data evaluation Users Manual,". https://www.osti.gov/biblio/1108585.

[72] E. S. Soukhovitskii, S. Chiba, J.-Y. Lee, O. Iwamoto, and T. Fukahori, "Global coupled-channel optical potential for nucleon–actinide interaction from 1 keV to 200 MeV," *Journal of Physics G: Nuclear and Particle Physics* **30** no. 7, (May, 2004) 905–920. https://doi.org/10.1088/0954-3899/30/7/007.

[73] J. Kopecky and M. Uhl, "Test of gamma-ray strength functions in nuclear reaction model calculations," *Phys. Rev. C* **41** (May, 1990) 1941–1955. https://link.aps.org/doi/10.1103/PhysRevC.41.1941.

[74] N. Patronis, Z. Eleme, M. Diakaki, A. Tsinganis, R. Vlastou, M. Kokkoris, M.-E. Stamati, V. Michalopoulou, A. Stamatopoulos, M. Barbagallo, N. Colonna, J. Heyse, M. Mastromarco, A. Mengoni, A. Moens, G. Noguere, A. J. Praena, P. Schillebeeckx, G. Sibbens, L. Tassan-Got, and D. Vanleeuw, "Measurement of the fission cross-section of ^{243}Am at EAR-1 and EAR-2 of the CERN n_TOF facility," tech. rep., CERN, Geneva, 2020. https://cds.cern.ch/record/2730930.